NASA
Technical
Paper
2352

September 1984

136p.

Effects of Tail Span and Empennage Arrangement on Drag of a Typical Single-Engine Fighter Aft End

James R. Burley II
and Bobby L. Berrier

(NASA-TP-2352) EFFECTS OF TAIL SPAN AND EMPENNAGE ARRANGEMENT ON DRAG OF A TYPICAL SINGLE-ENGINE FIGHTER AFT END (NASA) 136 p CSCL 01A

N87-10833

Unclas

H1/02 43836

[redacted]

NASA

NASA
Technical
Paper
2352

1984

Effects of Tail Span and Empennage Arrangement on Drag of a Typical Single-Engine Fighter Aft End

James R. Burley II
and Bobby L. Berrier

Langley Research Center
Hampton, Virginia

[redacted]

NASA
National Aeronautics
and Space Administration

Scientific and Technical
Information Branch

Summary

An investigation has been conducted in the Langley 16-Foot Transonic Tunnel to determine the effects of tail span and empennage arrangement on drag of a single-engine nozzle/afterbody model. Tests were conducted at Mach numbers from 0.50 to 1.20, nozzle pressure ratios from 1.0 (jet off) to 8.0, and angles of attack from $-3°$ to $9°$, depending upon Mach number. Three empennage arrangements (aft, staggered, and forward) were investigated with several different tail spans.

The results of the investigation indicate that tail span and position have a significant effect on the drag at transonic speeds. The full-span aft-tails arrangement was representative of current single-engine fighters and produced the highest drag and interference drag of all configurations tested. The unfavorable tail interference was largely due to the outer portion of the tail surfaces. The inner portion near the nozzle and afterbody did little to increase drag other than surface skin friction. Locating the tails forward of the nozzle generally reduced the unfavorable tail interference.

Introduction

Past experimental investigations (refs. 1 to 3) on current high-performance fighter aircraft concepts have shown that sizable airplane performance penalties are associated with the integration of the propulsion system into the airframe. Drag penalties on the nozzle and afterbody can result from interference effects originating from base areas, horizontal and vertical tails, ventral fins, tail actuator housings, and structural support booms (ref. 4). The horizontal and vertical tails have been found to be the major contributor to the afterbody/nozzle drag problem (refs. 5 to 8). These drag penalties can be especially acute when the nozzle operates in a closed-down (dry or partial afterburning) mode (ref. 8).

Because of the large effect of tail surfaces on afterbody/nozzle drag, an extensive experimental program to determine these effects on single- and twin-engine fighter aft-end configurations is being conducted at the Langley Research Center. A summary of this experimental program is reported in reference 9. Detailed data can be found in references 8 and 10 for single-engine configurations and in references 11 to 13 for twin-engine configurations. The present paper addresses the effects of tail span and empennage arrangement on afterbody/nozzle drag of a single-engine fighter aft end.

The investigation was conducted in the Langley 16-Foot Transonic Tunnel at Mach numbers from 0.50 to 1.20. The axisymmetric single-engine propulsion model was investigated with three different empennage arrangements; namely, aft tails, staggered tails (vertical tail forward, horizontal tails aft), and forward tails. Tail spans (relative to full-span tails) of 100, 75, 50, 30, 20, 10, and 0 percent (tails off) were investigated for each empennage arrangement. A typical dry power convergent-divergent nozzle was installed for the entire test. Nozzle pressure ratio was varied from 1.0 (jet-off) to 8.0, depending on Mach number, and angle of attack was varied from $-3°$ to $9°$ at selected subsonic Mach numbers and from $-3°$ to $6°$ at a Mach number of 1.20.

Symbols

A_{an}	area of annular clearance gap at model base, meters^2
A_{int}	internal cross-sectional area of afterbody and nozzle outer shell, 0.0171 meter^2
A_{ref}	reference area (cross-sectional area at metric break), 0.0273 meter^2
b	span (root to tip excluding root filler) of baseline tail surface (used for both vertical and horizontal tails), meters
C_D	drag coefficient
$C_{D,a}$	afterbody drag coefficient, $D_a/q_\infty A_{\text{ref}}$
$C_{D,n}$	nozzle drag coefficient, $D_n/q_\infty A_{\text{ref}}$
$C_{D,pn}$	nozzle pressure drag coefficient, $D_{p,n}/q_\infty A_{\text{ref}}$
$C_{D,t}$	total aft-end drag coefficient, $D_t/q_\infty A_{\text{ref}}$
$C_{D,\text{tails}}$	tail drag coefficient, $D_{\text{tails}}/q_\infty A_{\text{ref}}$
$\Delta C_{D,ia}$	increment in tail interference drag coefficient on afterbody, $\Delta D_{i,a}/q_\infty A_{\text{ref}}$
$\Delta C_{D,in}$	increment in tail interference drag coefficient on nozzle, $\Delta D_{i,n}/q_\infty A_{\text{ref}}$
$\Delta C_{D,it}$	increment in tail interference drag coefficient on total aft end, $\Delta D_{i,t}/q_\infty A_{\text{ref}}$
C_p	static-pressure coefficient, $(p_l - p_\infty)/q_\infty$
D_a	afterbody drag, newtons
D_{bal}	drag measured by balance, newtons
D_n	nozzle drag, newtons
$D_{p,n}$	nozzle pressure drag, newtons
D_t	total aft-end drag (afterbody, nozzle, and tails), newtons
D_{tails}	tail drag, newtons
$\Delta D_{i,a}$	increment in tail interference drag on afterbody, newtons

$\Delta D_{i,n}$	increment in tail interference drag on nozzle, newtons
$\Delta D_{i,t}$	increment in tail interference drag on total aft end, newtons
d_{ref}	reference diameter (diameter at metric break), 0.1864 meter
L	model length, 1.6747 meters
l	length of nozzle, 0.1713 meter
M	free-stream Mach number
NPR	nozzle pressure ratio, $p_{t,j}/p_{\infty}$
p_{an}	local pressure at nozzle annular clearance gap, newtons per meter^2
p_{int}	internal static pressure, newtons per meter^2
p_l	local static pressure, newtons per meter^2
$p_{t,j}$	jet total pressure, newtons per meter^2
p_{∞}	free-stream static pressure, newtons per meter^2
q_{∞}	free-stream dynamic pressure, newtons per meter^2
r	radius, meters
r_{ref}	reference radius (radius at metric break), 0.0932 meter
t/c	tail thickness ratio
X	axial distance from model nose, positive downstream, meters
x	axial distance from nozzle connect station, positive downstream, meters
y	distance from root to tip (excluding root filler) of tail surface (used for both vertical and horizontal tails), meters
α	model angle of attack, degrees
Λ	tail leading-edge sweep angle, degrees
ϕ	meridian angle about model axis, positive in clockwise direction when facing upstream, degrees

Abbreviations:

L.E.	leading edge
sta.	model station

Apparatus and Methods

Wind Tunnel

The experimental investigation was conducted in the Langley 16-Foot Transonic Tunnel, a single-return atmospheric tunnel with a slotted octagonal test section and continuous air exchange. The wind tunnel has a variable airspeed up to a Mach number of 1.30. Test-section plenum suction is used for speeds above Mach 1.10. A complete description of this facility and its operating characteristics can be found in reference 14.

Model and Support System

A sketch of the sting-strut-supported single-engine model with a dry power nozzle installed is presented in figure 1, and a photograph of the model installed in the Langley 16-Foot Transonic Tunnel is shown in figure 2. The overall model arrangement represents a typical single-engine fighter aft end and is composed of four major parts, located as follows:

	X, cm	X/L
Forebody	0–89.38	0–0.534
Afterbody	89.38–150.34	0.543–0.898
Nozzle	150.34–167.47	0.898–1.000
Empennage surfaces	Variable	Variable

The term "aft end" in this paper refers to the metric portion of the model (that portion on which forces and moments are measured) beginning at the metric break (sta. 89.38 cm) and includes the afterbody, nozzle, and tail surfaces when present. The axisymmetric forebody was nonmetric. As shown in figure 1, a 0.15-cm gap in the external skin at the metric break station prevented fouling between the nonmetric forebody and metric aft end. A Du Pont Teflon strip inserted into grooves machined into the forebody and aft end was used as a seal to prevent external flow from entering the model. The metric aft end was attached to a six-component strain-gage balance which was grounded to the nonmetric internal air system. A 0.16-cm annular clearance gap between the external and internal nozzle parts was required to prevent fouling between the metric aft end and the nonmetric internal air system.

The centerline of the model was located on the centerline of the wind tunnel. A complete description of the model support system can be found in reference 14. The nozzle exhaust flow was simulated by a continuous flow of clean, dry air at a controlled temperature of about 291 K and was provided by an external high-pressure air supply.

The geometric details of the axisymmetric afterbody (sta. 89.38 cm to 150.34 cm) are presented in figure 3.

The afterbody was designed to simulate afterbody closure ahead of the nozzle typical of a single-engine fighter configuration. The afterbody had provisions for mounting the vertical and horizontal tails at two different axial locations (forward and aft). Sketches showing geometric details of the tail surfaces are presented in figure 4. The tails were tested individually (vertical tail alone and horizontal tails alone) and in combinations utilizing both the forward and aft axial locations (aft, staggered, and forward tails). Each empennage arrangement was investigated with different tail spans; values of y/b (ratio of tail span to baseline tail span) from 1.00 (baseline tail span) to 0.10 were obtained by successive simultaneous cutting of the baseline horizontal and vertical tail surfaces at the locations shown in figure 4. A value of y/b equal to 0.00 was obtained by testing the model with tails off. The baseline vertical and horizontal tails ($y/b = 1.00$) were sized with the afterbody and nozzle areas to be representative of a typical single-engine fighter configuration.

A sketch showing geometry details of the nozzle used in this investigation is presented in figure 5. For the current investigation, nozzle geometry was not varied and an existing nozzle was used. Since empennage interference effects can be especially large when the nozzle operates in a dry power mode (ref. 8), the existing long, subsonic-cruise, dry power nozzle reported in reference 10 was selected for the current test. This nozzle simulated a variable-geometry (fixed in dry power mode for current test), convergent-divergent, conical nozzle typical of those currently in use on modern fighter aircraft.

Instrumentation

External static-pressure orifices were located on the afterbody and nozzle at the locations indicated in figures 3 and 5. Stagnation pressure and temperature of the jet exhaust were measured just ahead of the nozzle throat as indicated in figure 1.

Forces and moments on the metric aft end (afterbody, nozzle, and tails) were measured with a temperature-compensated six-component strain-gage balance. Forces on the internal flow system (thrust) were not measured. Four internal cavity pressures and two pressures in the annular gap between the inner and outer nozzle hardware were measured for pressure-area corrections to the balance data.

Tests

Data were obtained at an angle of attack of 0° at Mach numbers from 0.50 to 1.20. Nozzle pressure ratio was varied from 1.0 (jet-off) to 8.0, depending on Mach number. At selected Mach numbers and nozzle pressure ratios, angle of attack was varied from −3° to 9° at subsonic Mach numbers and from −3° to 6° at $M = 1.20$. Reynolds number based on model length L varied from approximately 1.7×10^7 at $M = 0.50$ to 2.4×10^7 at $M = 1.20$. To ensure a turbulent boundary layer over the aft end, a 0.38-cm-wide transition strip of No. 100 grit was fixed 5.72 cm from the model nose. Transition strips, 0.13 cm wide, of No. 90 grit were fixed 2.08 cm and 1.61 cm from the leading edges of the vertical and horizontal tails, respectively.

Data Reduction

All data for both the model and wind tunnel were recorded simultaneously by computer on magnetic tape. Fifty frames of data taken at a rate of 10 frames per second were averaged for each data point; these average values were used to compute standard force and pressure coefficients. All force coefficients in this report are referenced to the model cross-sectional area at the metric break.

The drag as measured by the balance D_{bal} includes external and internal axial forces on the afterbody/nozzle external shell. The drag D_{bal} also includes base drag, jet effects on the external shell, and tail drag when tails are present. The internal forces are computed from

$$D_{\text{int}} = \sum_{k=1}^{4} (p_{\text{int},k} - p_\infty) \frac{A_{\text{int}}}{4}$$

and are a result of the model design. The drag D_{int} would not be present in a real aircraft, and D_{an} accounts for the annular clearance gap between the nozzle internal and external hardware. (See fig. 5.) This term

$$D_{an} = \sum_{k=1}^{2} (p_{an,k} - p_\infty) \frac{A_{an}}{2}$$

is not felt by the balance but is included in the total aft-end drag D_t, which is defined as

$$D_t = D_{\text{bal}} - D_{\text{int}} - D_{an}$$

and represents the total drag acting on the afterbody, nozzle, and tails.

Nozzle drag D_n was obtained by adding nozzle pressure drag to a computed value of nozzle skin-friction drag. Nozzle pressure drag was obtained by a pressure-area integration of measured static pressures over the external nozzle boattail surface. Nozzle skin-friction drag was computed from the Frank and Voishel equation given in reference 15 (page 1109).

Tail drag D_{tails} was computed for each tail-on configuration and was composed of friction drag plus form drag at subsonic speeds ($M < 0.89$) and friction drag plus wave drag at supersonic speeds ($M > 1.00$). For M greater than 0.89 and less than 1.00, a smooth fairing between the subsonic and supersonic values was used to obtain tail drag. Friction drag and wave drag were computed from methods outlined in references 15 and 16, respectively. Subsonic form factors for the tails were obtained from empirical correlations of unpublished NASA data and may be calculated from

$$\text{Form factor} = 1.0 + 1.44(t/c) + 2.0(t/c)^2$$

Since all definitions and increments that utilize D_{tails} were computed at $\alpha = 0°$ only, it was not necessary to include drag due to lift in the term D_{tails}. Afterbody drag D_a can be obtained for each configuration from

$$D_a = D_t - D_n - D_{\text{tails}}$$

One of the primary objectives of this investigation was to determine empennage interference on aft-end drag. Empennage interference-drag increments on the total aft end were obtained from

$$\Delta D_{i,t} = (D_t)_{\text{tails on}} - (D_t)_{\text{tails off}} - D_{\text{tails}}$$

where $(D_t)_{\text{tails on}}$ is the experimentally measured value of tail-on aft-end drag (afterbody, nozzle, and tails), $(D_t)_{\text{tails off}}$ is the experimentally measured value of tail-off aft-end drag (afterbody and nozzle), and D_{tails} is the computed value of tail drag. Positive values of $\Delta D_{i,t}$ indicate adverse interference effects of tail surfaces on aft-end drag. Tail interference drag increments on the nozzle alone were obtained from

$$\Delta D_{i,n} = (D_n)_{\text{tails on}} - (D_n)_{\text{tails off}}$$

Tail interference drag increments on the afterbody alone can be computed from

$$\Delta D_{i,a} = \Delta D_{i,t} - \Delta D_{i,n}$$

Note that any interference effects on the tails themselves (assumed to be negligible) are included in the afterbody interference drag term $\Delta D_{i,a}$.

Presentation of Results

The results of this investigation are plotted in coefficient form in the following figures:

Discussion

Basic Data

Total aft-end drag coefficient $C_{D,t}$ and nozzle pressure drag coefficient $C_{D,pn}$ for each test configuration are presented in figures 6 through 11. Drag coefficients are presented as a function of nozzle pressure ratio at a nominally constant angle of attack of 0° on the left side of each figure and as a function of angle of attack at a nominally constant nozzle pressure ratio (typical engine operating value at each Mach number, see fig. 14) on the right side of each figure. Note that angle of attack was varied only at selected Mach numbers. The effect of support system interference on the current model was evaluated in reference 10 and found to have little or no effect on the metric aft end.

Aft-end drag and nozzle pressure drag exhibit expected variations with increasing nozzle pressure ratio. As a result of a base bleed effect, a drag reduction generally occurs with initial operation of the jet (low NPR). As nozzle pressure ratio is increased, aft-end drag and nozzle pressure drag increase as a result of the aspiration caused by the pumping action of the jet exhaust. Jet-on drag reaches a maximum at a nozzle pressure ratio generally between 3.0 and 4.0, and any further increase in nozzle pressure ratio reduces drag as the compression region at the nozzle exit increases in strength with growth of the jet exhaust plume.

Although the effects of angle of attack are small when the horizontal tails were not present (figs. 6 and 7), increasing angle of attack tended to slightly increase total aft-end drag and decrease nozzle pressure drag. With horizontal tails installed (figs. 8 to 11), total aft-end drag (includes tail drag) is significantly increased by increasing angle of attack. This result was expected because of drag due to lift on the horizontal tails.

The effect of angle of attack on nozzle pressure drag (horizontal tails installed) is generally small when compared with the effect on total aft-end drag and appears to be dependent on tail span. It is reasonable to assume that the horizontal tails at lifting angles of attack induce a substantial downwash in the nozzle region. The increased velocities, hence lower static pressures, acting on the rearward sloping boattail result in higher nozzle drag at lifting angles of attack. The trend that nozzle drag decreases with decreasing span is consistent with the fact that centerline downwash would diminish as the tail aspect ratio is reduced. The conclusion is that nozzle drag can be reduced by separating the nozzle from the horizontal tail downwash field, that is, moving the tail surfaces forward. This conclusion is consistent with nozzle drag data of figures 10 and 11 which show the forward horizontal tail arrangement to have less nozzle drag at angle of attack than the aft one. Similar empennage arrangement effects on nozzle drag could be expected from the vertical tail under sideslip conditions.

Pressure Distributions

The effects of tail span on afterbody/nozzle pressure distributions at four meridian angles are shown in figure 12. Since tail interference effects have been found to be largest at transonic speeds (ref. 8), data are presented for Mach numbers of 0.95 and 1.20 only. For clarity, only tail-off ($y/b = 0.00$) data have been faired; differences between tail-on ($y/b > 0.00$) data and tail-off data constitute tail interference.

Several observations about the data of figure 12 can be made. First, by examining the most isolated row of pressures ($\phi = 180°$), it is clear that tail interference effects are not localized but feed around the entire nozzle. Also, as expected, tail interference effects increase with increasing number of tail surfaces. (Compare data at $\phi = 180°$ for one surface, fig. 12(a); two surfaces, fig. 12(b); and three surfaces, fig. 12(c).) Second, at $M = 0.95$, the separation point moves upstream for $y/b \geq 0.50$ as the number of tail surfaces increases. The increased flow separation caused substantially lower pressures over the aft portion of the nozzle boattail. Similar results were indicated by ink flow photographs in reference 8. Last, installation of tails of any span generally decreased measured pressure coefficients on the afterbody ($\phi = 315°$). This result would indicate an adverse tail interference on the afterbody and increased afterbody drag.

The effect of tail arrangement on afterbody/nozzle static pressure distributions for several different tail spans is presented in figure 13. The aft tail arrangement generally produced the most adverse pressure distributions over the afterbody and nozzle. At $M = 0.95$, severe flow separation on the nozzle occurred for the aft tail arrangement. Separation was significantly reduced by moving the vertical tail forward (staggered tail arrangement). With exception of the first afterbody pressure measurement ($x/\imath = -0.627$), the most positive pressure coefficients on the afterbody and nozzle are shown for the forward tails. In fact, the pressures measured on the nozzle ($x/\imath > 0.0$) would indicate a favorable tail interference (tail-on pressure higher than tail-off pressure) for the forward tails. Similar results on the effects of empennage arrangement are reported in reference 10.

Drag Characteristics

Total aft end. The effect of tail span on total aft-end drag coefficient with Mach number for each tail arrangement investigated is presented in figure 16. The drag coefficient $C_{D,t}$ increases with tail span largely because of the increase in skin-friction drag associated with tail surface area. Above the critical Mach number of 0.85, wave drag and interference drag become significant parts of the total aft-end drag. The effect of tail span on the total aft-end tail interference coefficient increment $\Delta C_{D,it}$ is shown in figure 17. Below the critical Mach number, the tail interference is negligible; however, at Mach number 0.95 and to a lesser extent at Mach number 1.20, the tail interference is significant and can amount to as much as 30 percent of the total aft-end drag (ref. 10, aft tails at $M = 0.95$). The data show that total aft-end drag and total tail interference drag coefficients increase with tail span above Mach number 0.85 regardless of the tail arrangement. Staggered tails produce the least adverse interference below Mach number 1.00; however, above 1.00, the forward tail arrangement produces the least adverse interference.

Nozzle. Variations of nozzle drag coefficient $C_{D,n}$ and nozzle tail interference drag coefficient increment $\Delta C_{D,in}$ with tail span for different tail arrangements are shown in figures 18 and 19, respectively. Negative nozzle drag (thrust) was measured at several test conditions, especially for aft vertical tail configurations. The low values of nozzle drag at subsonic Mach numbers are caused not only by excellent pressure recovery on the nozzle boattail (ref. 10) but also by a favorable interference from the tail surfaces (fig. 19(b)). Nozzle drag trends with tail span are dependent on the tail arrangement. For aft tails below Mach number 0.90, nozzle drag decreases with increasing tail span. (See fig. 18(b).) At Mach number 0.95, no discernible trend with tail span is evident, and at 1.20, nozzle drag increases with tail span. The staggered tail arrangement shows little change in nozzle drag or interference increment with tail span, even at Mach number 0.95 when compared with that of the aft tails. The forward tails configuration shows a decreasing nozzle drag and interference increment with increasing tail span at all Mach numbers except 1.20.

Afterbody. The afterbody drag by definition is the difference between the measured total aft-end drag and the computed nozzle/tail drag. (See section "Data Reduction.") The effect of tail span on afterbody drag coefficient for each tail arrangement is shown in figure 20. Unlike the nozzle, afterbody drag increases with tail span for all Mach numbers regardless of tail arrangement. The staggered tail arrangement is noticeably different in that the transonic drag rise is almost nonexistent; this is caused primarily by the smoother area distribution of the staggered tails as opposed to either the aft or forward tails. The tail span effect on the afterbody interference increment $\Delta C_{D,ia}$ is presented in figure 21. The interference increment on the afterbody mirrors the afterbody drag in every way. The trends with tail span are identical, and the only real difference is that the interference increment is smaller in magnitude.

Adverse tail interference. Contrary to the expected result, the data of figure 22 indicate that most of the adverse tail interference ($\Delta C_{D,it}$) on the aft end is not caused by the portion of the tails closest to the afterbody but by the outer portion. For example, at $M = 0.95$, tail interference effects on the aft end were favorable (negative $\Delta C_{D,it}$) for y/b less than 0.43, 0.30, and 0.16, for the staggered, forward, and aft tails, respectively. For $M \leq 0.85$, tail interference effects were small or favorable for all tail arrangements when $y/b < 0.50$. These results indicate that it is possible to integrate a short-span surface such as a ventral fin with an increase in aft-end drag equal to or less than the drag on the surface itself.

Synergistic tail interference. Tests on the aft end with either the vertical tail installed alone or horizontal tails installed alone were conducted to determine if tail interference effects from individual surfaces were additive, or if any synergistic interference occurred. The results on total aft-end, nozzle, and afterbody tail interference are presented in figure 23. The dashed lines in figure 23 indicate the algebraic sum of measured tail interference from the vertical tail installed alone and the horizontal tails installed alone on the total aft end (fig. (23(a)), nozzle (fig. 23(b)), and afterbody (fig. 23(c)). Tests with individual tails were conducted with the tails in the aft position only. The individual components of the algebraic sum are shown as unfaired data points. The solid lines in figure 23 indicate the measured tail interference with all tail surfaces installed aft. The difference between the dashed and solid lines is termed synergistic interference.

As shown in figure 23(a), synergistic tail interference on the total aft end is negligible for $M \leq 0.85$ (data at $M = 0.85$ typical for $M < 0.85$) and also for $M = 1.20$. Although not tested, synergistic tail interference probably remains negligible at Mach numbers higher than 1.20 since disturbances do not readily propagate upstream or laterally in a supersonic flow. However, at $M = 0.90$ and 0.95, adverse synergistic tail interference is present and becomes quite large at $M = 0.95$. As shown, tail interference effects on the aft end increase with increasing tail span (y/b). These results indicate a possible cause for the sharp drag rise shown in figure 16(c) for the long-span aft tail arrangement and also suggest that staggered tails may minimize synergistic tail interference effects at transonic speeds and produce lower levels of aft-end drag. (Compare figs. 16(c) and (d).) Results shown in figures 23(b) and (c) indicate that most of the synergistic tail interference on the aft end at $M = 0.90$ occurs on the afterbody ahead of the nozzle, whereas at $M = 0.95$, a large part occurs on the nozzle.

Conclusions

An investigation has been conducted in the Langley 16-Foot Transonic Tunnel to determine the effects of tail span and empennage arrangement on drag of a single-engine nozzle/afterbody model. Tests were conducted at Mach numbers from 0.50 to 1.20, nozzle pressure ratios from 1.0 to 8.0, and angles of attack from $-3°$ to $9°$, depending on Mach number. Three empennage arrangements (aft, staggered, and forward tails) were investigated with several different tail spans. The results of this study indicate the following conclusions:

1. For Mach numbers above 0.85, total aft-end drag and total tail interference drag coefficients increase with increasing tail span regardless of tail arrangement. From this it is concluded that afterbody drag associated with full-span tail configurations cannot be accurately measured or theoretically predicted using partial-span tail surfaces.

2. For Mach numbers less than 1.00, staggered tails produce the least adverse interference effects. Above 1.00, forward tails produce the least adverse interference.

3. Most of the adverse tail interference is associated with the outer portion of the tail surfaces. This means that a short-span surface (ventral fin, for example) may

be integrated with the aft end with little increase in drag other than surface skin friction.

4. Synergistic tail interference on the total aft end was negligible except near Mach number 0.95 where significant adverse synergistic effects were noted with increasing tail span.

Langley Research Center
National Aeronautics and Space Administration
Hampton, VA 23665
July 11, 1984

References

1. Schmeer, James W.; Lauer, Rodney F., Jr.; and Berrier, Bobby L.: *Performance of Blow-in-Door Ejector Nozzles Installed on a Twin-Jet Variable-Wing-Sweep Fighter Airplane Model.* NASA TM X-1383, 1967.
2. Reubush, David E.; and Mercer, Charles E.: *Effects of Nozzle Interfairing Modifications on Longitudinal Aerodynamic Characteristics of a Twin-Jet, Variable-Wing-Sweep Fighter Model.* NASA TN D-7817, 1975.
3. Maiden, Donald L.; and Berrier, Bobby L.: *Effect of Airframe Modifications on Longitudinal Aerodynamic Characteristics of a Fixed-Wing, Twin-Jet Fighter Airplane Model.* NASA TM X-2523, 1972.
4. Berrier, Bobby L.; and Staff, Propulsion Integration Section: *A Review of Several Propulsion Integration Features Applicable to Supersonic-Cruise Fighter Aircraft.* NASA TM X-73991, 1976.
5. Glasgow, E. R.: Integrated Airframe-Nozzle Performance for Designing Twin-Engine Fighters. AIAA Paper No. 73-1303, Nov. 1973.
6. *Exhaust System Interaction Program.* Volumes I–XVII. D162-10467-11 (Contract no. F33615-70-C-1450), Boeing Co., Apr. 1973.
7. Swavely, C. E.; and Soileau, J. F.: Aircraft Aftbody/Propulsion System Integration for Low Drag. AIAA Paper No. 72-1101, Nov.– Dec. 1972.
8. Berrier, Bobby L.: *Effect of Nonlifting Empennage Surfaces on Single-Engine Afterbody/Nozzle Drag at Mach Numbers From 0.5 to 2.2.* NASA TN D-8326, 1977.
9. Berrier, Bobby L.: Empennage/Afterbody Integration for Single and Twin-Engine Fighter Aircraft. AIAA-83-1126, June 1983.
10. Burley, James R., II; and Berrier, Bobby L.: *Investigation of Installation Effects on Single-Engine Convergent-Divergent Nozzles.* NASA TP-2078, 1982.
11. Leavitt, Laurence D.: *Effect of Empennage Location on Twin-Engine Afterbody/Nozzle Aerodynamic Characteristics at Mach Numbers From 0.6 to 1.2.* NASA TP-2116, 1983.
12. Leavitt, Laurence D.; and Bare, E. Ann: *Effects of Twin-Vertical-Tail Parameters on Twin-Engine Afterbody/Nozzle Aerodynamic Characteristics.* NASA TP-2158, 1983.
13. Bare, E. Ann; and Berrier, Bobby L.: *Investigation of Installation Effects on Twin-Engine Convergent-Divergent Nozzles.* NASA TP-2205, 1983.
14. Peddrew, Kathryn H., compiler: *A User's Guide to the Langley 16-Foot Transonic Tunnel.* NASA TM-83186, 1981.
15. Shapiro, Ascher H.: *The Dynamics and Thermodynamics of Compressible Fluid Flow,* Volume II. Ronald Press Co., c.1954.
16. Harris, Roy V., Jr.: *An Analysis and Correlation of Aircraft Wave Drag.* NASA TM X-947, 1964.

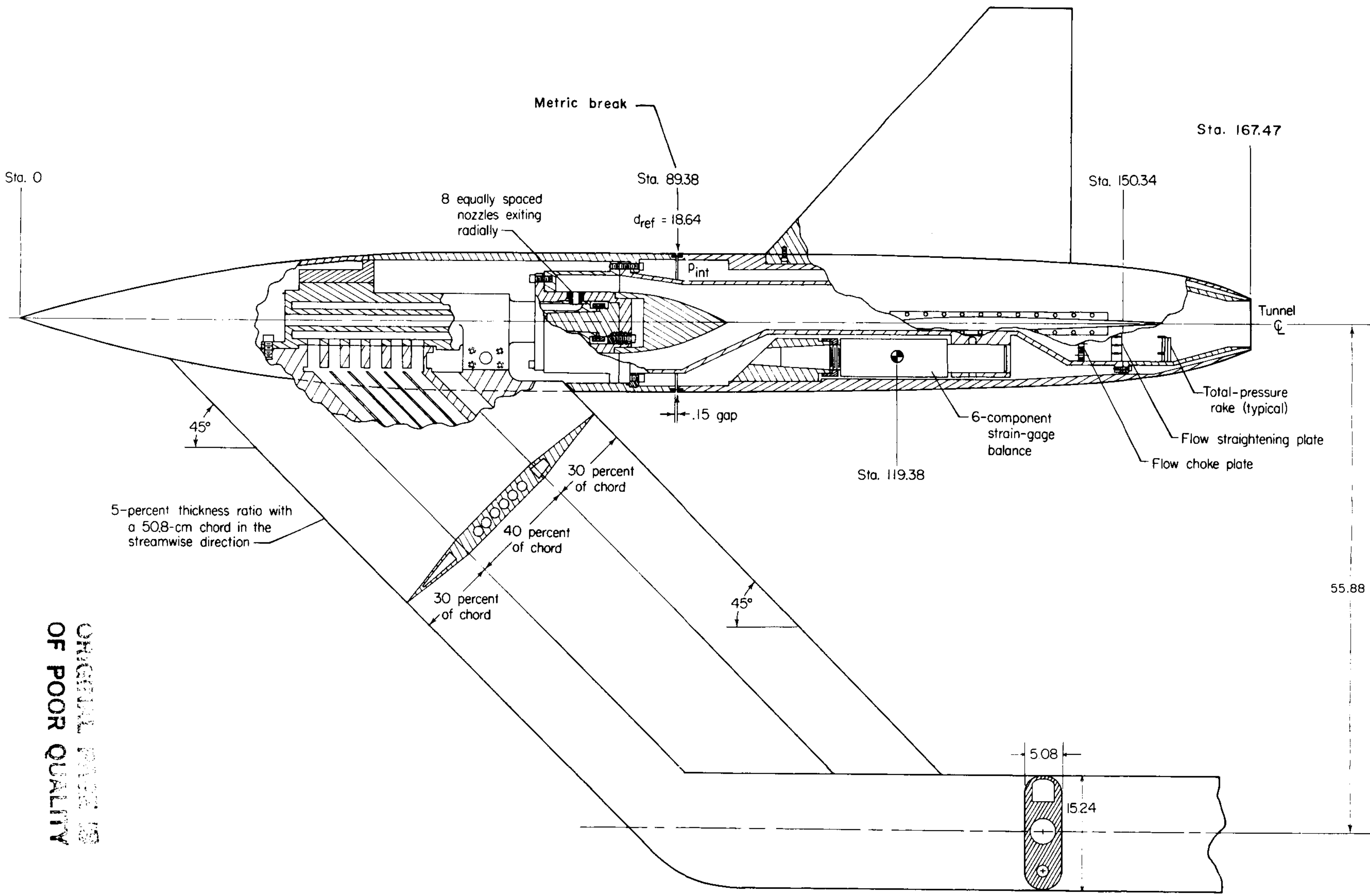

Figure 1. Sketch of air-powered single-engine model. All dimensions are in centimeters.

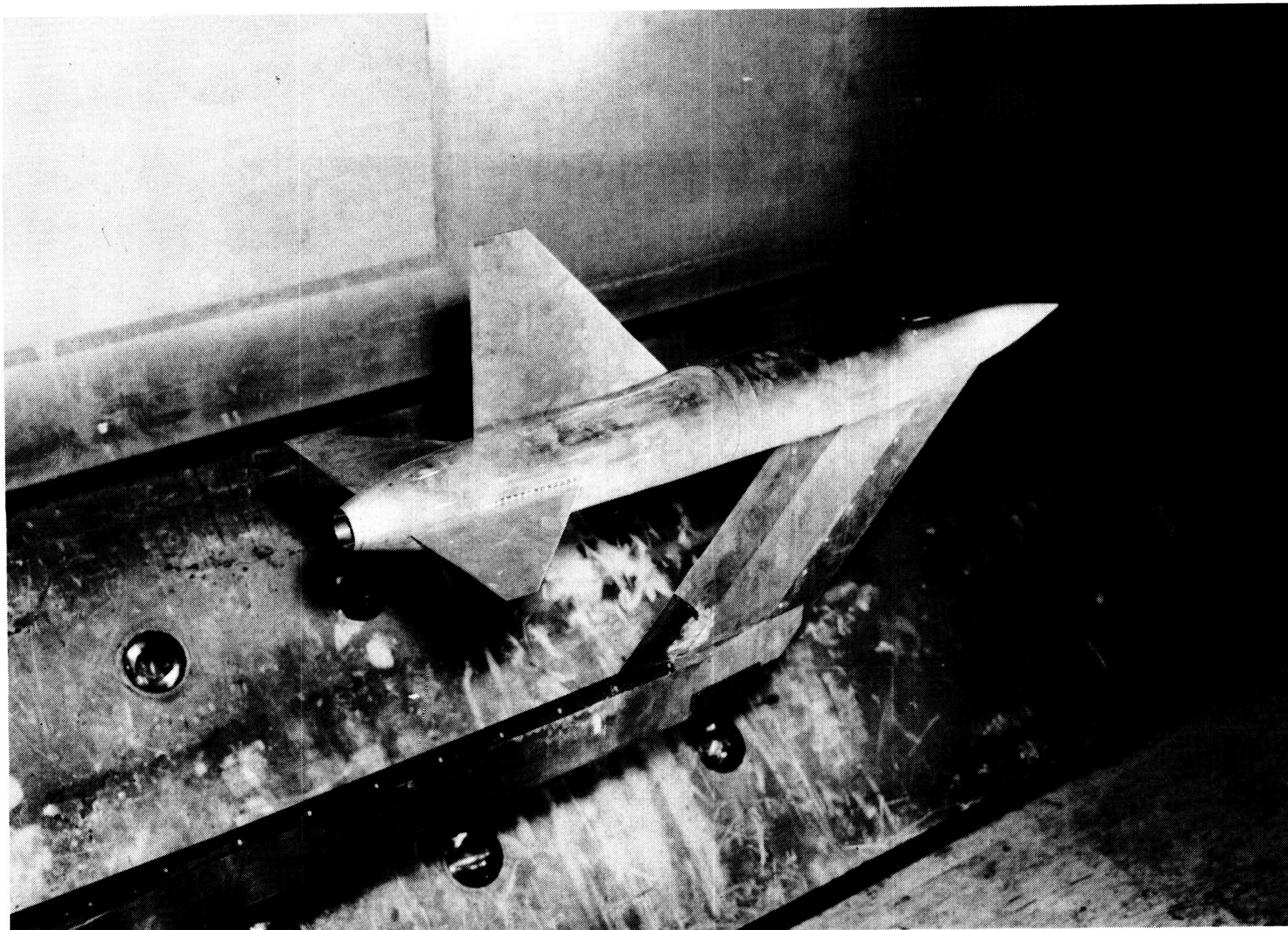

L-74-3994

Figure 2. Photograph of model in Langley 16-Foot Transonic Tunnel test section. Basic afterbody with dry power nozzle and staggered tails (vertical tail forward, horizontal tails aft).

Afterbody geometry		Orifice locations		
X/L	r/r_{ref}	Φ = 292°	Φ = 315°	Φ = 338°
0.534	1.000			
.607	.996			
.698	.975			
.759	.950			
.826	.923			
.834	.900		X	
.865	.867		X	
.880	.847			
.887	—	X	X	X
.898	.817			

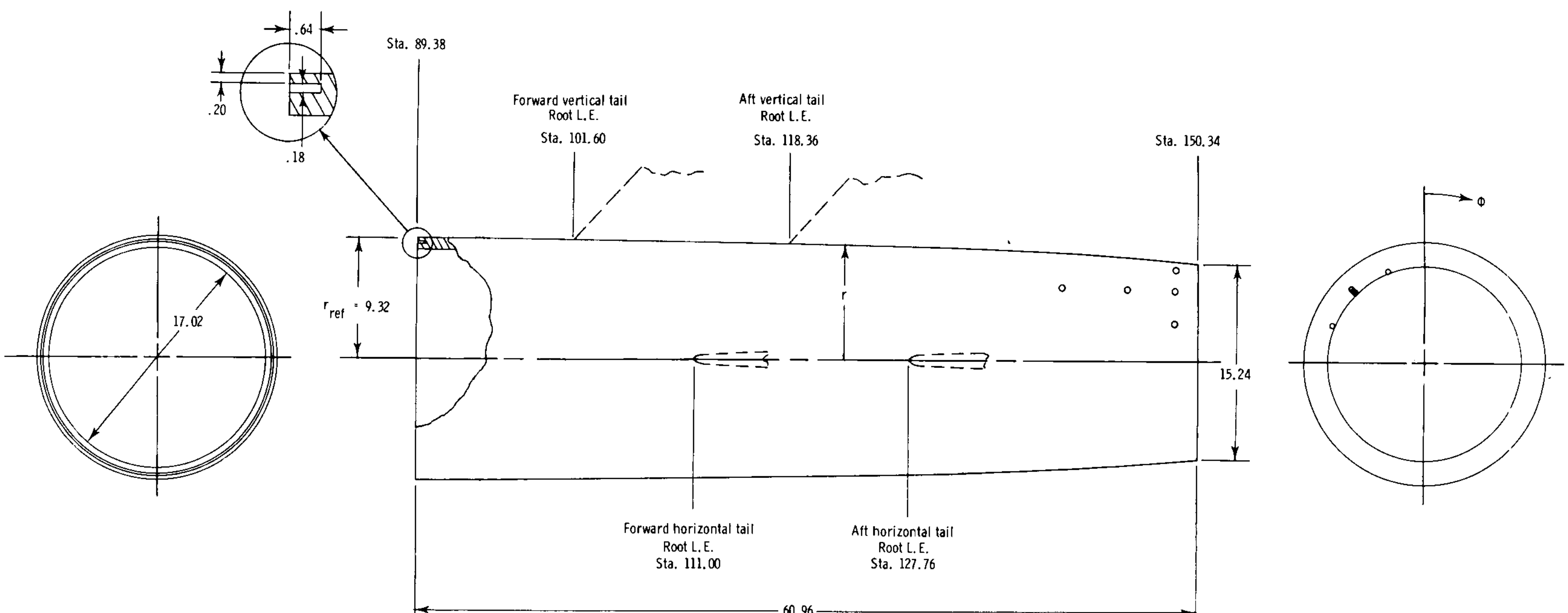

Figure 3. Sketch of basic axisymmetric afterbody showing important dimensions, tail locations, and pressure orifice locations. All dimensions are in centimeters.

Vertical tail geometry

Airfoil sections	
Tip	NACA 64-003
Root	NACA 64-005
Area (exposed, not including filler), m^2	0.0881
Tail height (root to tip), cm	33.68
Tip chord, cm	10.67
Root chord, cm	41.66
Taper ratio	0.256
Aspect ratio (exposed)	1.288
Λ, deg	42.62

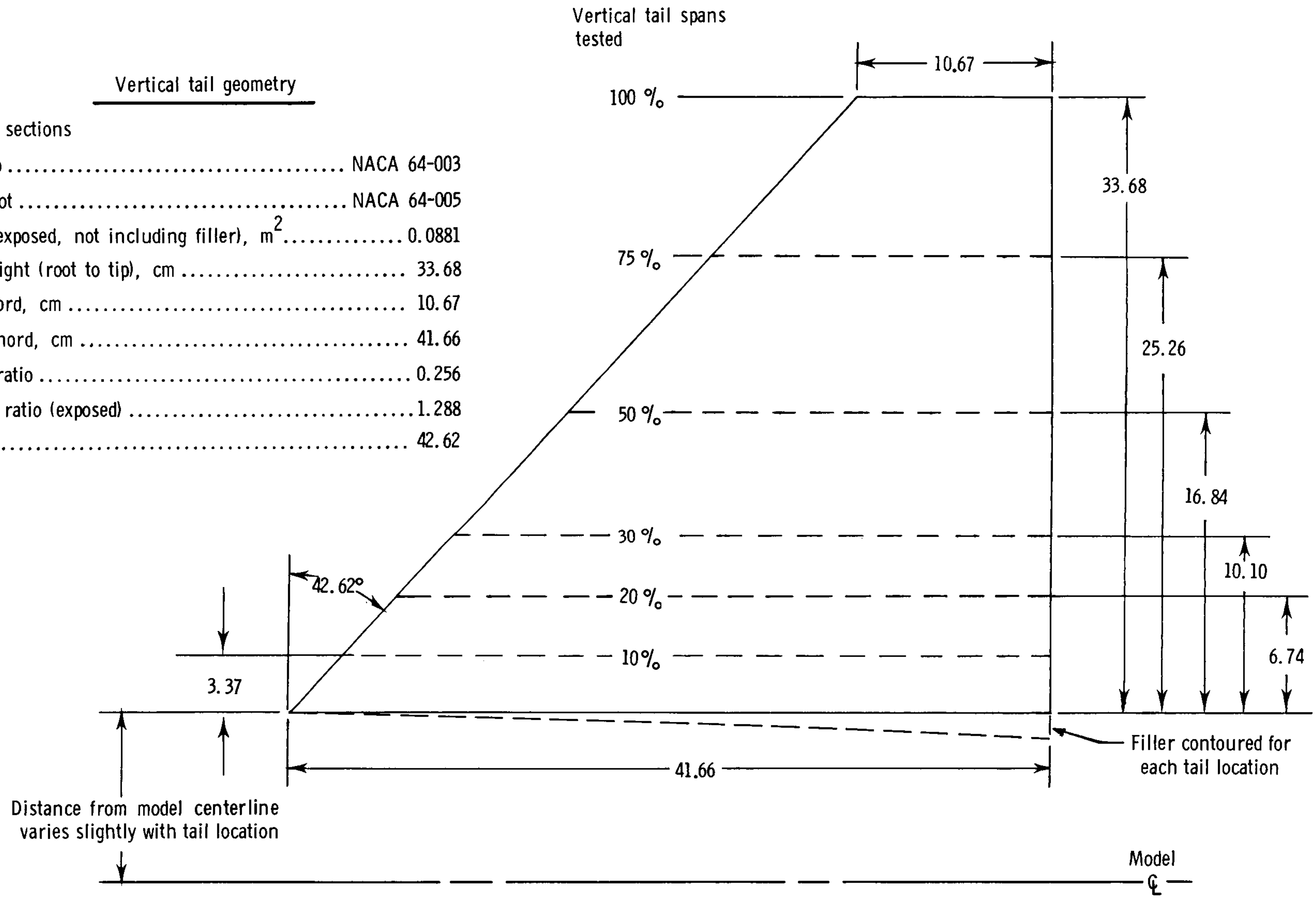

(a) Vertical tail.

Figure 4. Sketch of vertical and horizontal tail surfaces. All dimensions are in centimeters.

Horizontal tail geometry

Airfoil sections	
Tip	NACA 64-003
Root	NACA 64-005
Area (one side exposed, not including filler), m^2	0.0488
Area (total, aft tail location), m^2	0.1631
Span (aft tail location), cm	69.24
Tip chord, cm	5.59
Root chord, cm	32.26
Taper ratio	0.173
Aspect ratio (exposed)	2.724
Aspect ratio (aft tail location)	2.939
Λ, deg	45.97

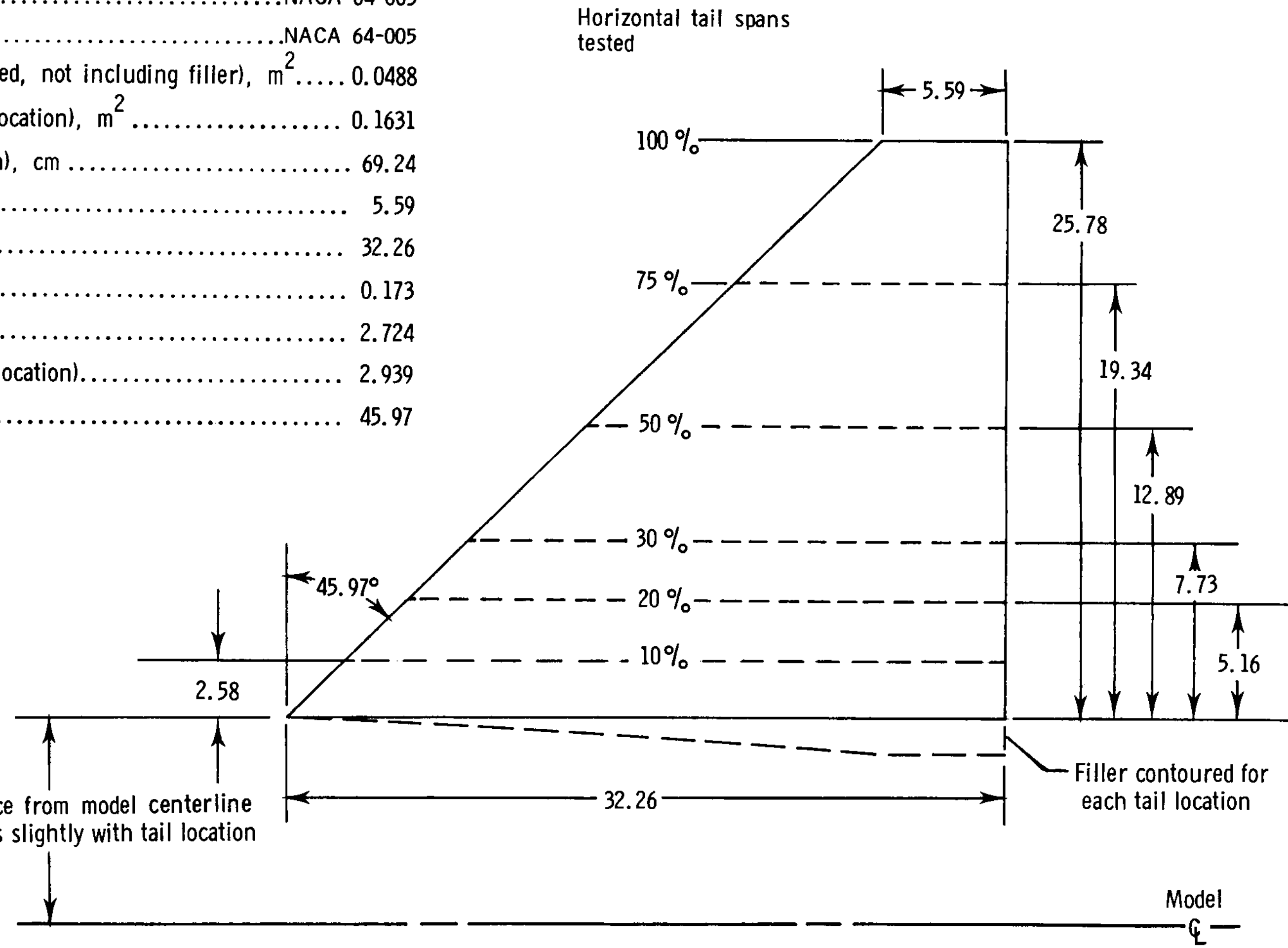

(b) Horizontal tails.

Figure 4. Concluded.

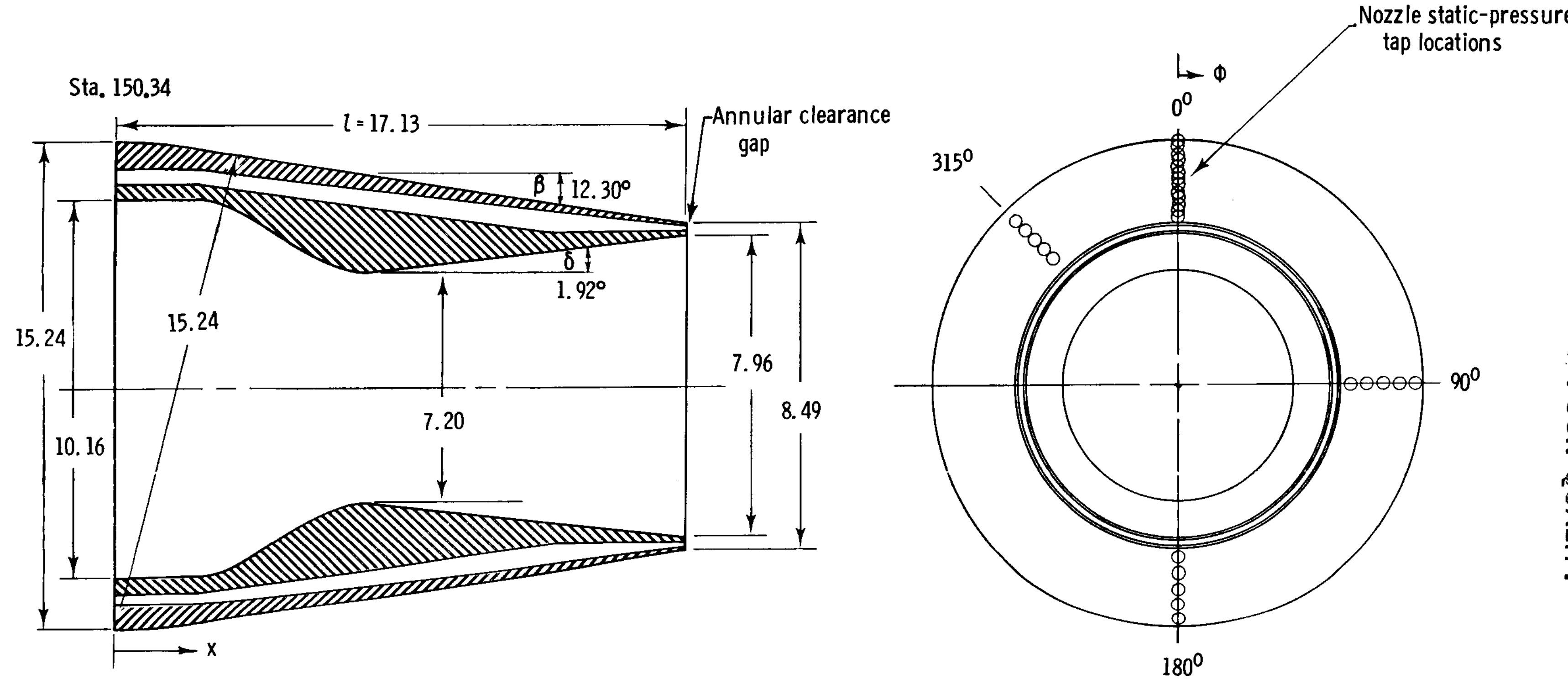

Orifice	x/l	Φ	Orifice	x/l	Φ	Orifice	x/l	Φ
1	0.025	0°	11	0.725	0°	21	0.200	180°
2	0.075		12	0.800		22	0.425	
3	0.125		13	0.875		23	0.725	
4	0.200		14	0.950		24	0.950	
5	0.275		15	0.075	90°	25	0.075	315°
6	0.350		16	0.200		26	0.200	
7	0.425		17	0.425		27	0.425	
8	0.500		18	0.725		28	0.725	
9	0.575		19	0.950		29	0.950	
10	0.650		20	0.075	180°			

Figure 5. Axisymmetric convergent-divergent nozzle with orifice locations and important dimensions. All dimensions are in centimeters.

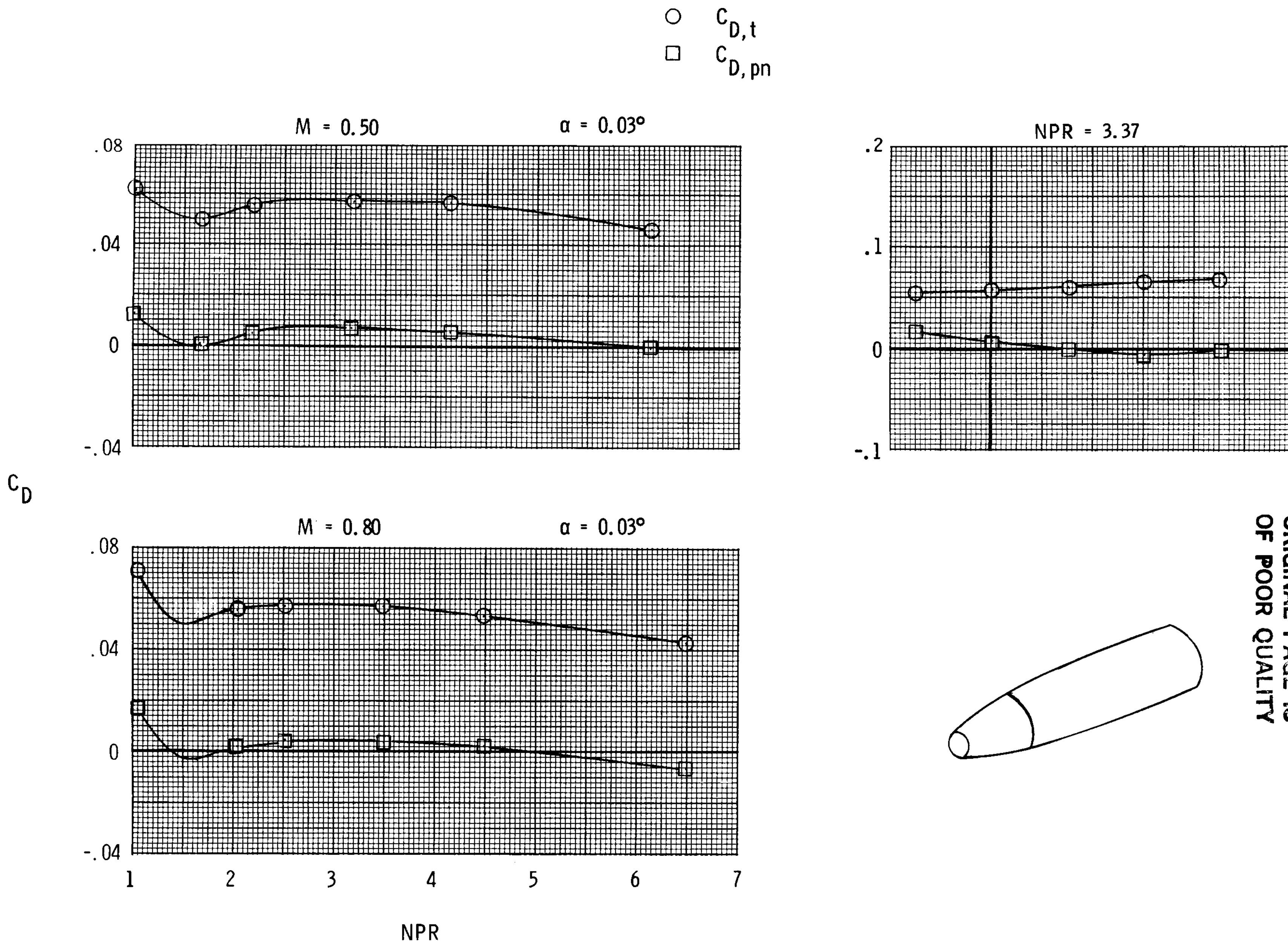

ORIGINAL PAGE IS
OF POOR QUALITY

Figure 6. Variation of total aft-end and nozzle pressure drag coefficients with nozzle pressure ratio and angle of attack for $y/b = 0.00$.

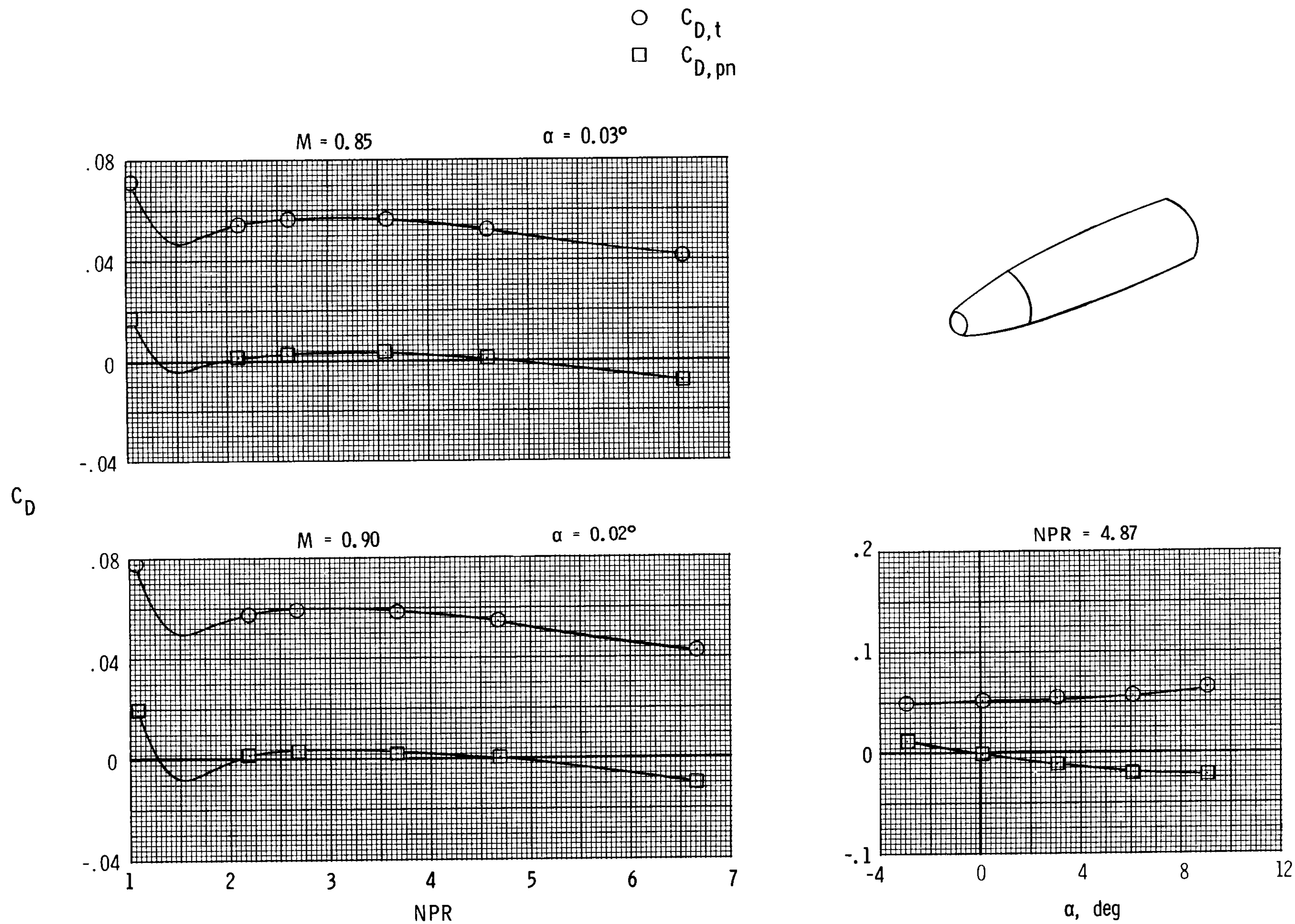

Figure 6. Continued.

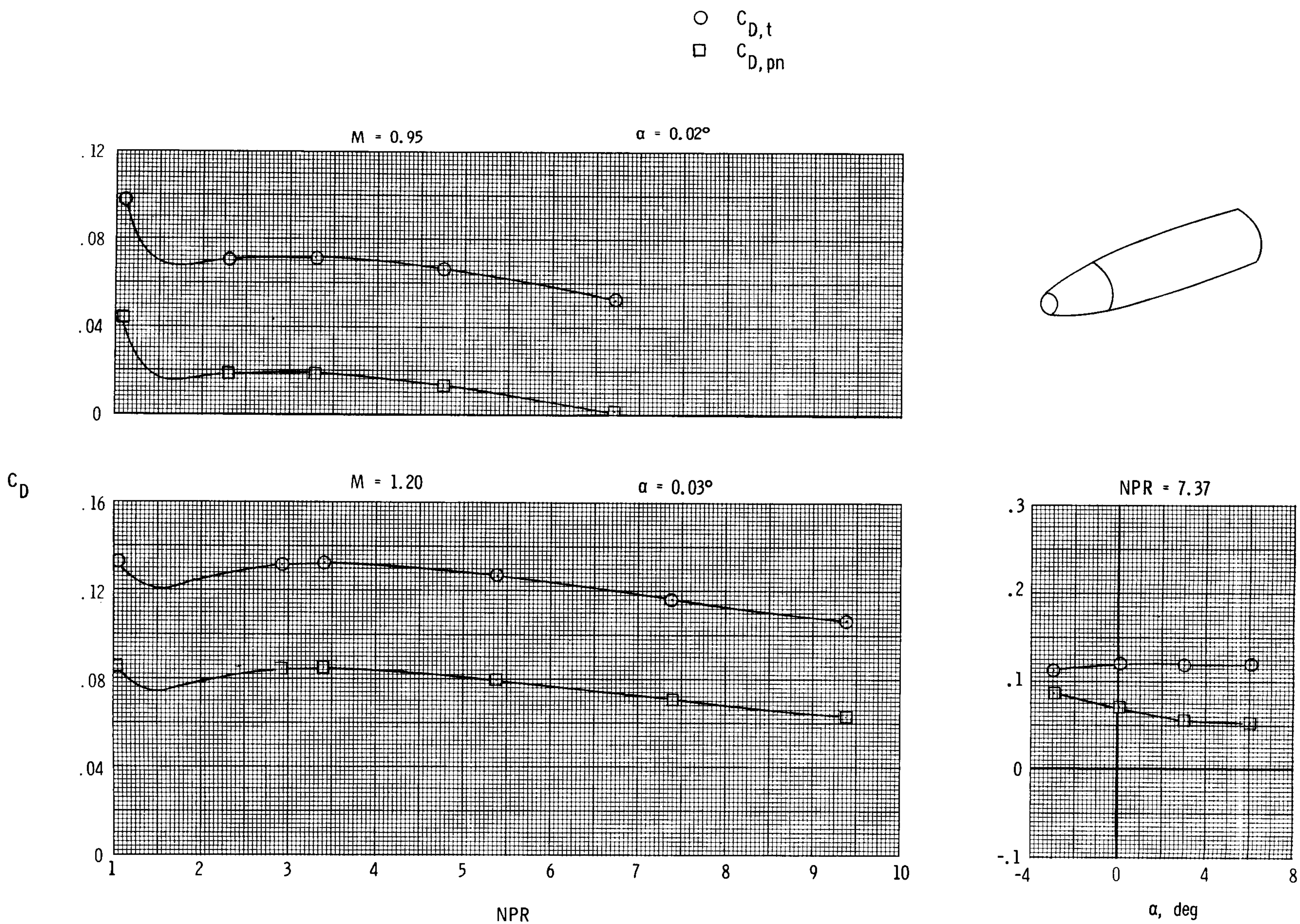

Figure 6. Concluded.

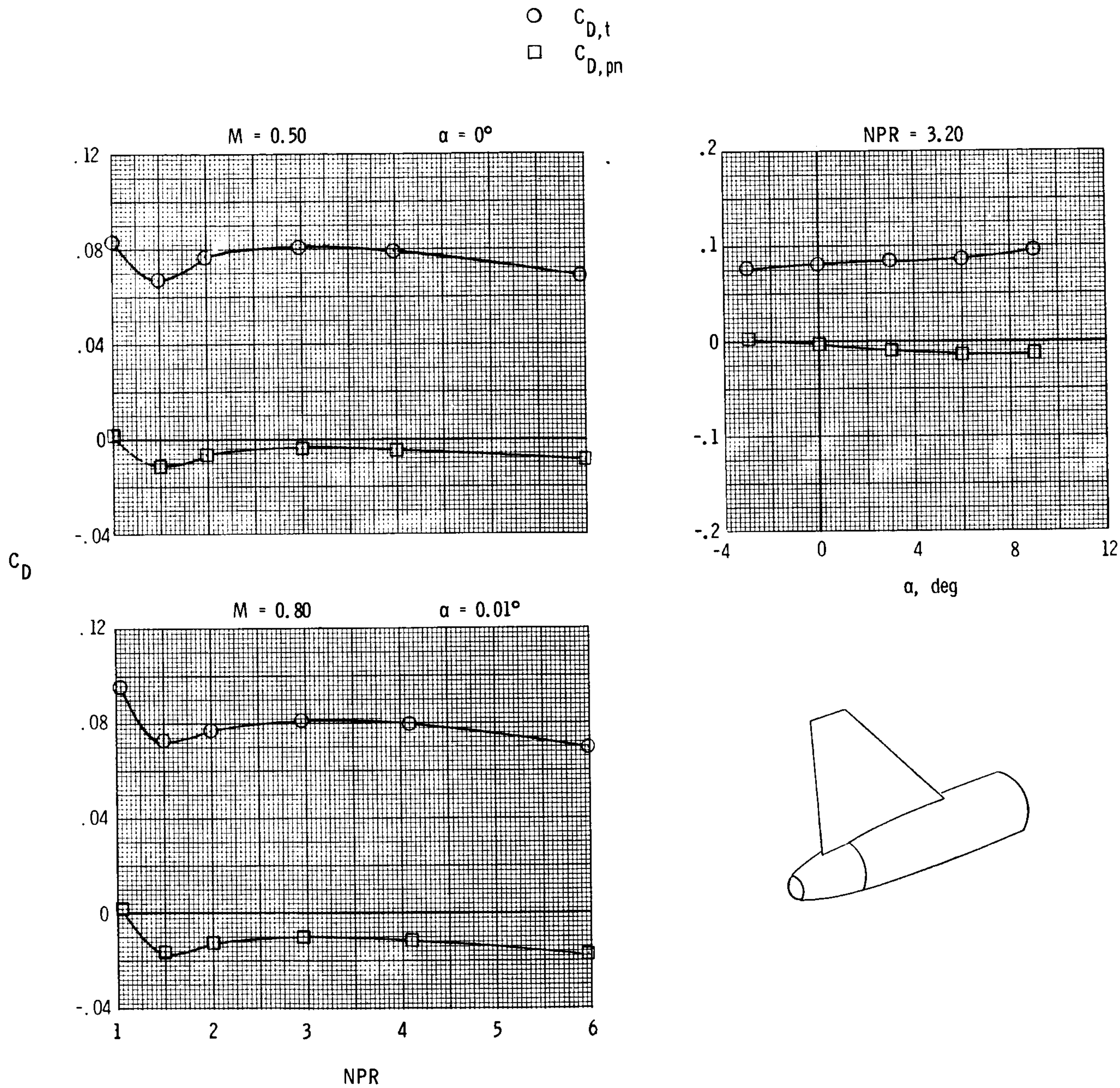

(a) $y/b = 1.00$.

Figure 7. Variation of total aft-end and nozzle pressure drag coefficients with nozzle pressure ratio and angle of attack for aft vertical tail, horizontal tails off.

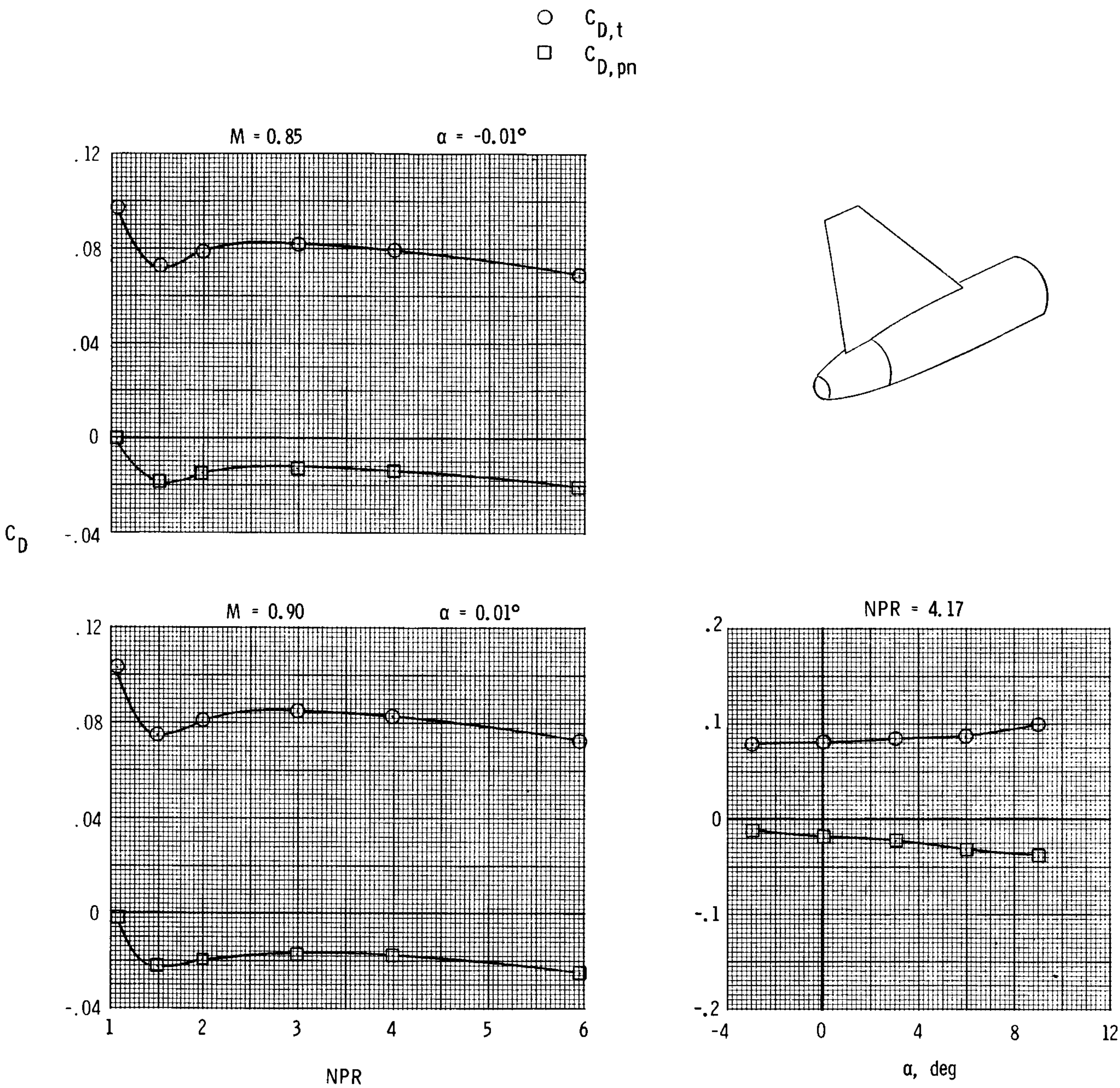

(a) Continued.

Figure 7. Continued.

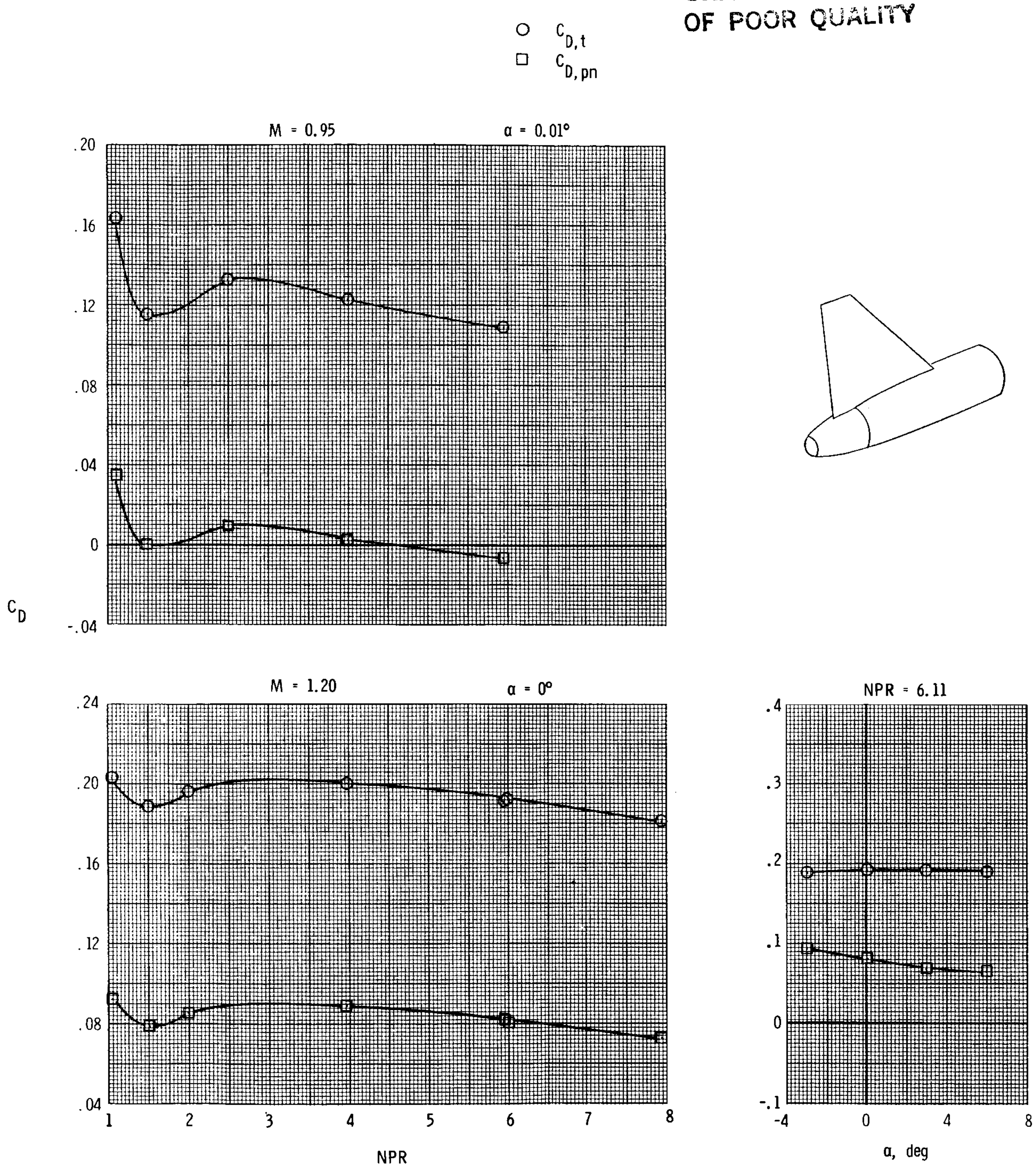

(a) Concluded.

Figure 7. Continued.

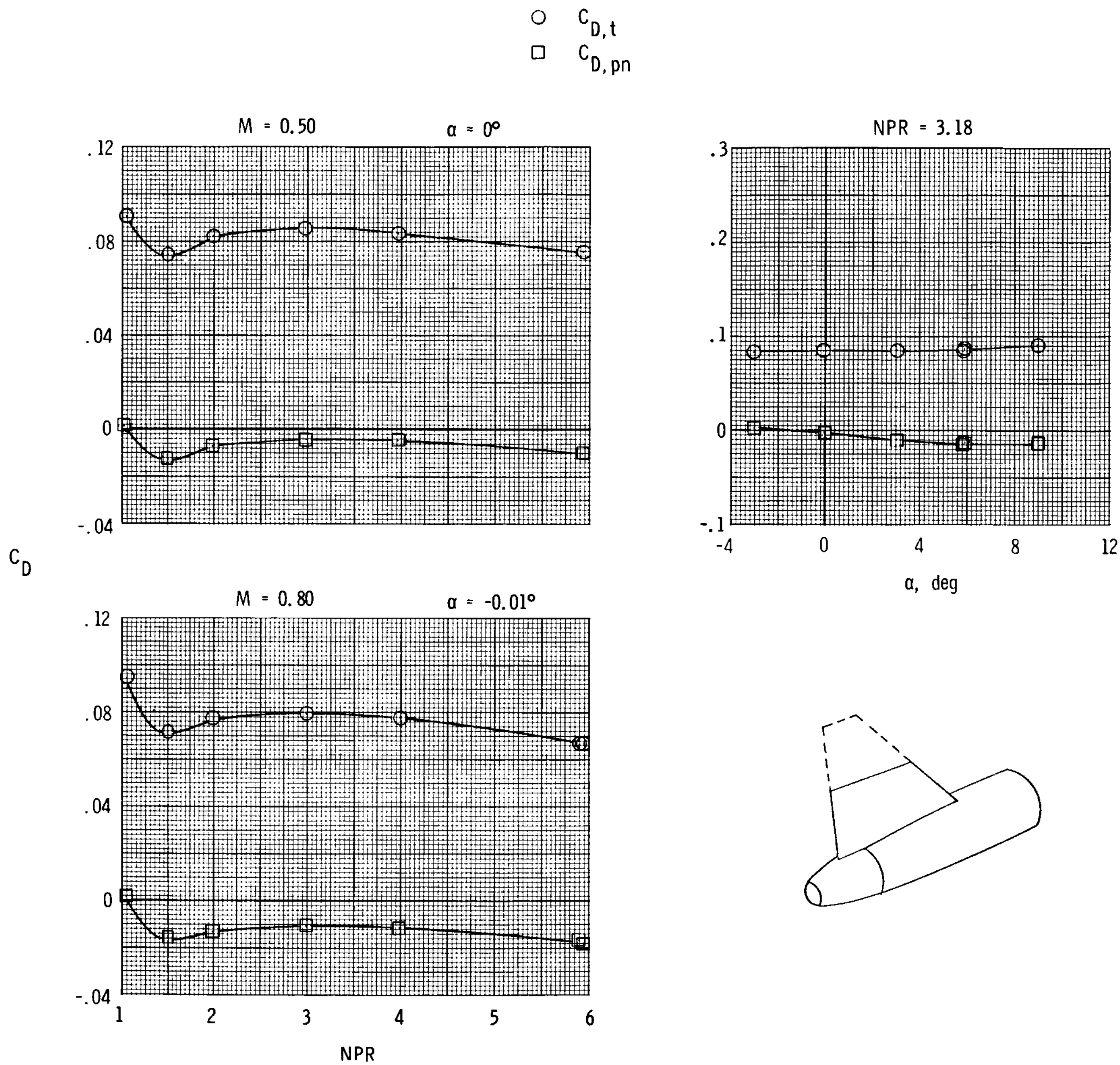

(b) $y/b = 0.50$.

Figure 7. Continued.

ORIGINAL PAGE IS
OF POOR QUALITY

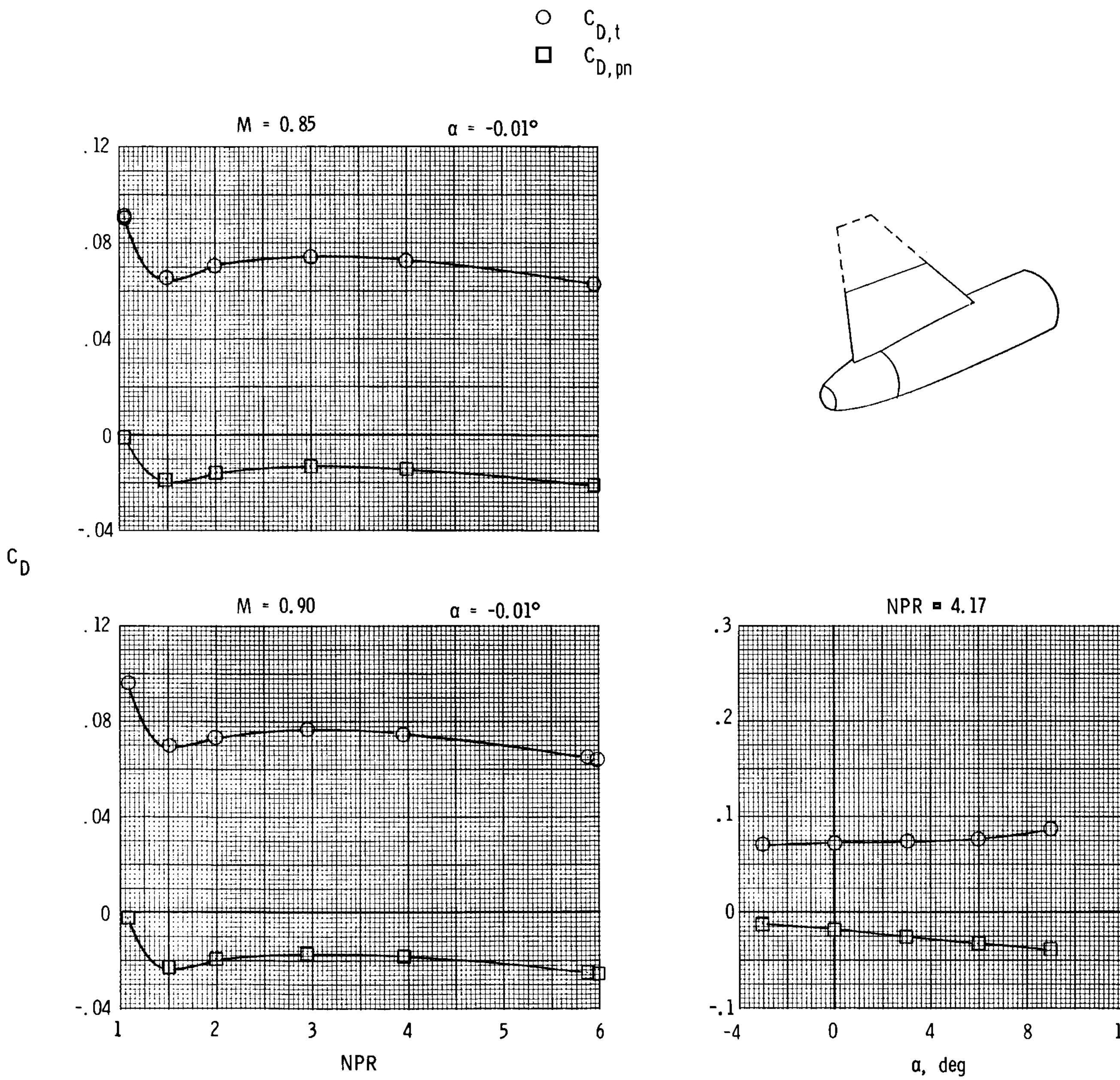

(b) Continued.

Figure 7. Continued.

ORIGINAL PAGE IS
OF POOR QUALITY

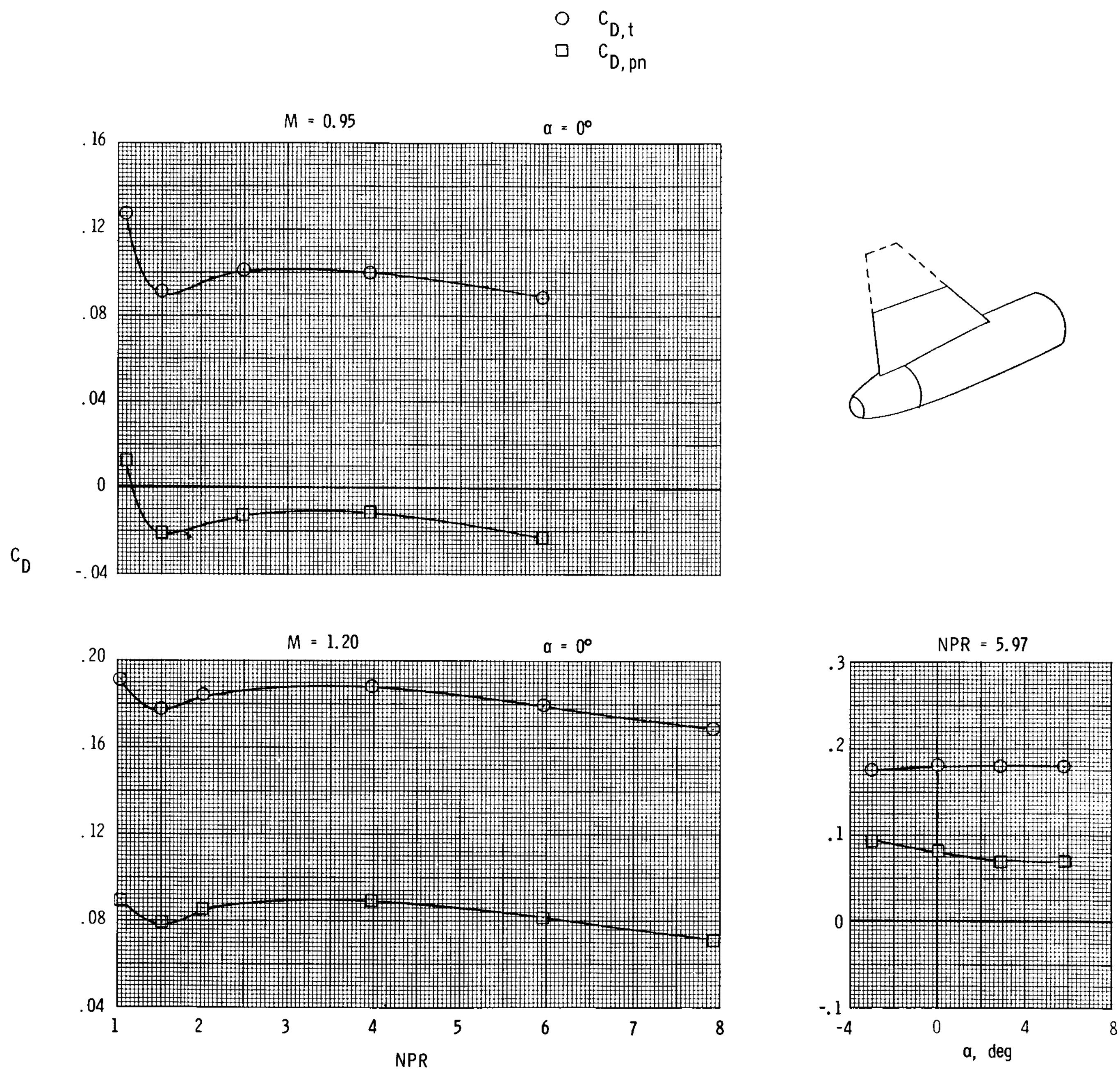

(b) Concluded.

Figure 7. Continued.

ORIGINAL PAGE IS
OF POOR QUALITY

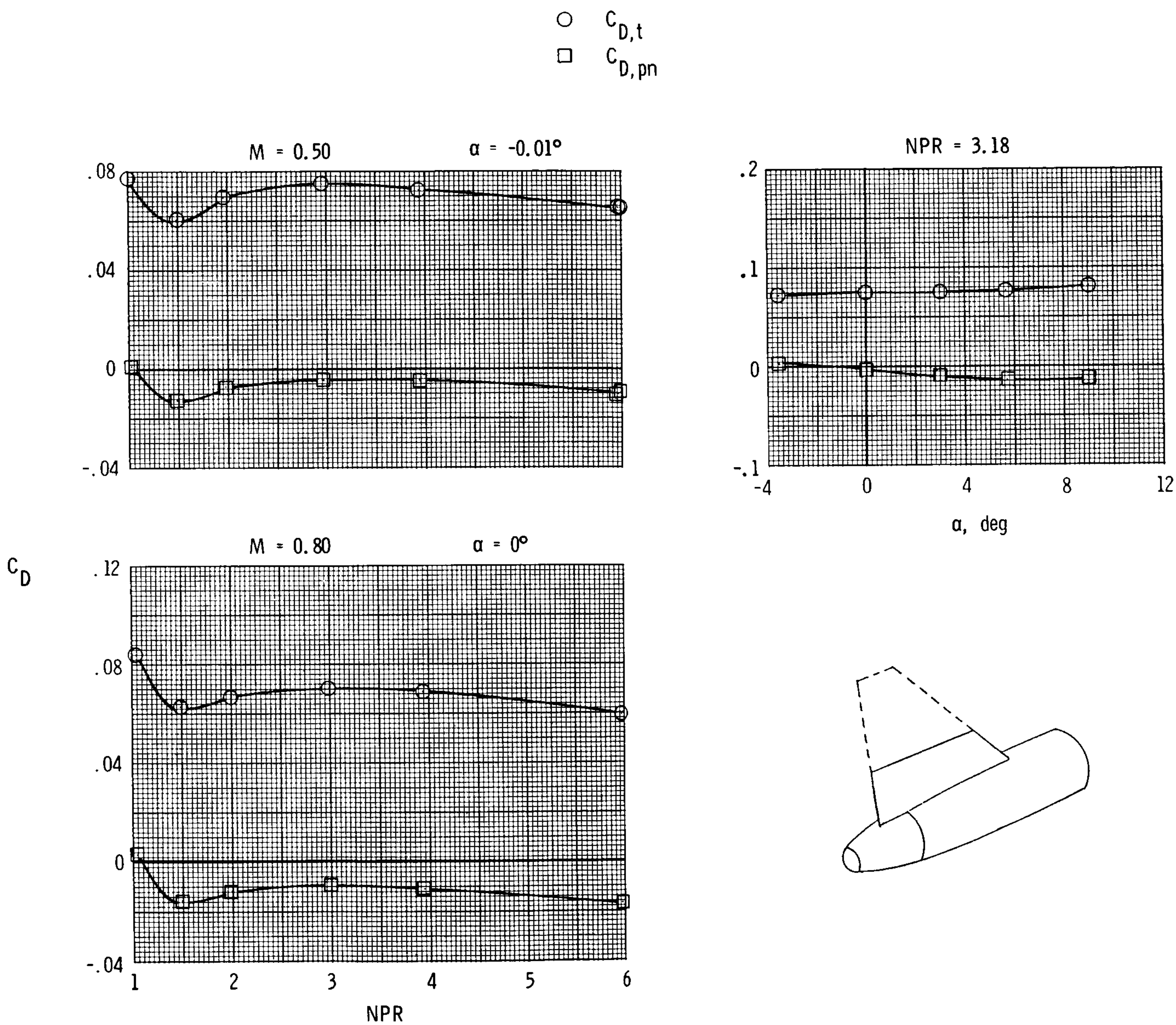

(c) $y/b = 0.30$.

Figure 7. Continued.

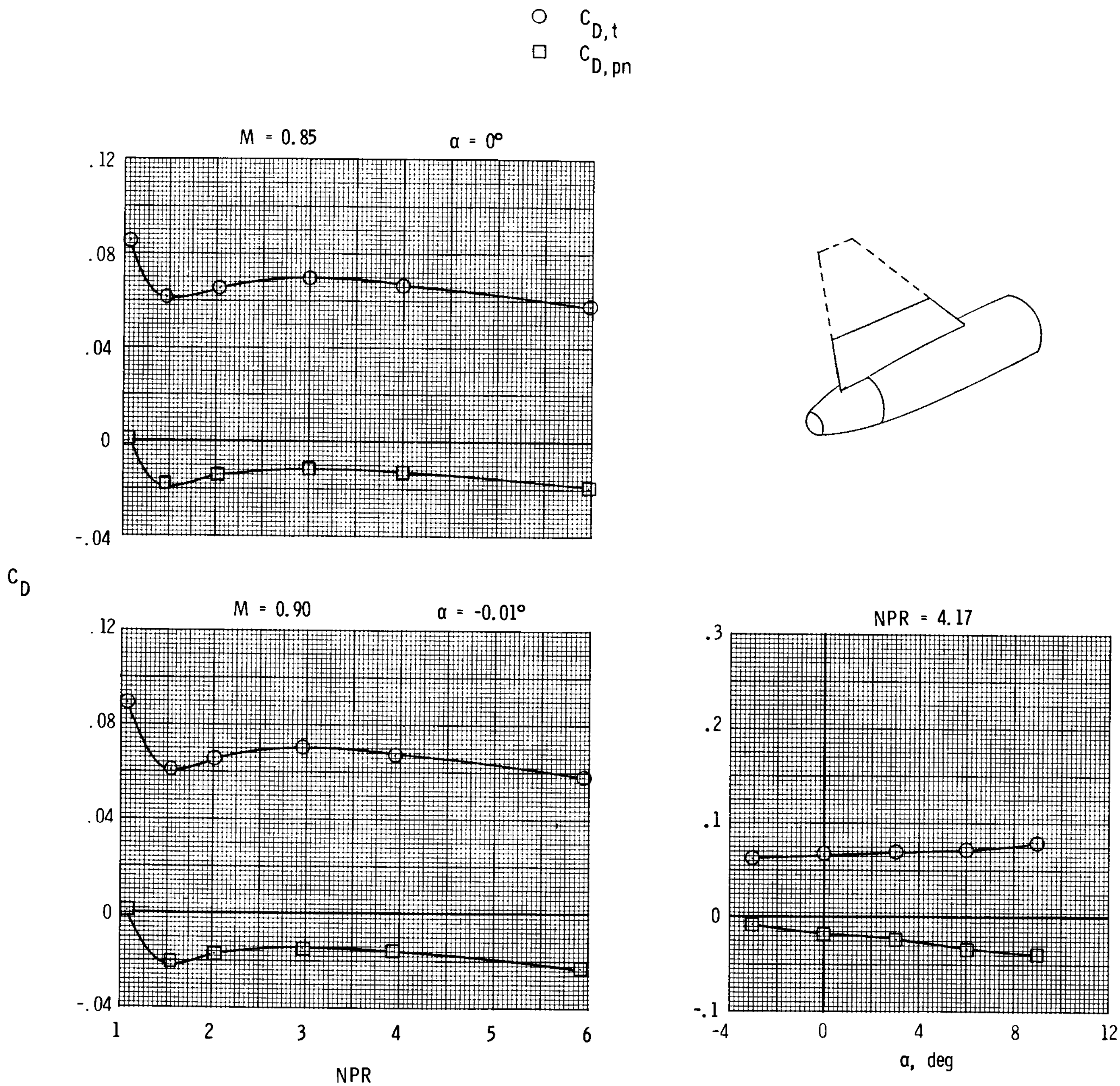

(c) Continued.

Figure 7. Continued.

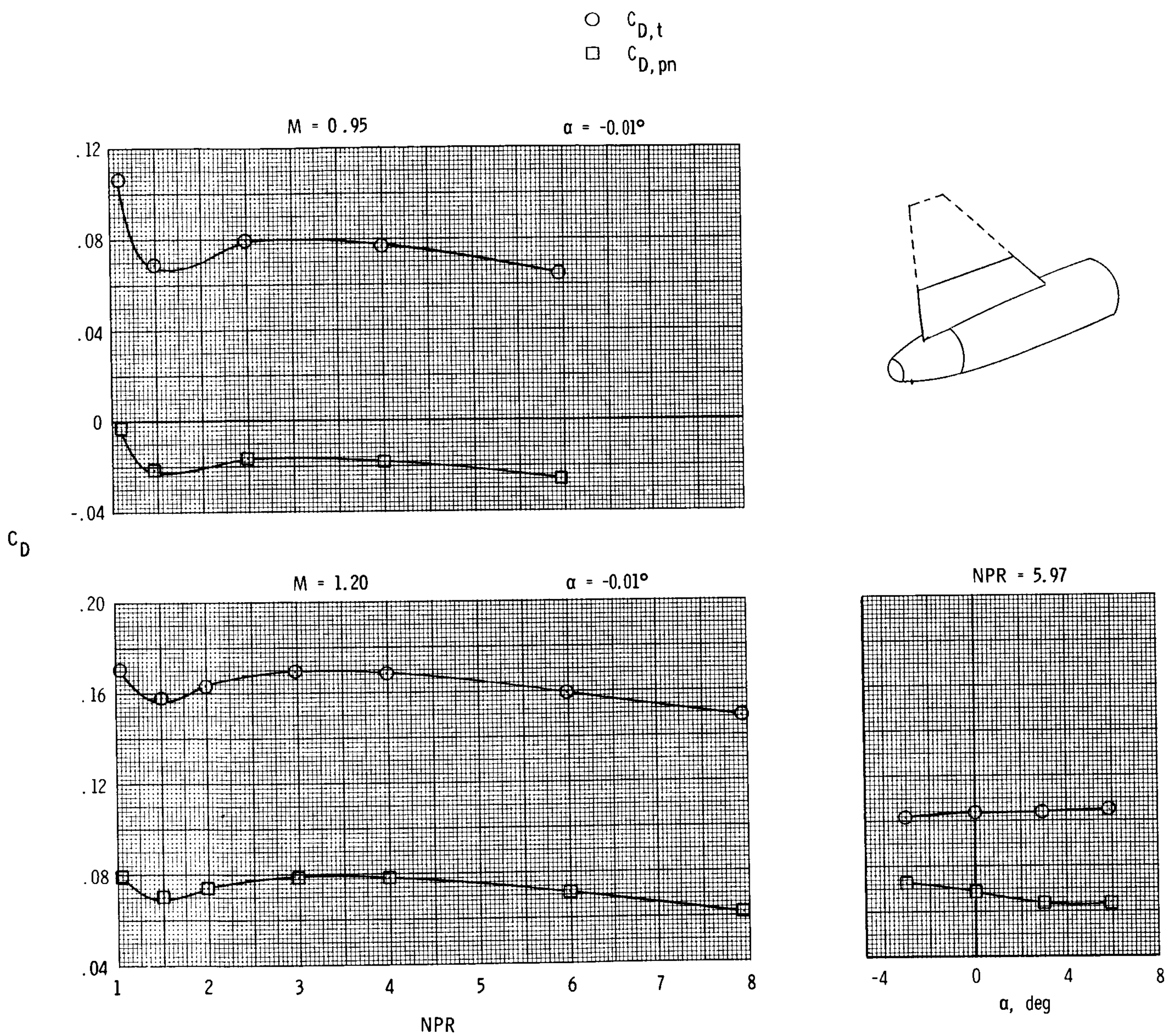

(c) Concluded.

Figure 7. Continued.

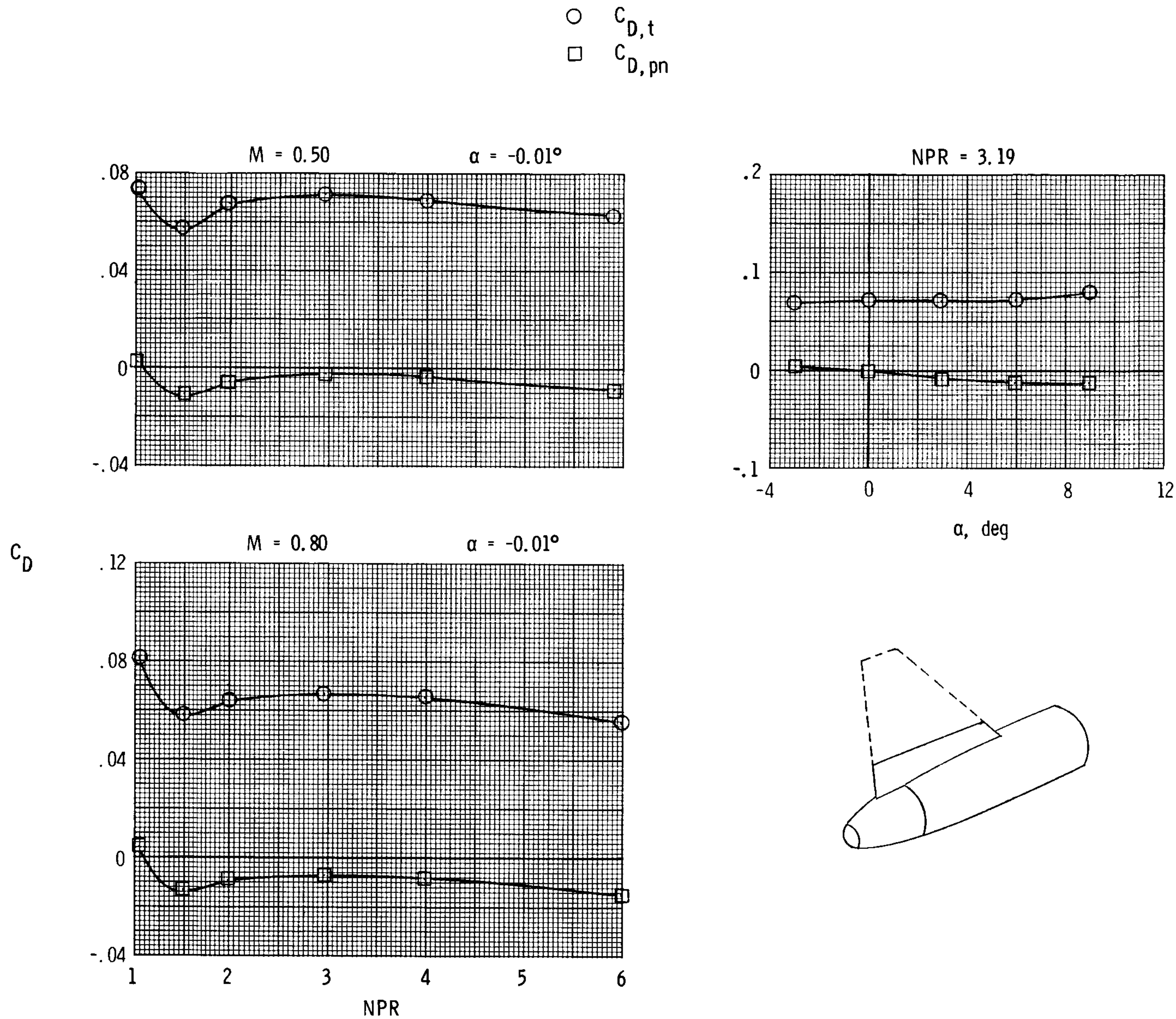

(d) $y/b = 0.20$.

Figure 7. Continued.

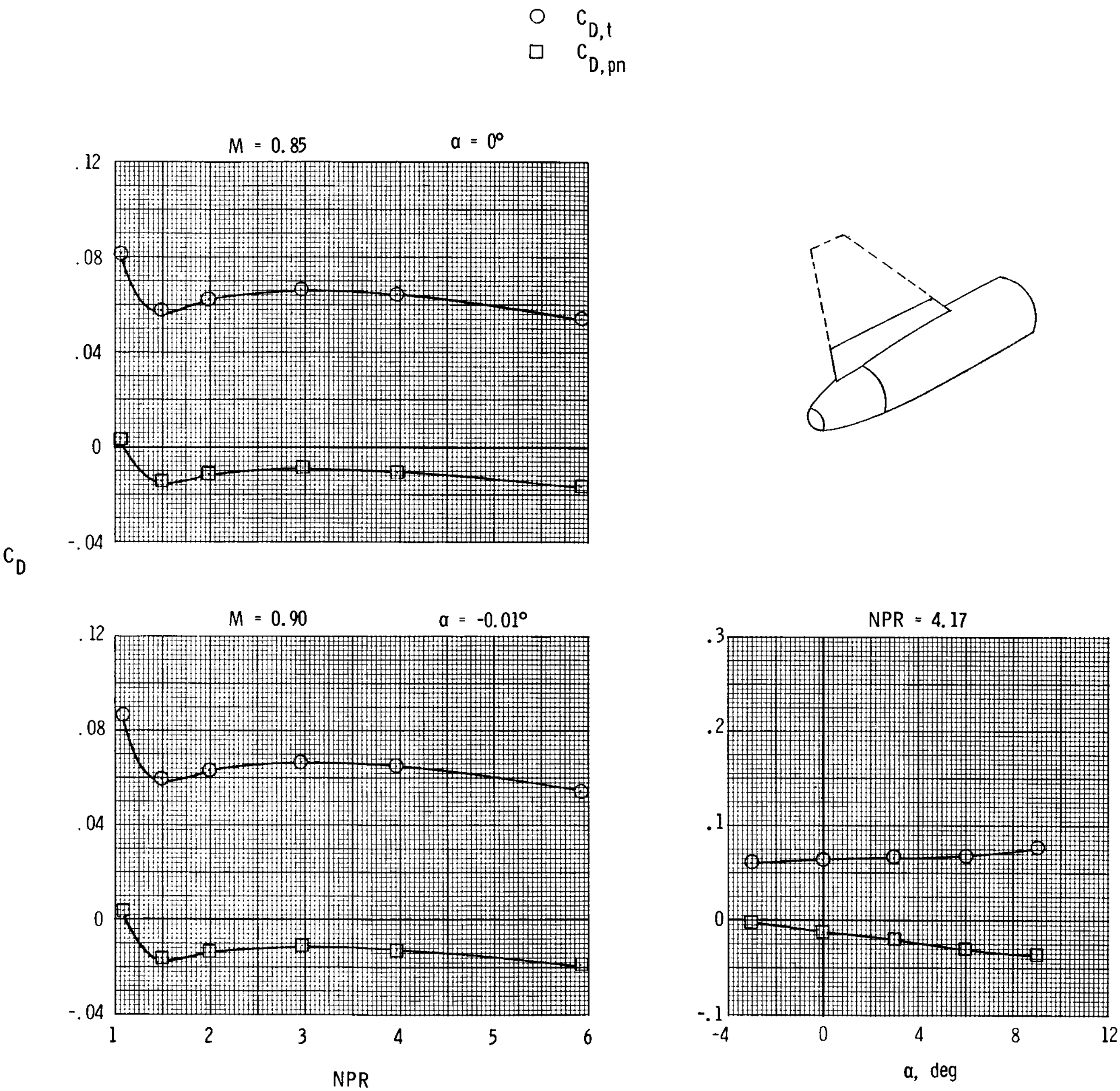

(d) Continued.

Figure 7. Continued.

ORIGINAL PAGE IS
OF POOR QUALITY

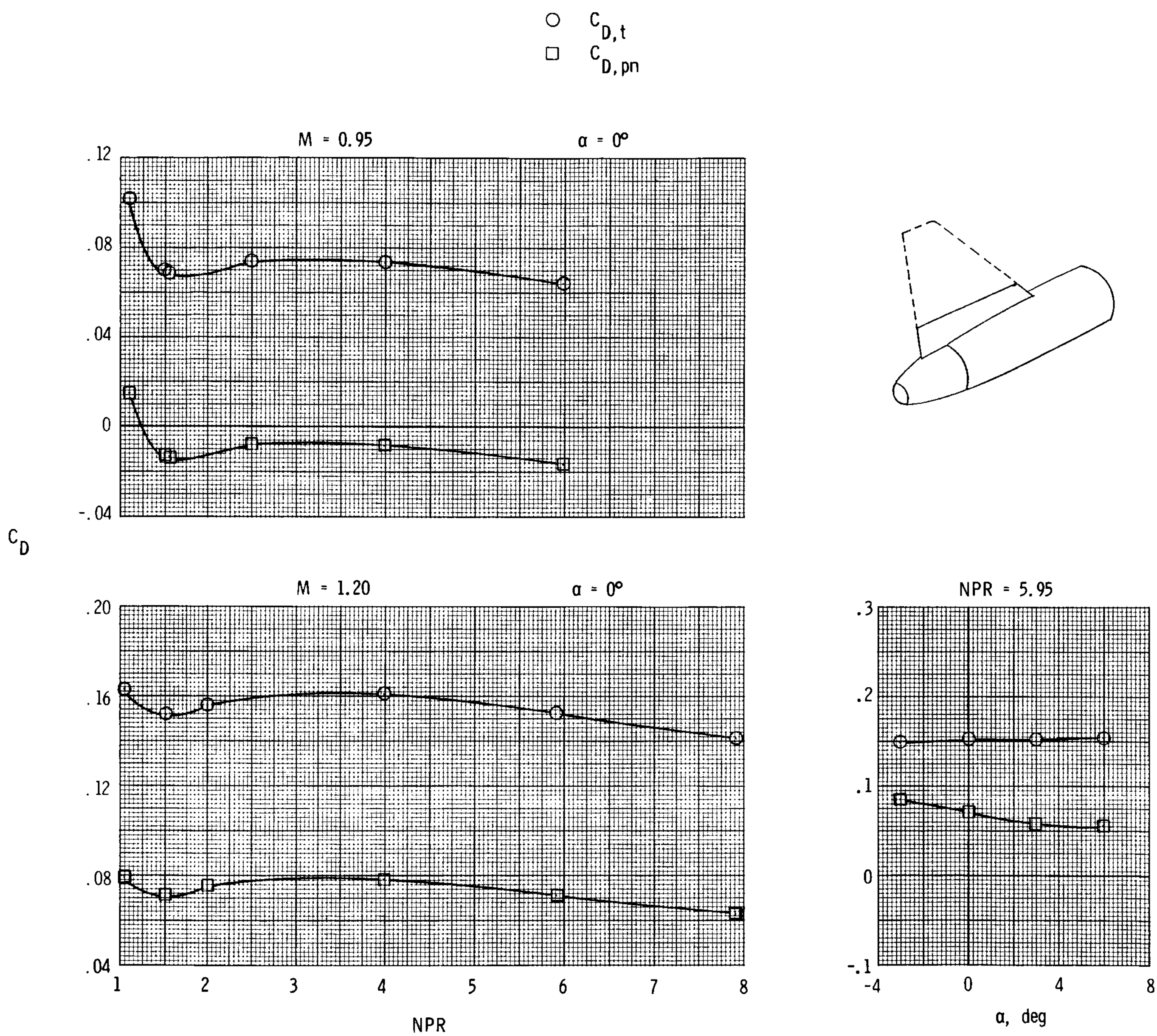

(d) Concluded.

Figure 7. Continued.

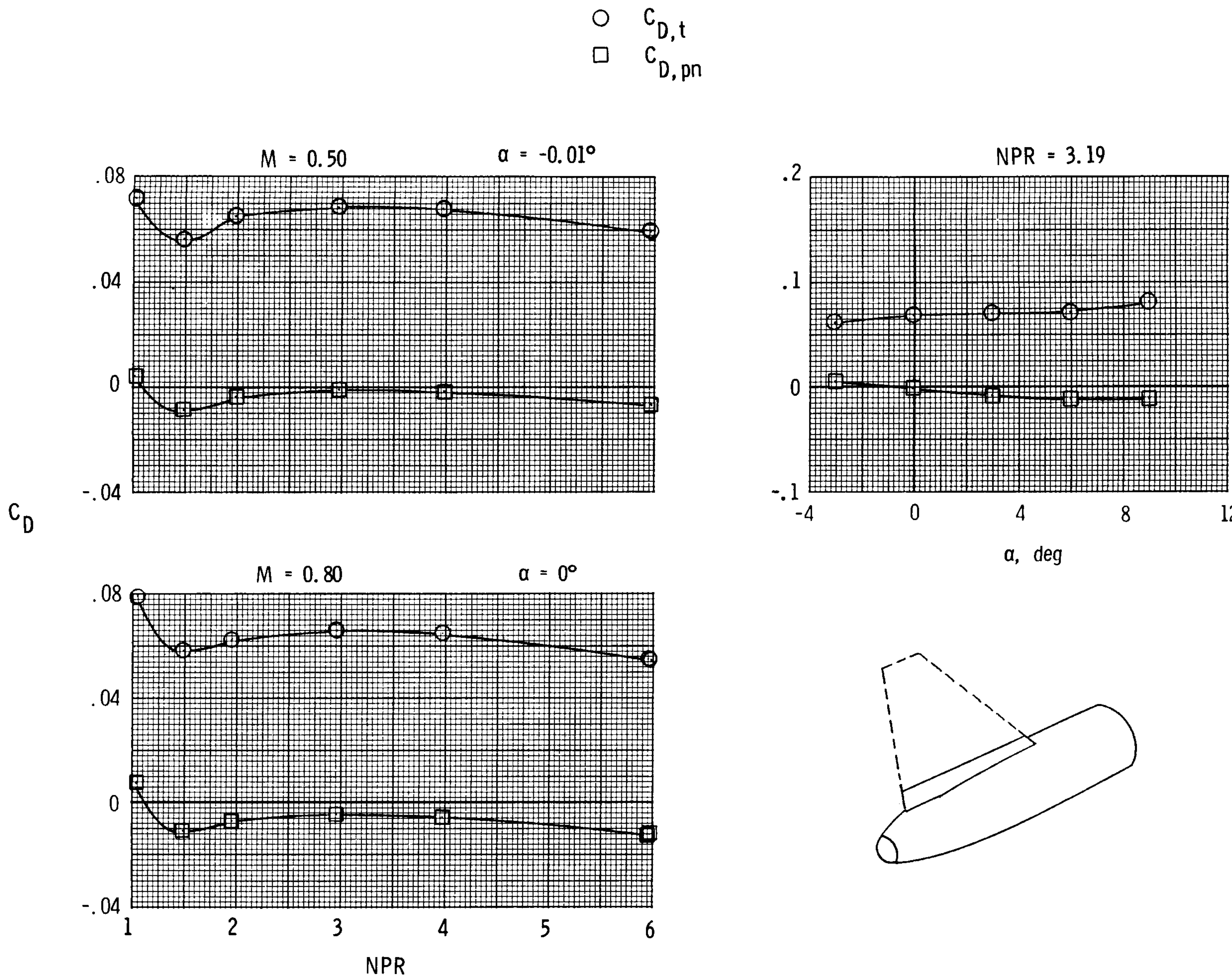

(e) $y/b = 0.10$.

Figure 7. Continued.

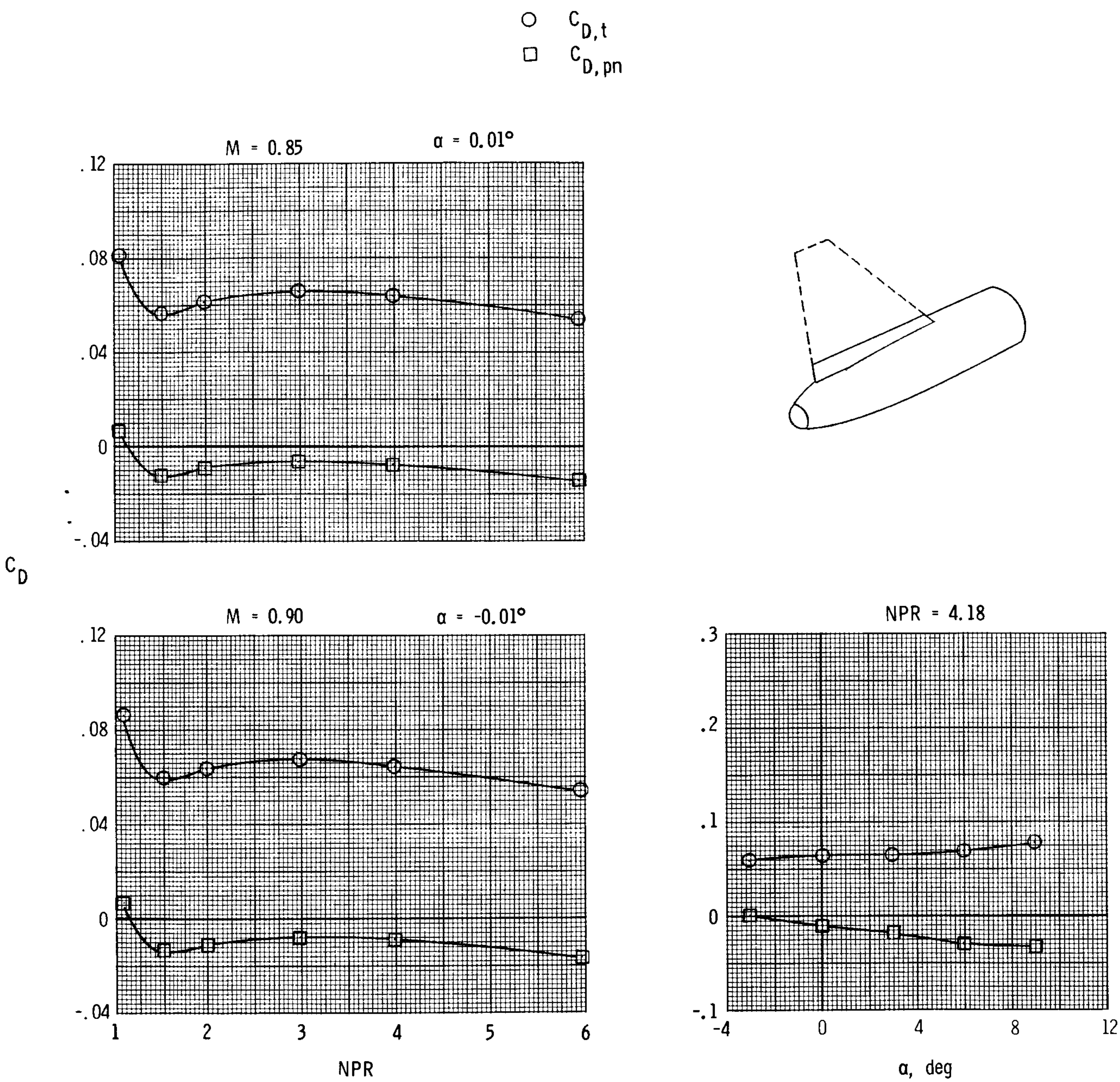

(e) Continued.

Figure 7. Continued.

ORIGINAL PAGE IS
OF POOR QUALITY

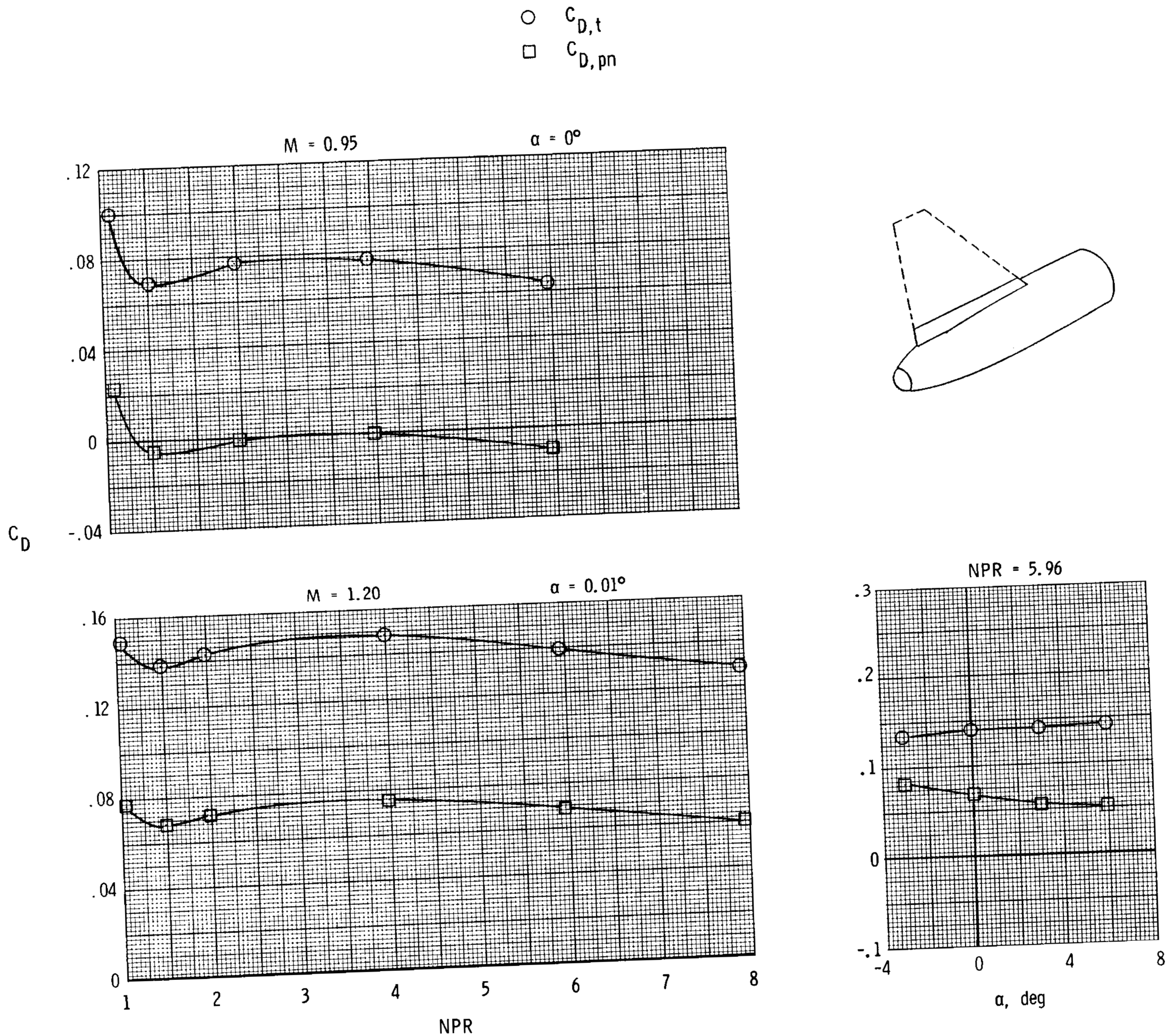

(e) Concluded.

Figure 7. Concluded.

ORIGINAL PAGE IS
OF POOR QUALITY

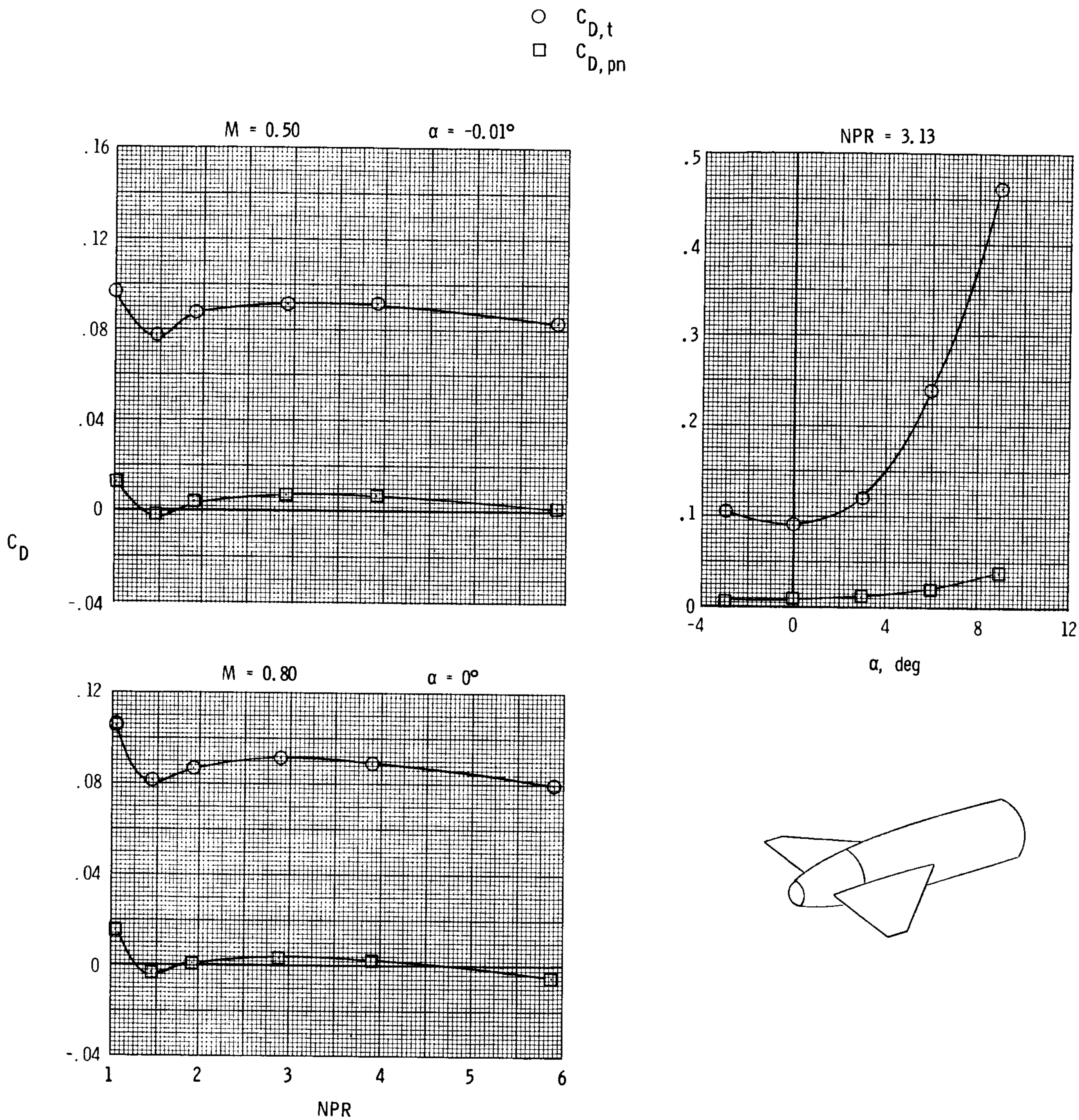

(a) $y/b = 1.00$.

Figure 8. Variation of total aft-end and nozzle pressure drag coefficients with nozzle pressure ratio and angle of attack for vertical tail off, aft horizontal tails.

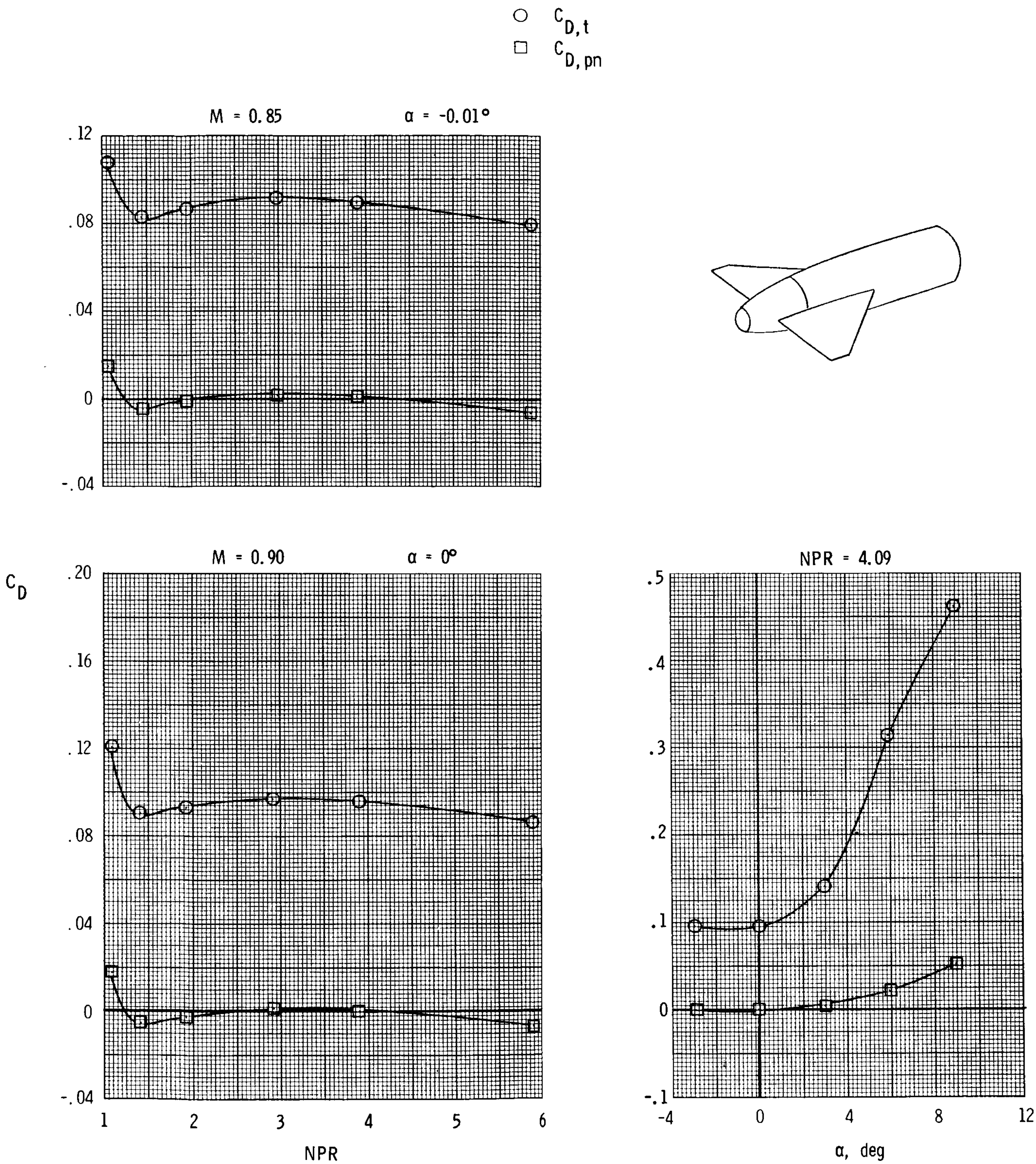

(a) Continued.

Figure 8. Continued.

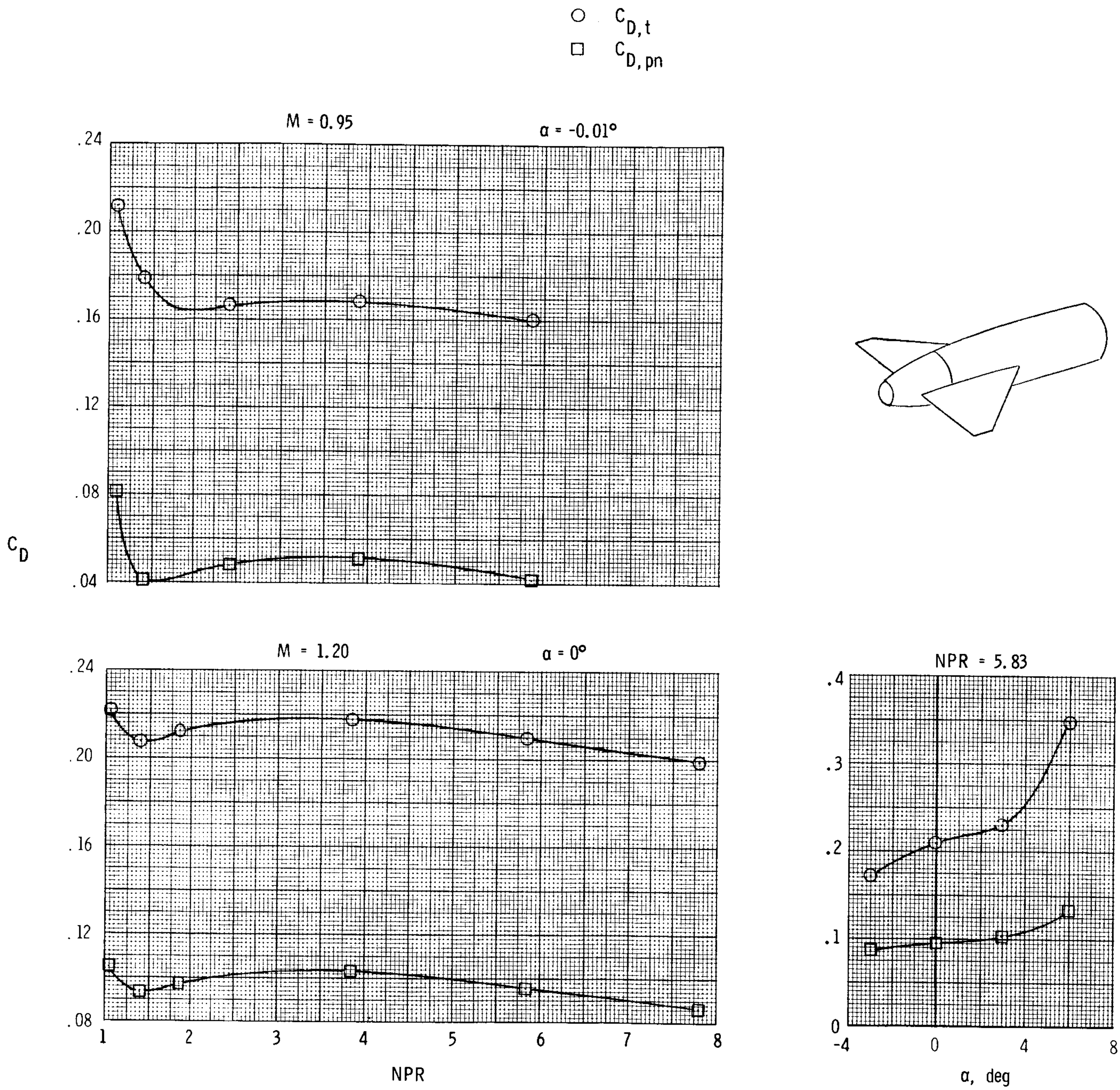

(a) Concluded.

Figure 8. Continued.

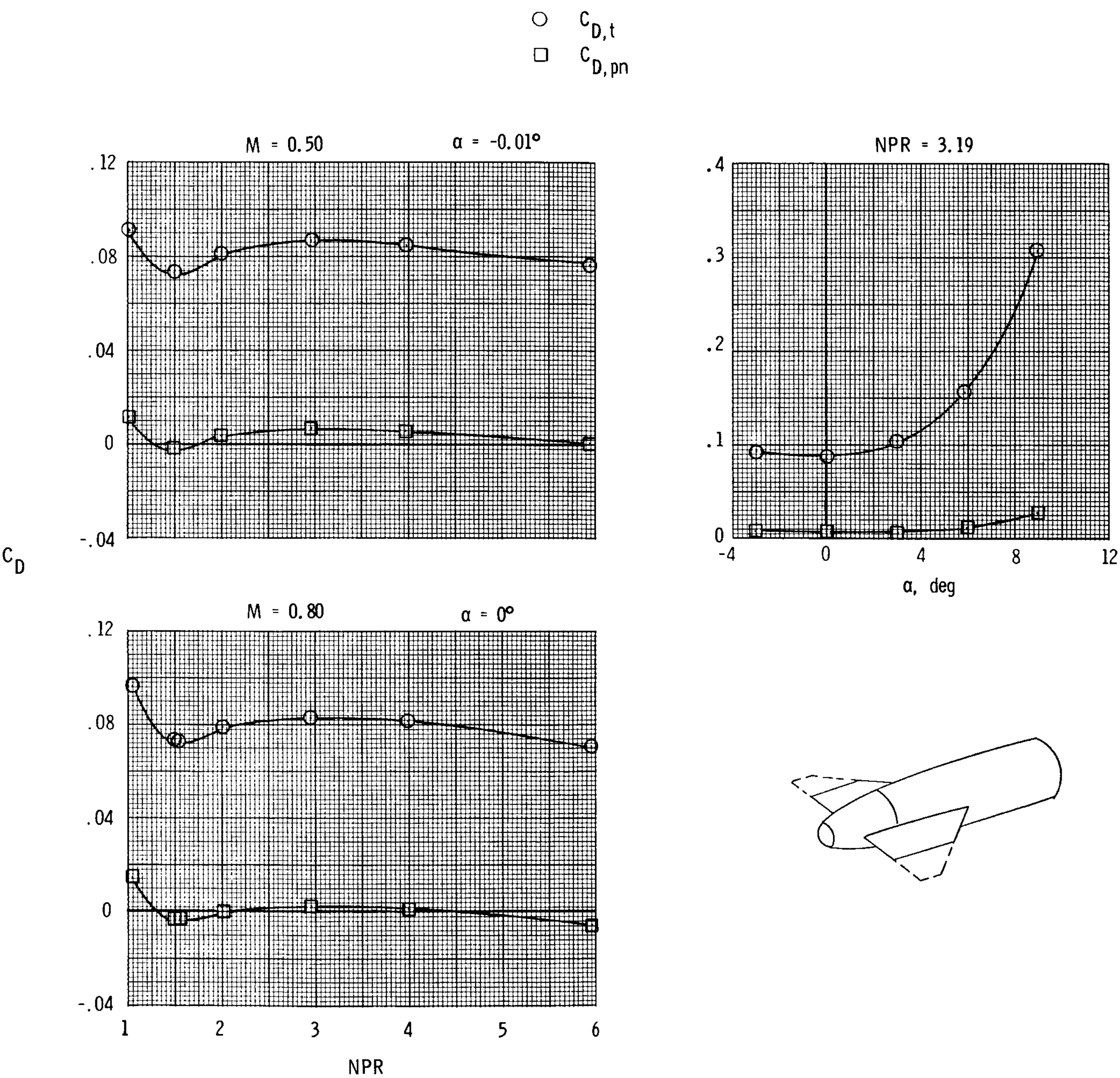

(b) $y/b = 0.50$.

Figure 8. Continued.

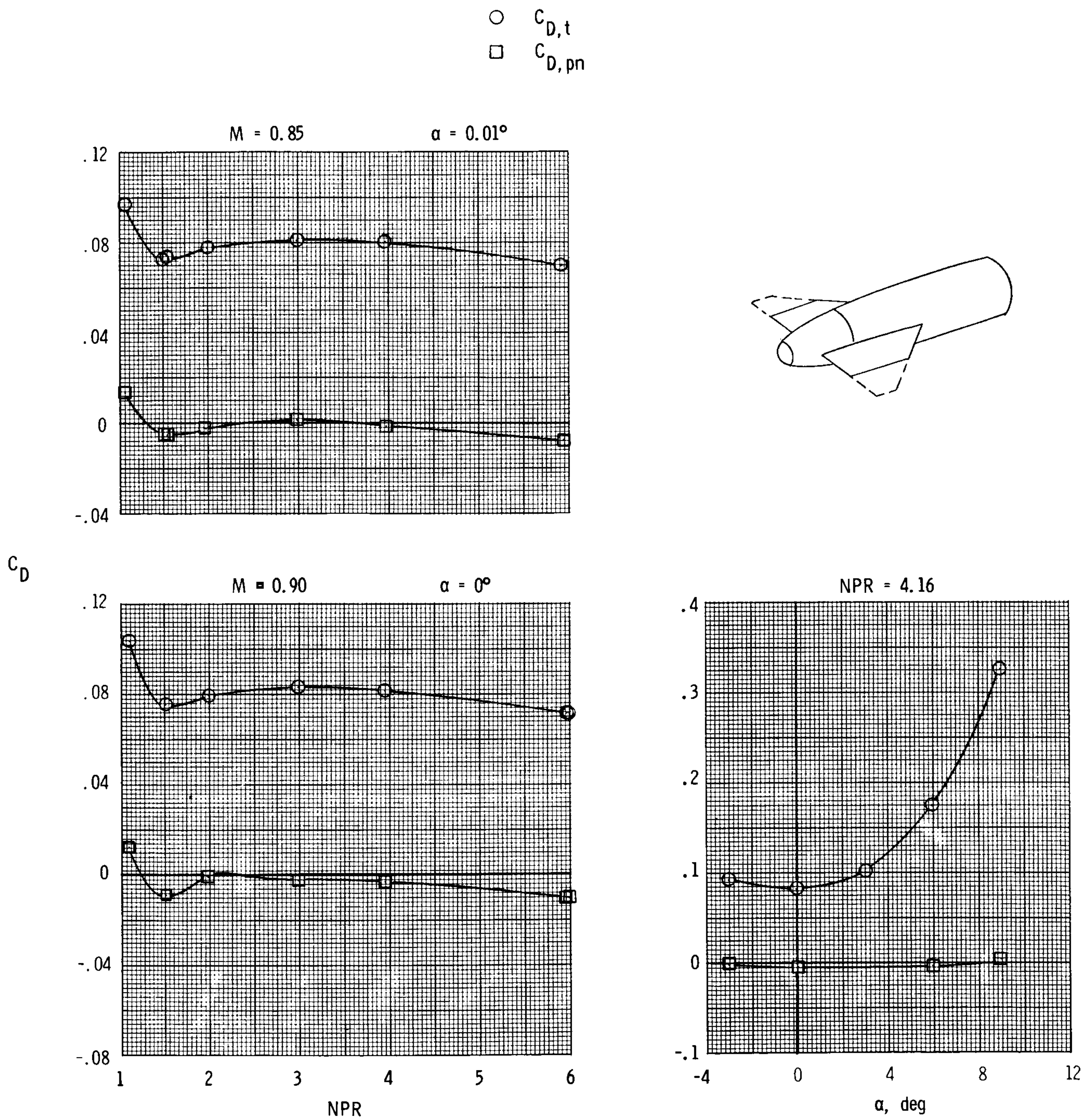

(b) Continued.

Figure 8. Continued.

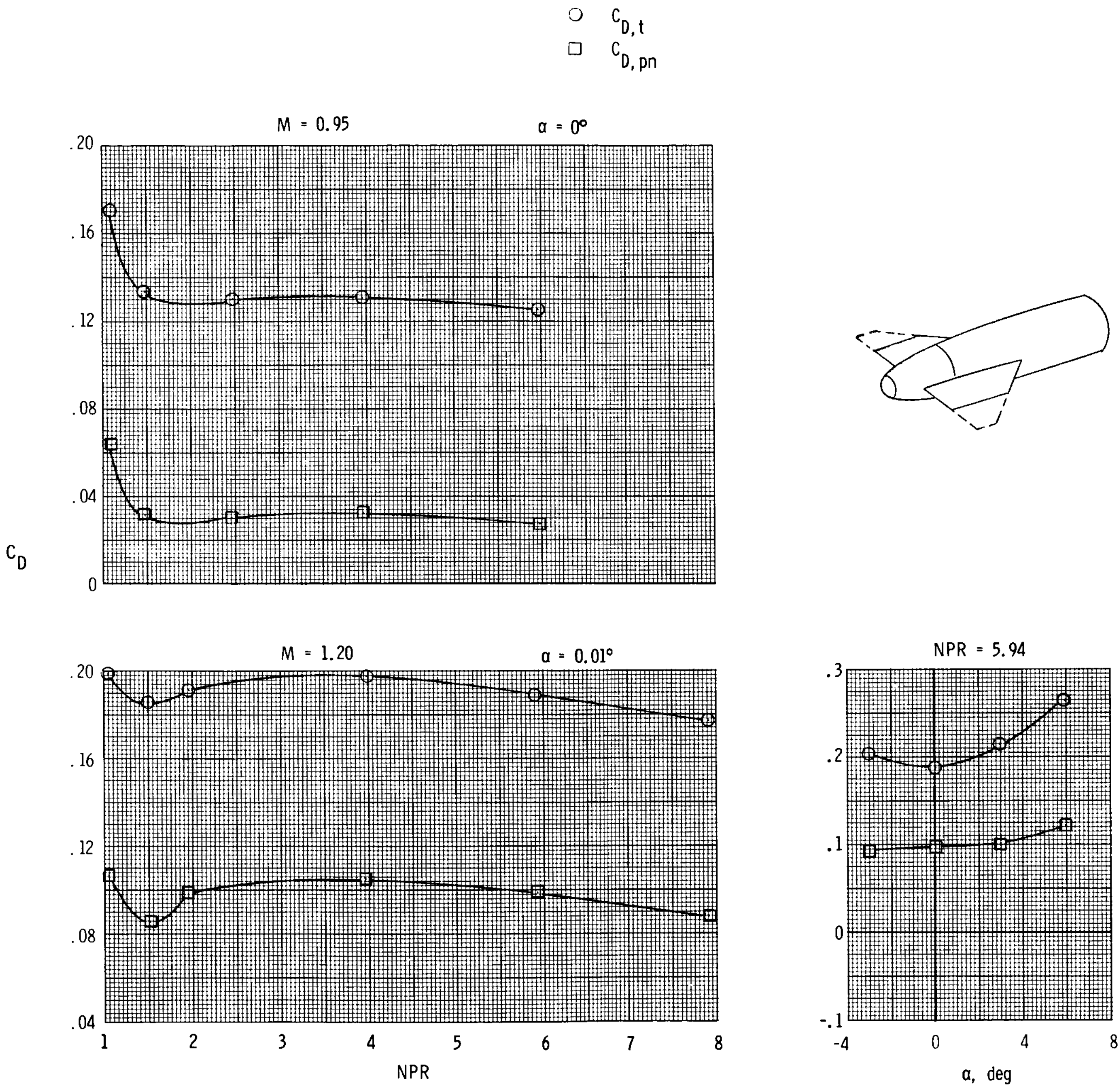

(b) Concluded.

Figure 8. Continued.

ORIGINAL PAGE IS
OF POOR QUALITY

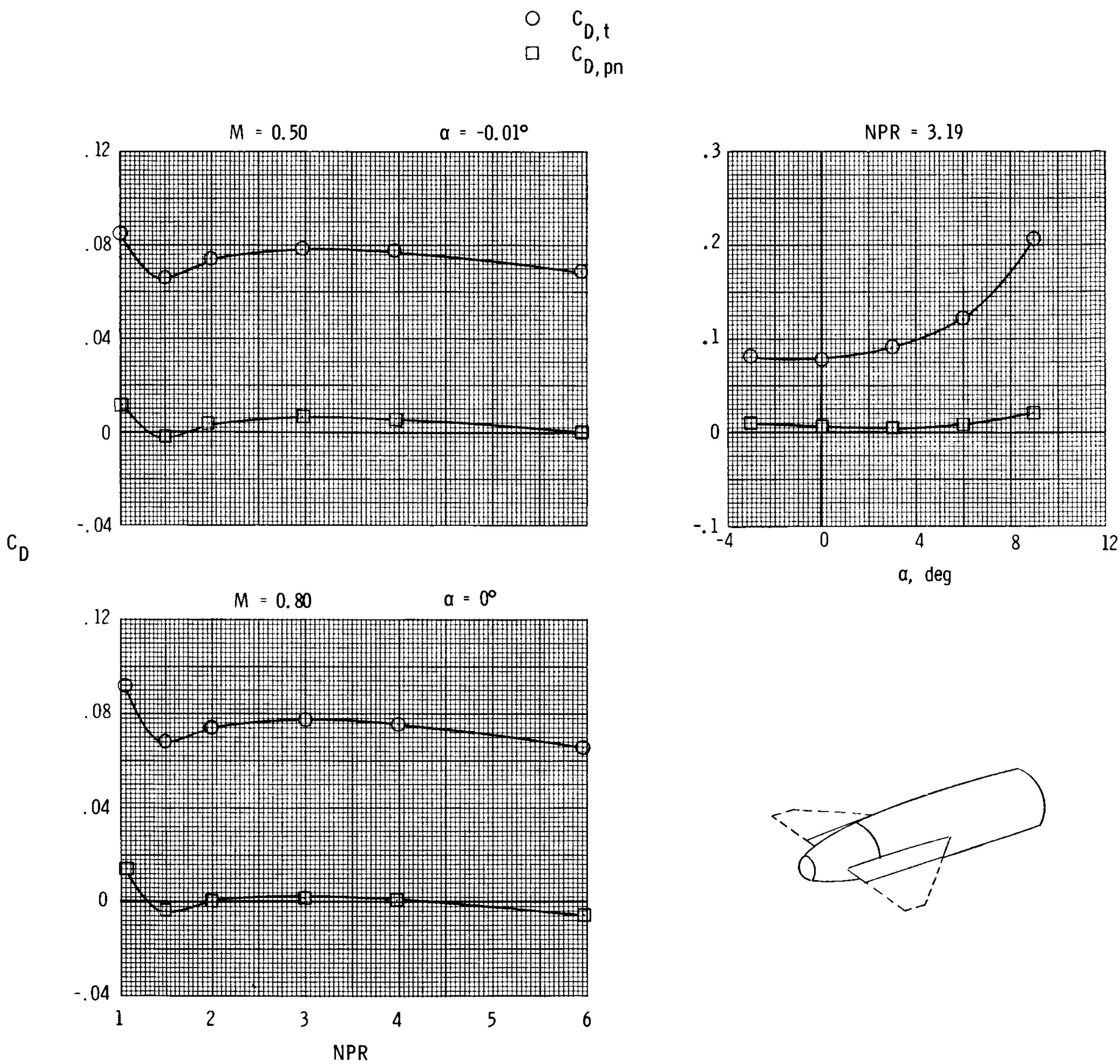

(c) $y/b = 0.30$.

Figure 8. Continued.

ORIGINAL PAGE IS
OF POOR QUALITY

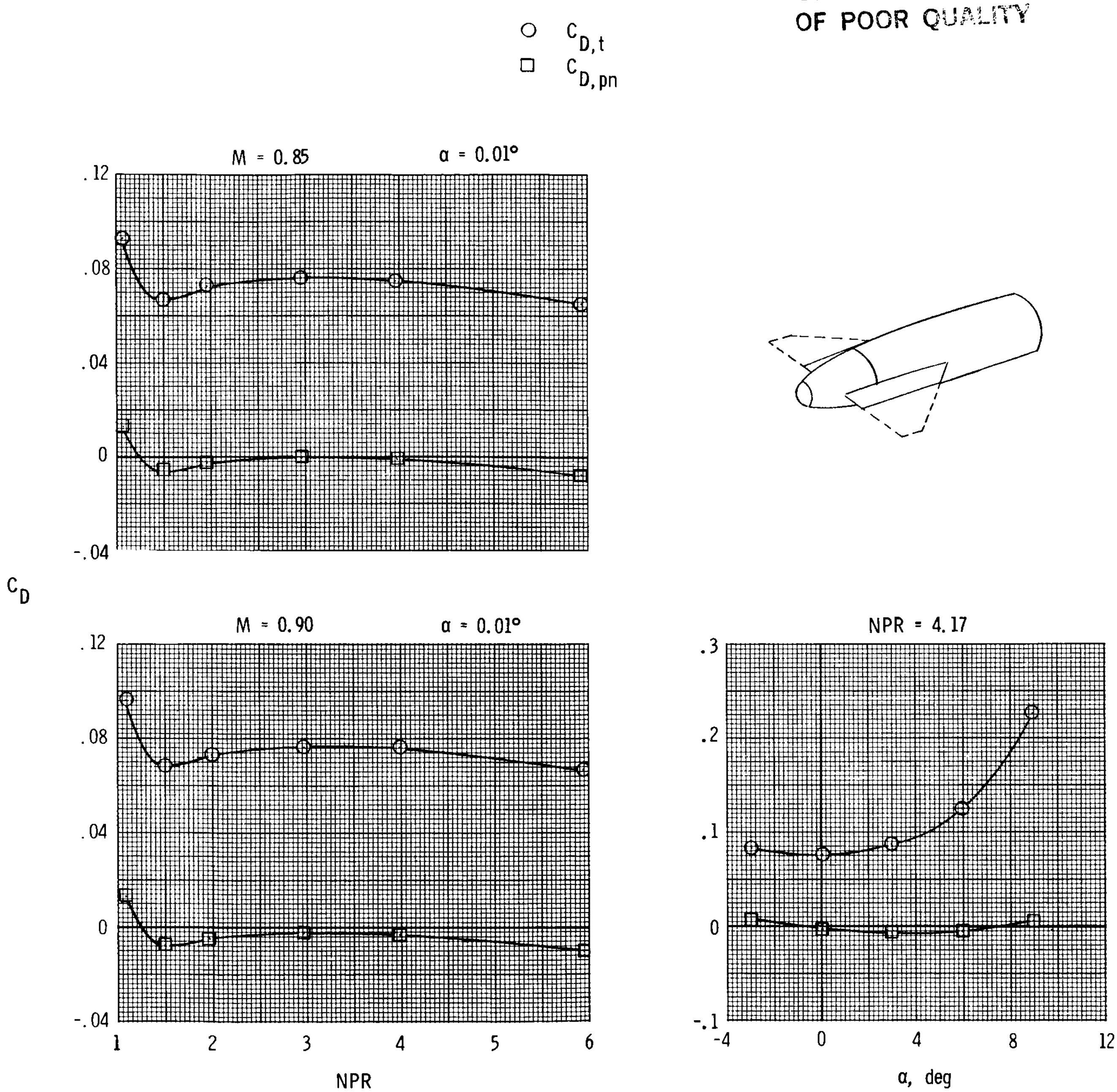

(c) Continued.

Figure 8. Continued.

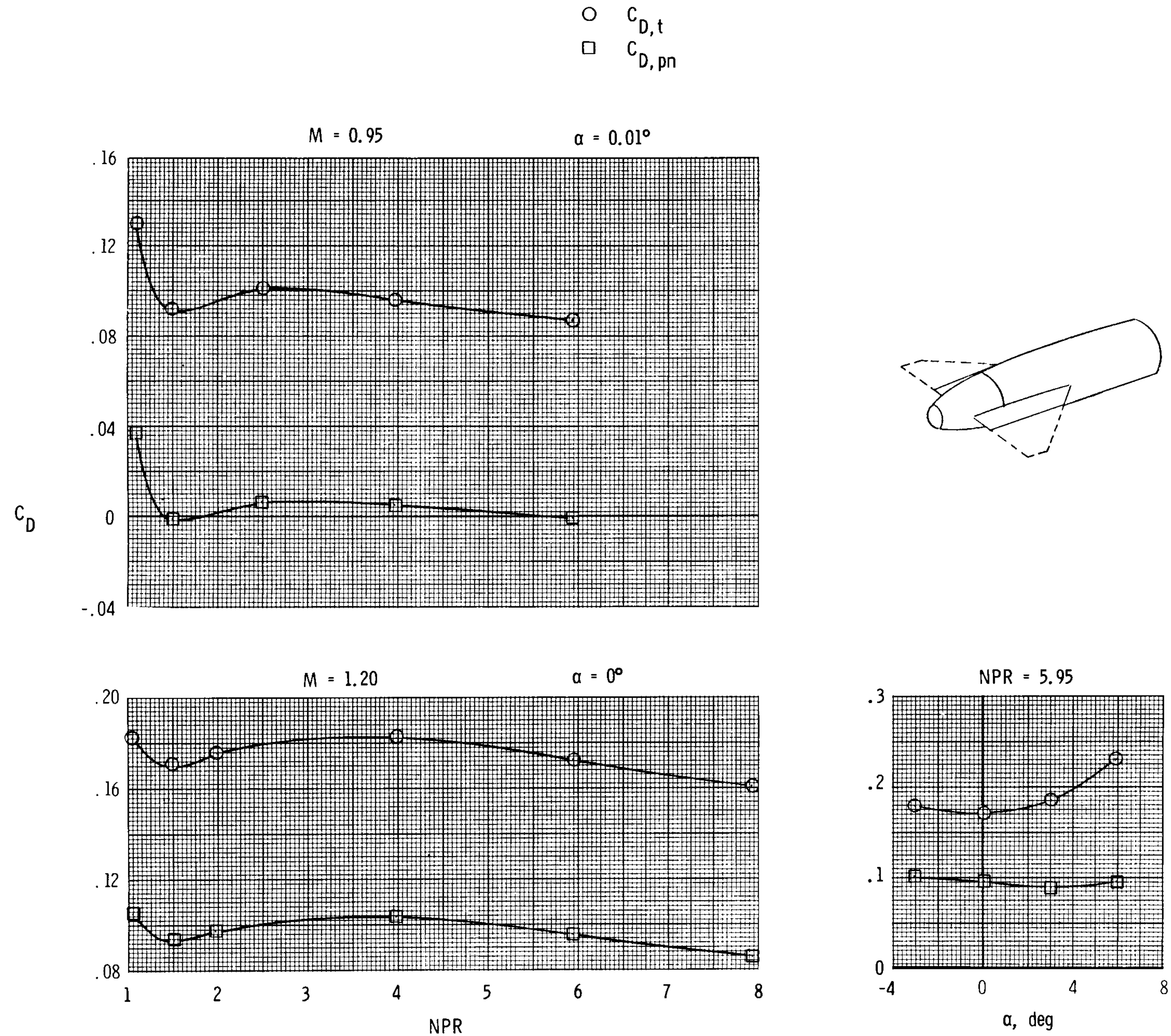

(c) Concluded.

Figure 8. Continued.

ORIGINAL PAGE IS
OF POOR QUALITY

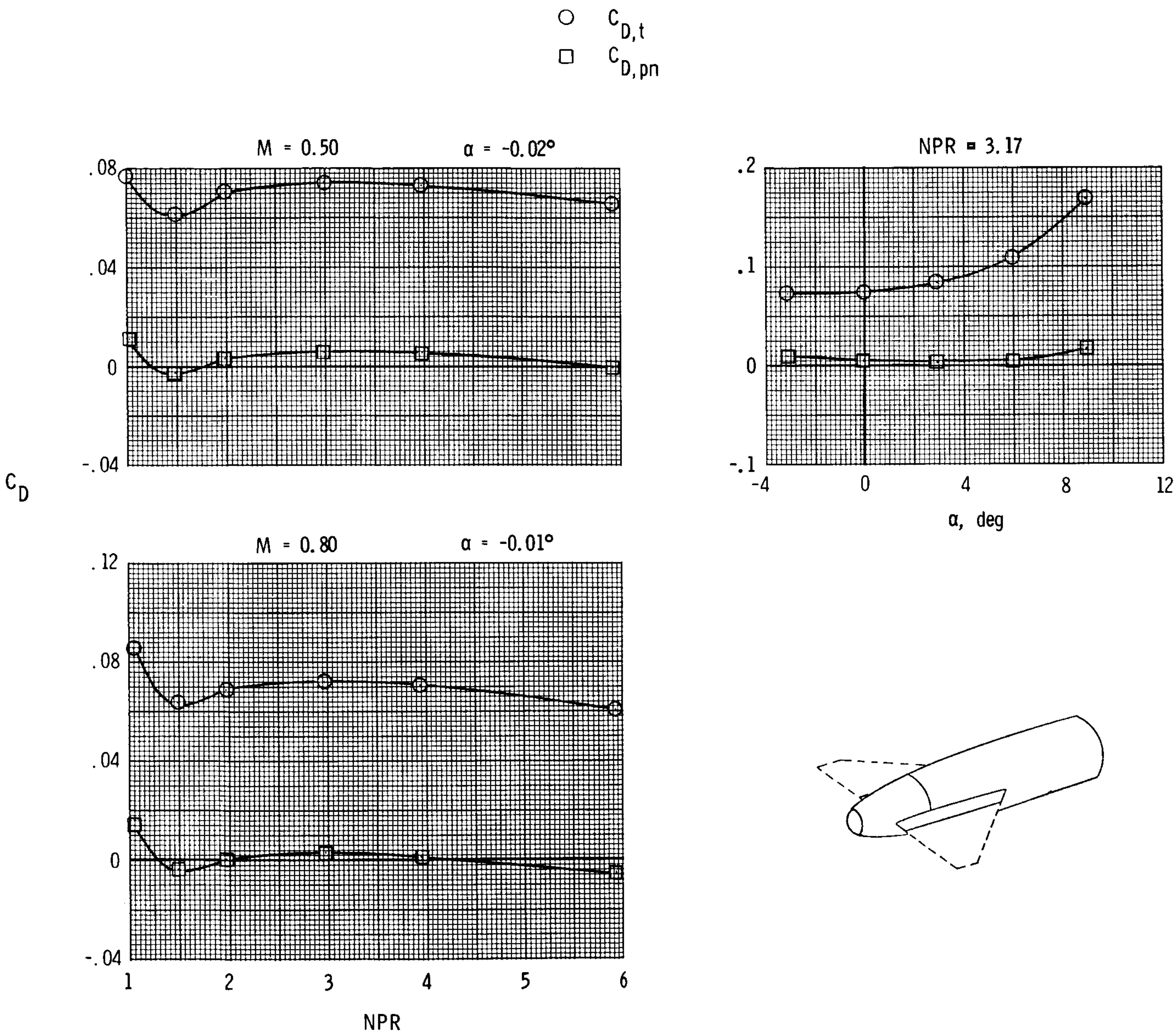

(d) $y/b = 0.20$.

Figure 8. Continued.

ORIGINAL PAGE IS
OF POOR QUALITY

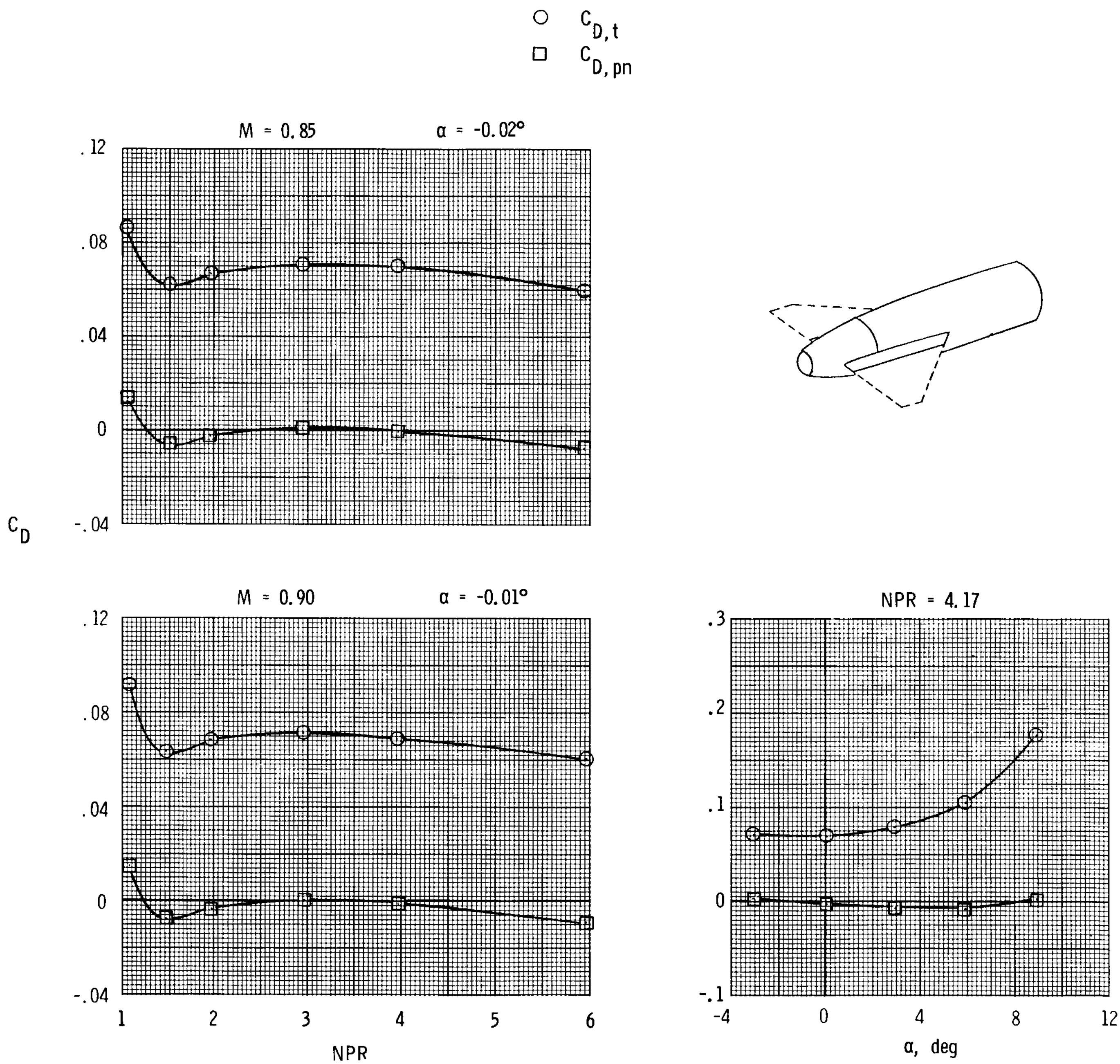

(d) Continued.

Figure 8. Continued.

ORIGINAL PAGE IS
OF POOR QUALITY

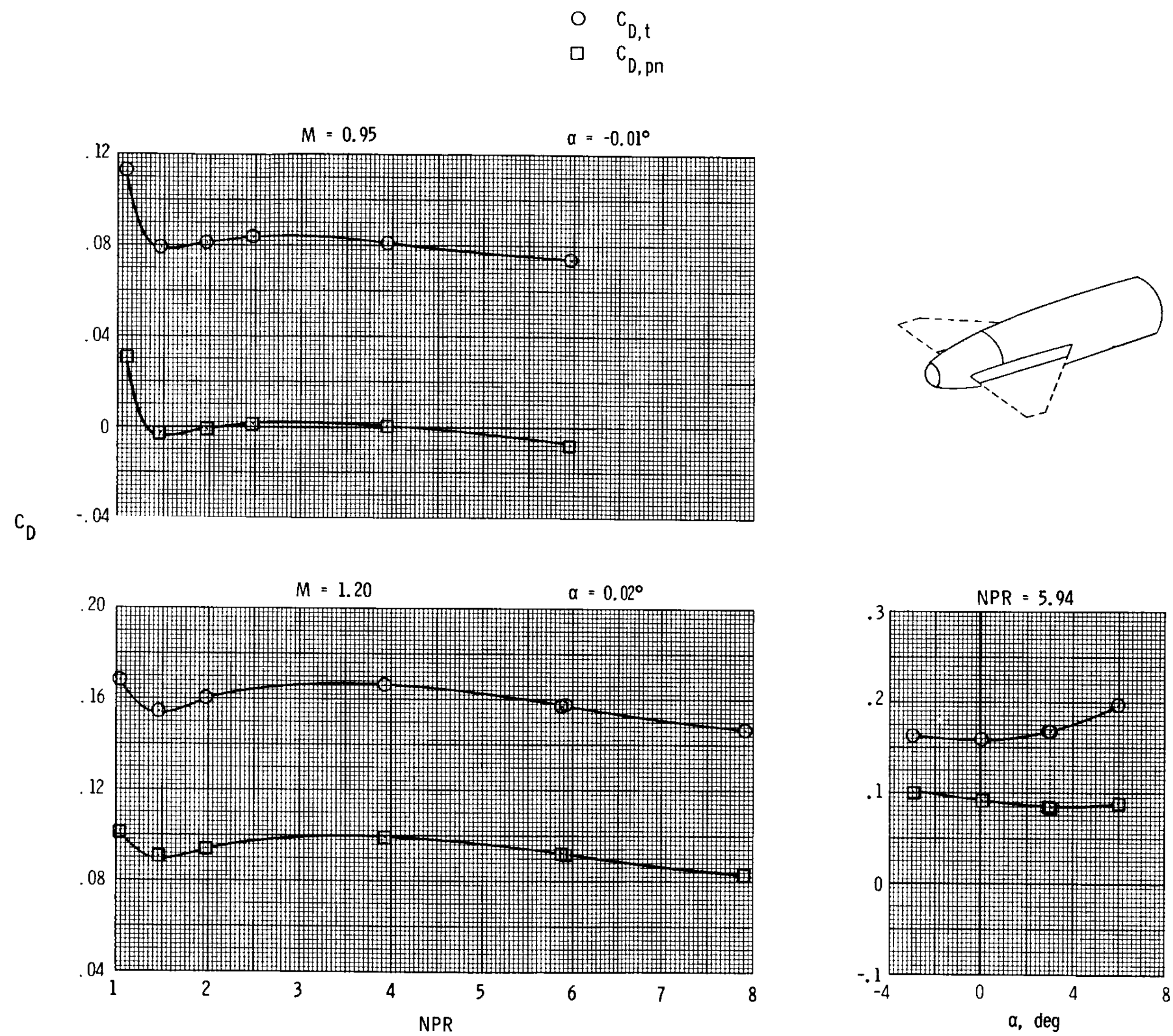

(d) Concluded.

Figure 8. Continued.

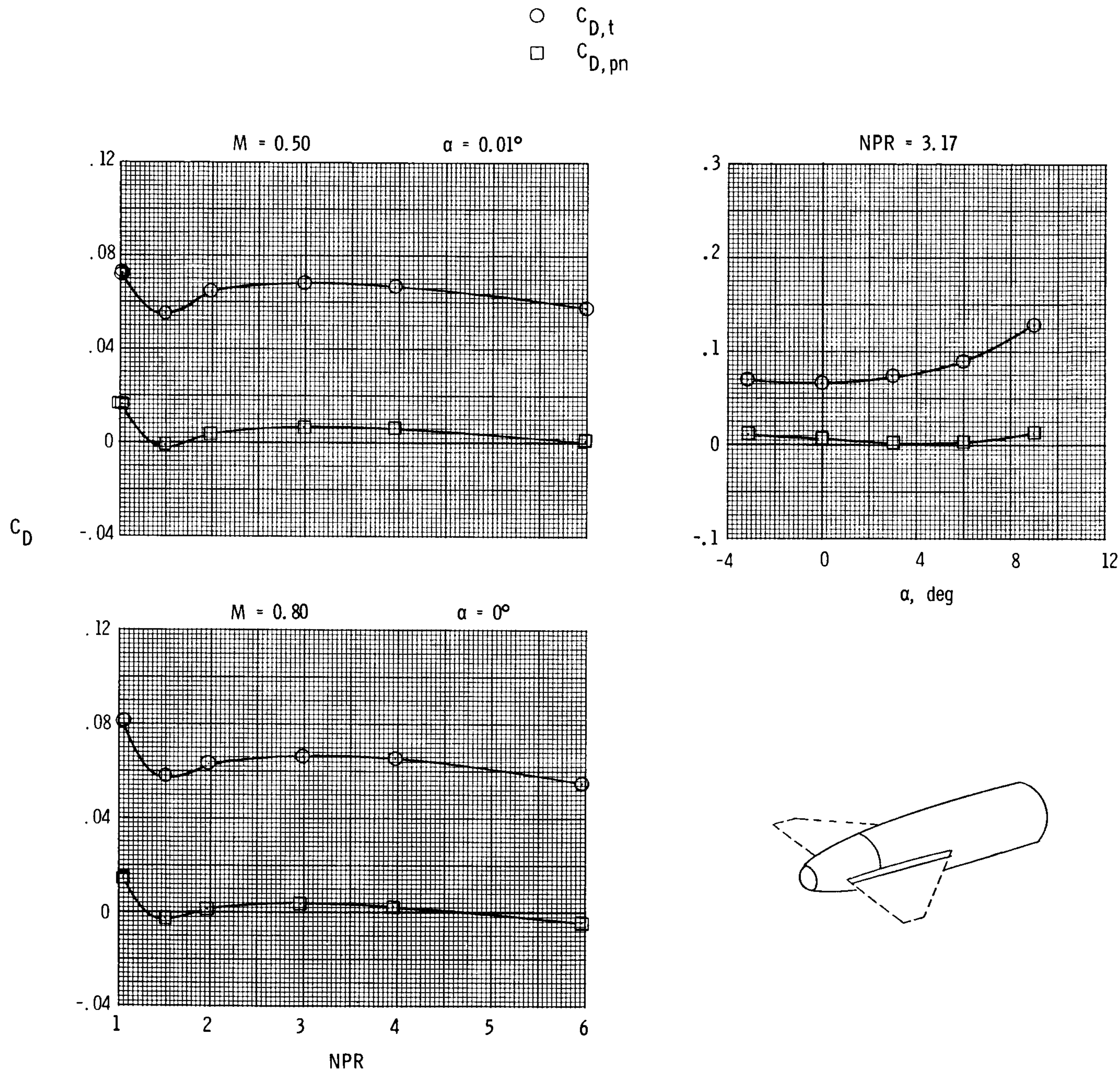

(e) $y/b = 0.10$.

Figure 8. Continued.

ORIGINAL PAGE IS
OF POOR QUALITY

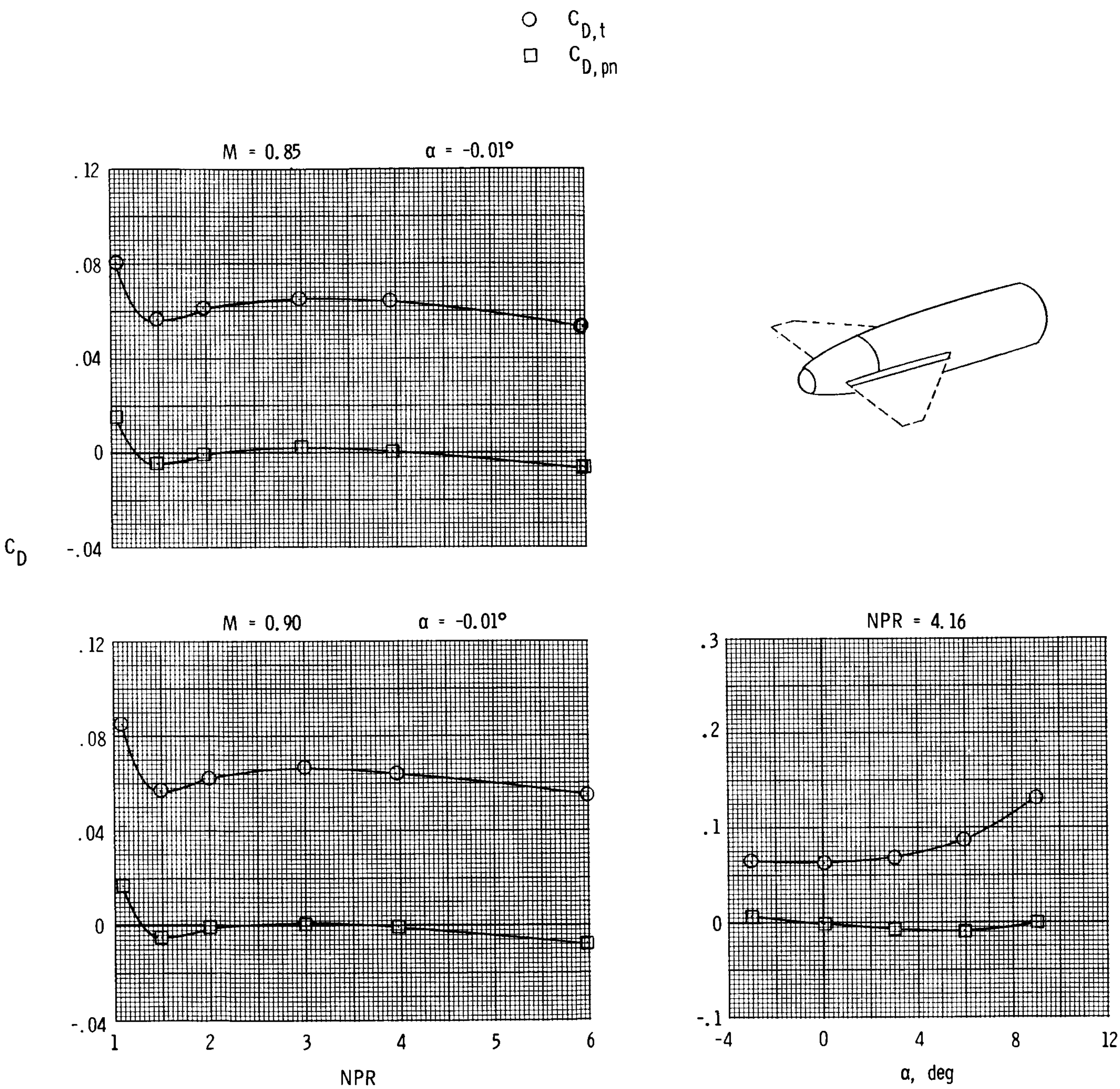

(e) Continued.

Figure 8. Continued.

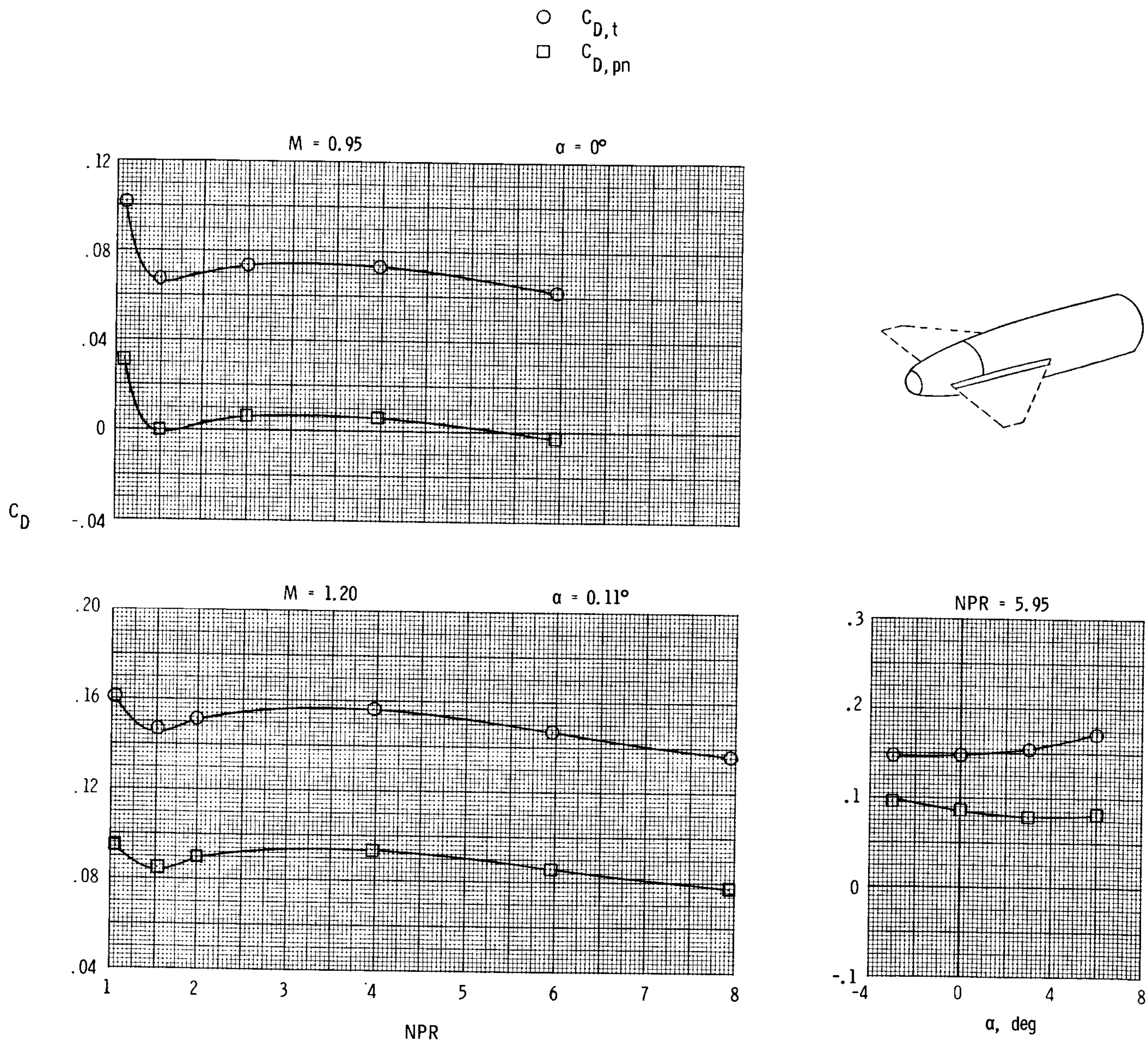

(e) Concluded.

Figure 8. Concluded.

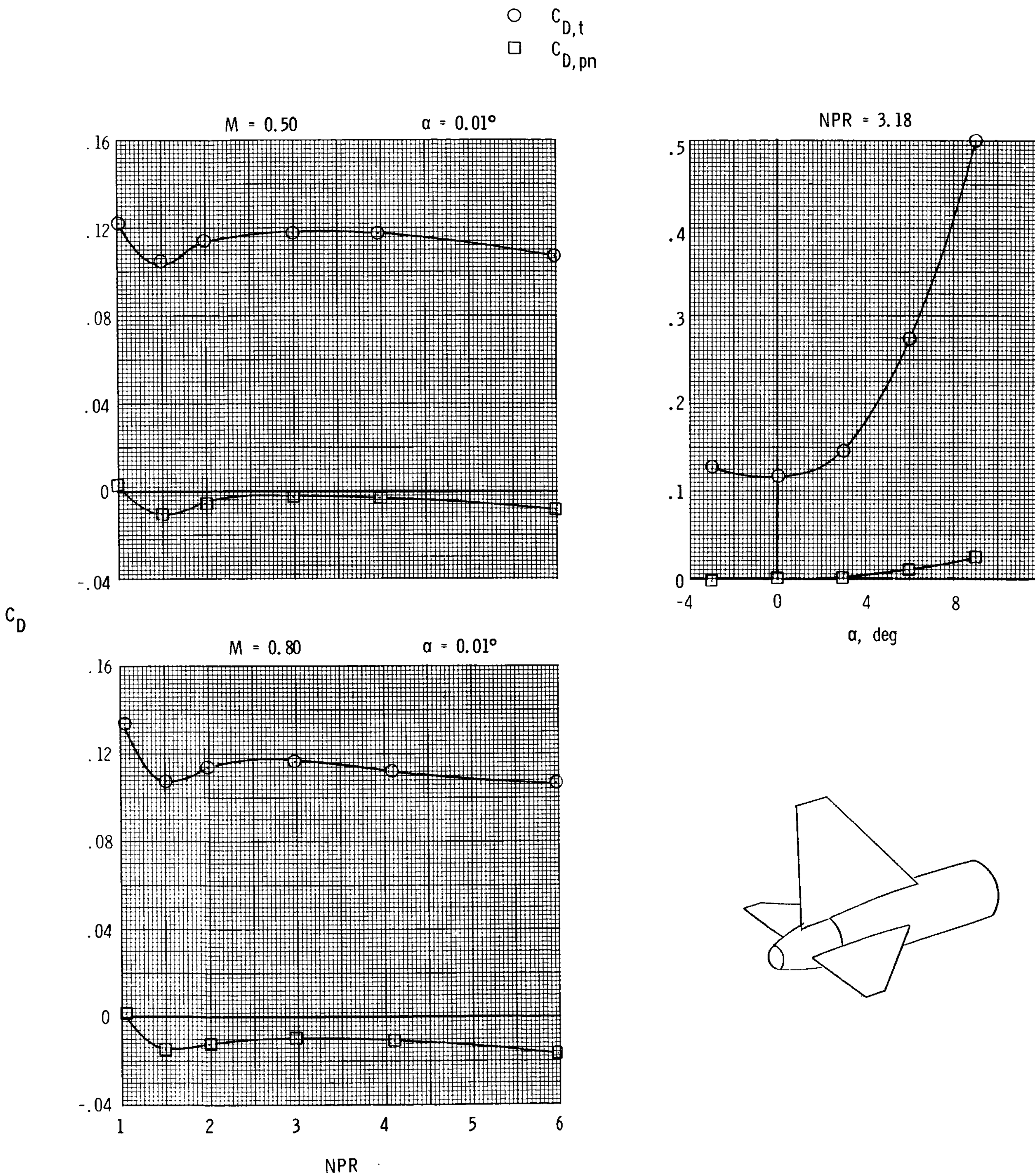

(a) $y/b = 1.00$.

Figure 9. Variation of total aft-end and nozzle pressure drag coefficients with nozzle pressure ratio and angle of attack for aft vertical tail, aft horizontal tails.

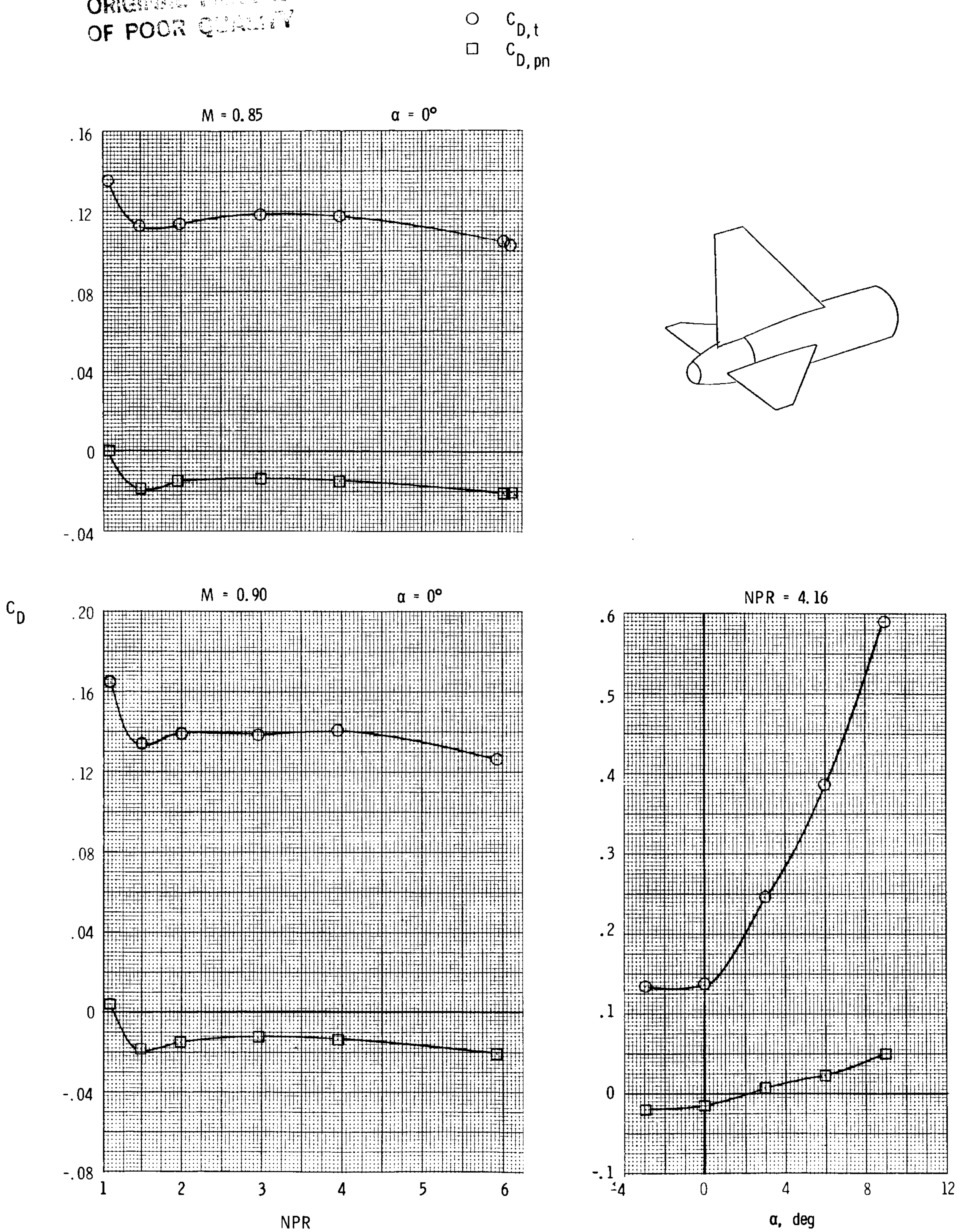

(a) Continued.

Figure 9. Continued.

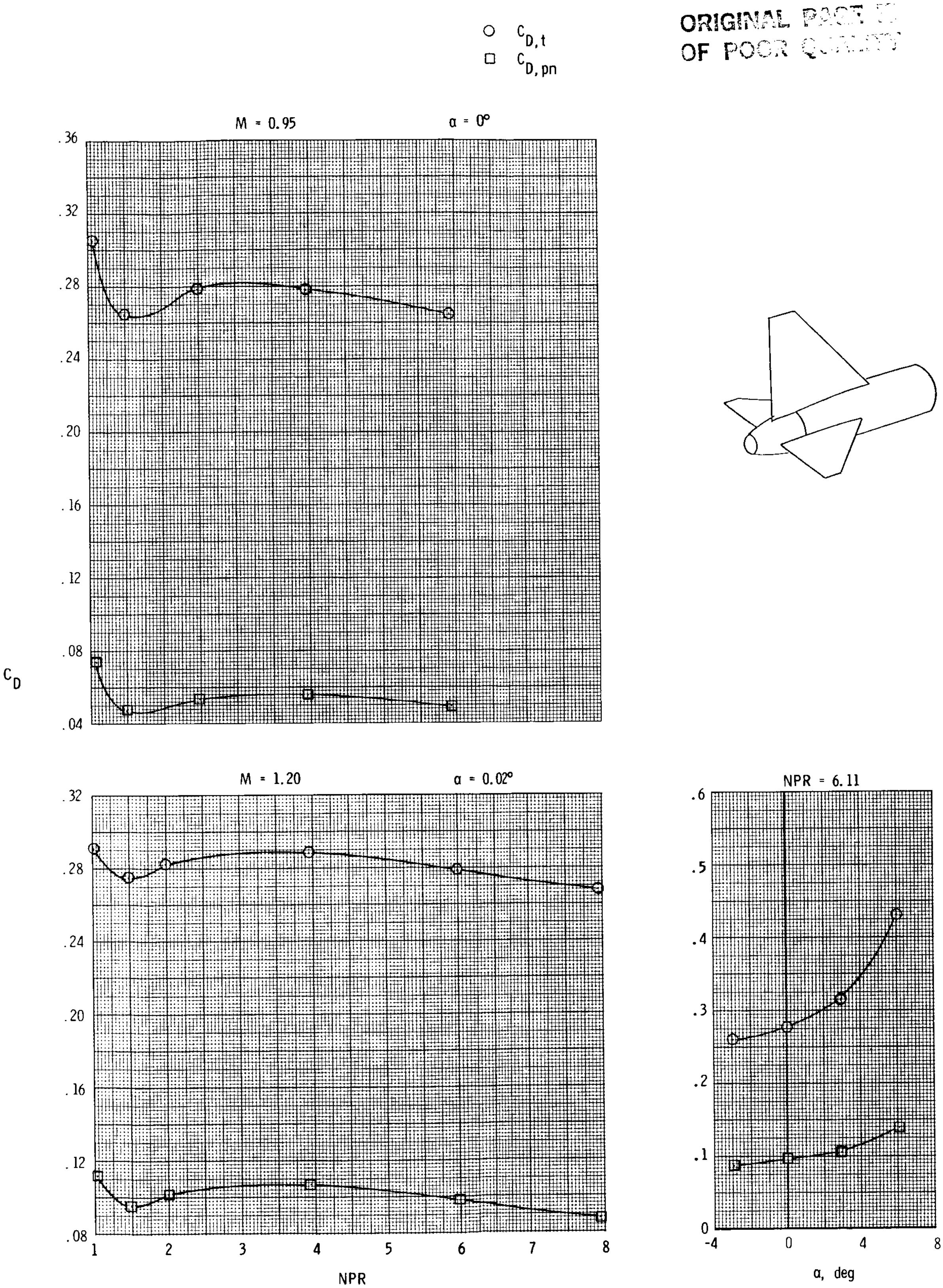

(a) Concluded.

Figure 9. Continued.

ORIGINAL PAGE IS
OF POOR QUALITY

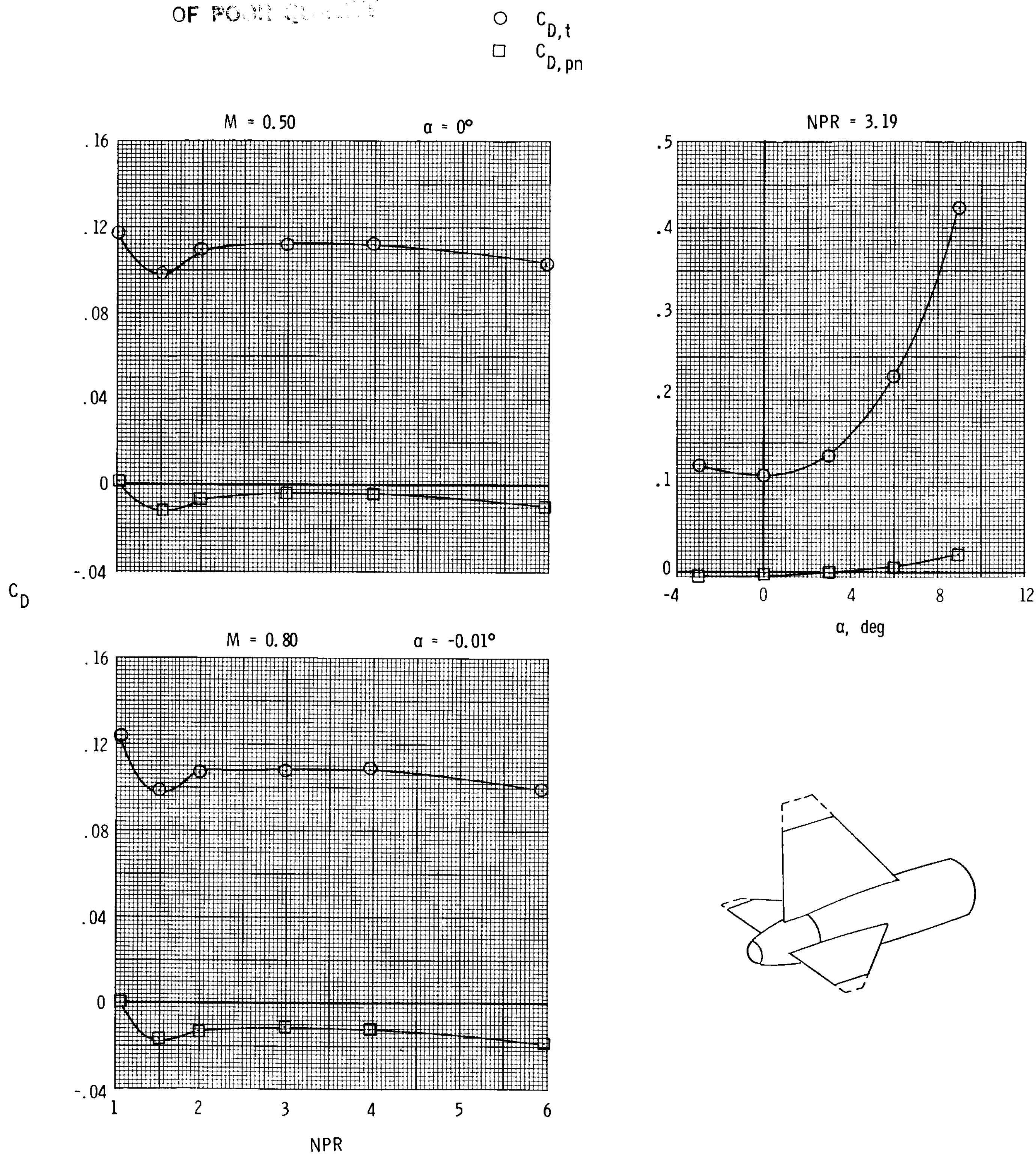

(b) $y/b = 0.75$.

Figure 9. Continued.

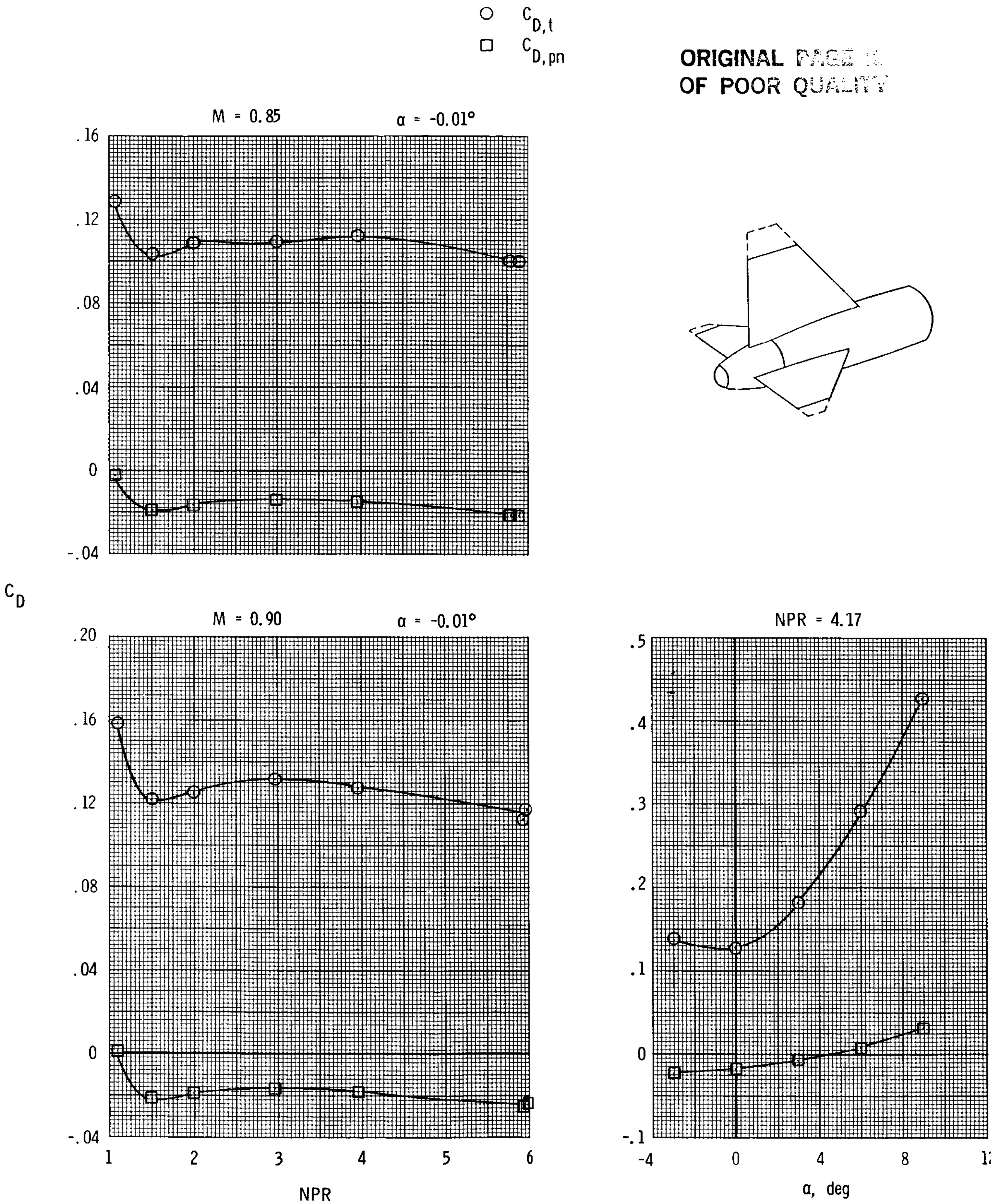

ORIGINAL PAGE IS
OF POOR QUALITY

(b) Continued.

Figure 9. Continued.

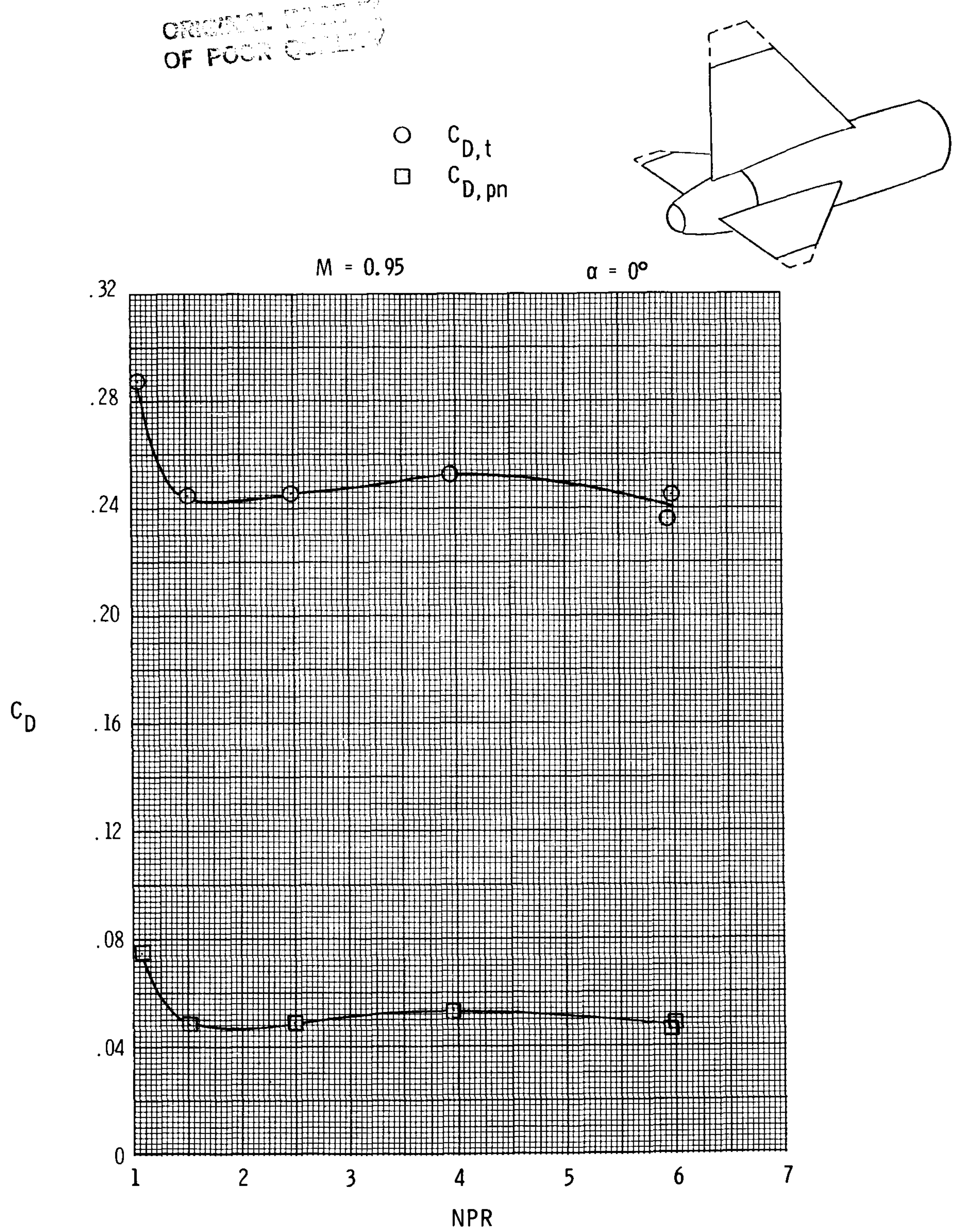

(b) Concluded.

Figure 9. Continued.

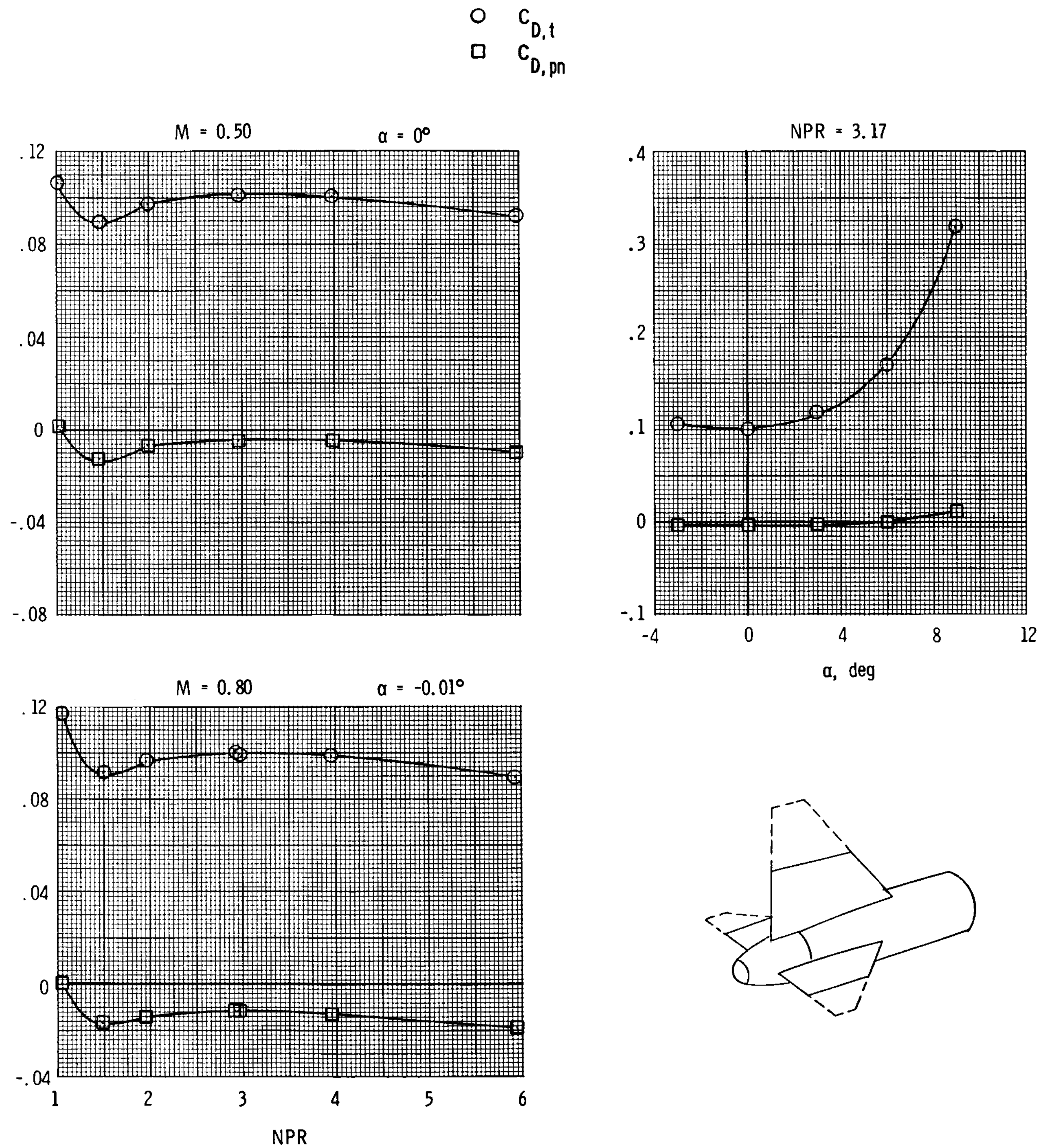

(c) $y/b = 0.50$.

Figure 9. Continued.

ORIGINAL PAGE IS
OF POOR QUALITY

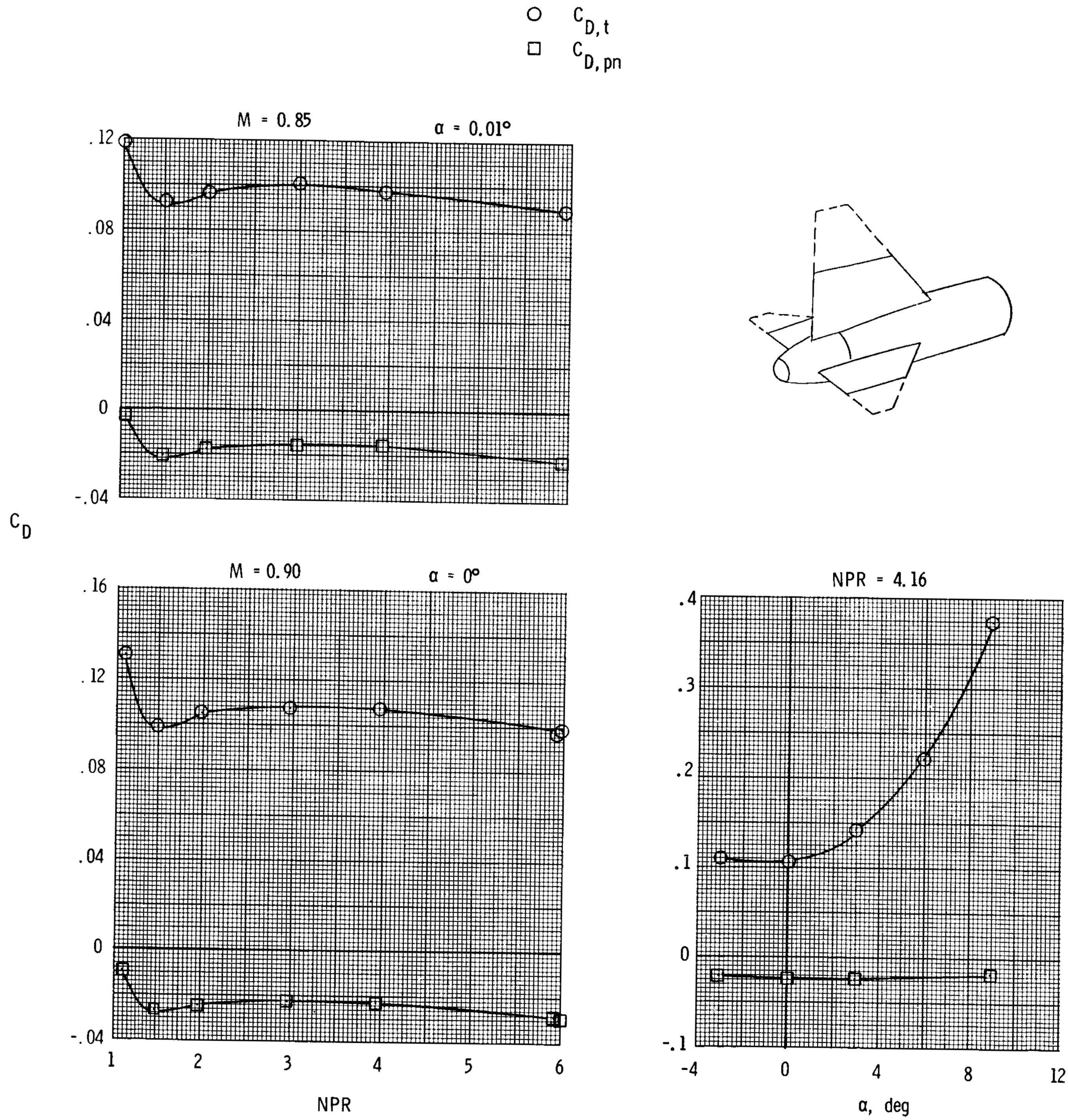

(c) Continued.

Figure 9. Continued.

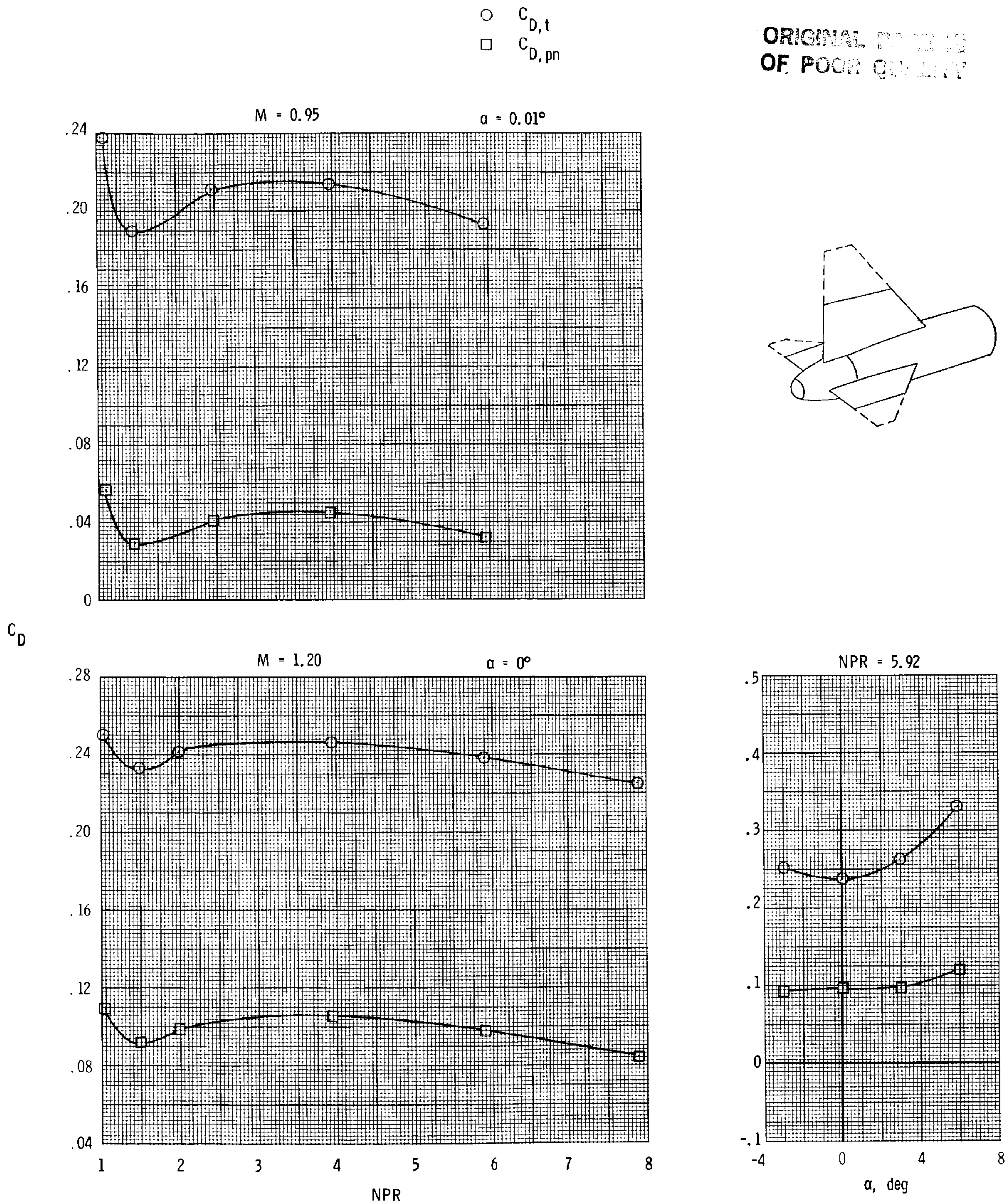

(c) Concluded.

Figure 9. Continued.

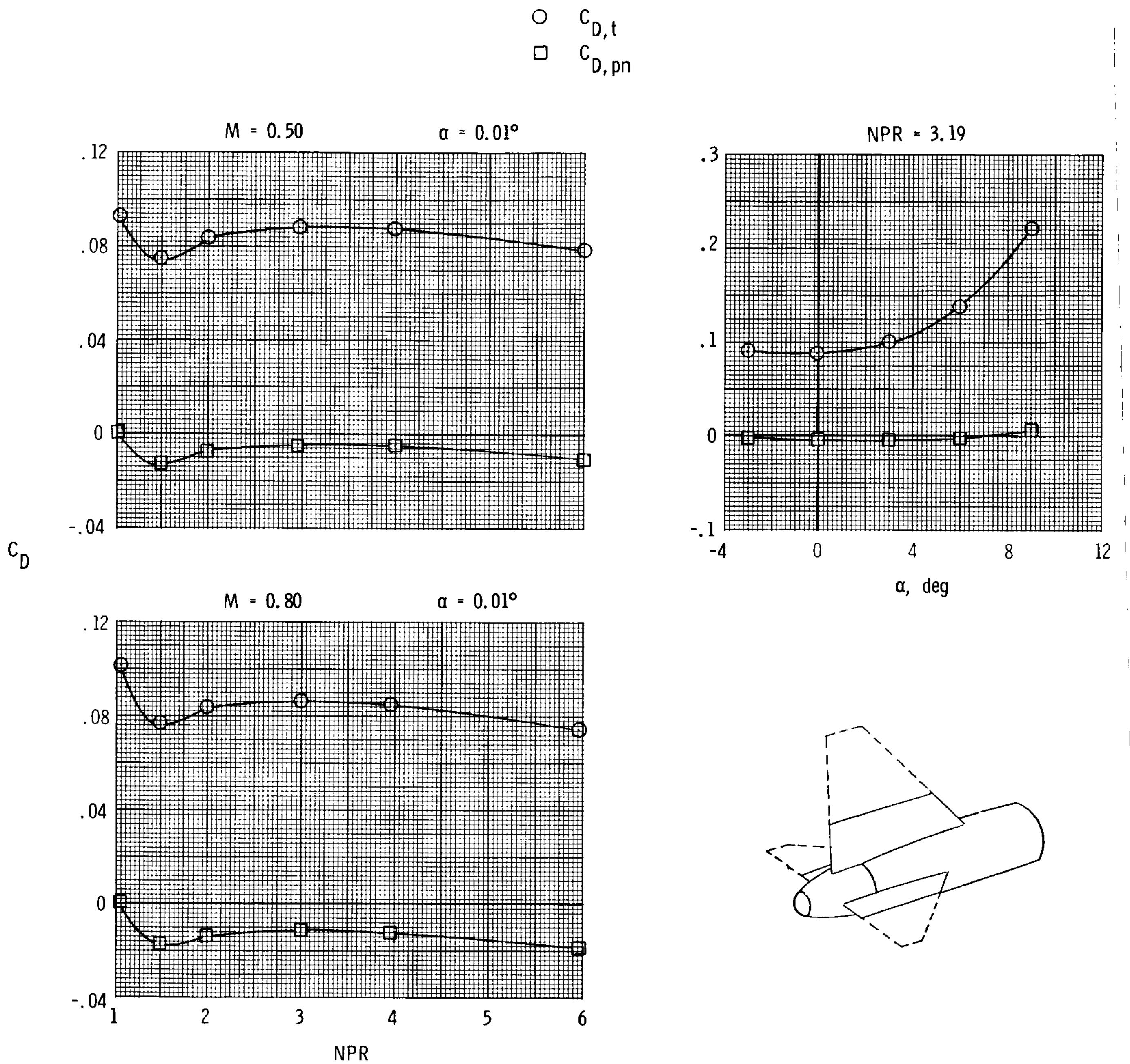

(d) $y/b = 0.30$.

Figure 9. Continued.

ORIGINAL PAGE IS
OF POOR QUALITY

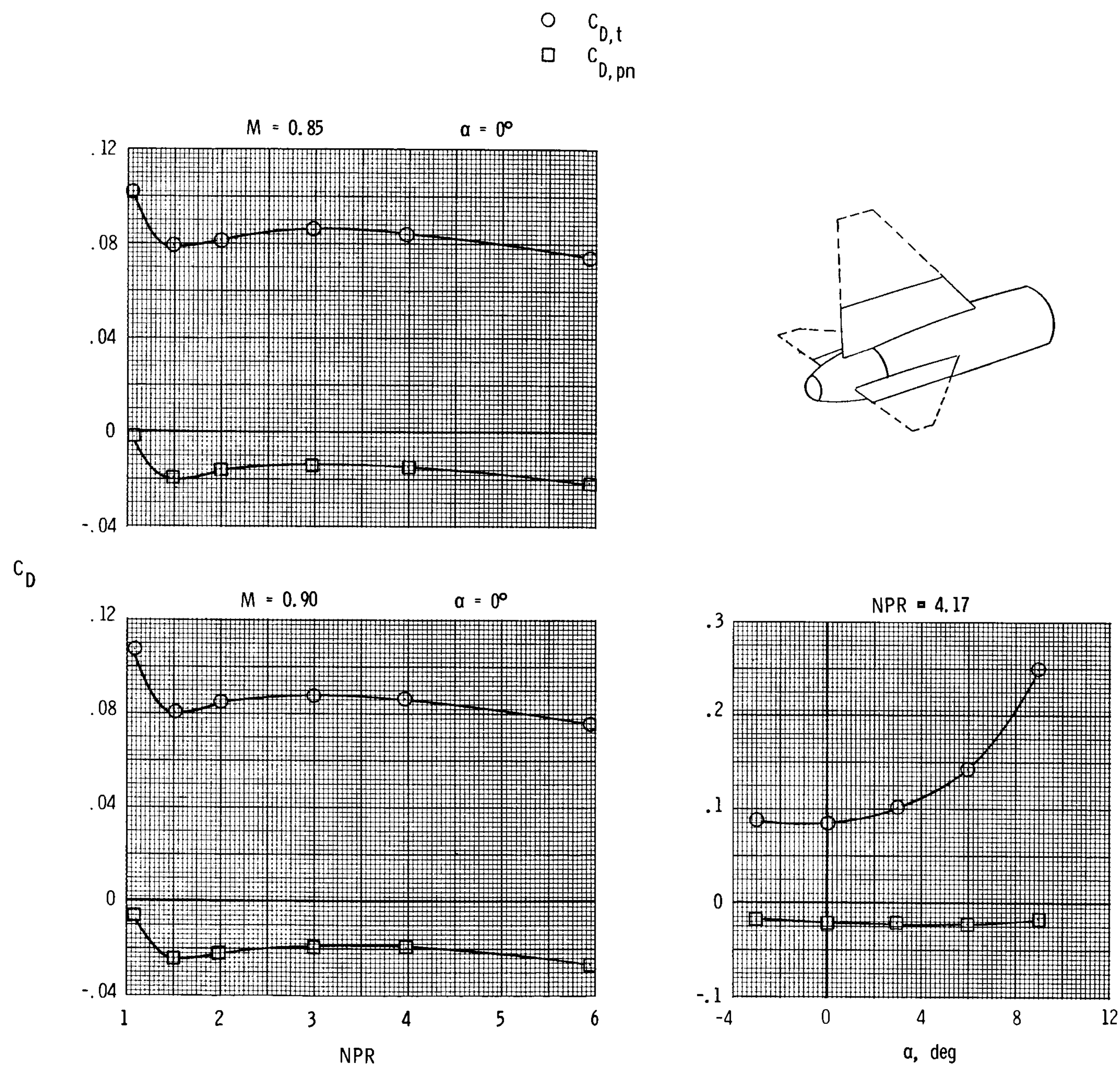

(d) Continued.

Figure 9. Continued.

ORIGINAL PAGE IS
OF POOR QUALITY

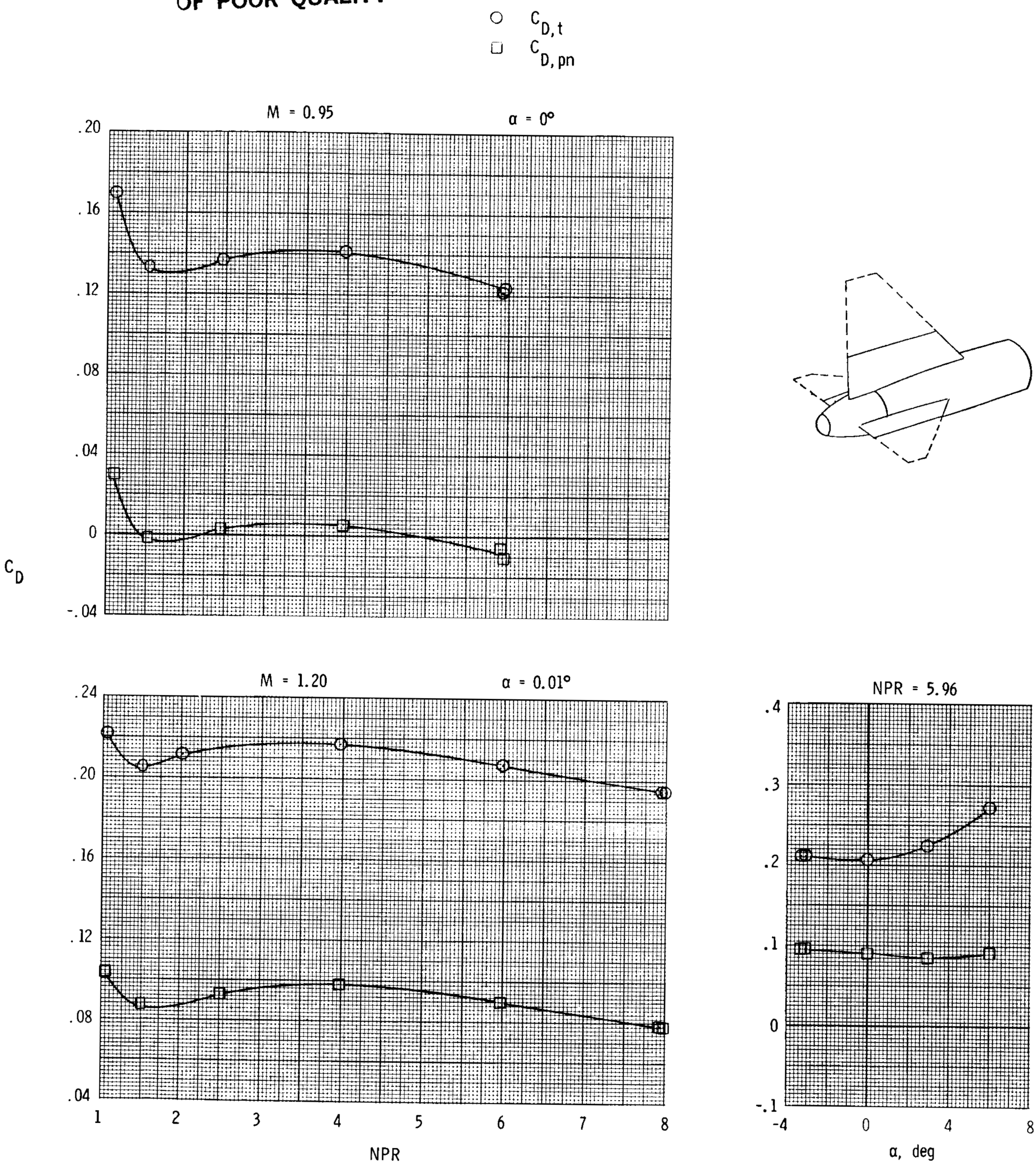

(d) Concluded.

Figure 9. Continued.

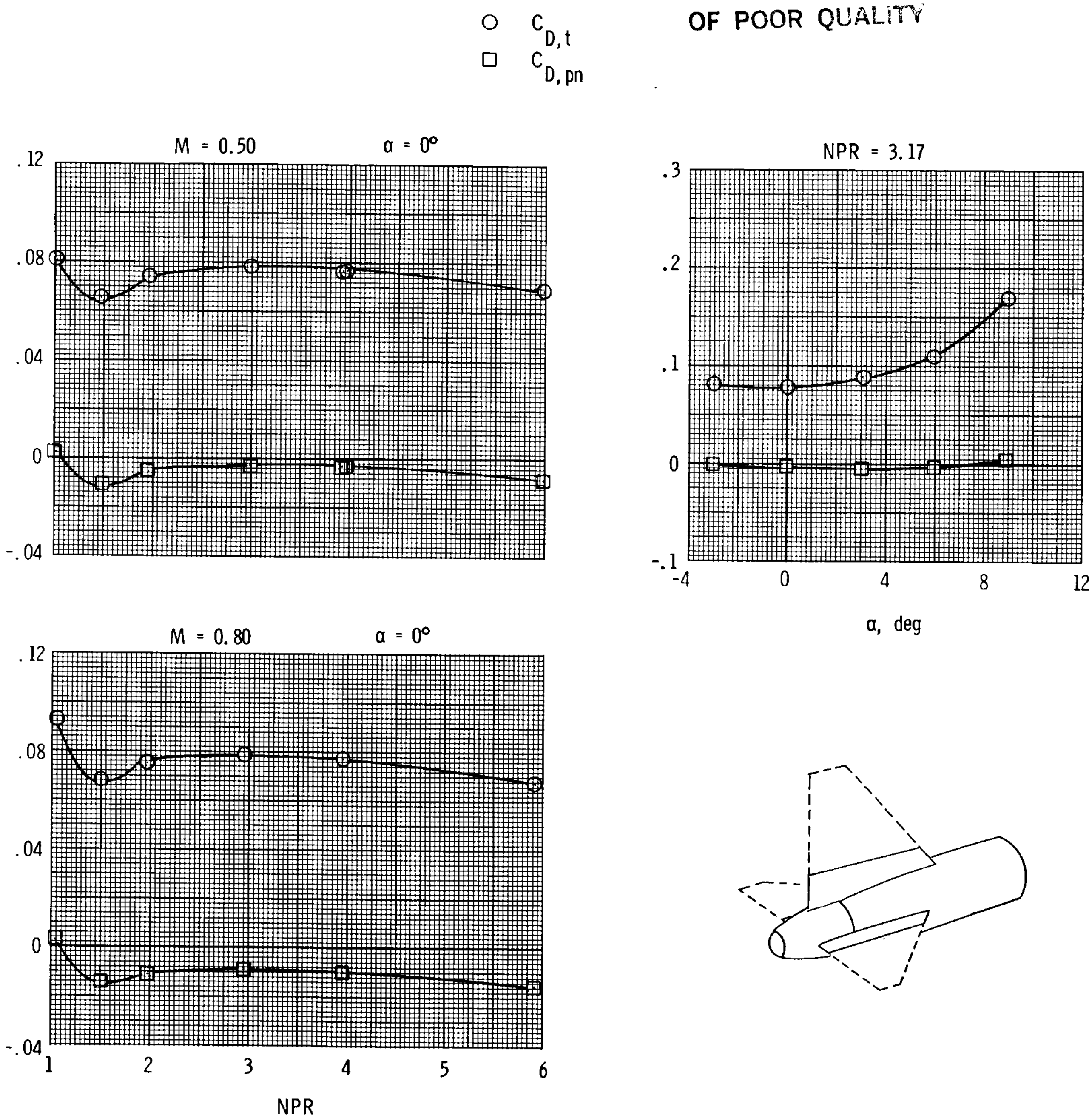

(e) $y/b = 0.20$.

Figure 9. Continued.

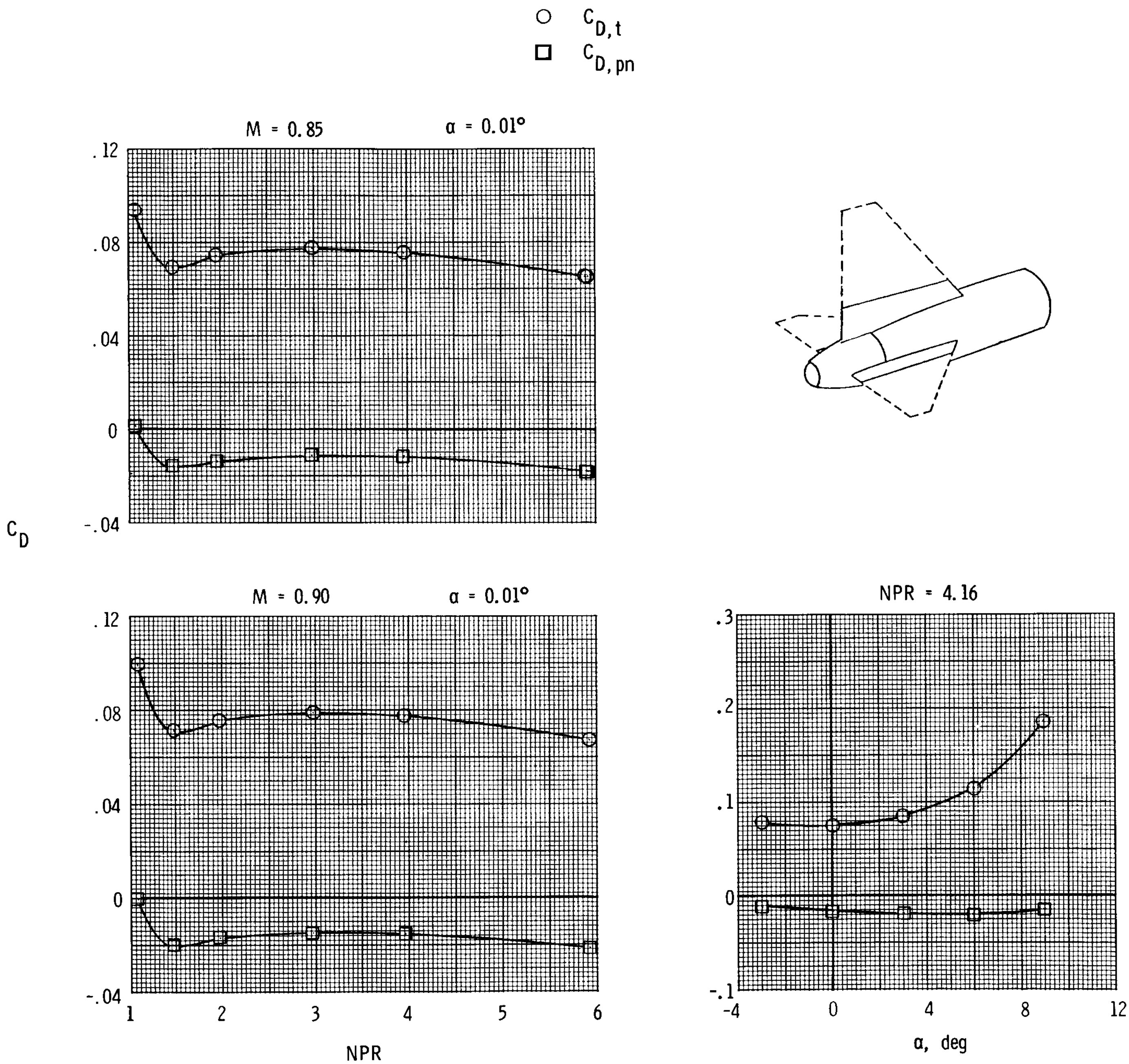

(e) Continued.

Figure 9. Continued.

ORIGINAL PAGE IS OF POOR QUALITY

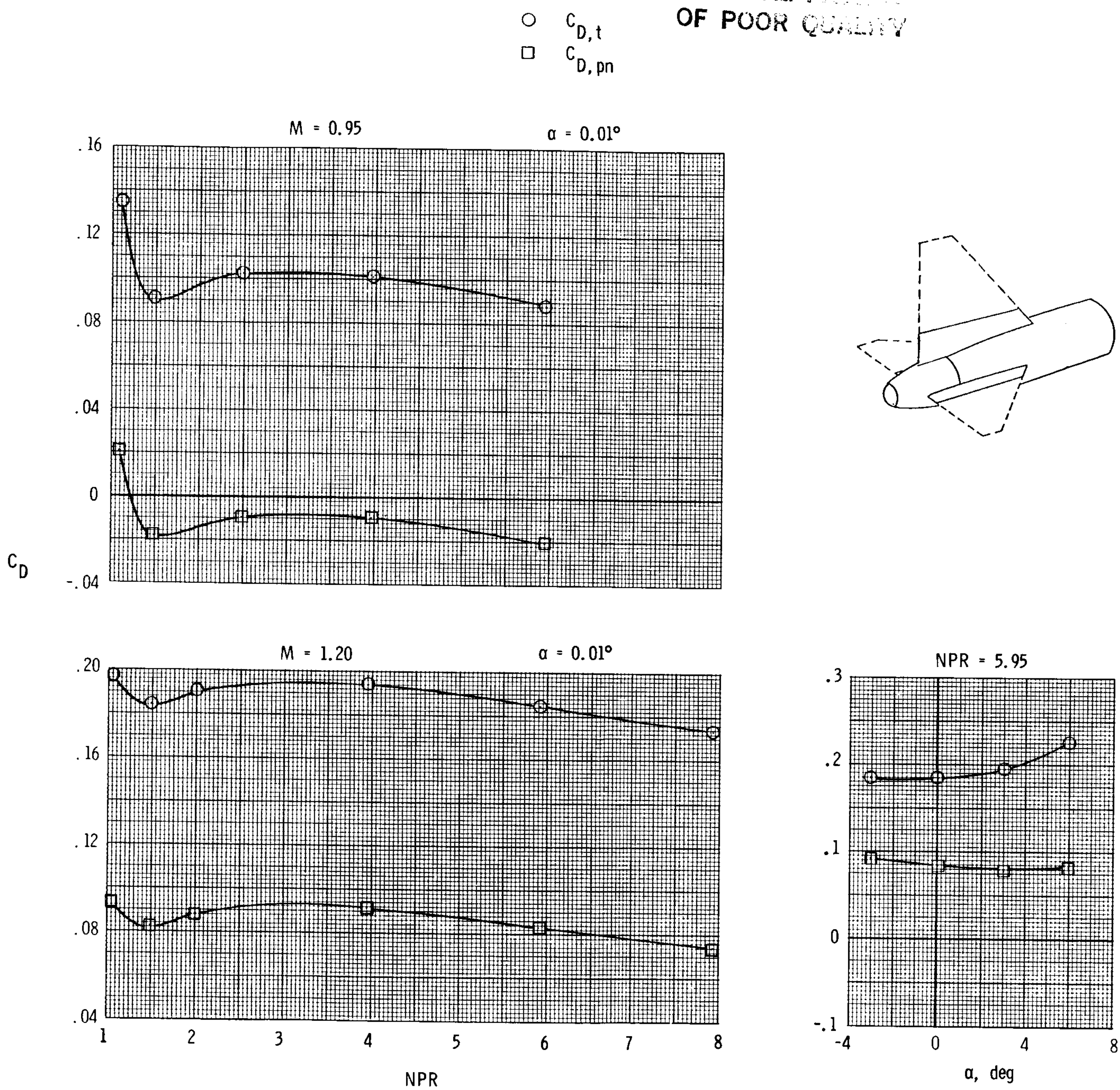

(e) Concluded.

Figure 9. Continued.

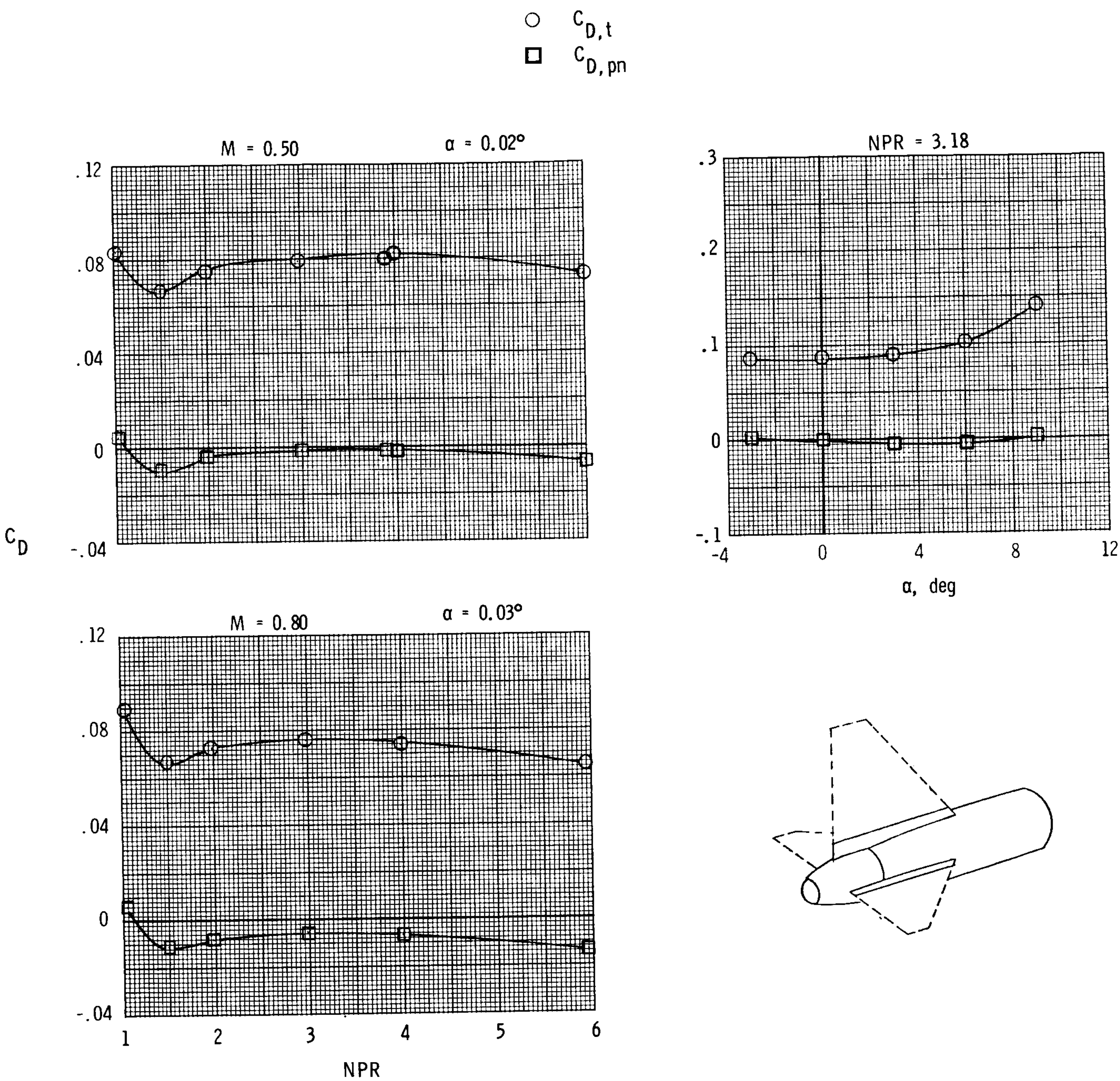

(f) $y/b = 0.10$.

Figure 9. Continued.

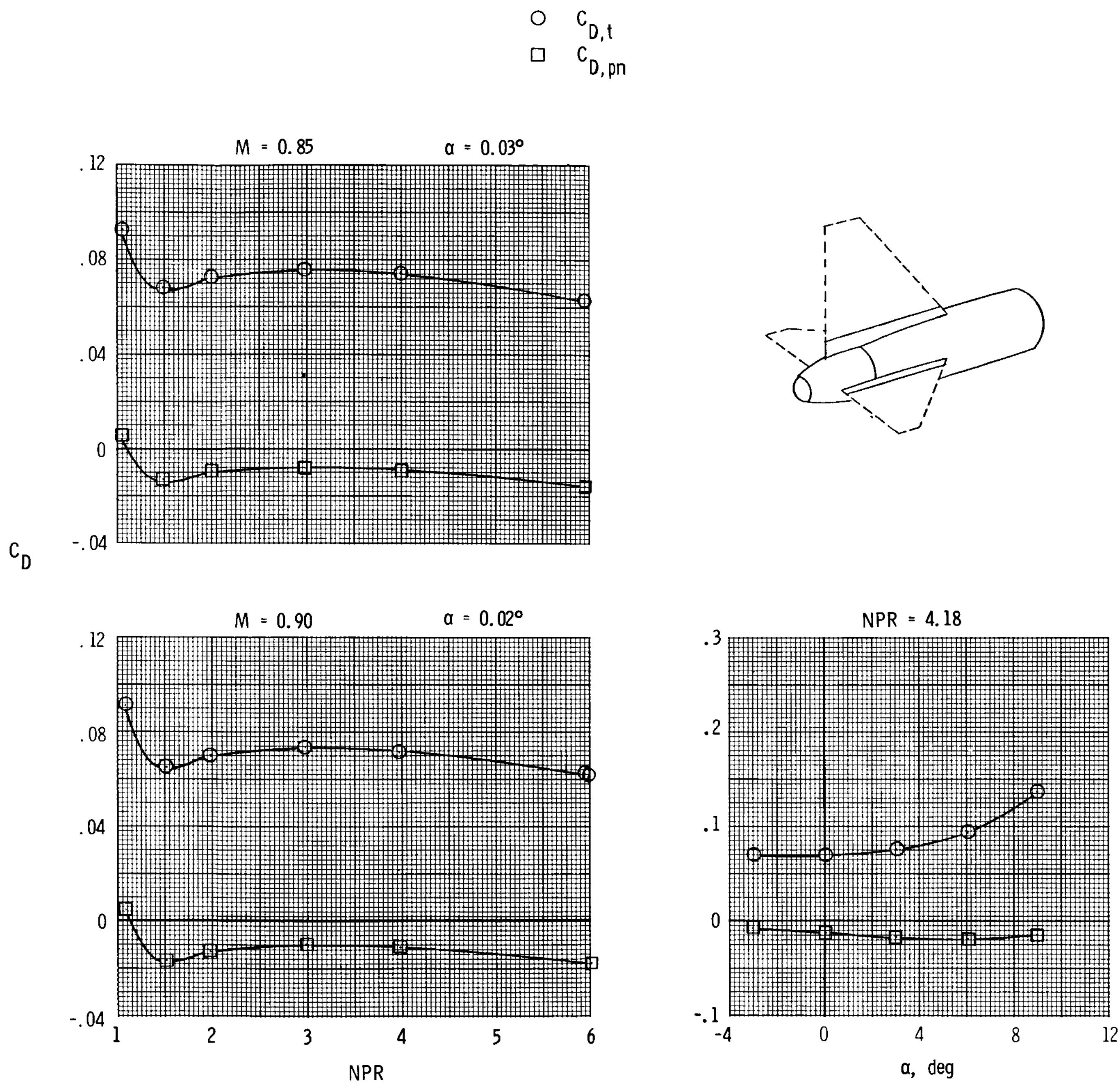

(f) Continued.

Figure 9. Continued.

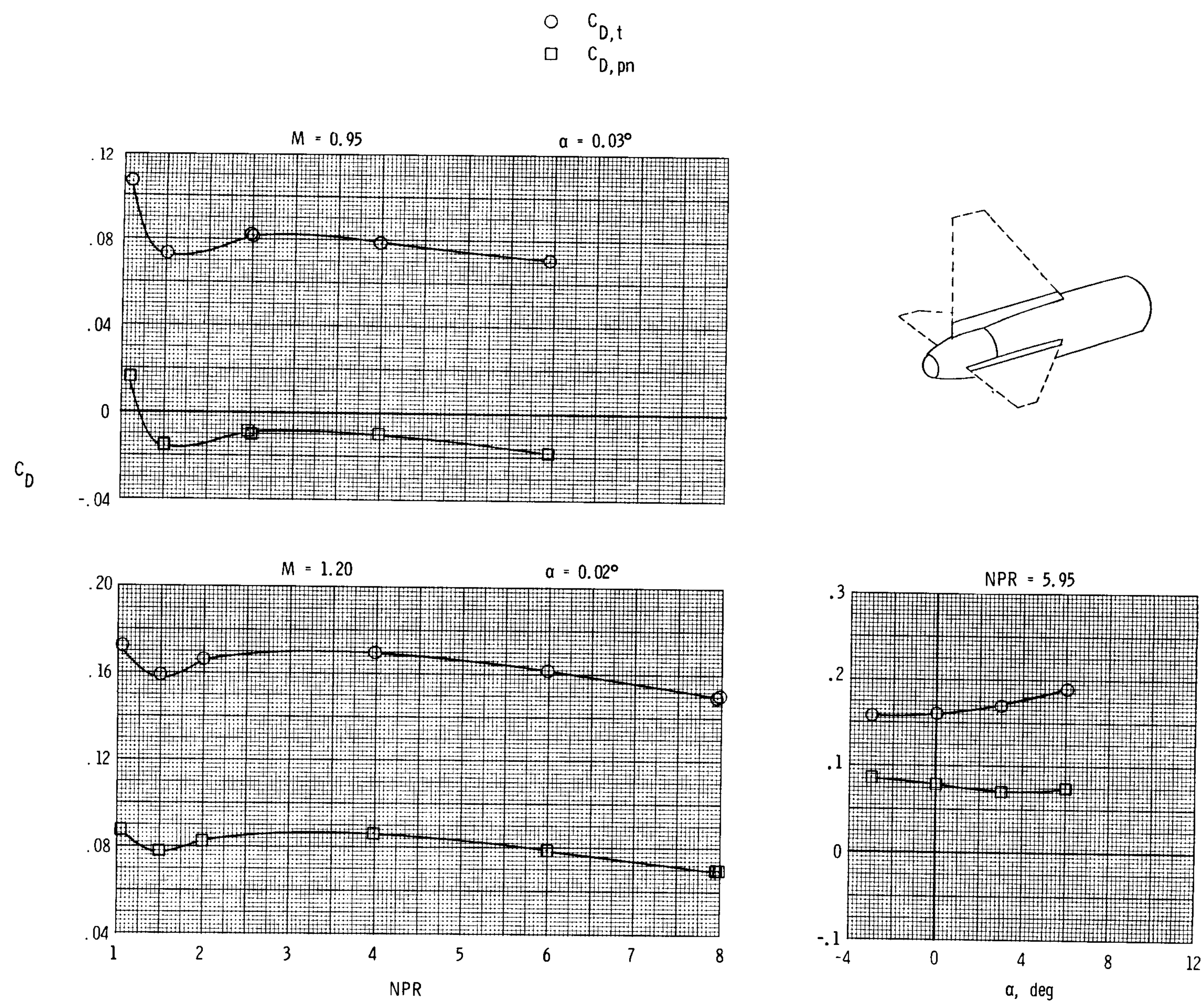

(f) Concluded.

Figure 9.- Concluded.

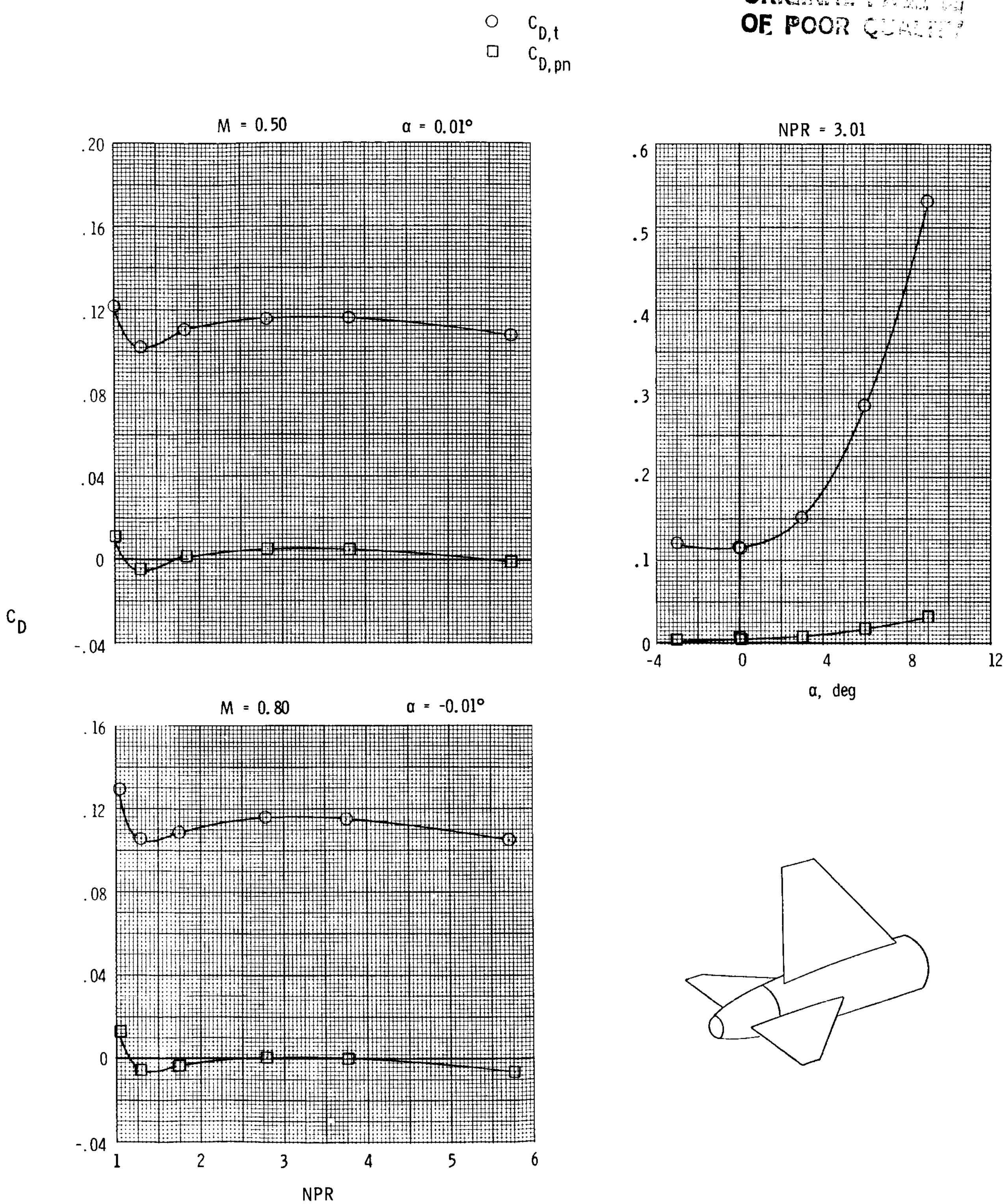

(a) $y/b = 1.00$.

Figure 10. Variation of total aft-end and nozzle pressure drag coefficients with nozzle pressure ratio and angle of attack for forward vertical tail, aft horizontal tails.

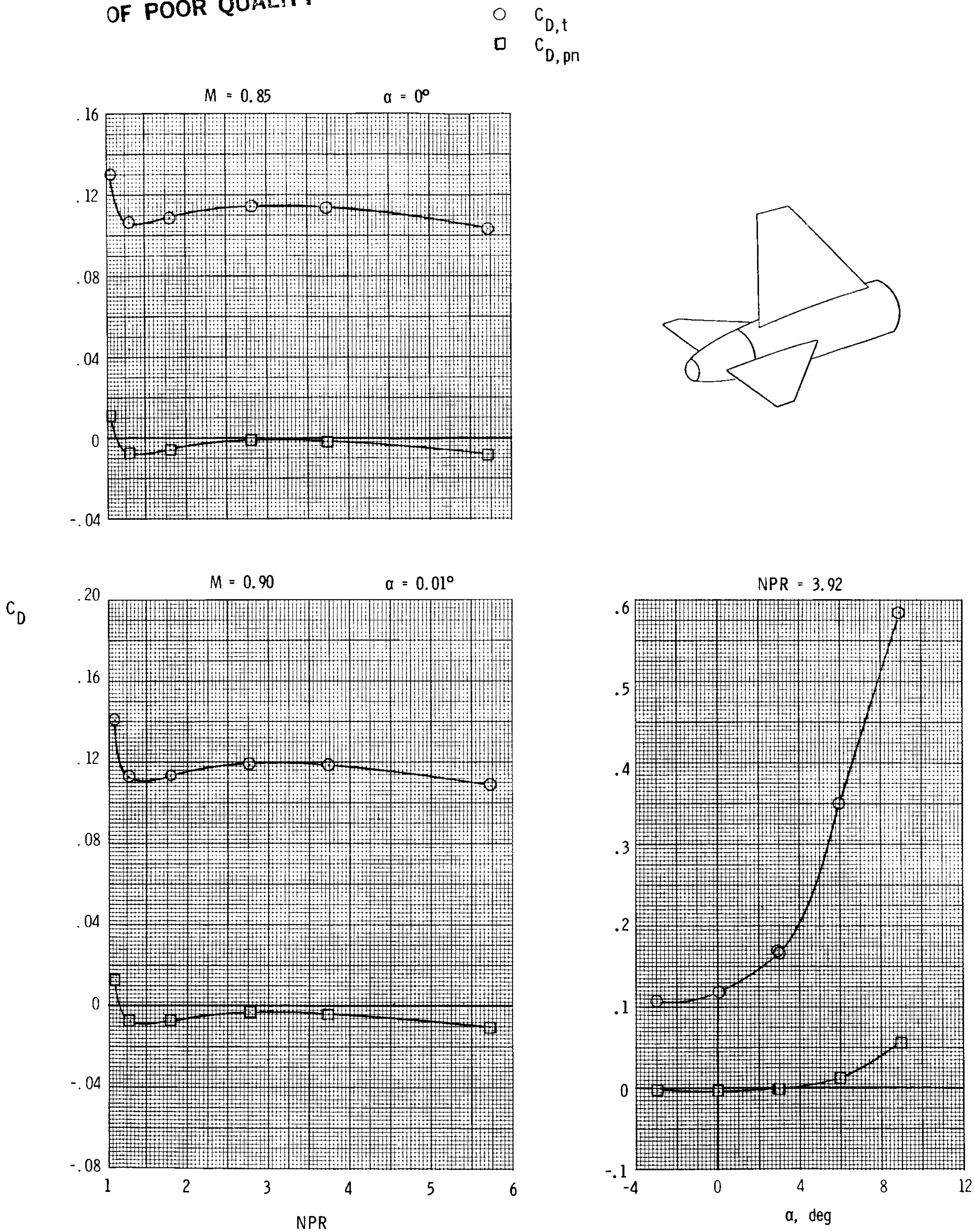

(a) Continued.

Figure 10. Continued.

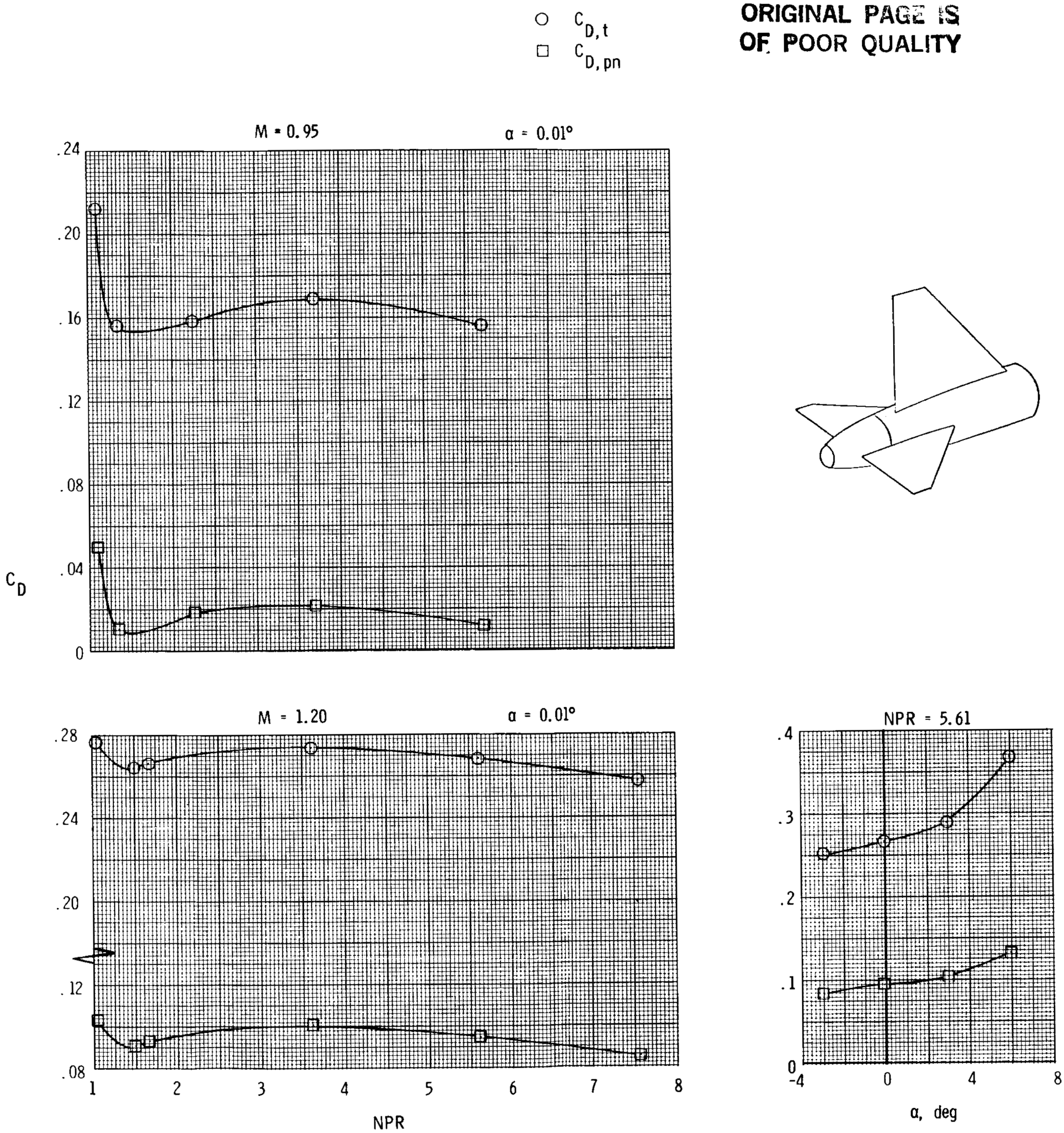

(a) Concluded.

Figure 10. Continued.

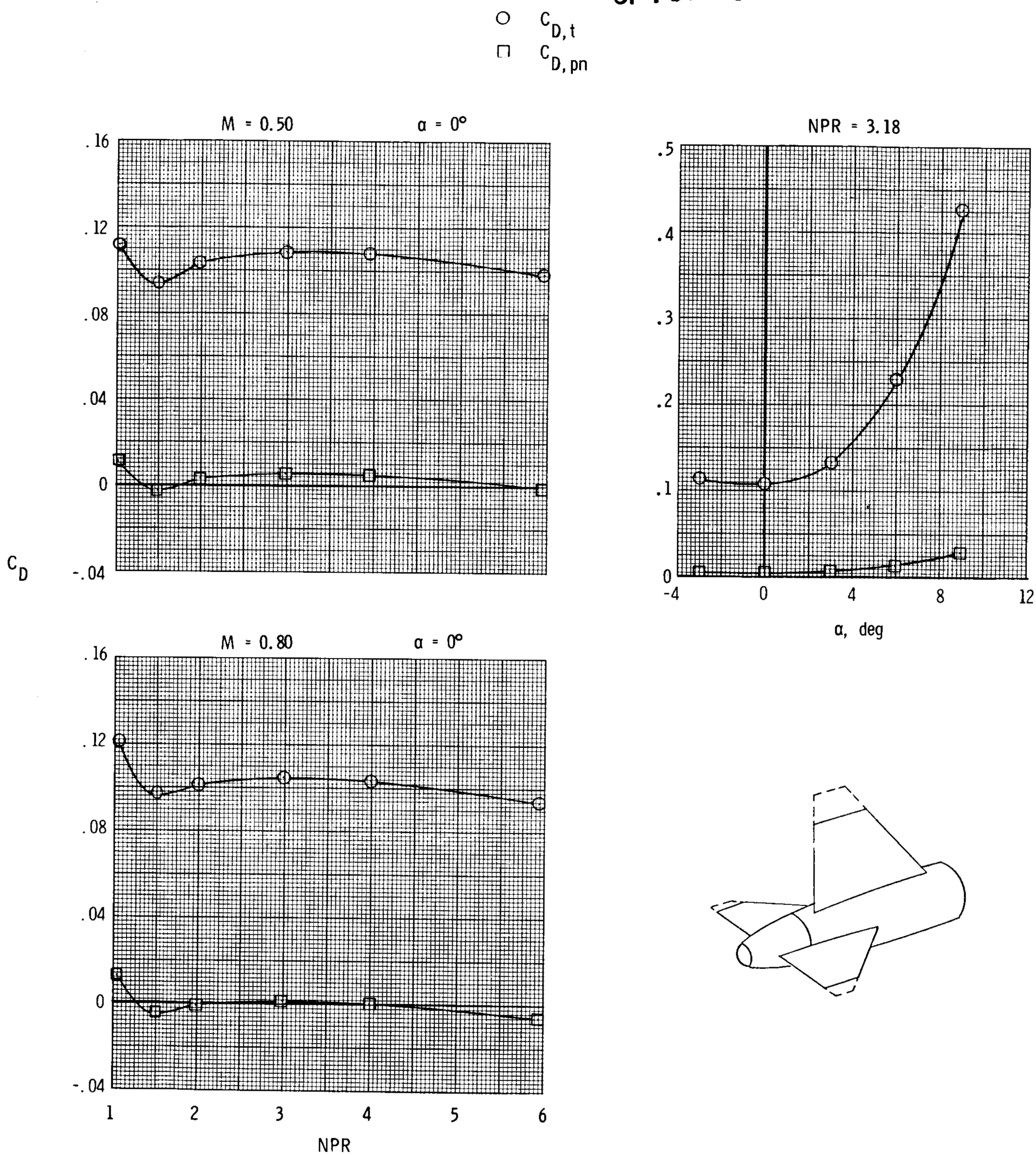

(b) $y/b = 0.75$.

Figure 10. Continued.

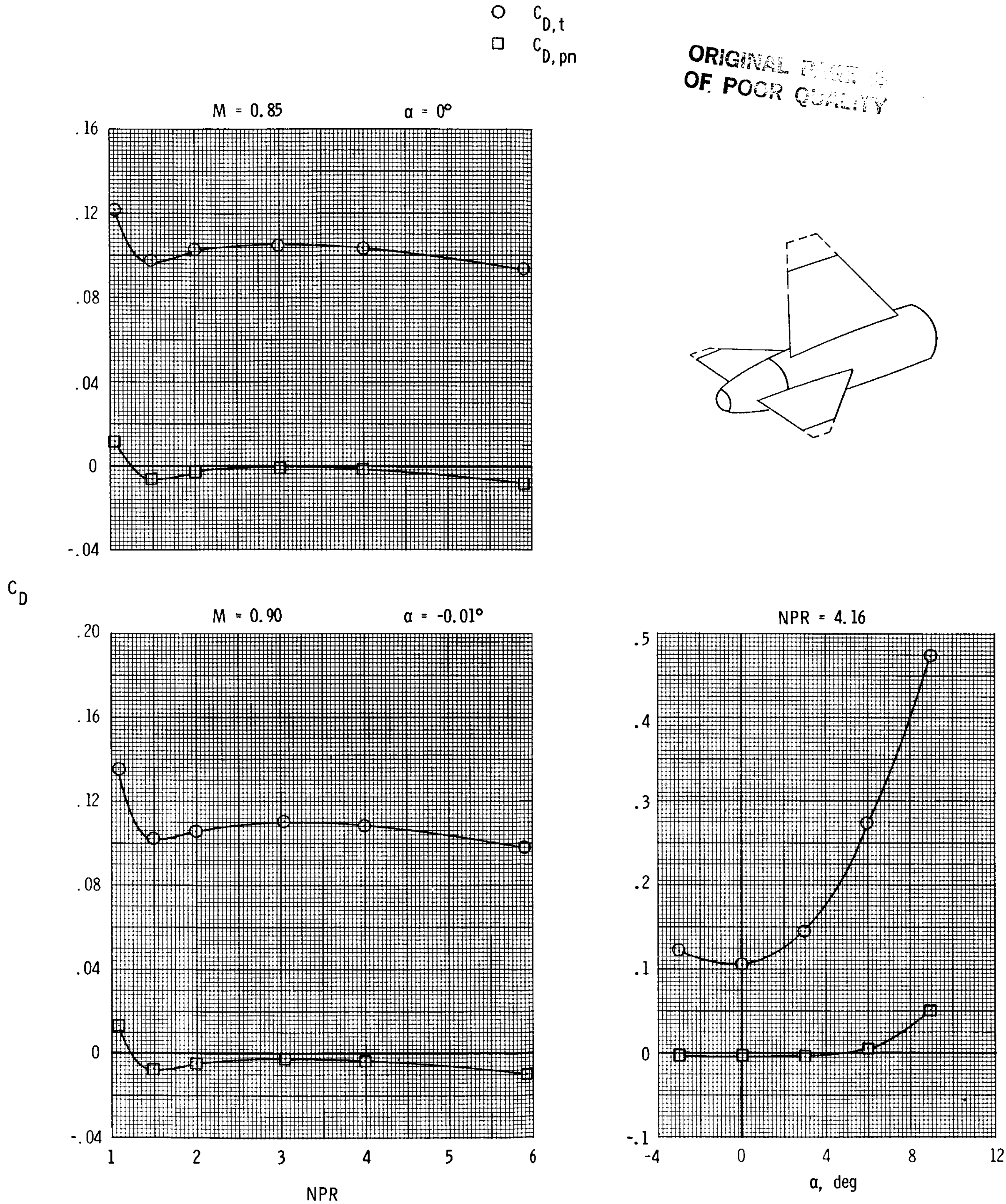

(b) Continued.

Figure 10. Continued.

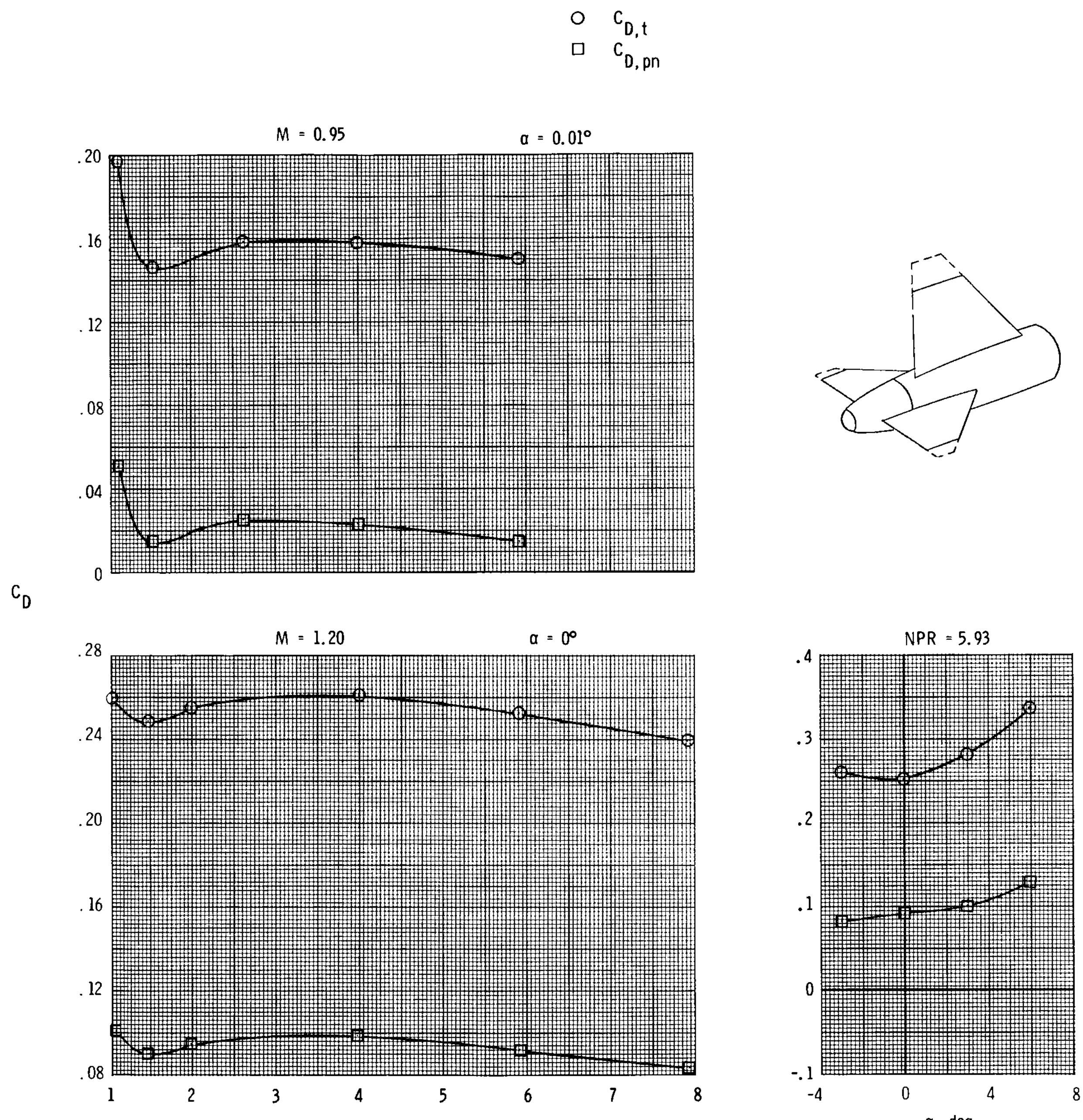

(b) Concluded.

Figure 10. Continued.

ORIGINAL PAGE IS
OF POOR QUALITY

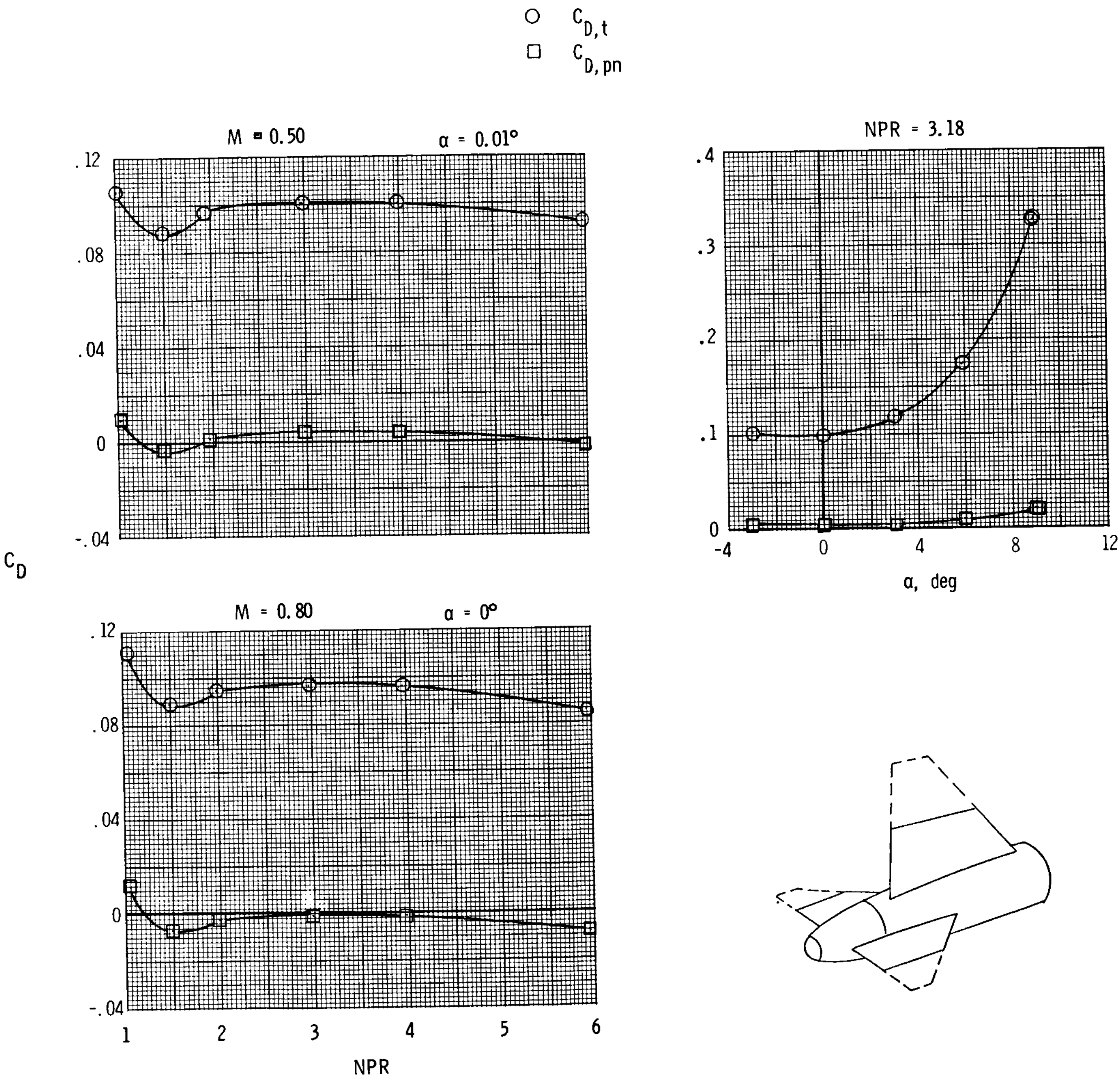

(c) $y/b = 0.50$.

Figure 10. Continued.

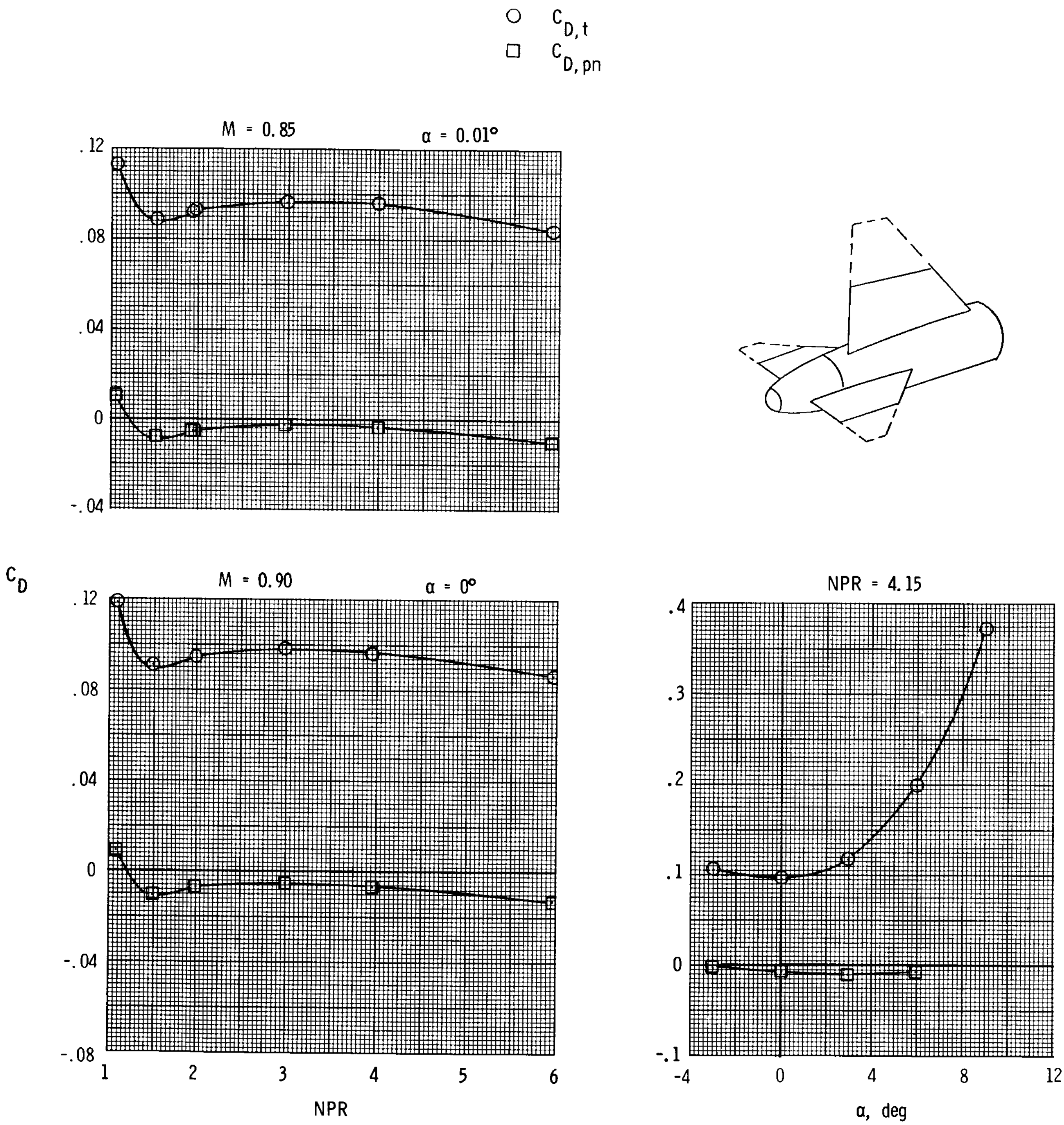

(c) Continued.

Figure 10. Continued.

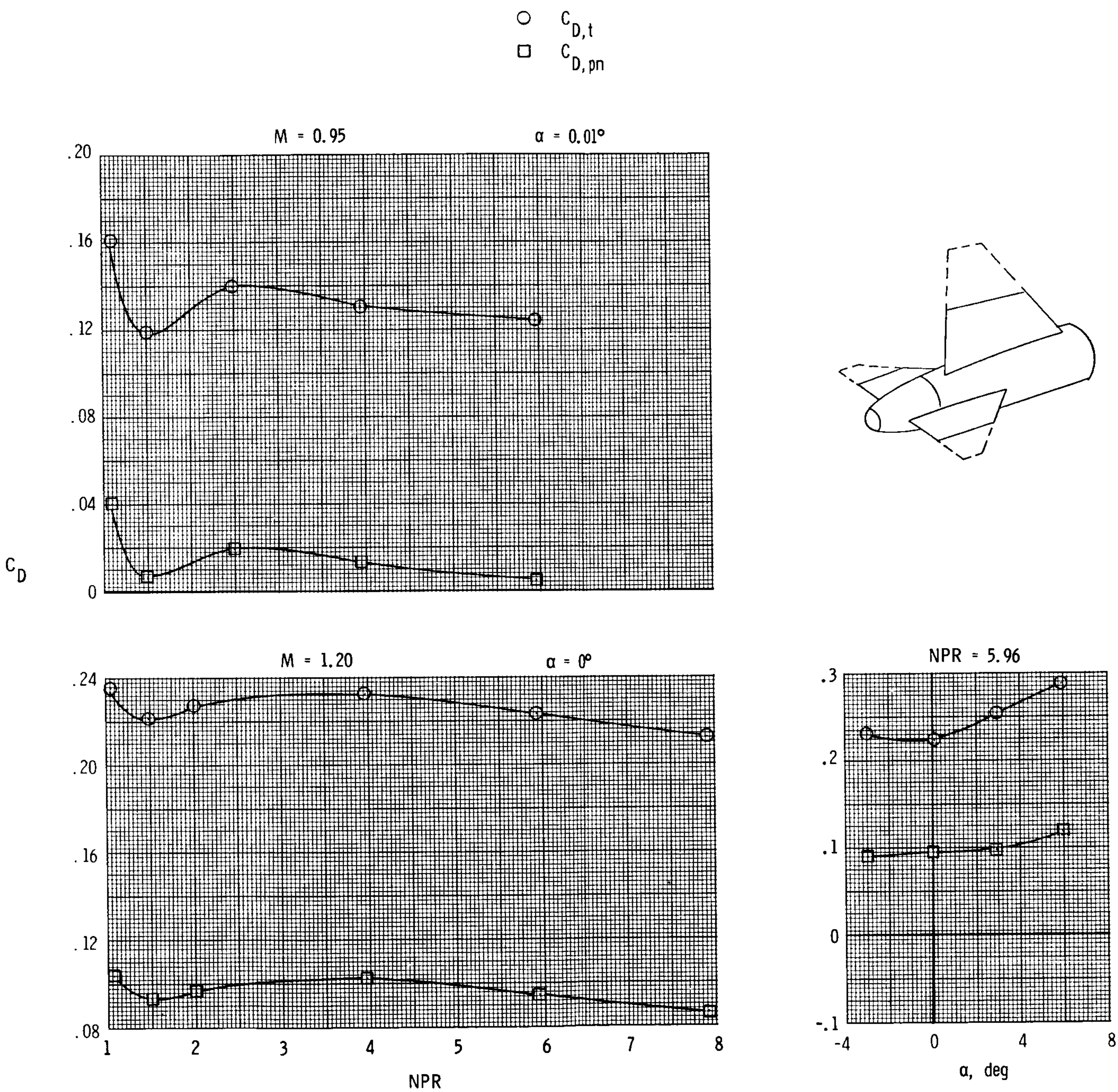

(c) Concluded.

Figure 10. Continued.

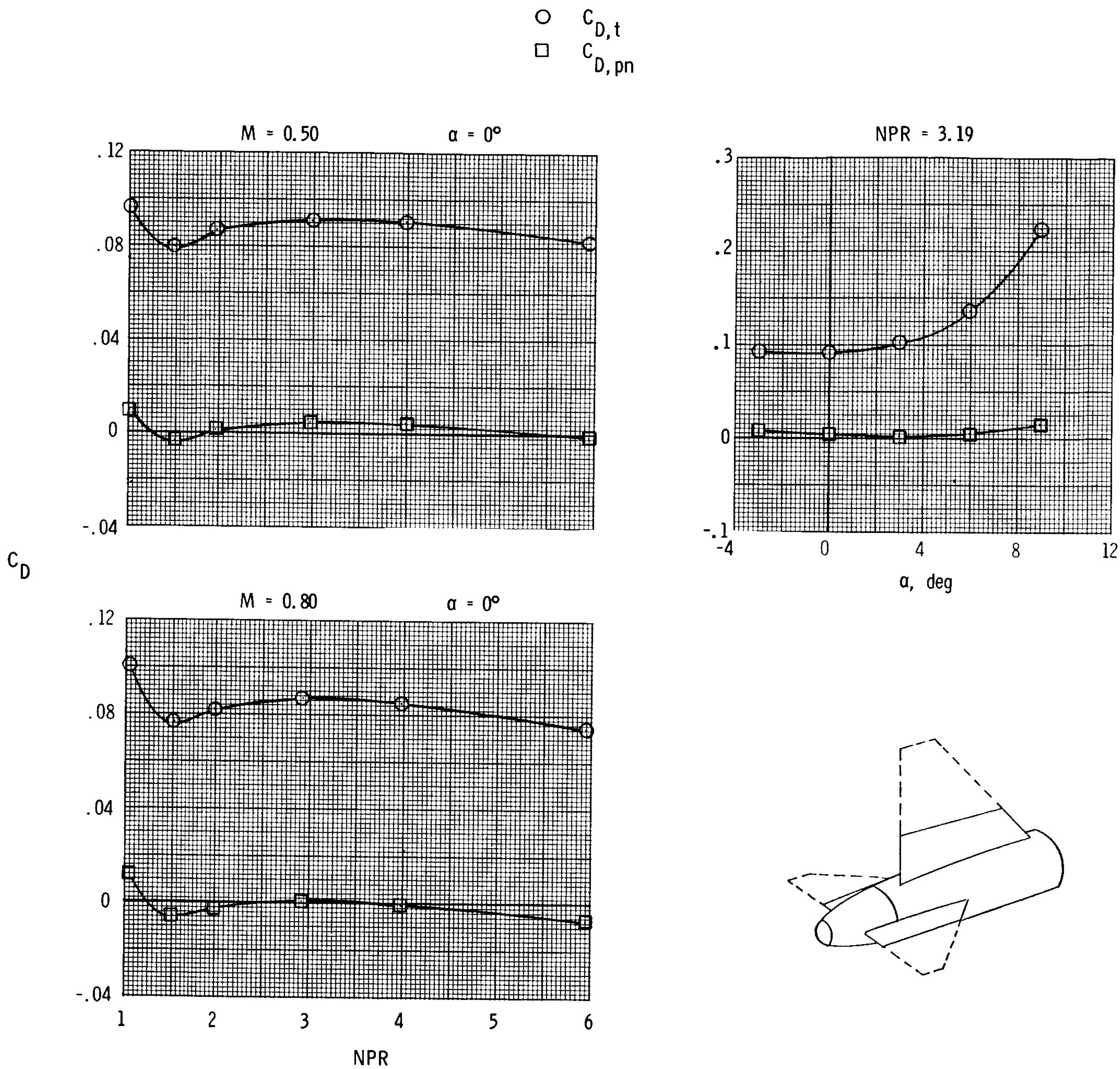

(d) $y/b = 0.30$.

Figure 10. Continued.

ORIGINAL PAGE IS
OF POOR QUALITY

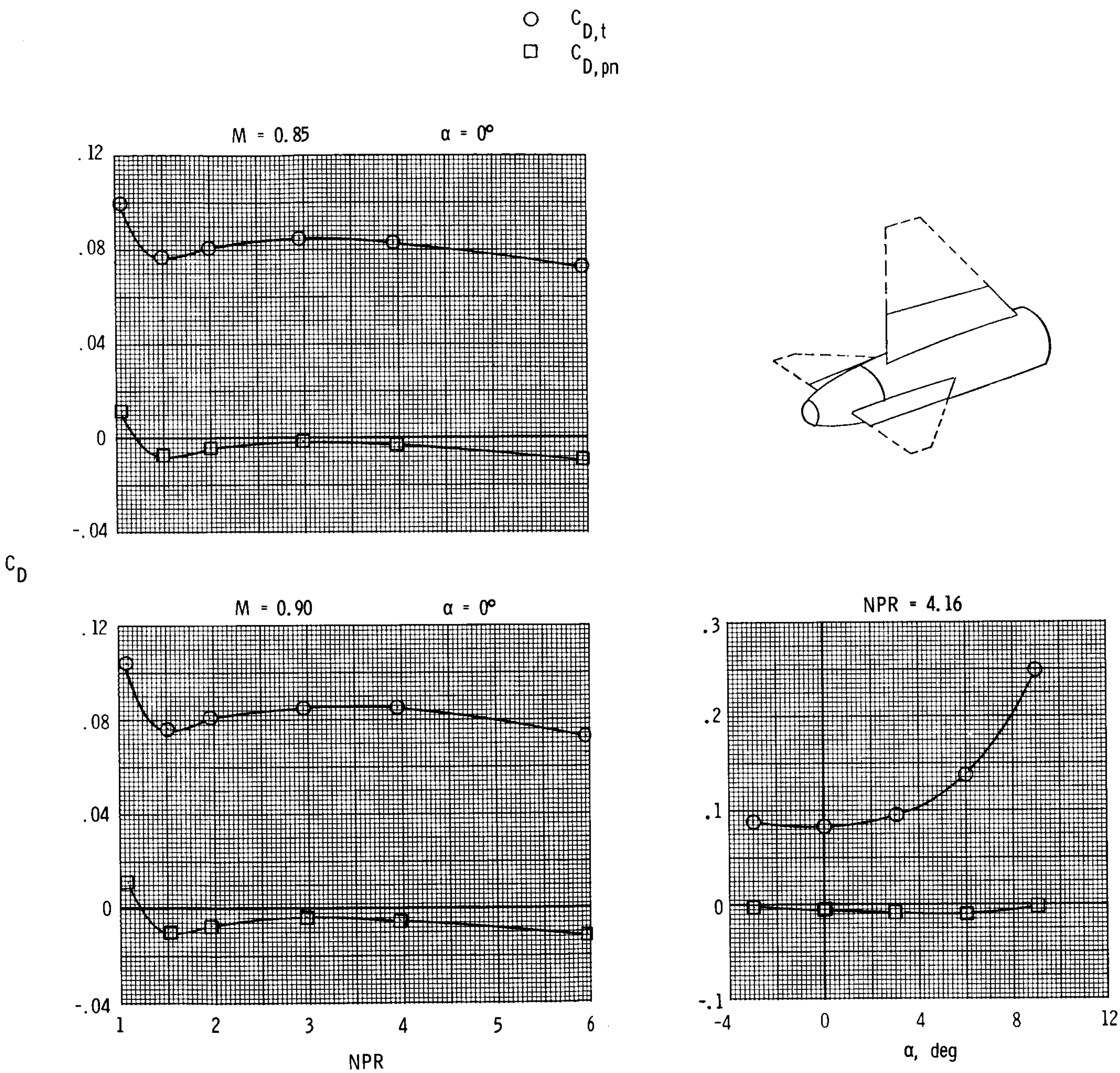

(d) Continued.

Figure 10. Continued.

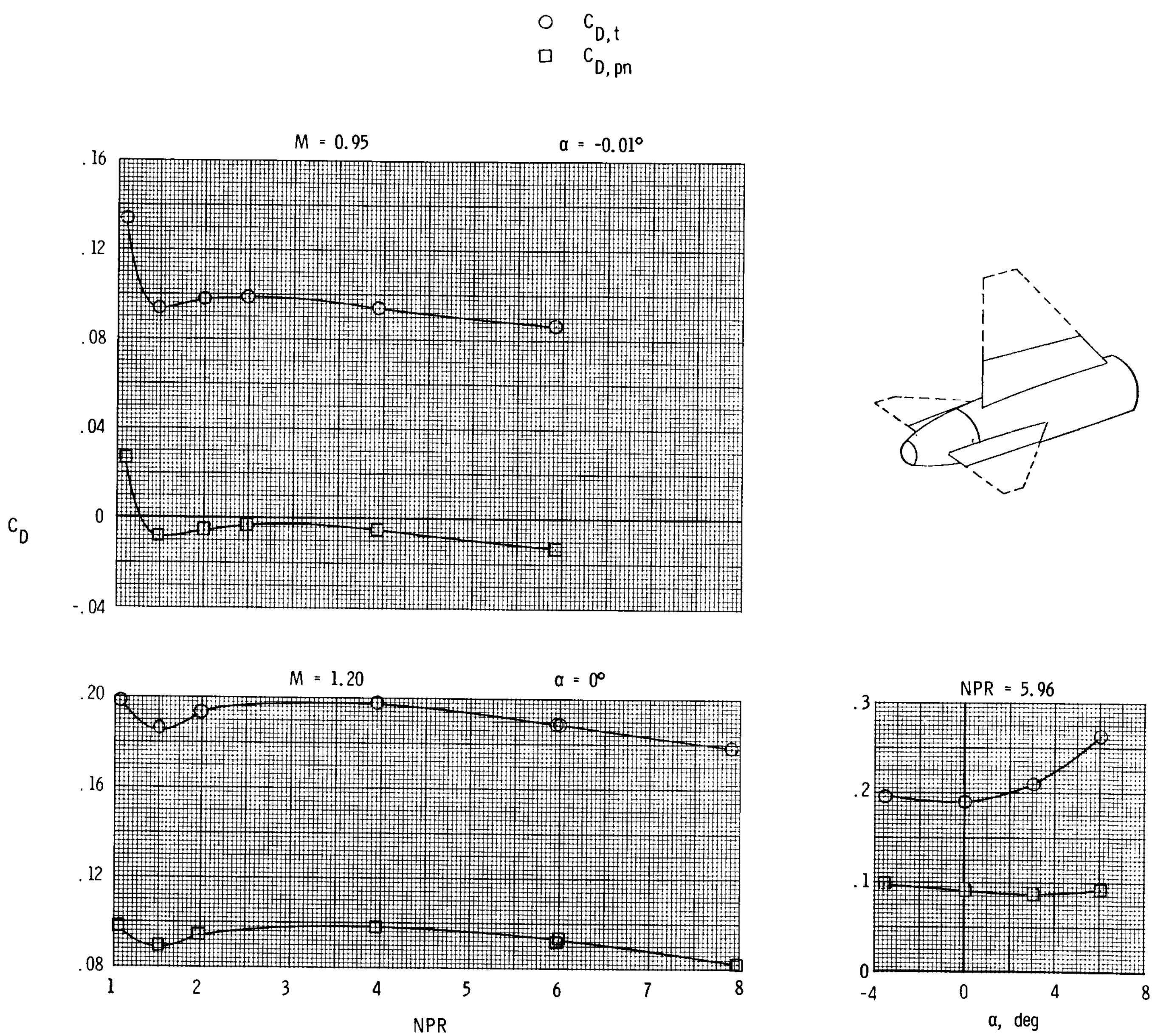

(d) Concluded.

Figure 10. Continued.

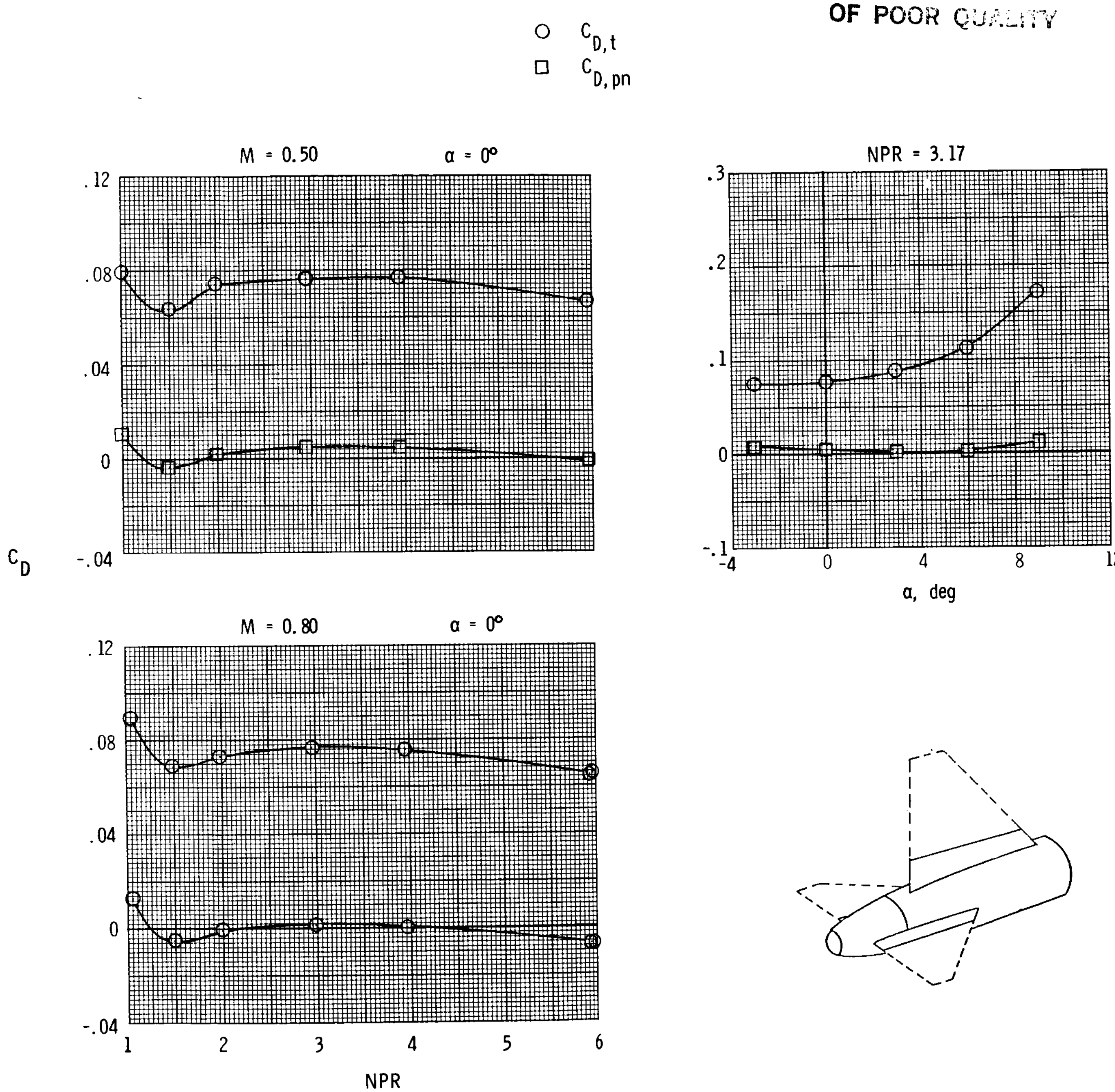

(e) $y/b = 0.20$.

Figure 10. Continued.

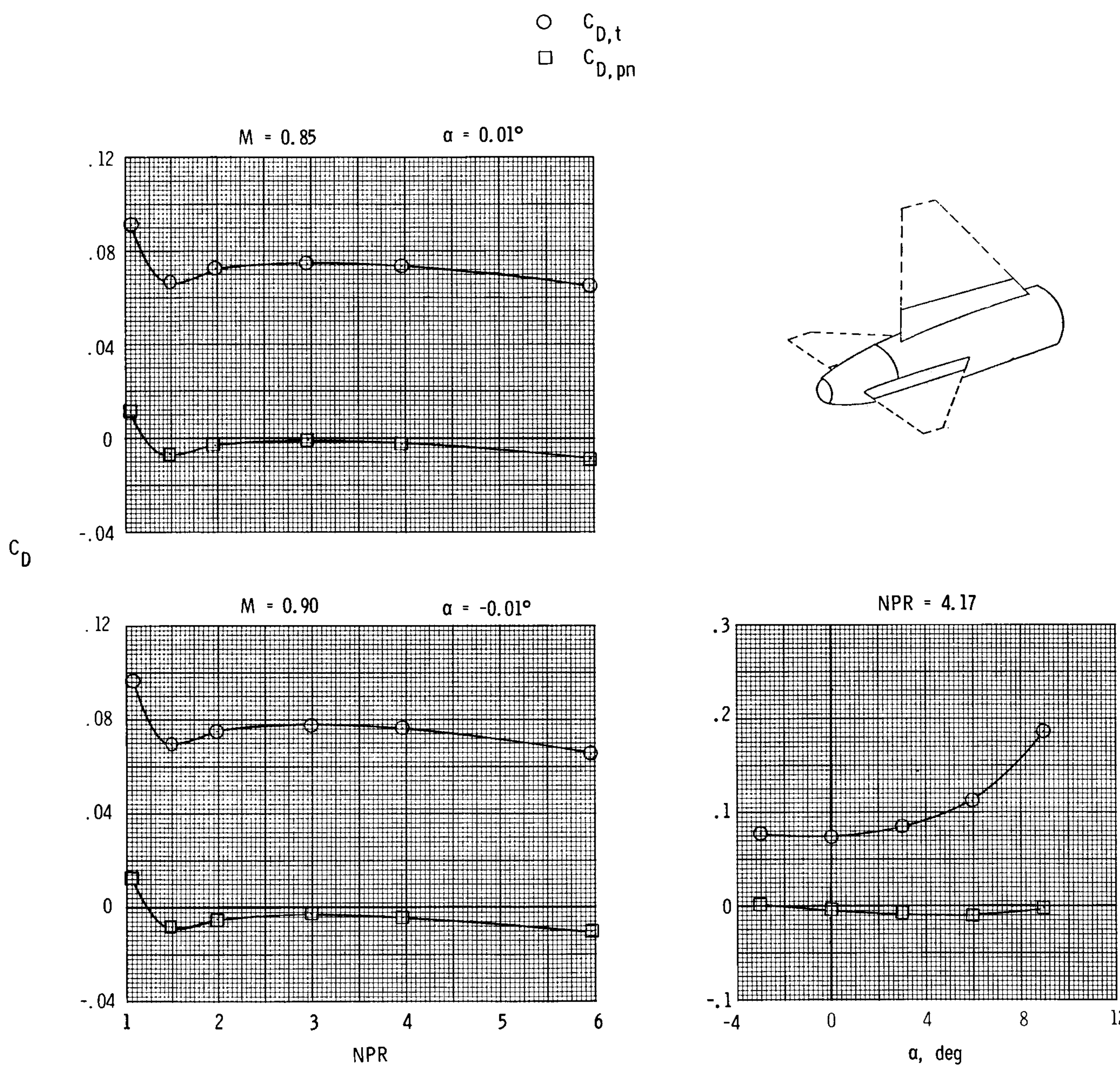

(e) Continued.

Figure 10. Continued.

ORIGINAL PAGE IS
OF POOR QUALITY

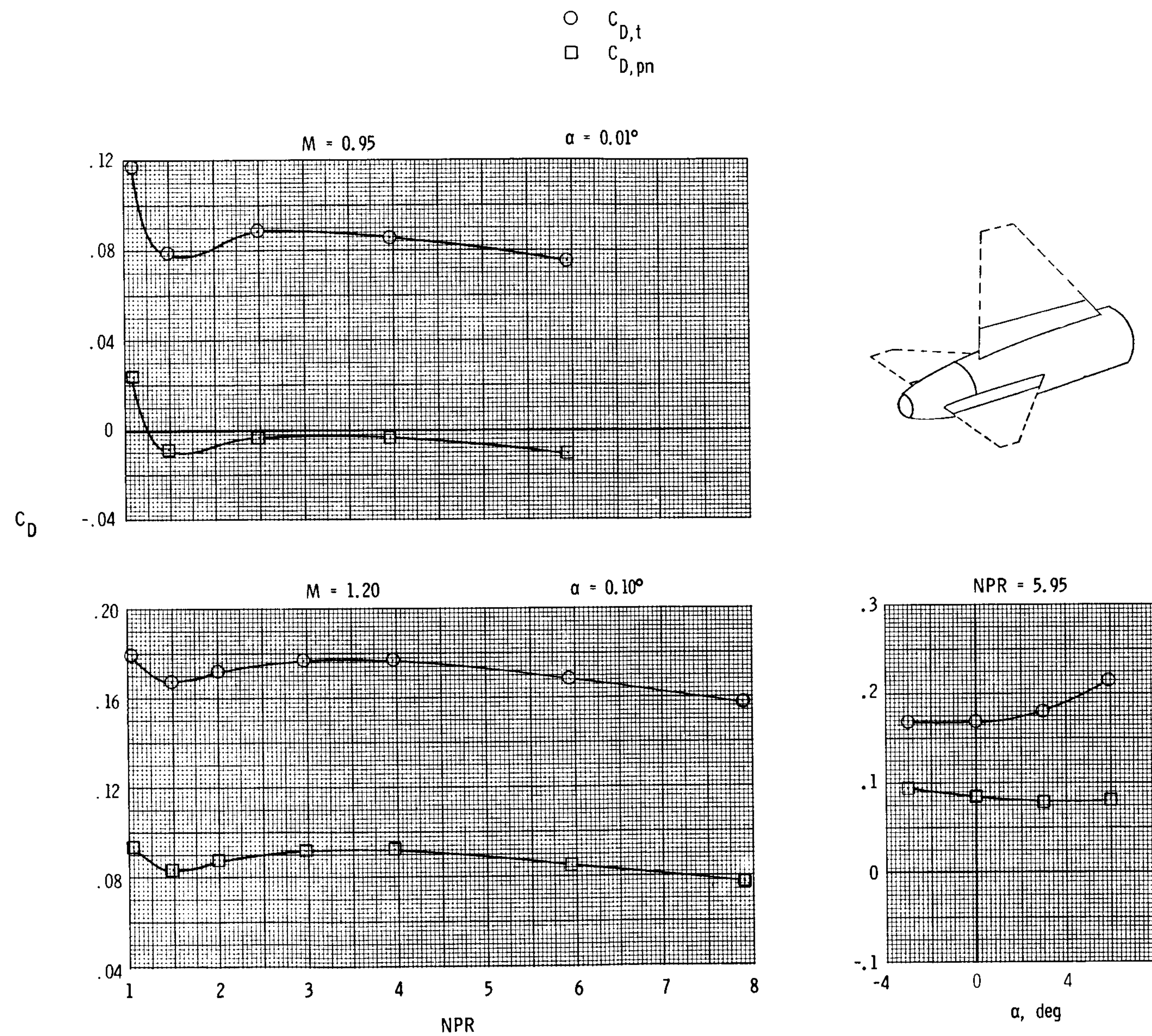

(e) Concluded.

Figure 10. Continued.

ORIGINAL PAGE IS
OF POOR QUALITY

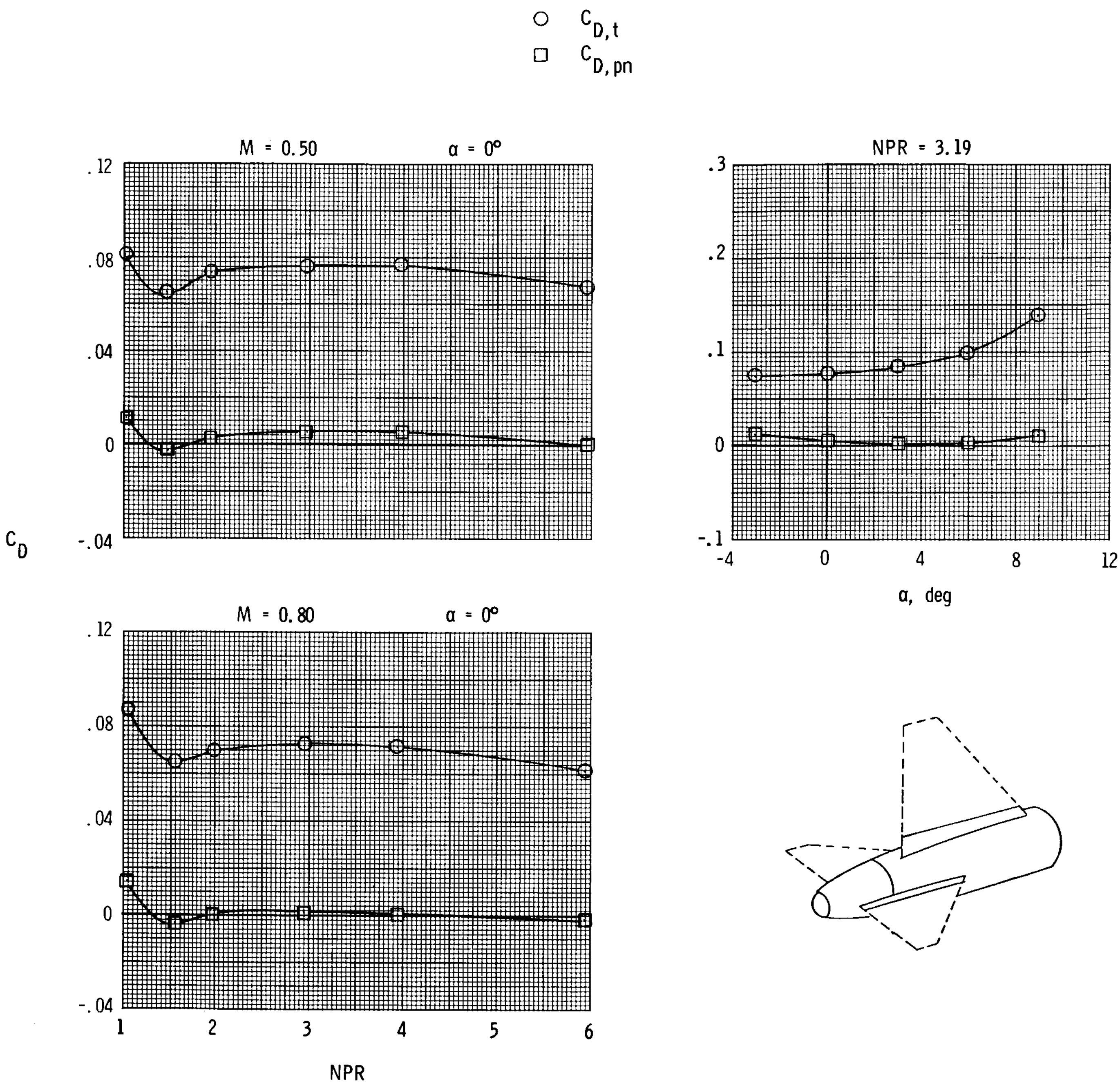

(f) $y/b = 0.10$.

Figure 10. Continued.

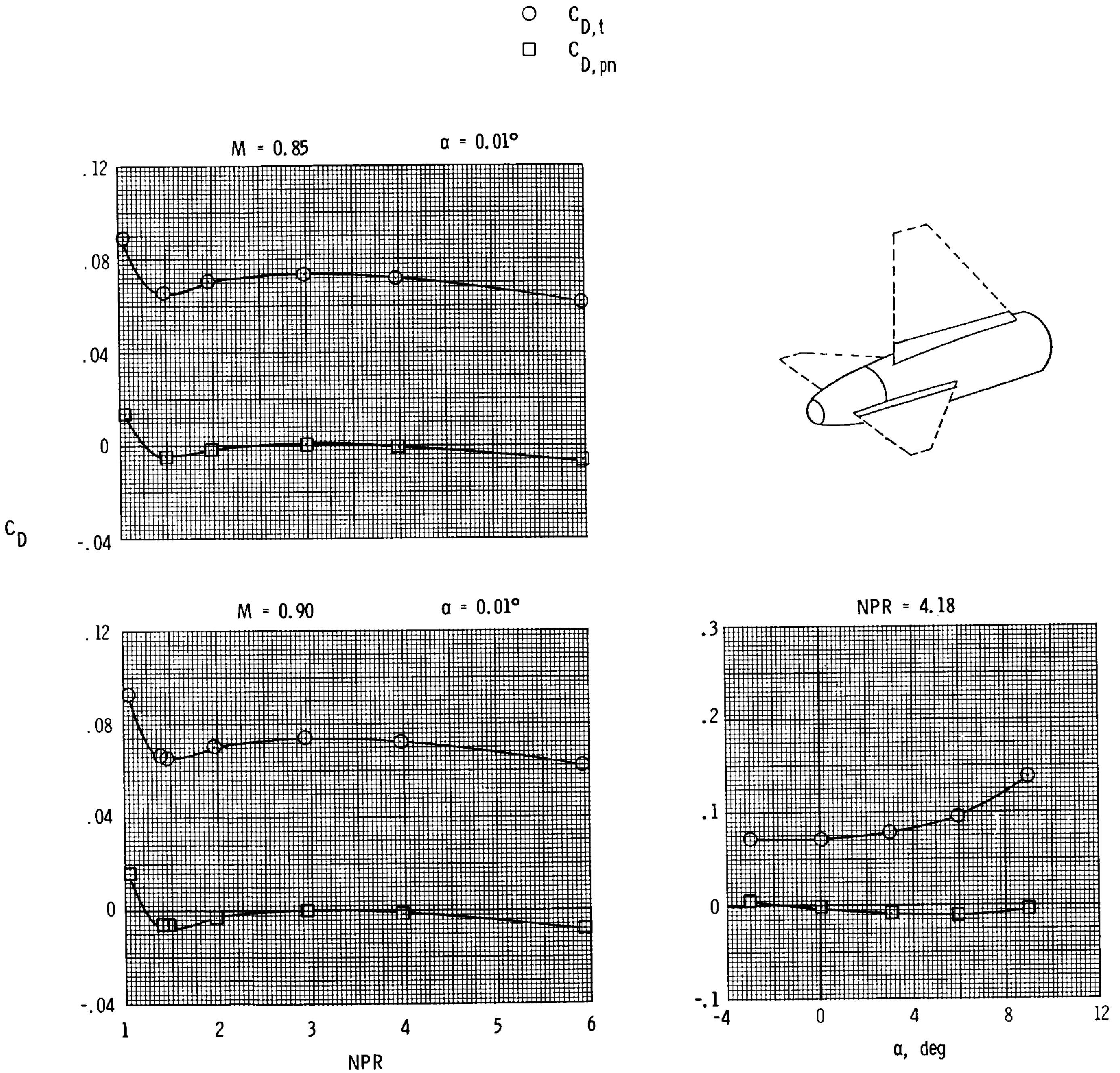

(f) Continued.

Figure 10. Continued.

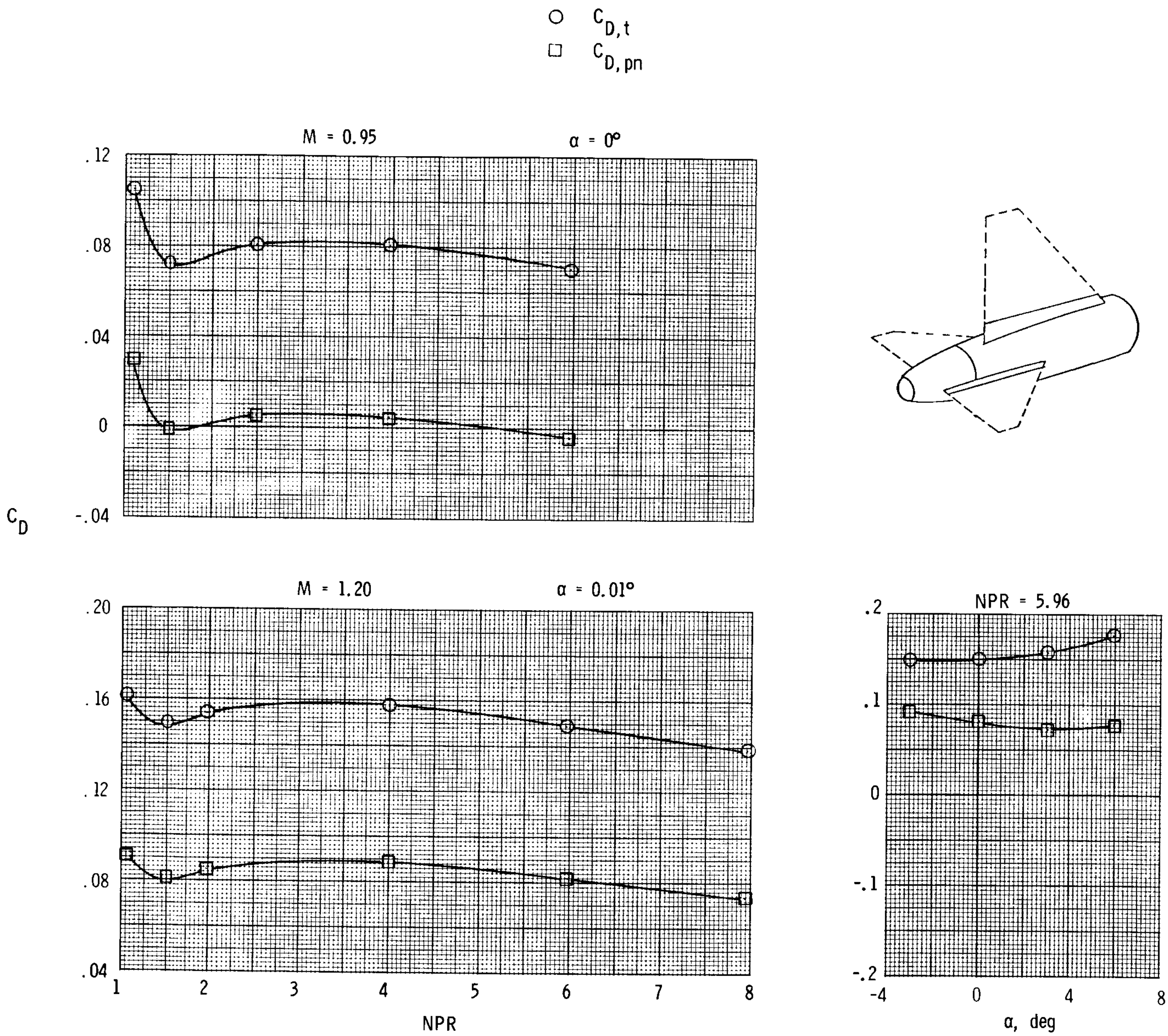

(f) Concluded.

Figure 10. Concluded.

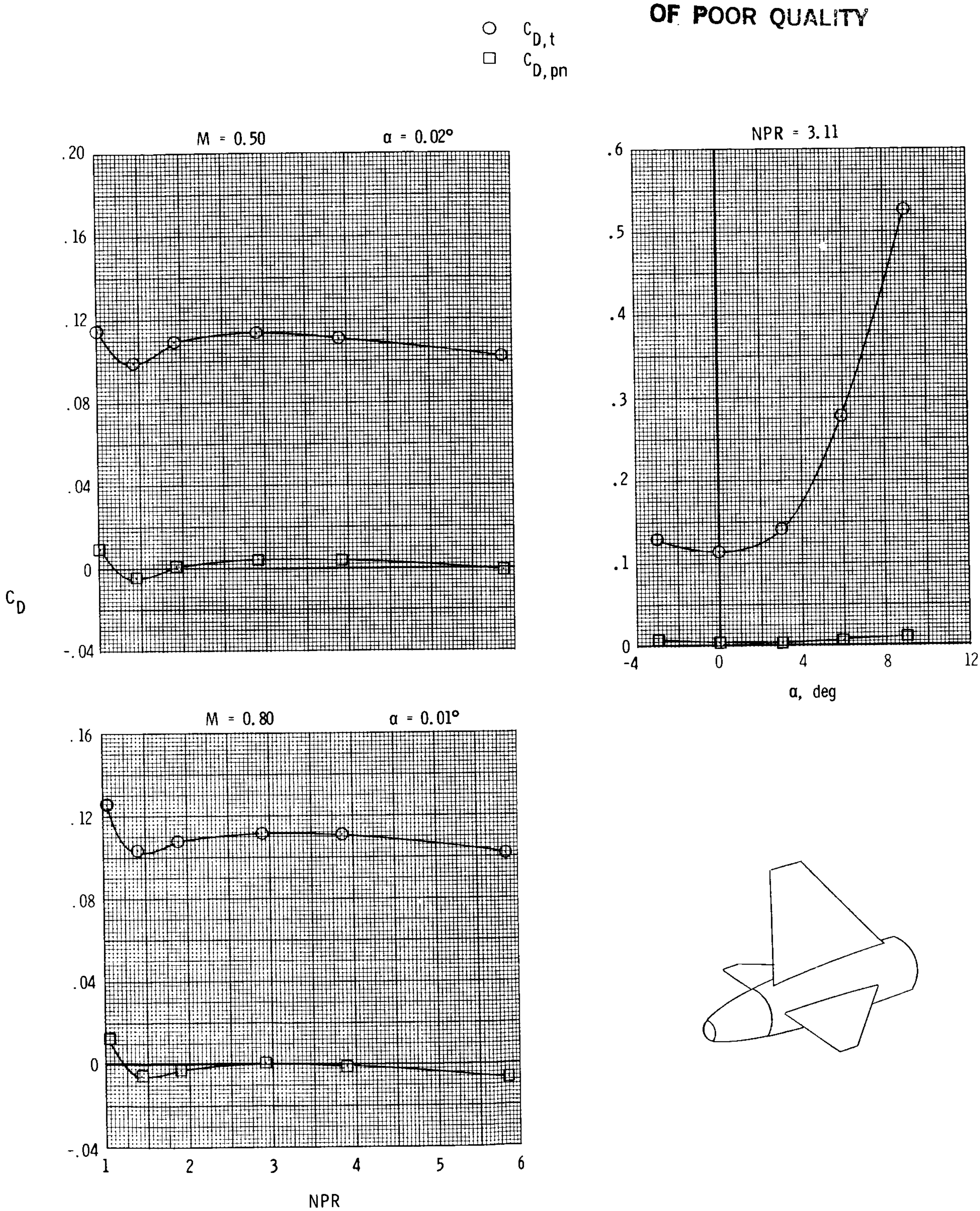

(a) $y/b = 1.00$.

Figure 11. Variation of total aft-end and nozzle pressure drag coefficients with nozzle pressure ratio and angle of attack for forward vertical tail, forward horizontal tails.

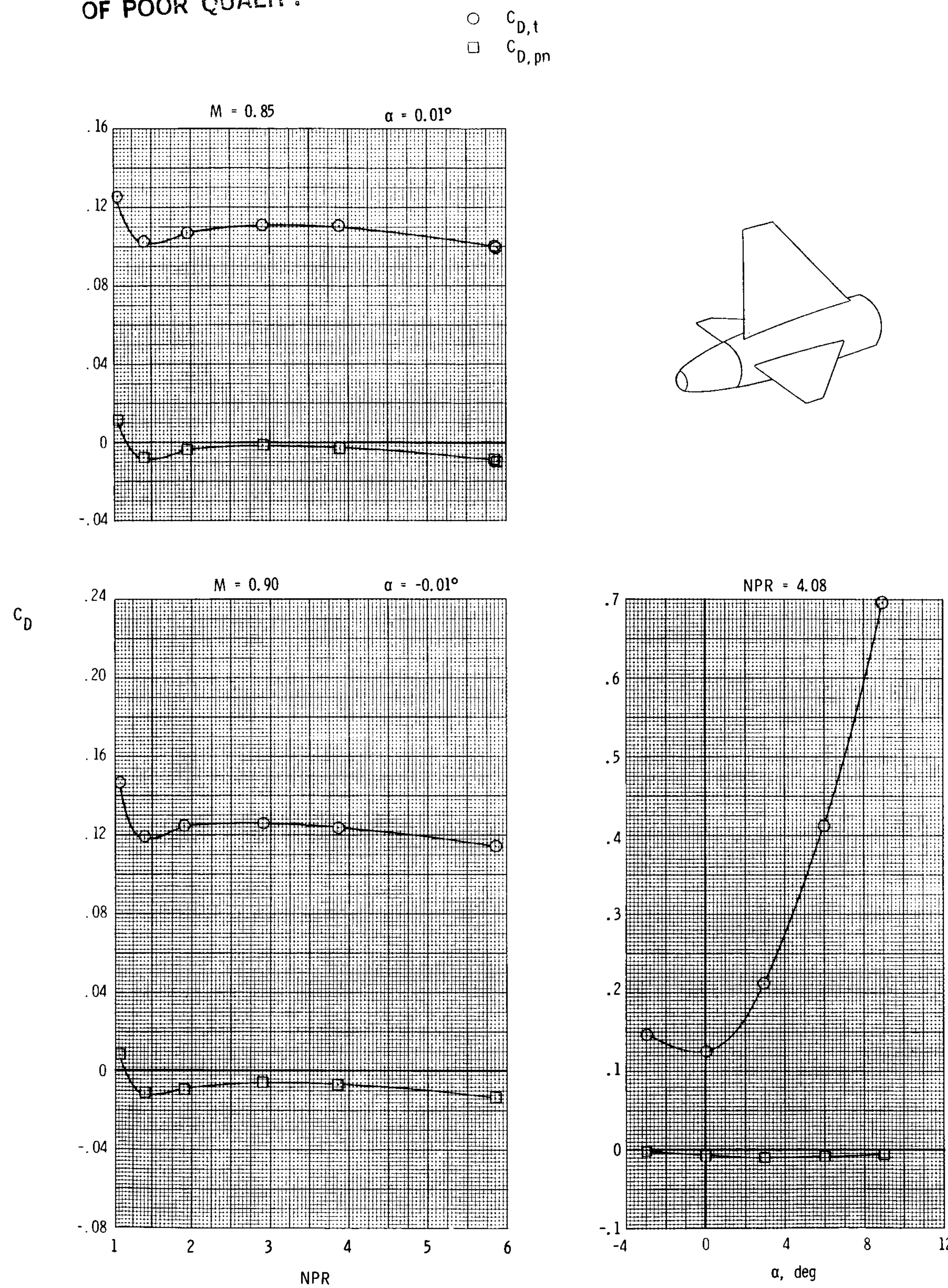

(a) Continued.

Figure 11. Continued.

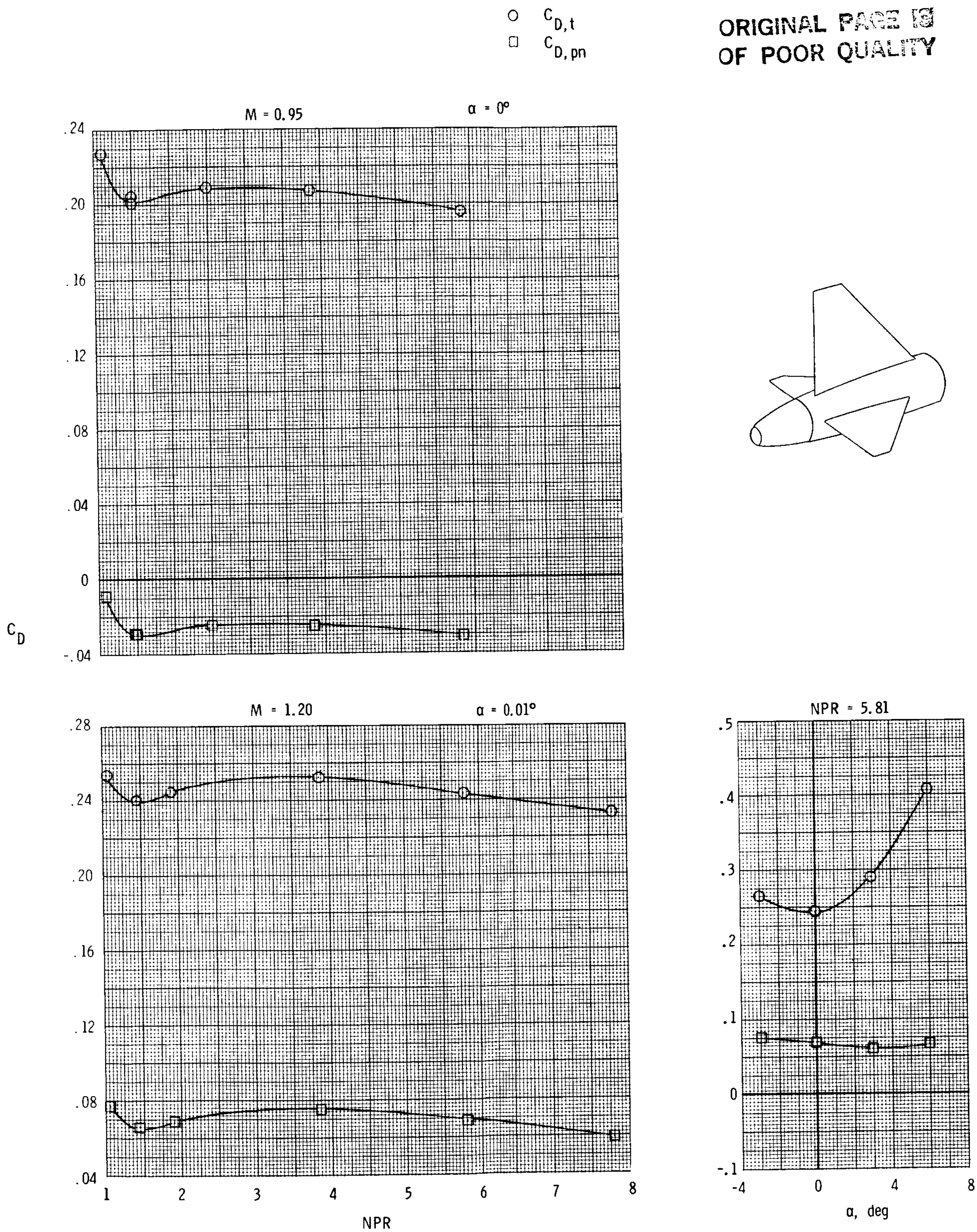

(a) Concluded.

Figure 11. Continued.

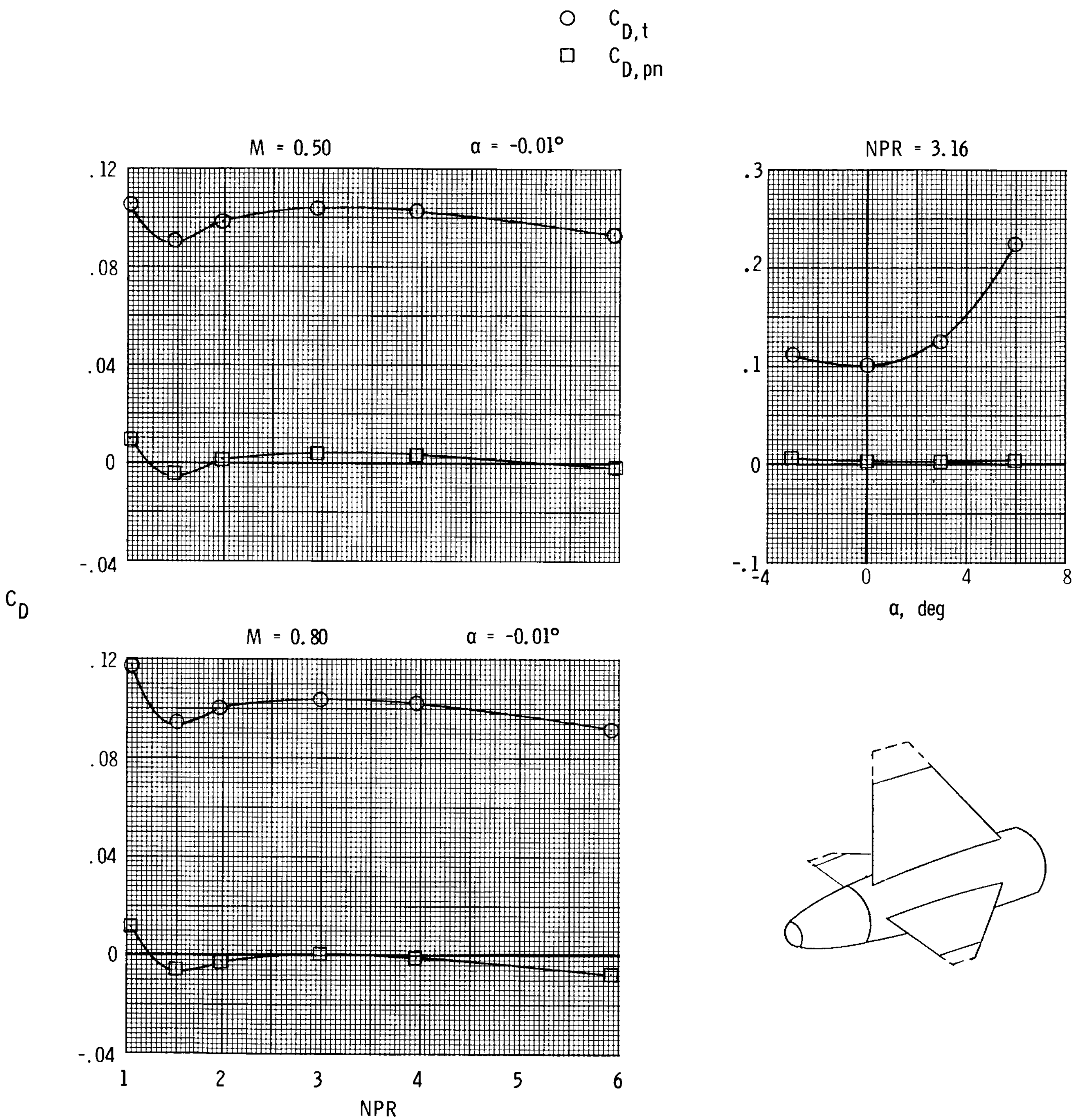

(b) $y/b = 0.75$.

Figure 11. Continued.

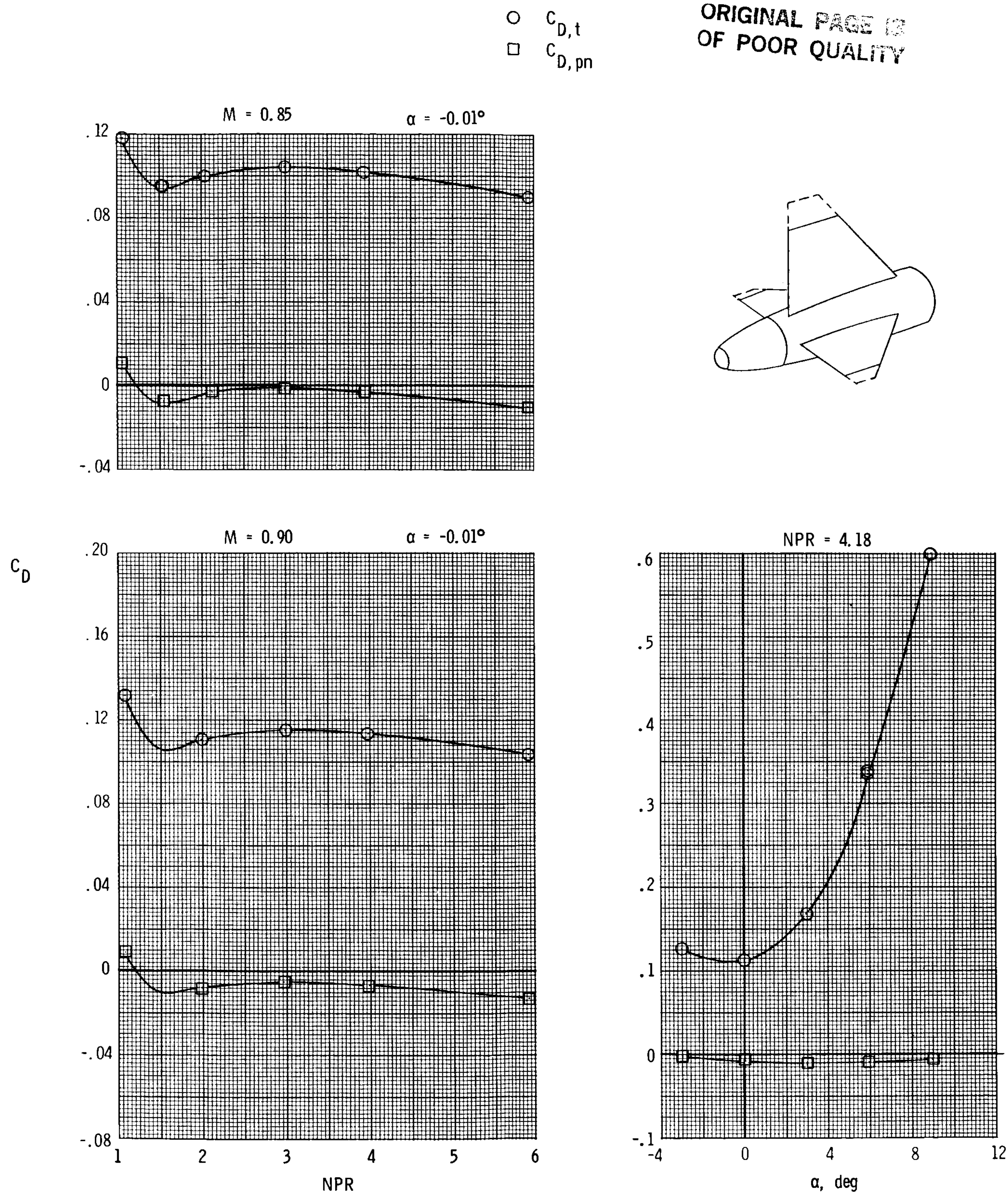

(b) Continued.

Figure 11. Continued.

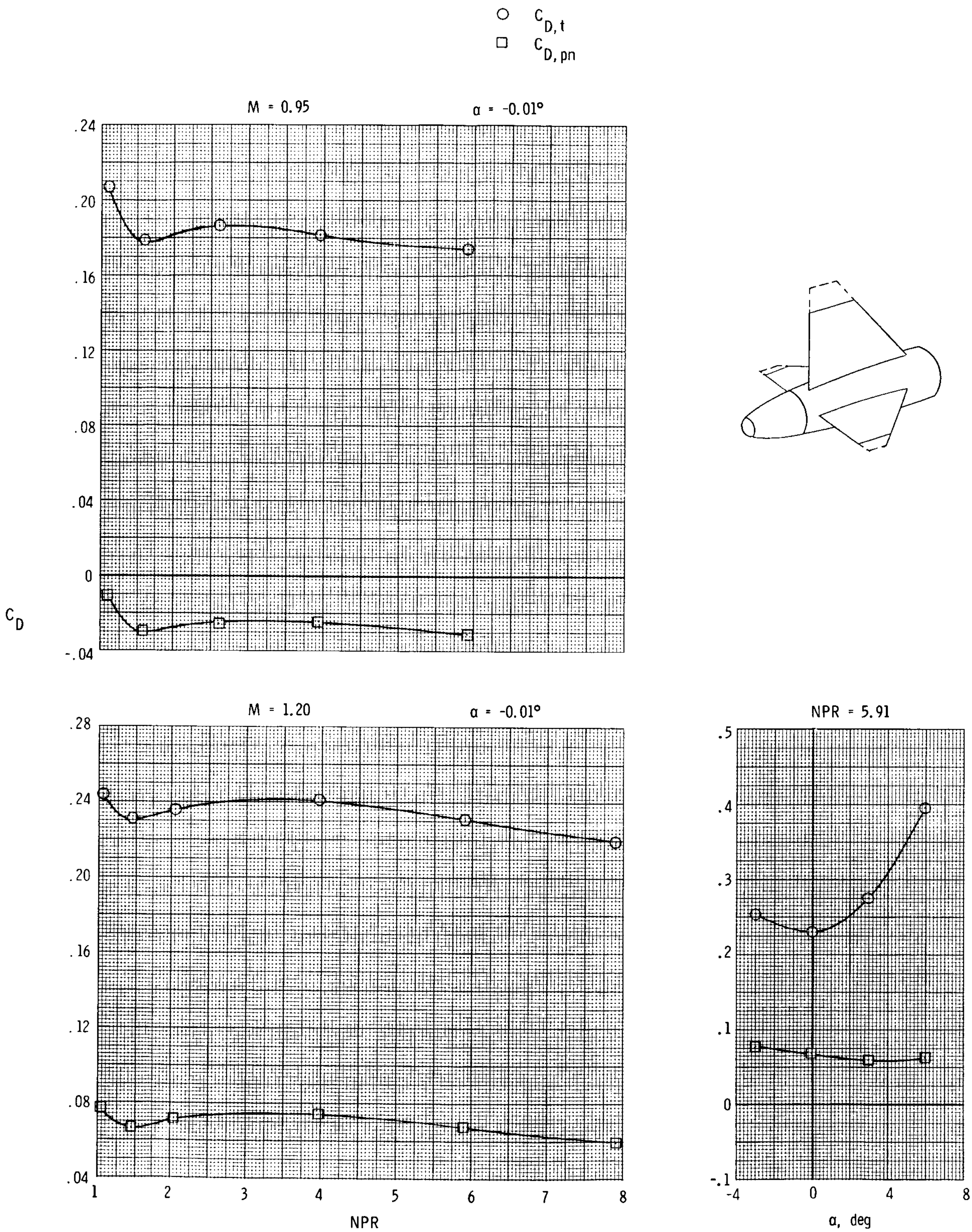

(b) Concluded.

Figure 11. Continued.

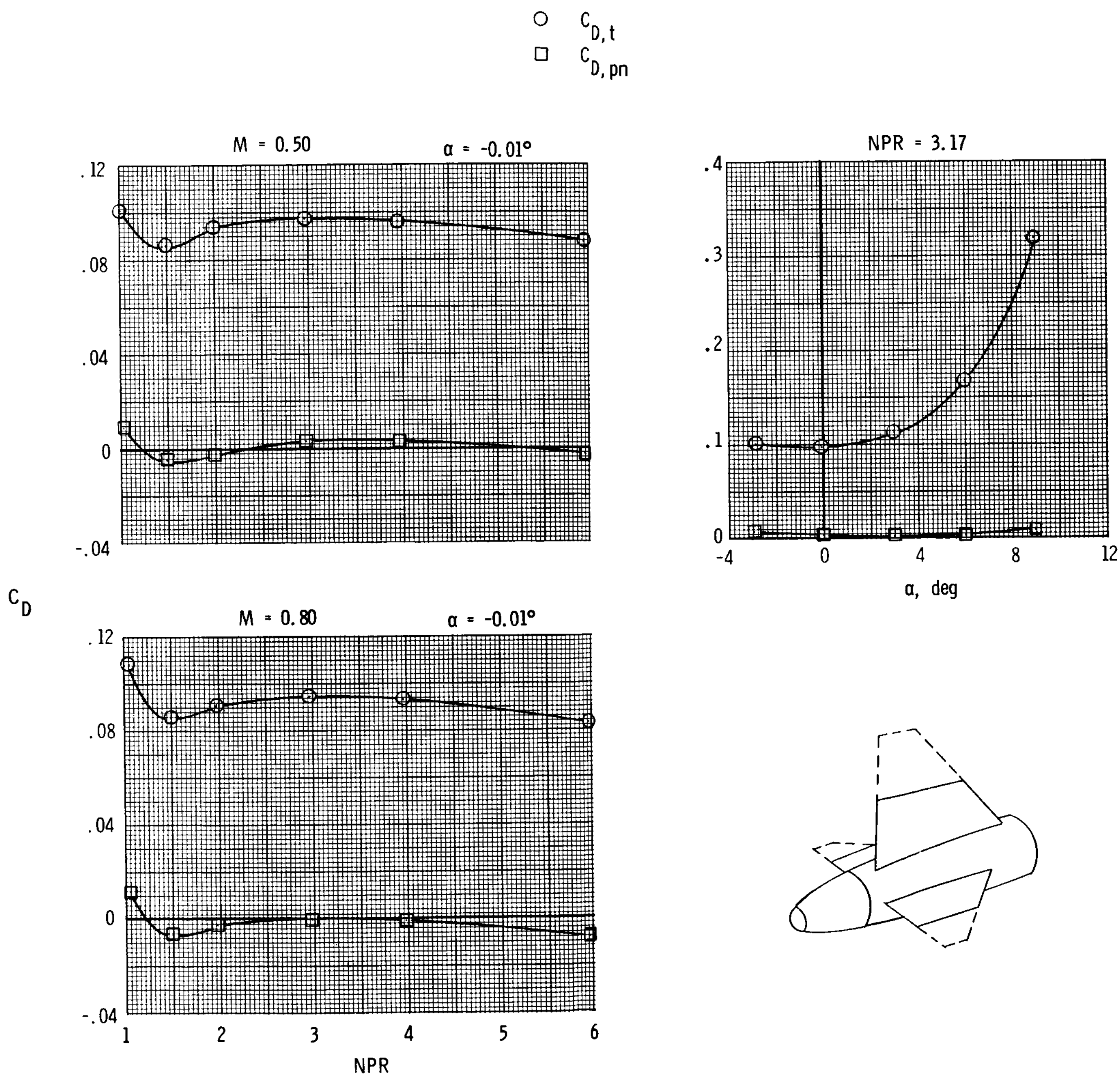

(c) $y/b = 0.50$.

Figure 11. Continued.

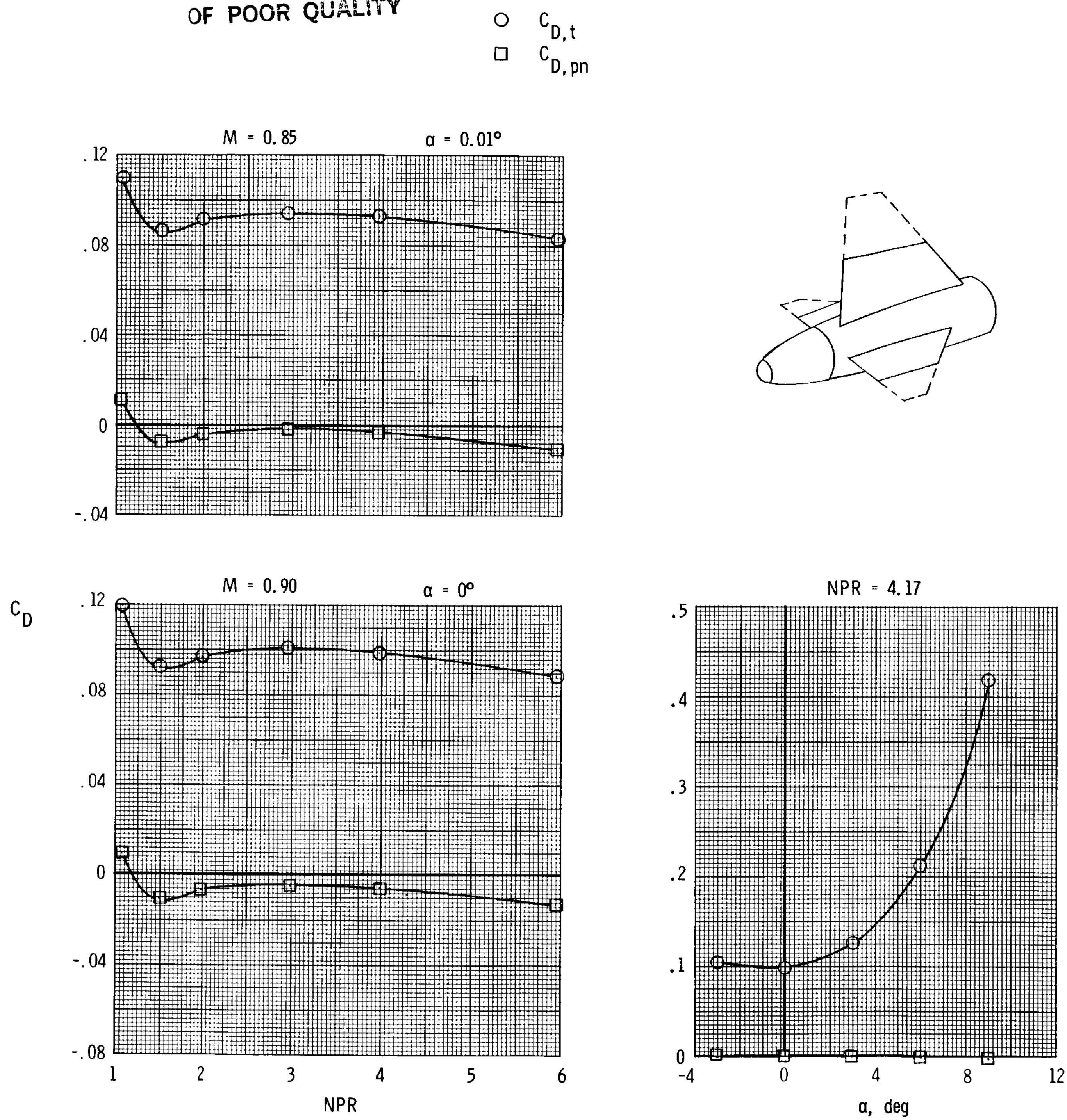

(c) Continued.

Figure 11. Continued.

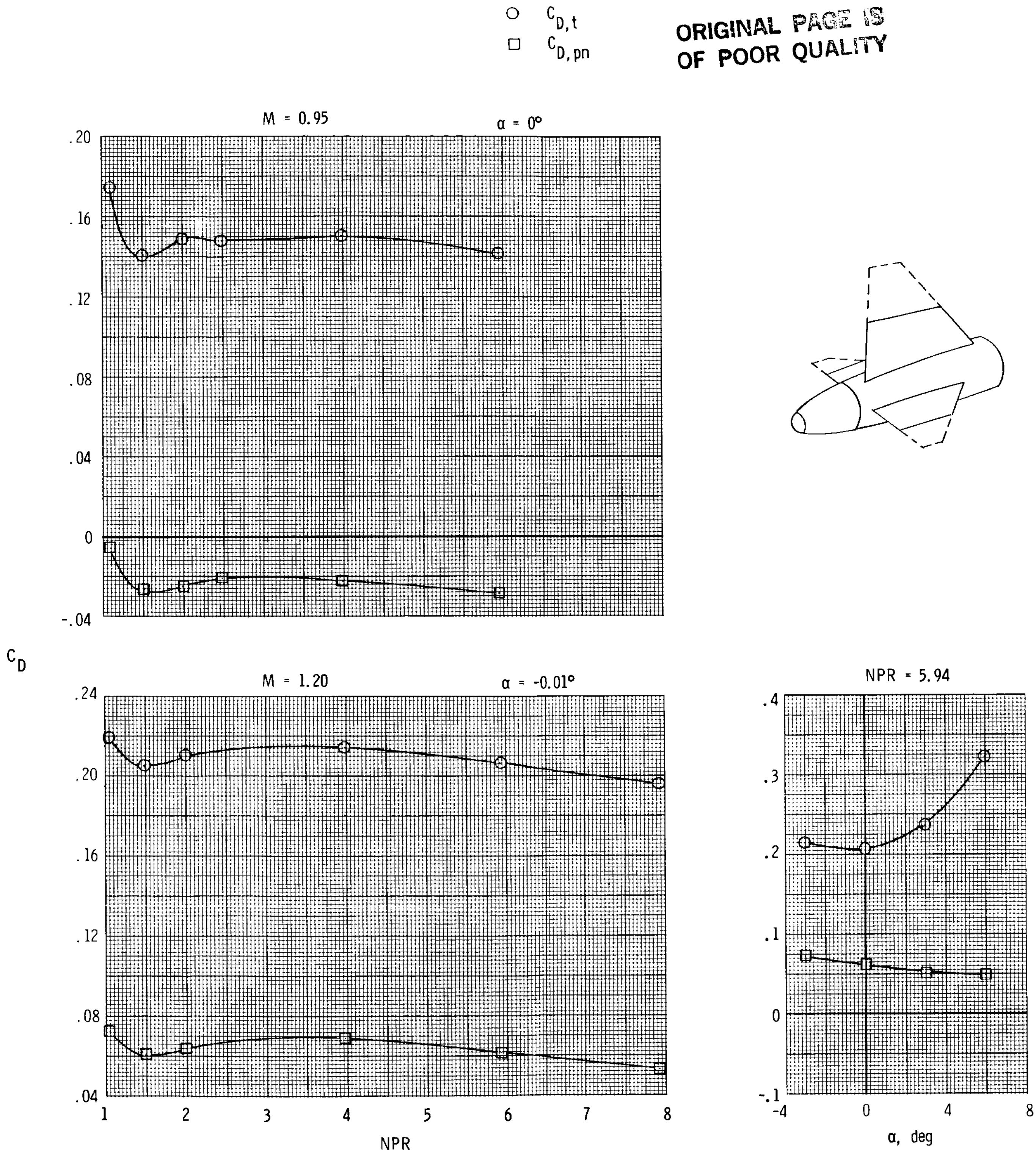

ORIGINAL PAGE IS OF POOR QUALITY

(c) Concluded.

Figure 11. Continued.

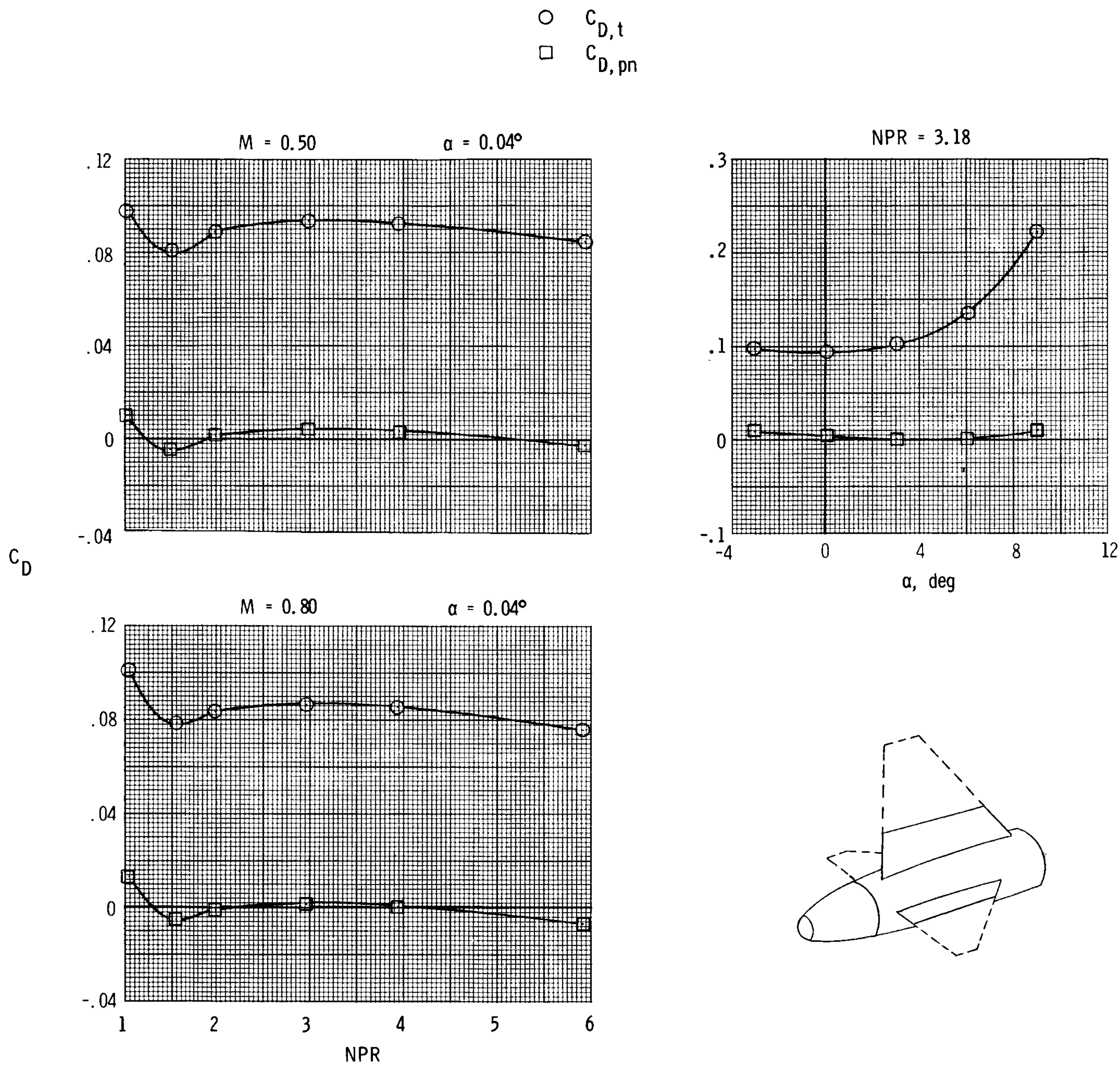

(d) $y/b = 0.30$.

Figure 11. Continued.

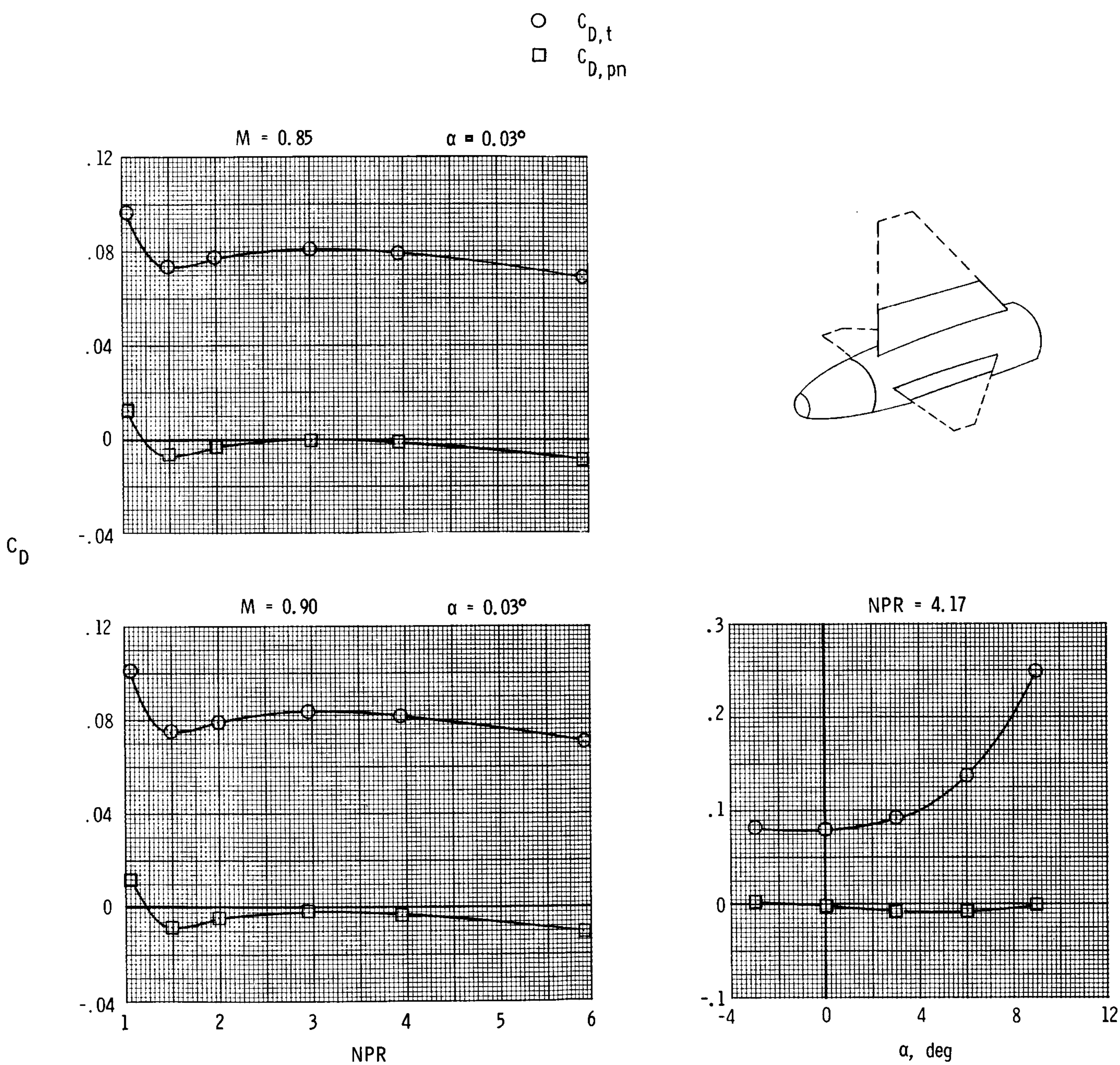

(d) Continued.

Figure 11. Continued.

ORIGINAL PAGE IS
OF POOR QUALITY

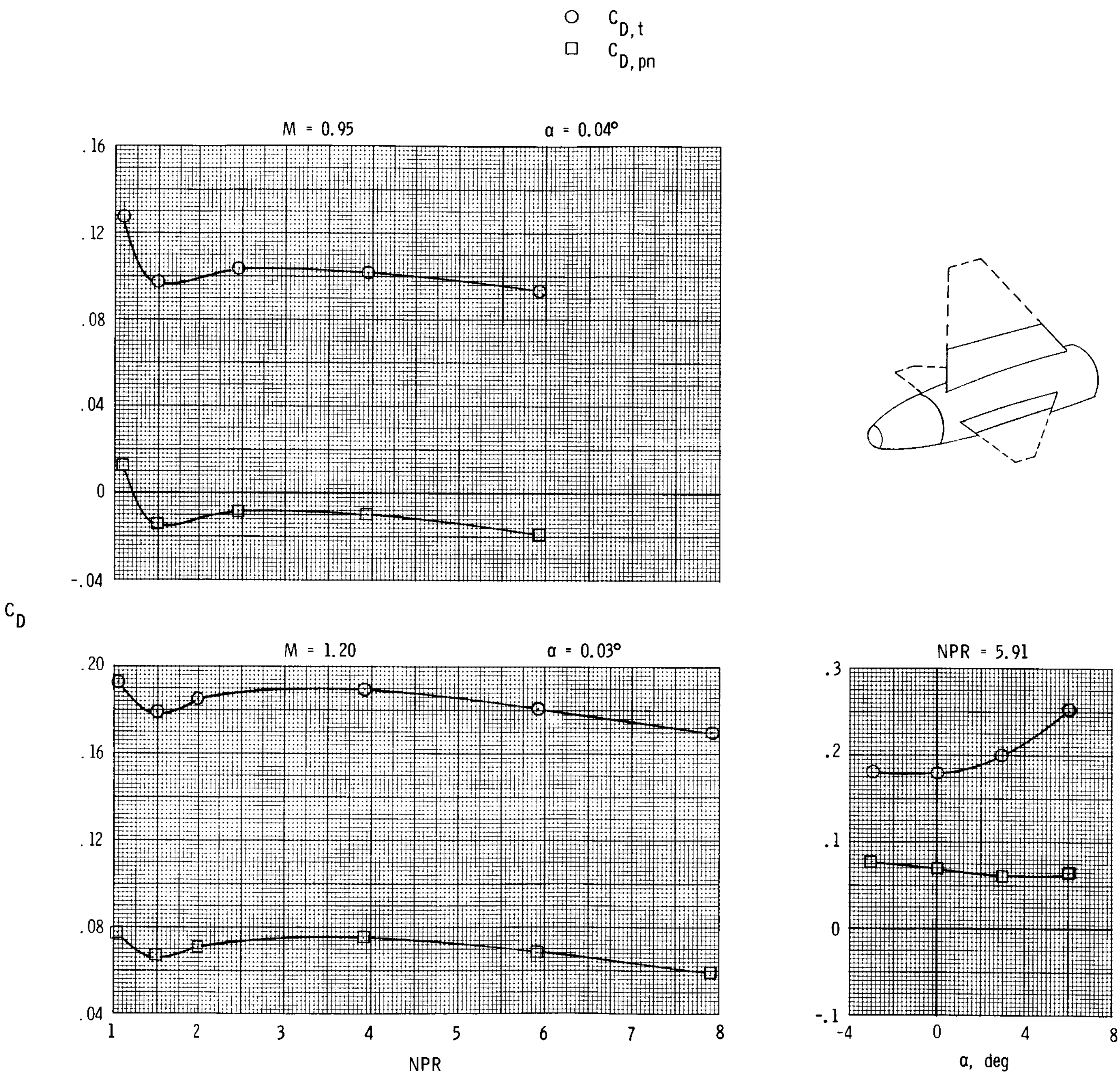

(d) Concluded.

Figure 11. Continued.

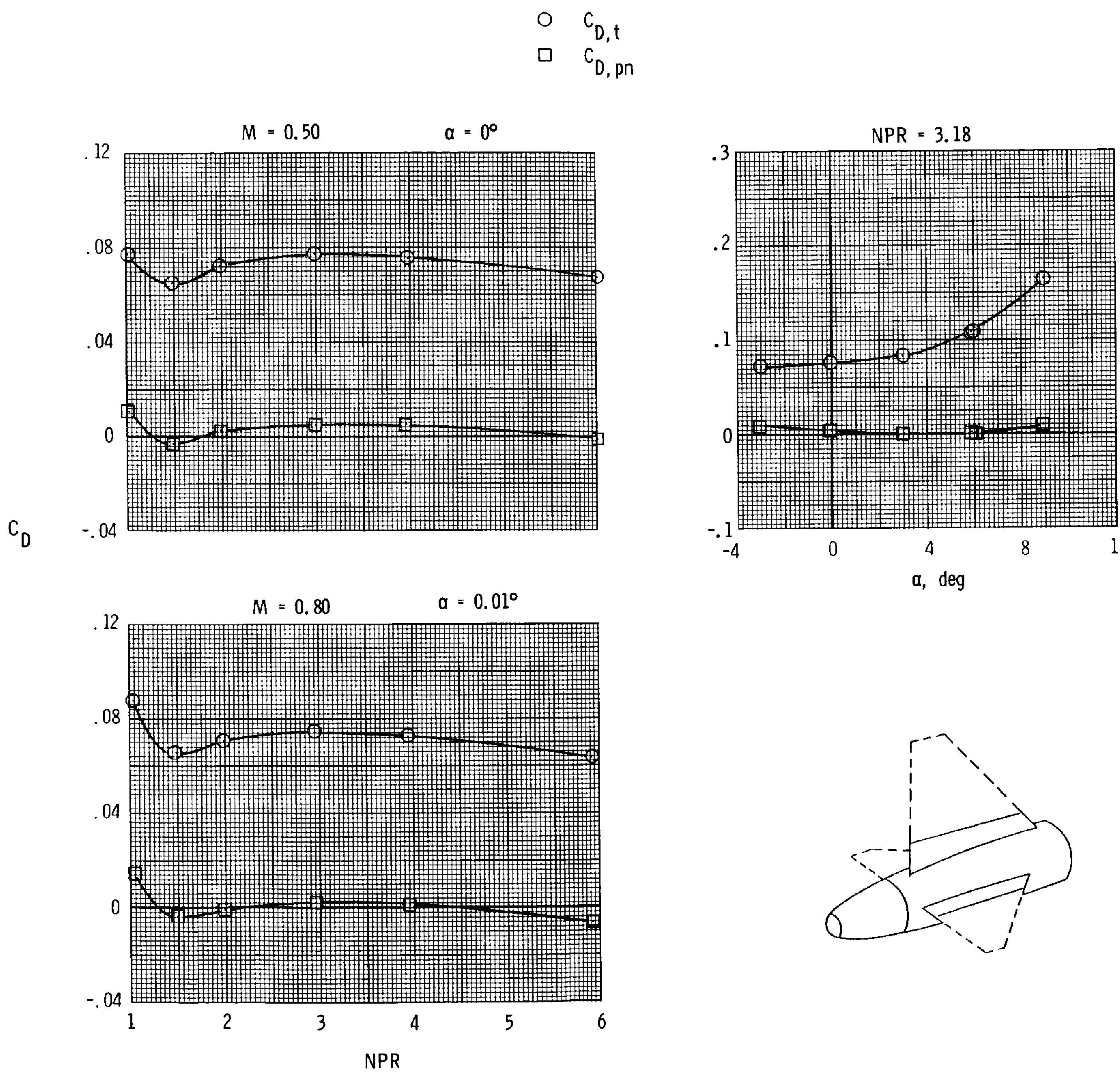

(e) $y/b = 0.20$.

Figure 11. Continued.

C-2

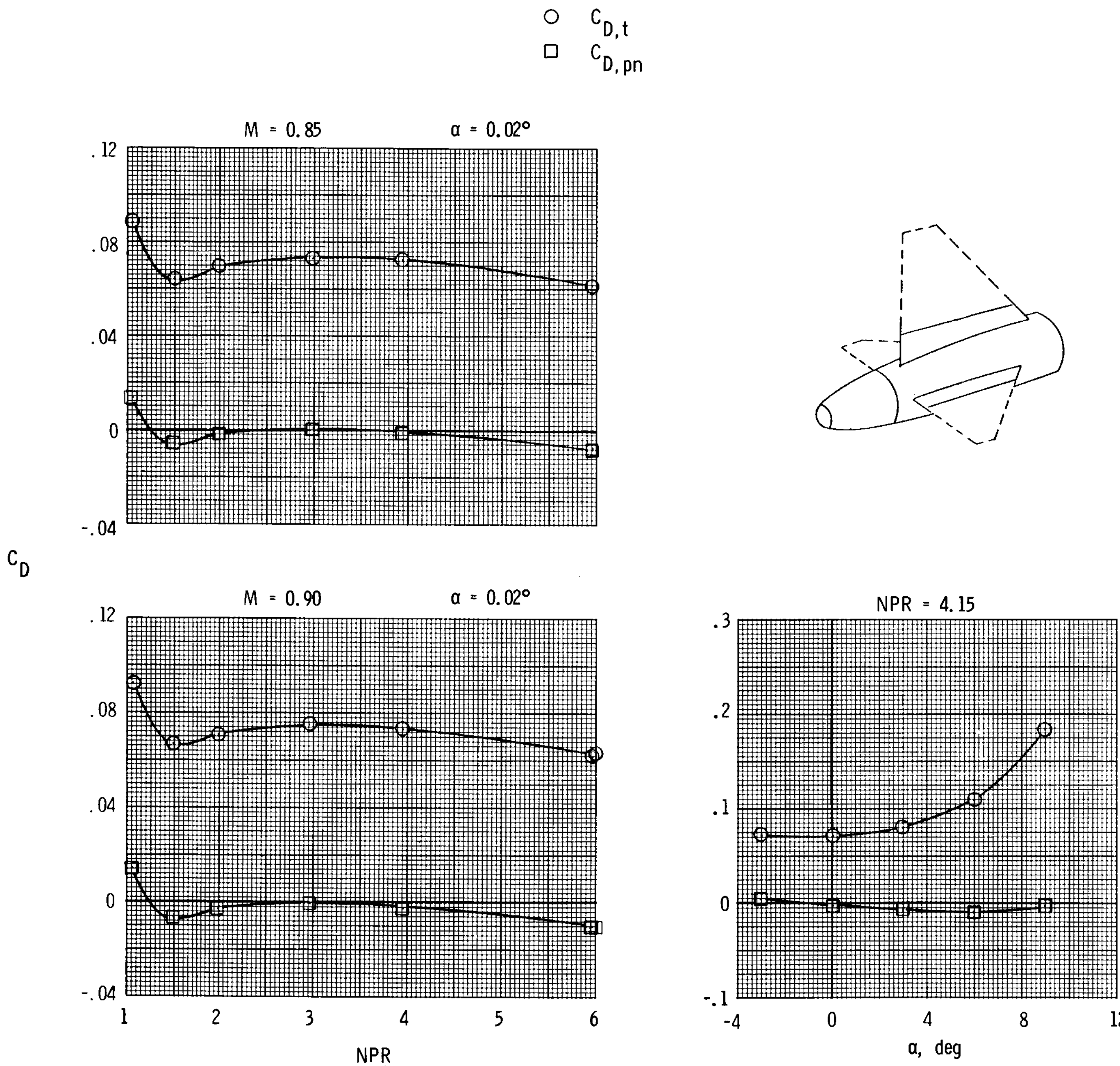

(e) Continued.

Figure 11. Continued.

C2

ORIGINAL PAGE IS
OF POOR QUALITY

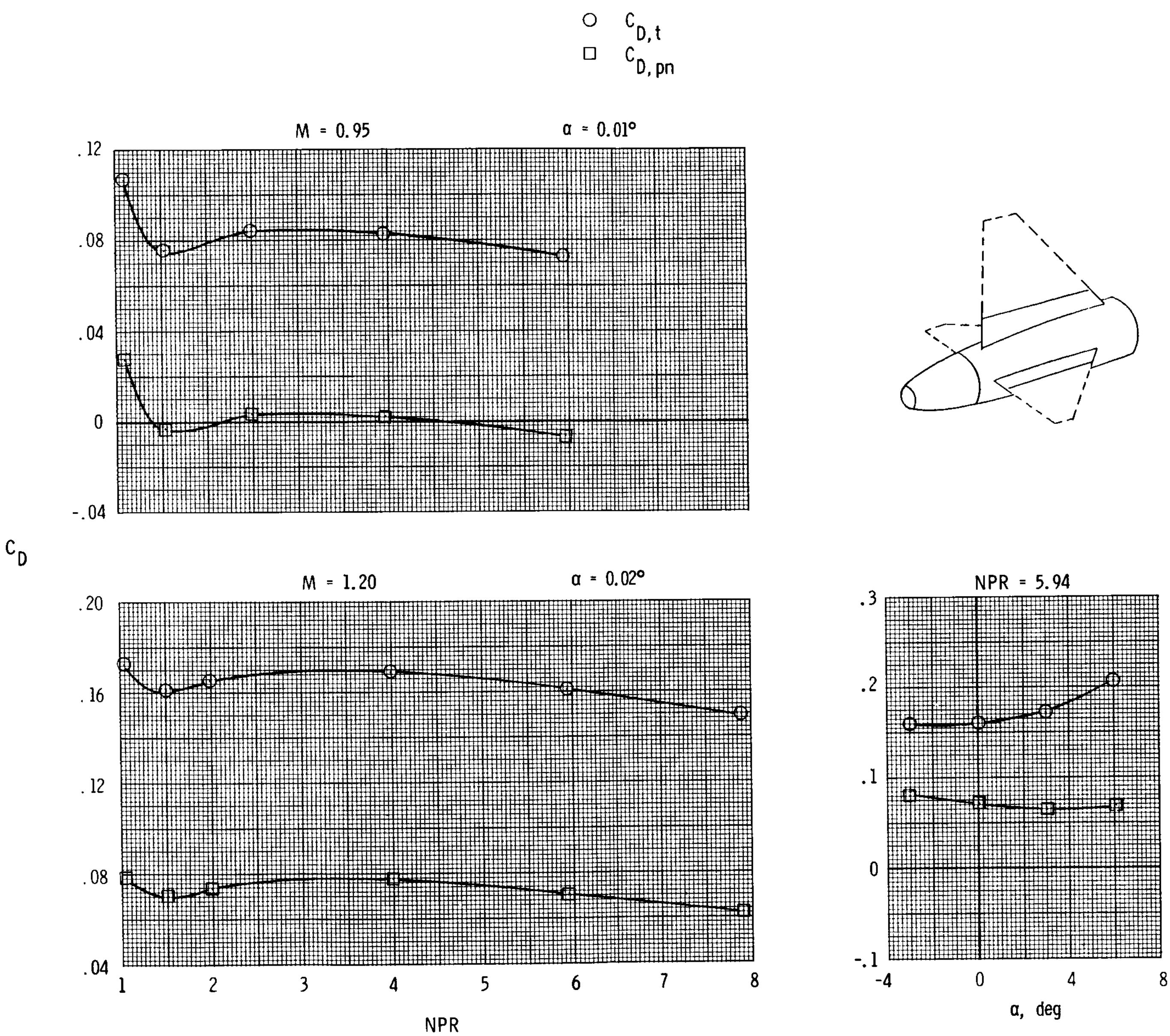

(e) Concluded.

Figure 11. Continued.

ORIGINAL PAGE IS
OF POOR QUALITY

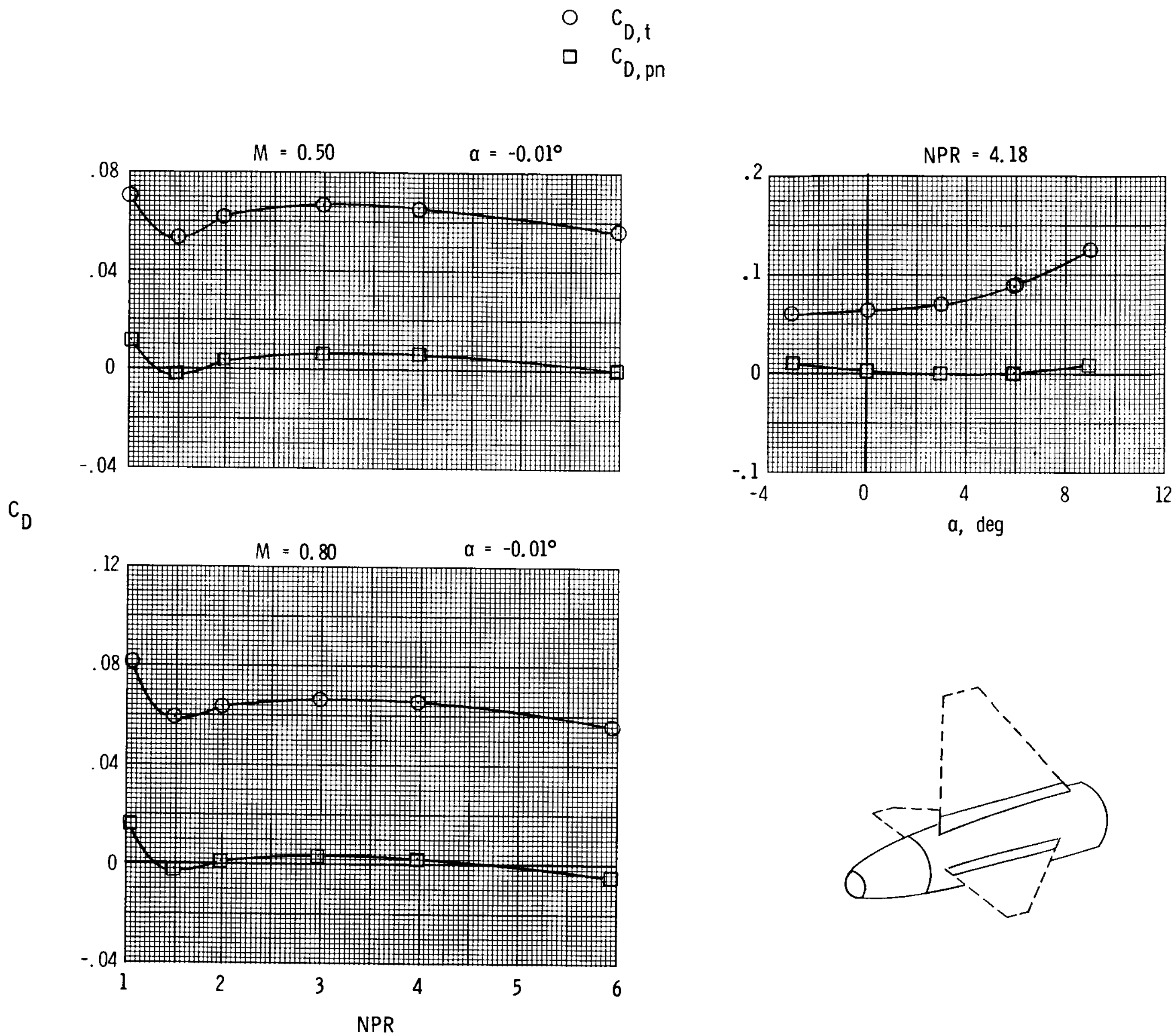

(f) $y/b = 0.10$.

Figure 11. Continued.

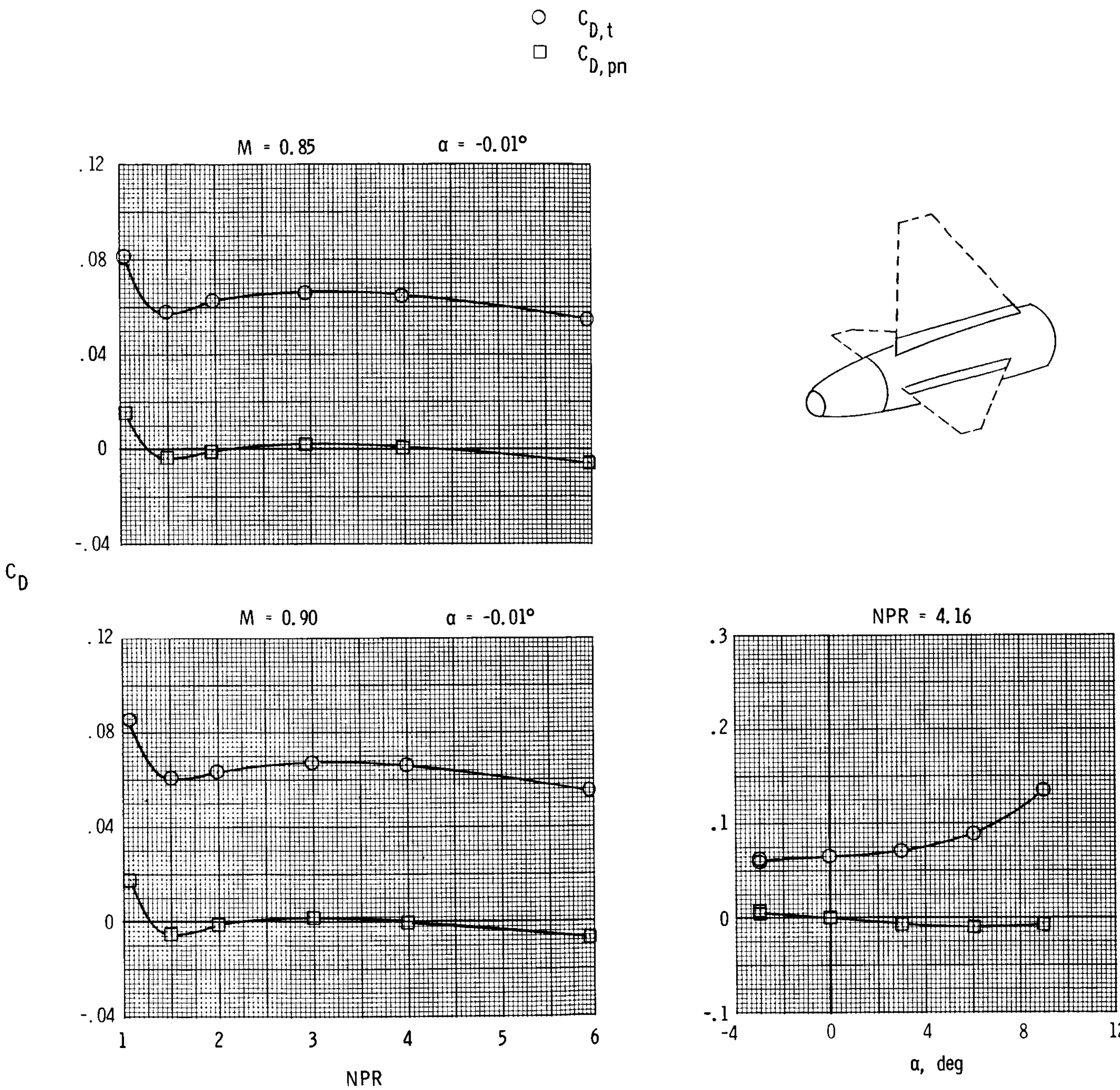

(f) Continued.

Figure 11. Continued.

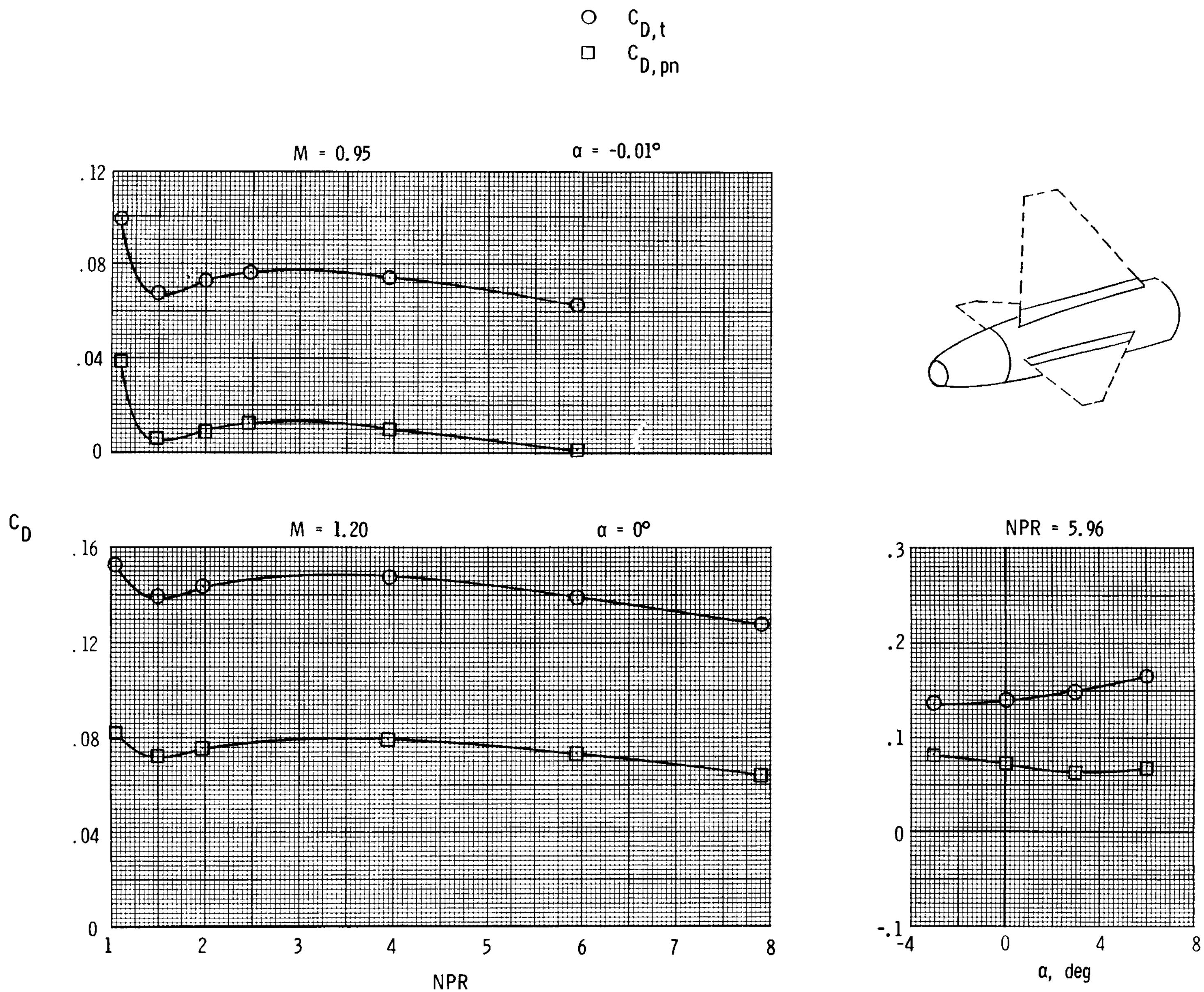

(f) Concluded.

Figure 11.- Concluded.

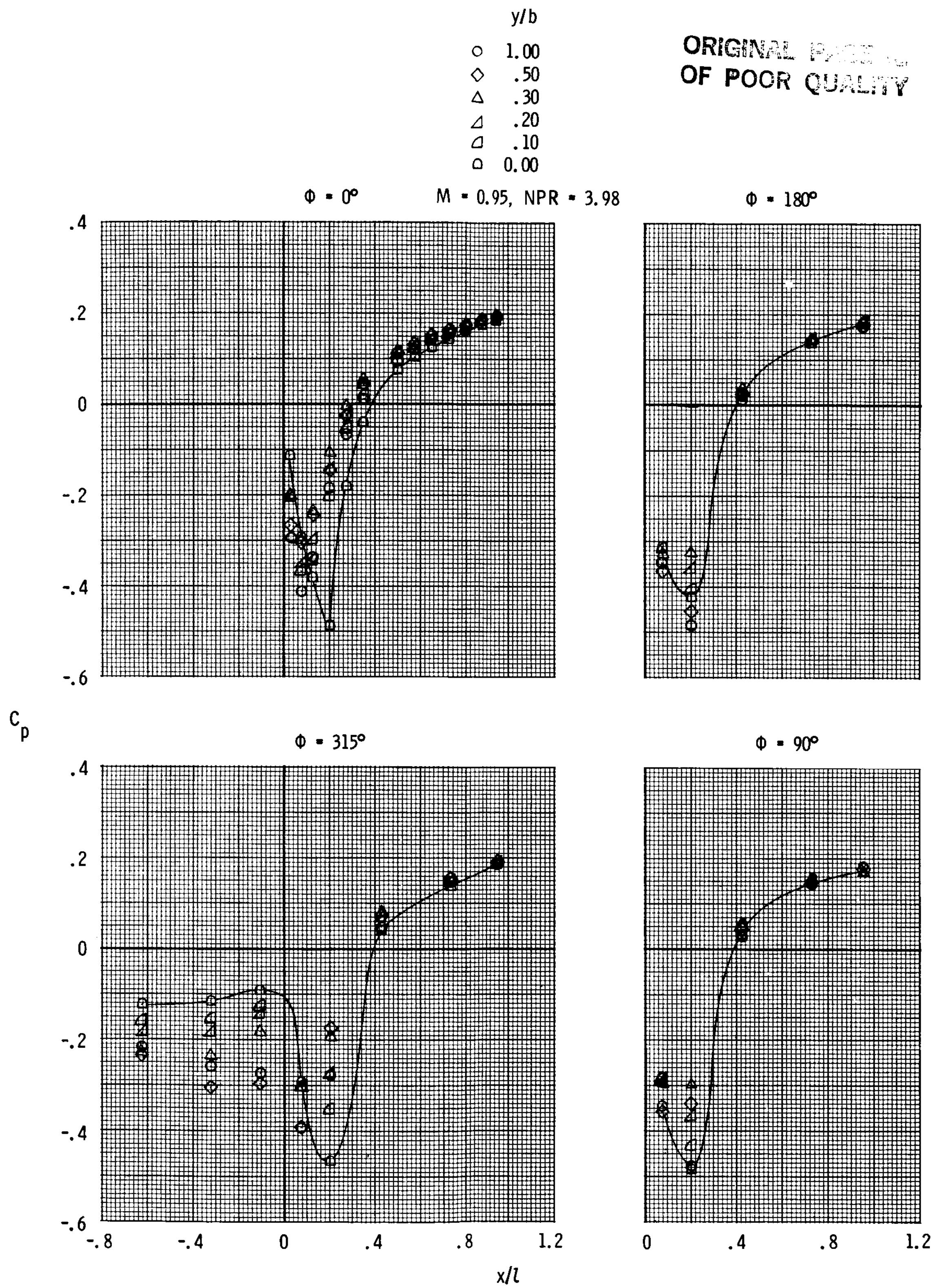

(a) Aft vertical tail, horizontal tails off.

Figure 12. Effect of tail span on afterbody/nozzle static pressure coefficient distributions. $\alpha = 0°$; for clarity, only tail-off ($y/b = 0.00$) data are faired.

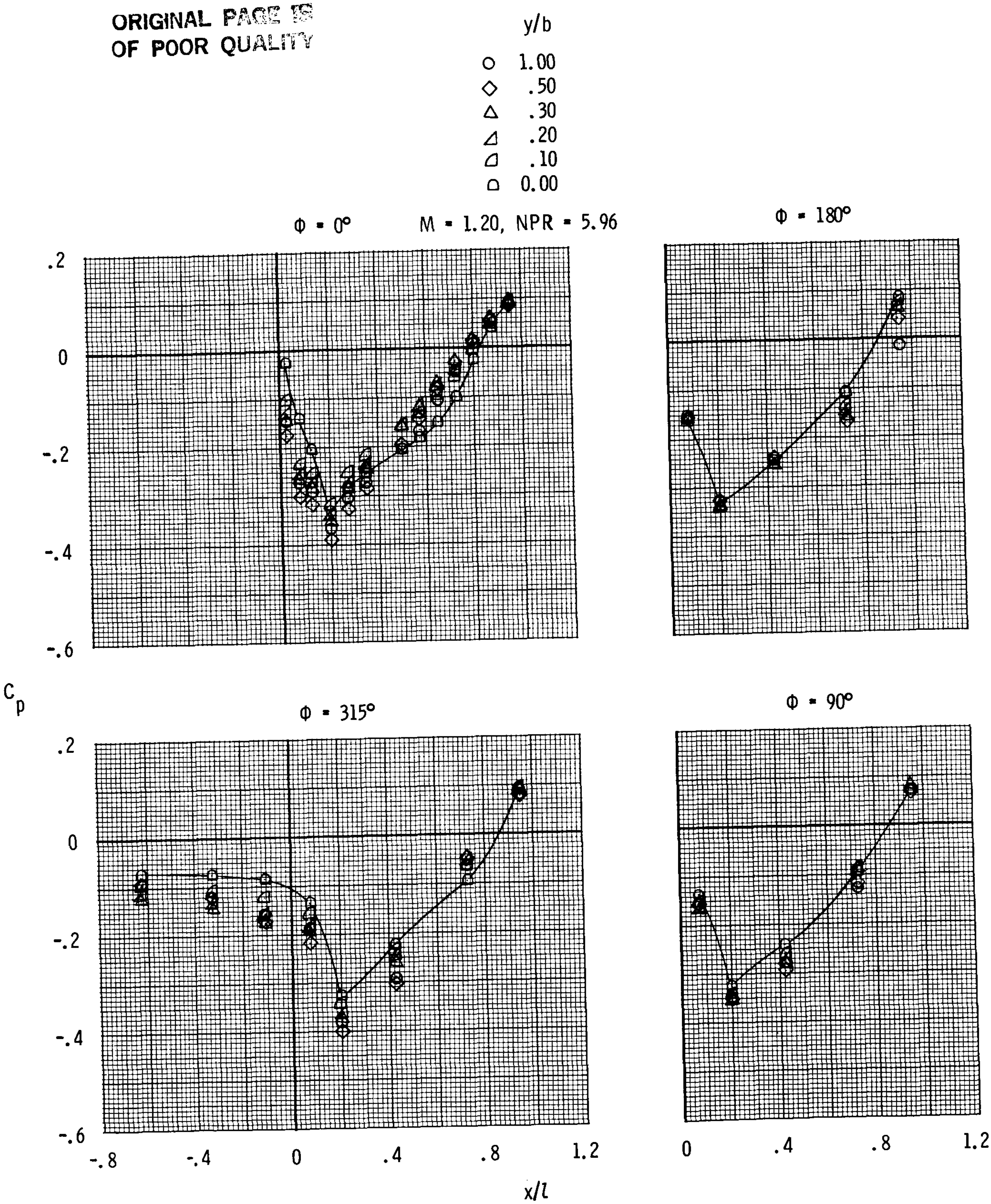

(a) Concluded.

Figure 12. Continued.

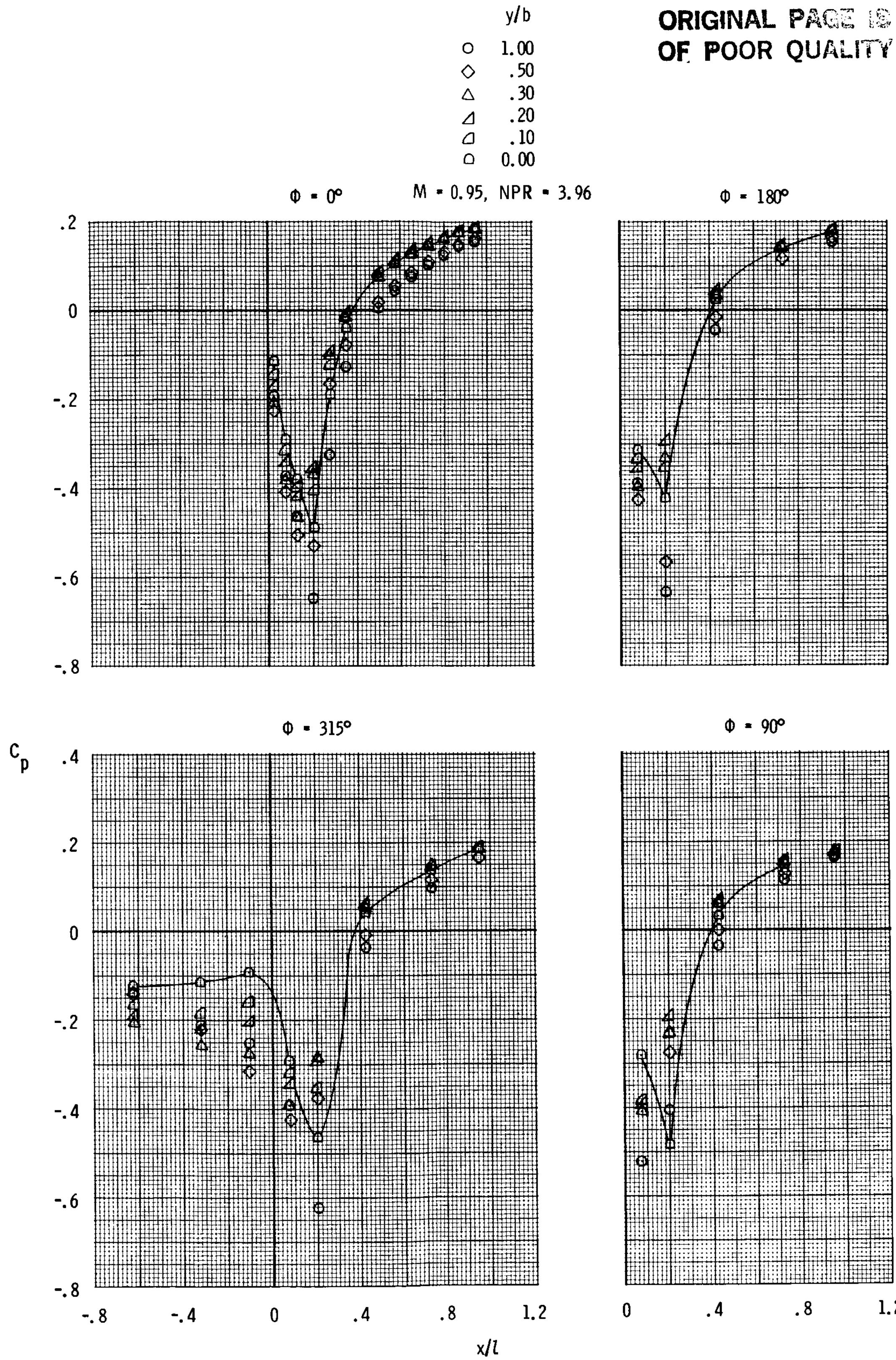

(b) Vertical tail off, aft horizontal tails.

Figure 12. Continued.

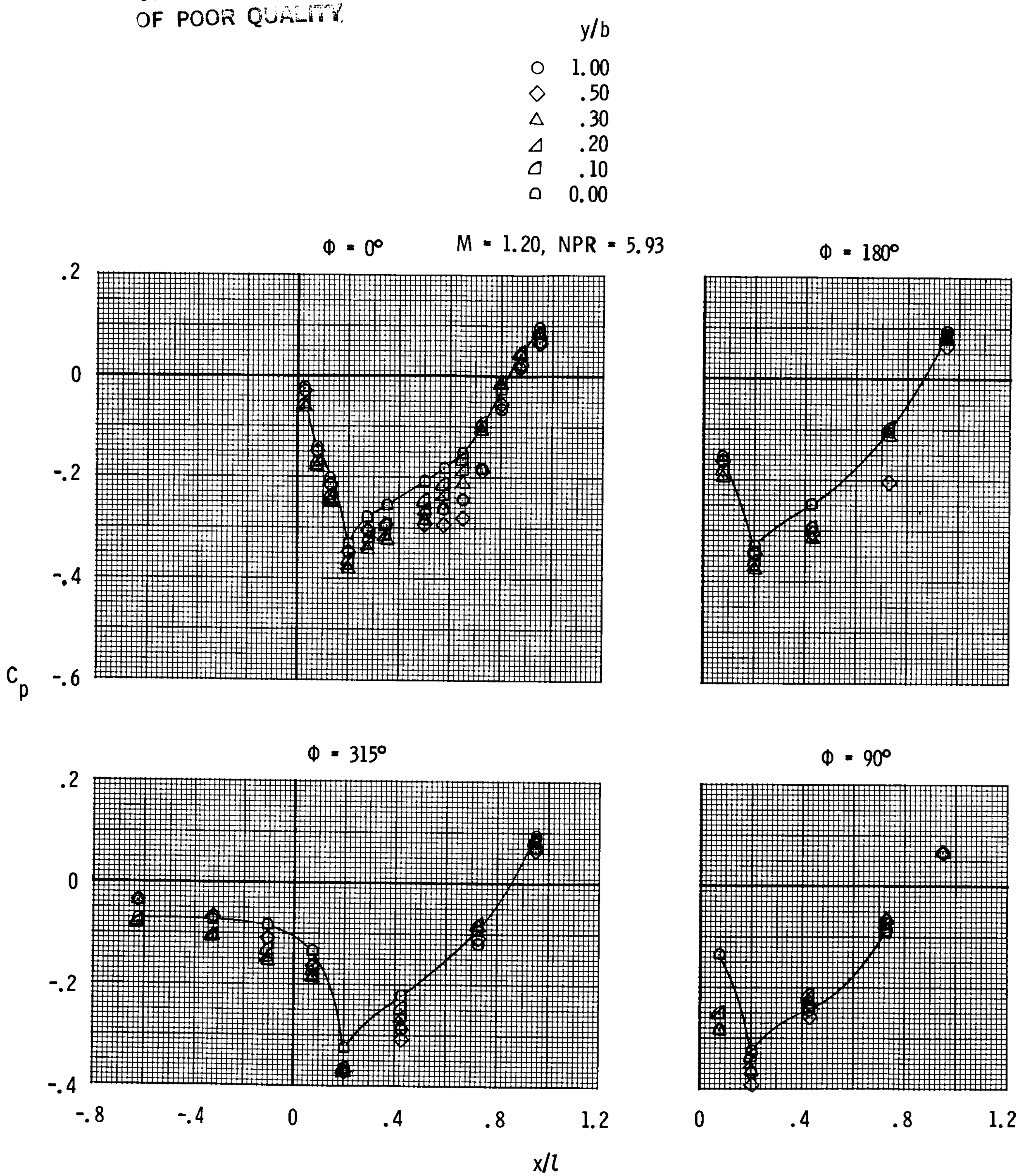

(b) Concluded.

Figure 12. Continued.

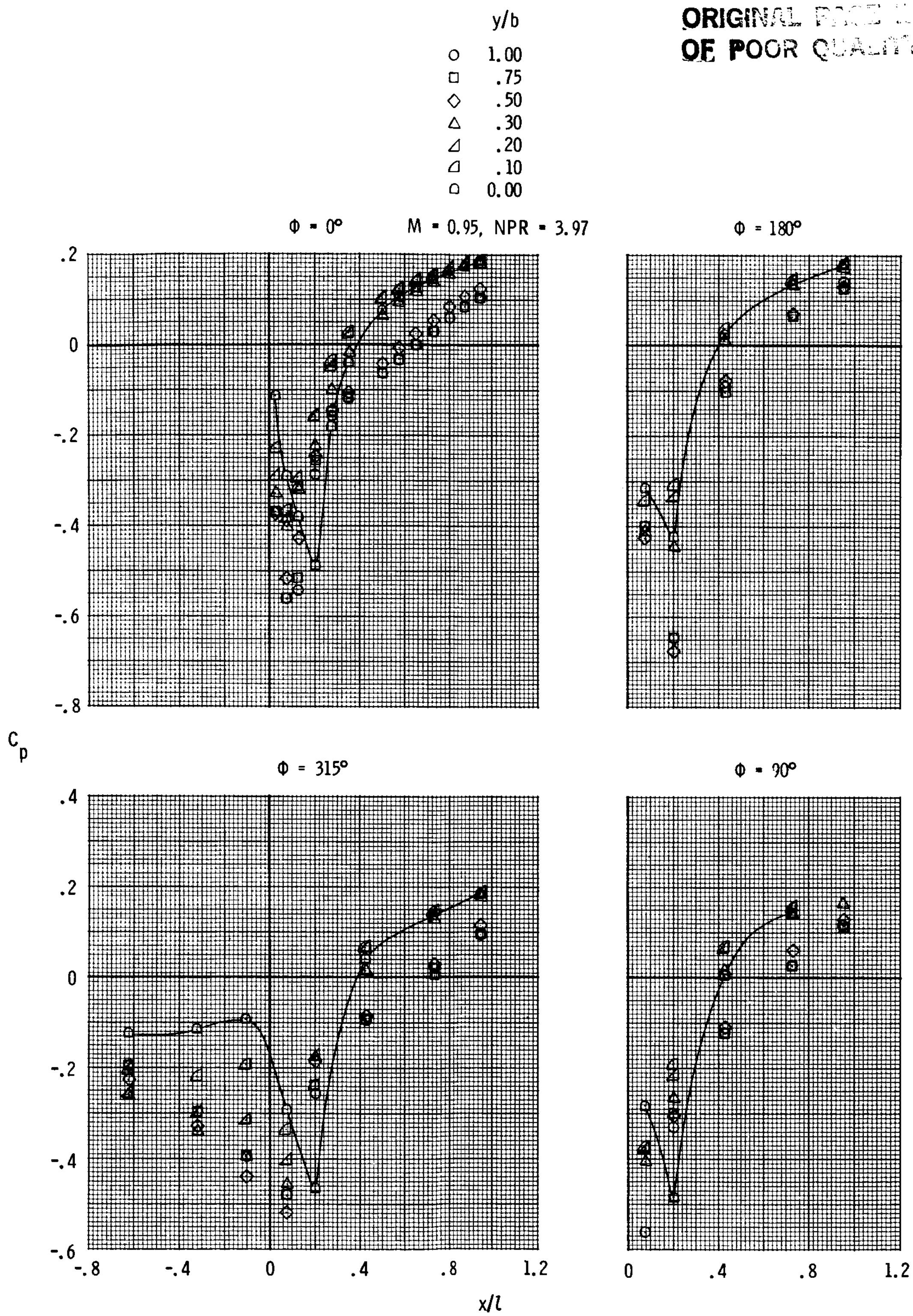

(c) Aft vertical tail, aft horizontal tails.

Figure 12. Continued.

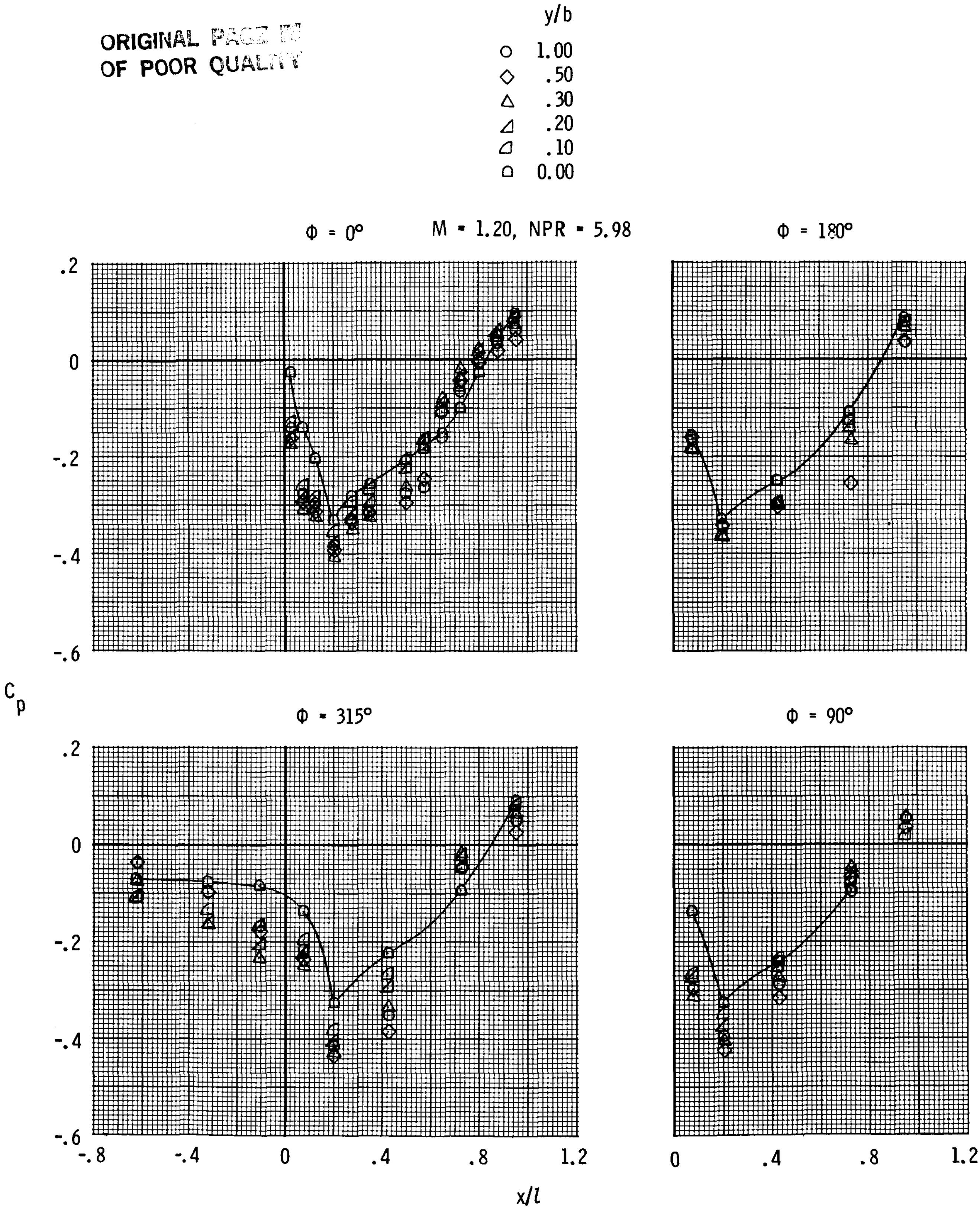

(c) Concluded.

Figure 12. Concluded.

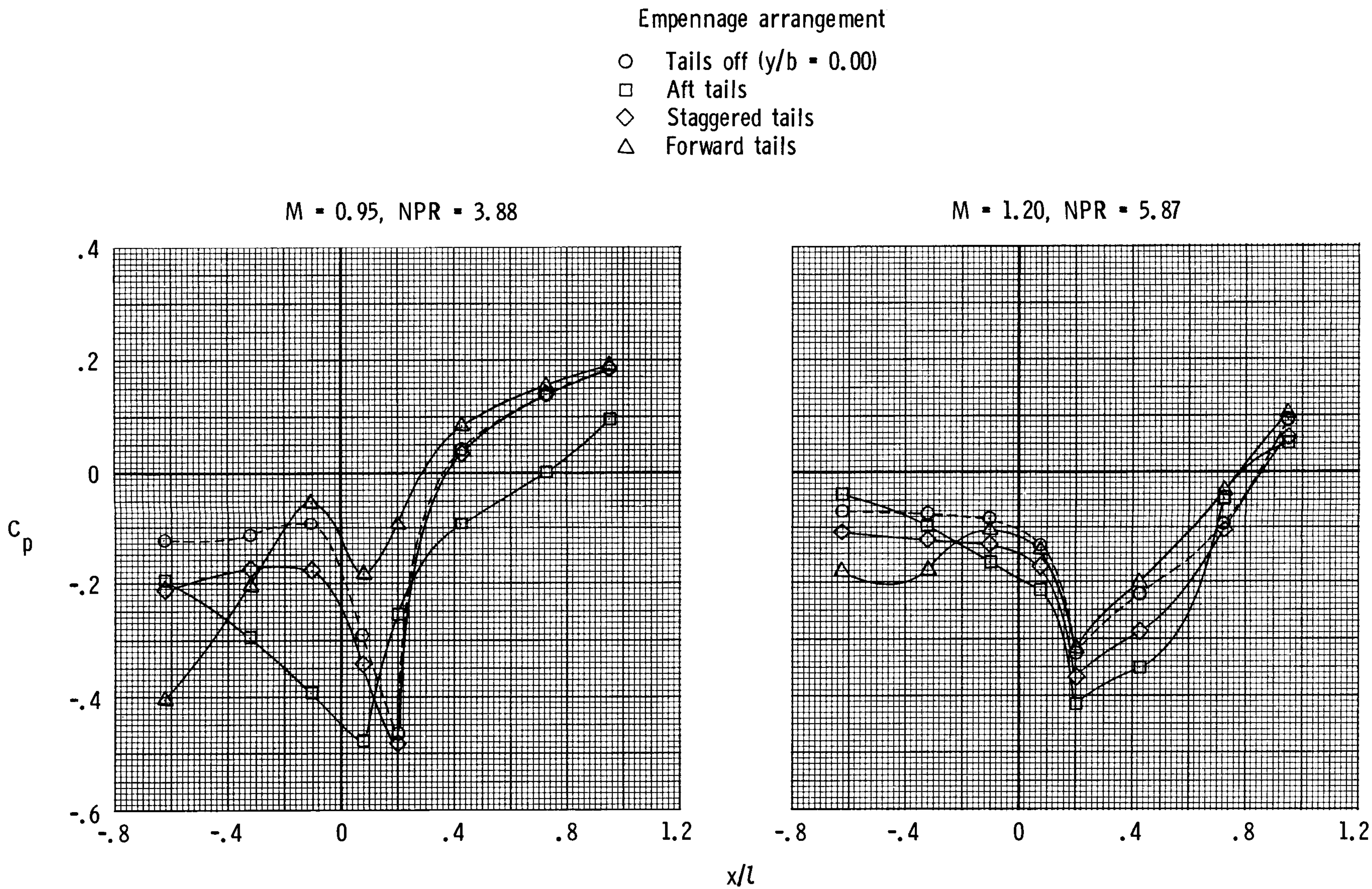

(a) $y/b = 1.00$.

Figure 13. Effect of empennage arrangement on afterbody/nozzle static-pressure coefficient distributions. $\phi = 315°$; $\alpha = 0°$; for clarity, tail-off ($y/b = 0.00$) data are faired as a dashed line.

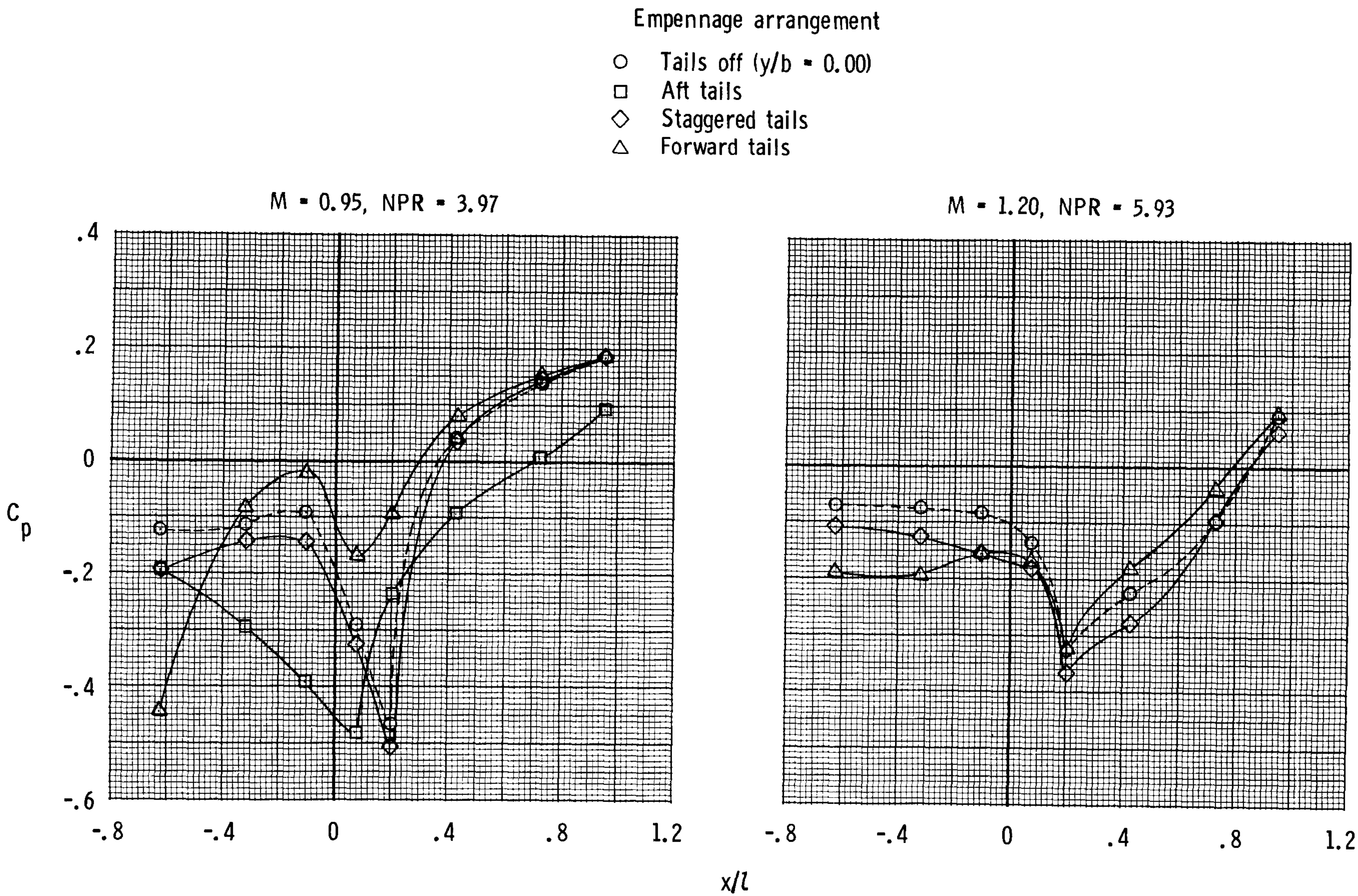

(b) $y/b = 0.75$.

Figure 13. Continued.

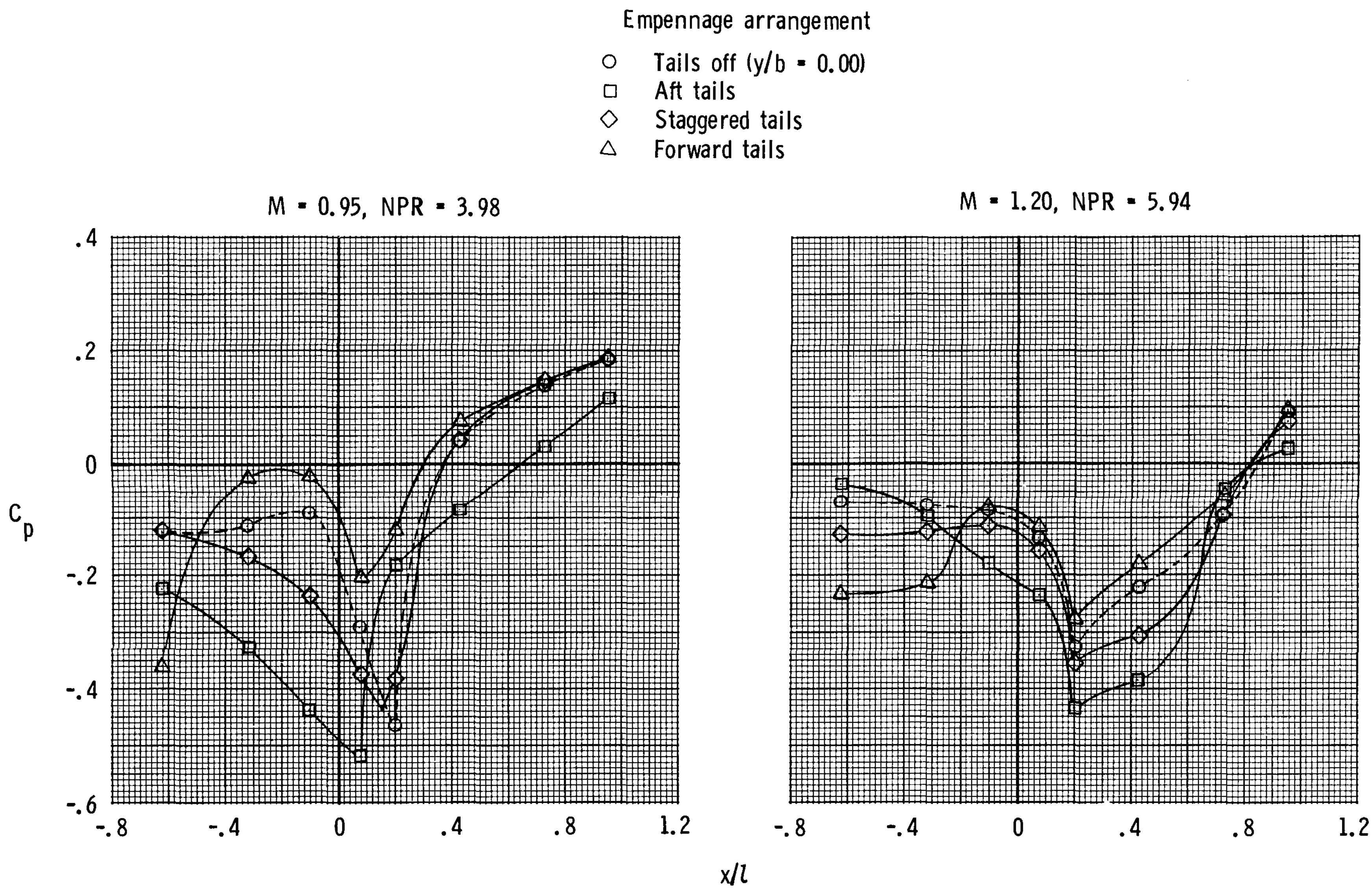

(c) $y/b = 0.50$.

Figure 13. Continued.

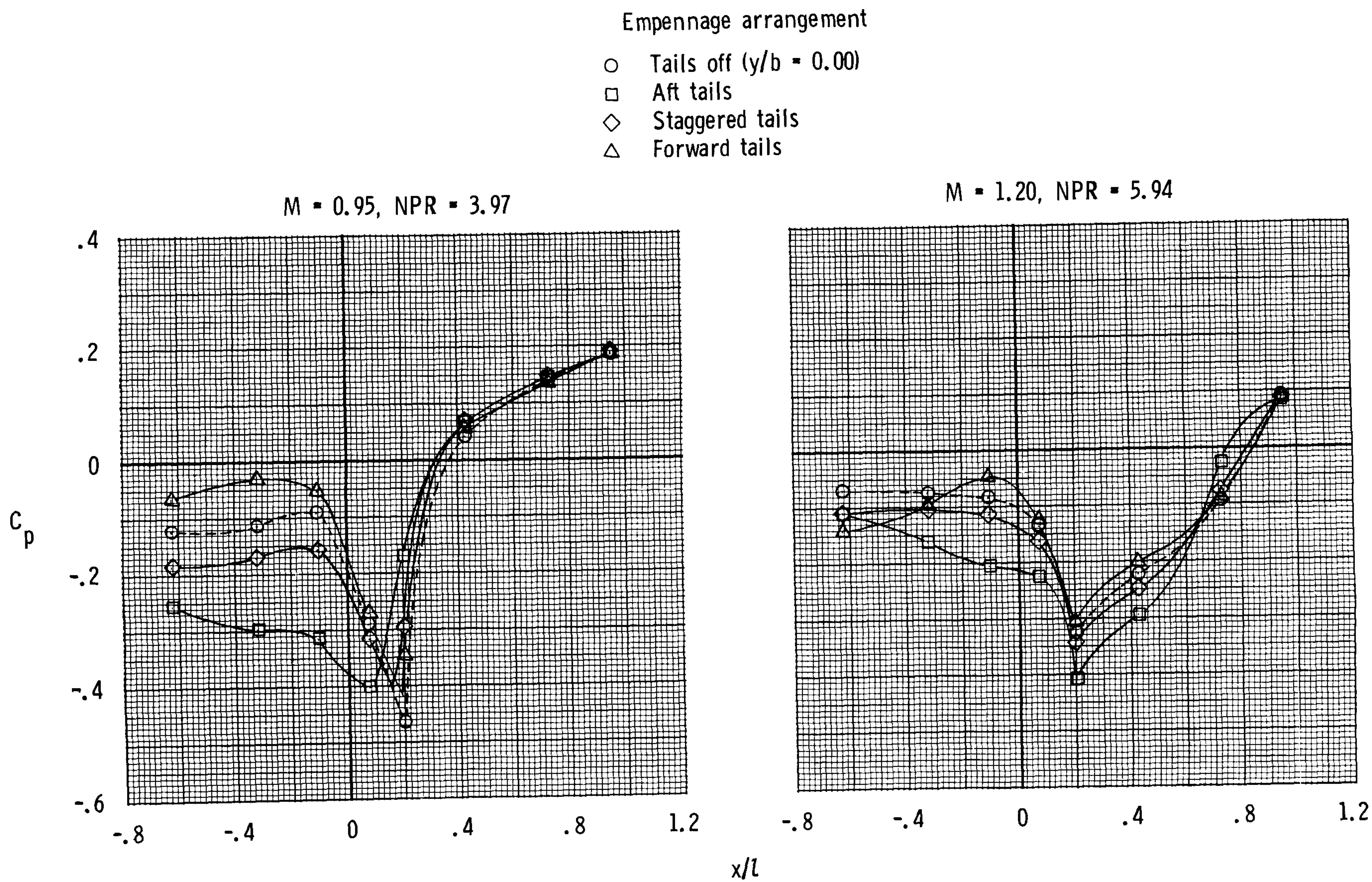

(d) $y/b = 0.20$.

Figure 13. Concluded.

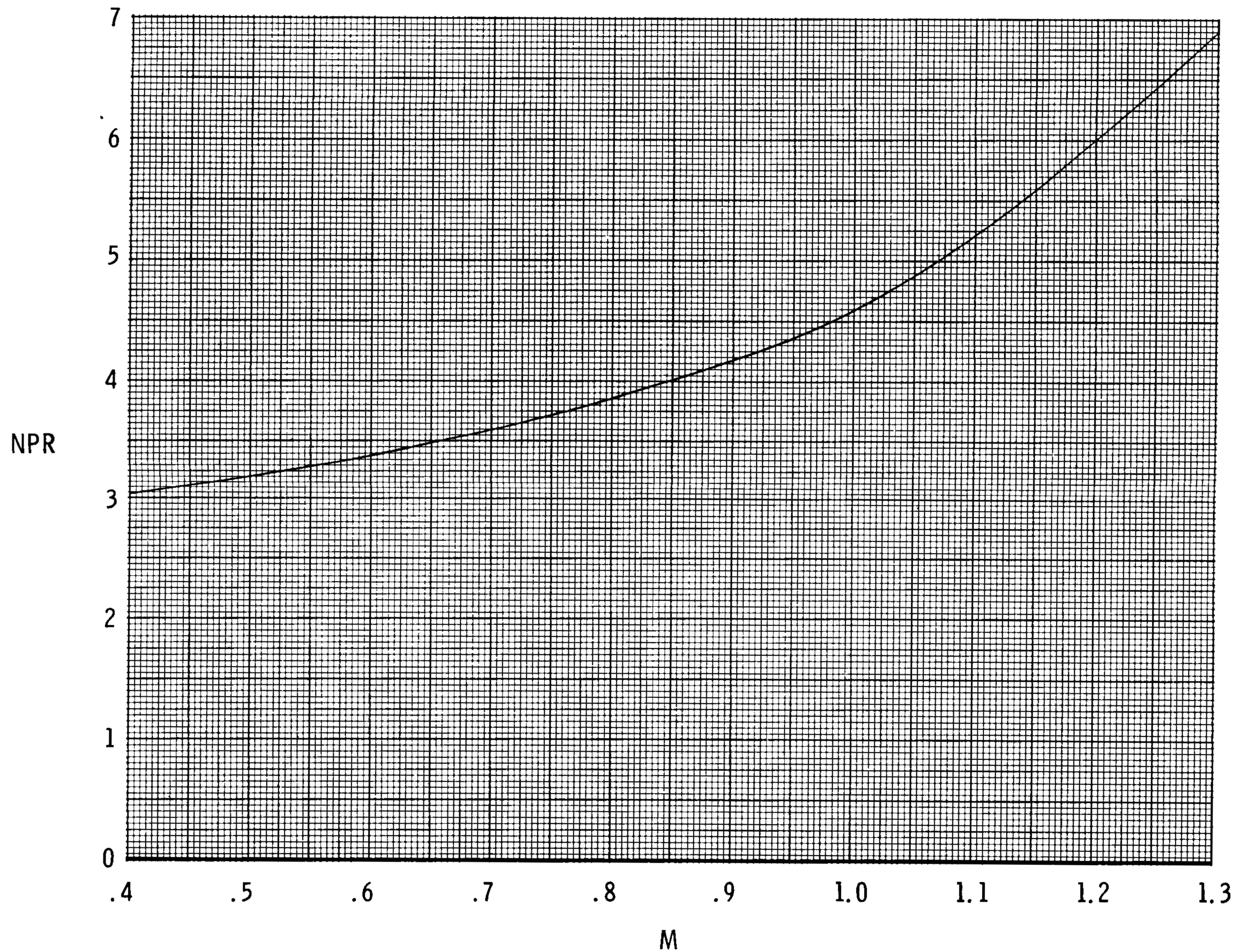

Figure 14. Typical nozzle pressure ratios for a turbofan engine.

ORIGINAL PAGE IS
OF POOR QUALITY

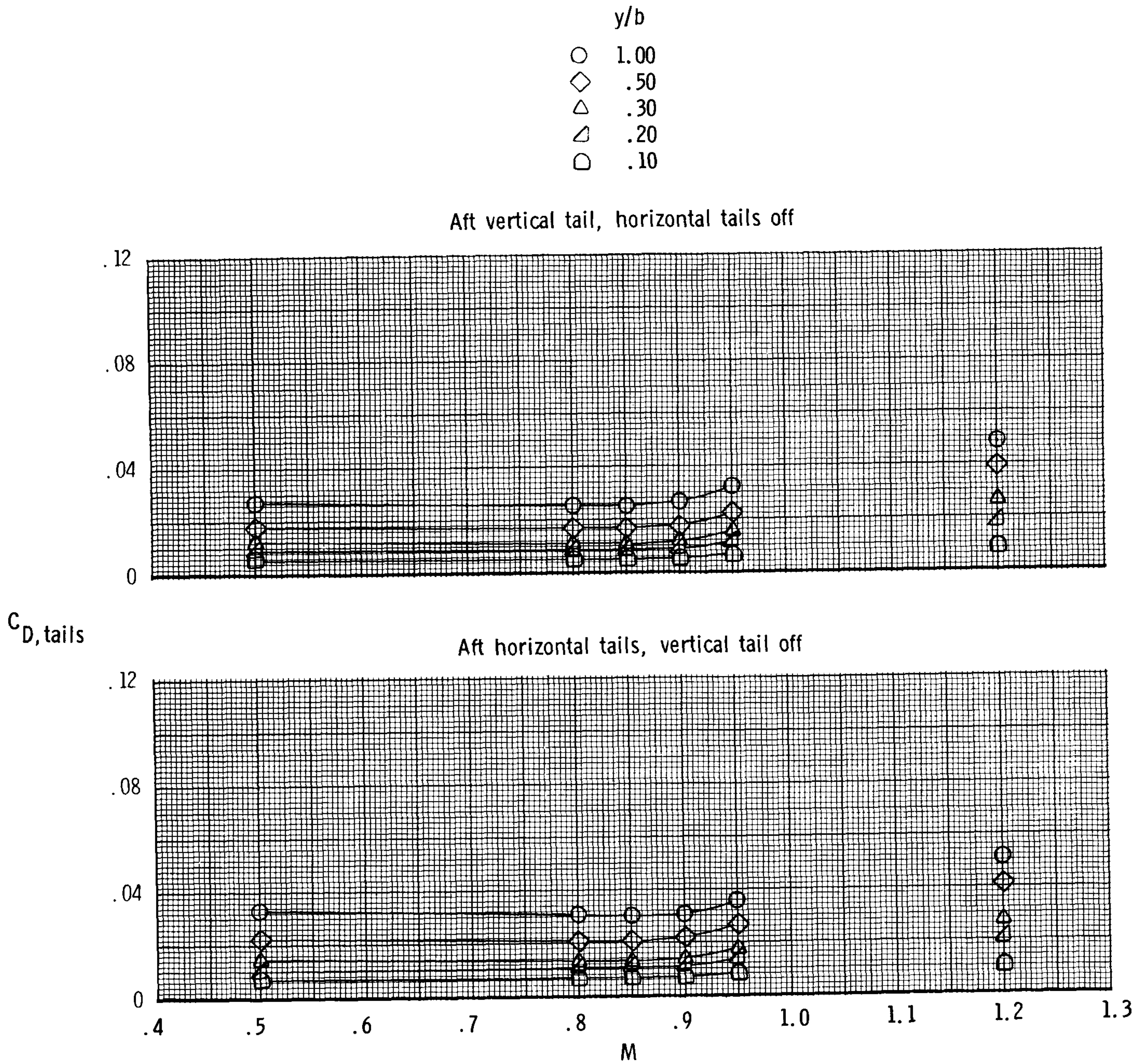

(a) Individual tail surfaces.

Figure 15. Effect of tail span on variation of computed tail drag coefficient with Mach number.

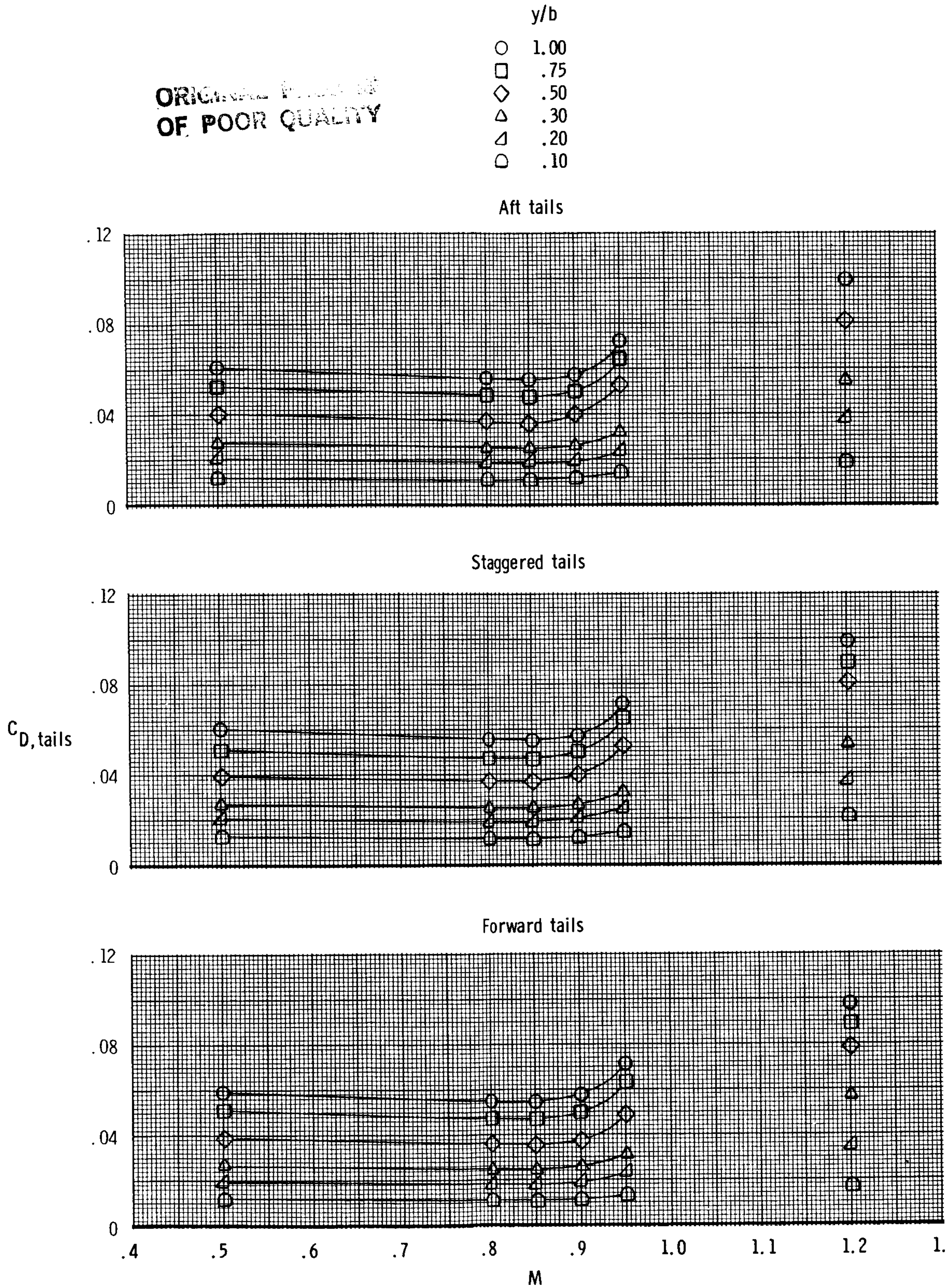

(b) Complete empennage arrangements.

Figure 15. Concluded.

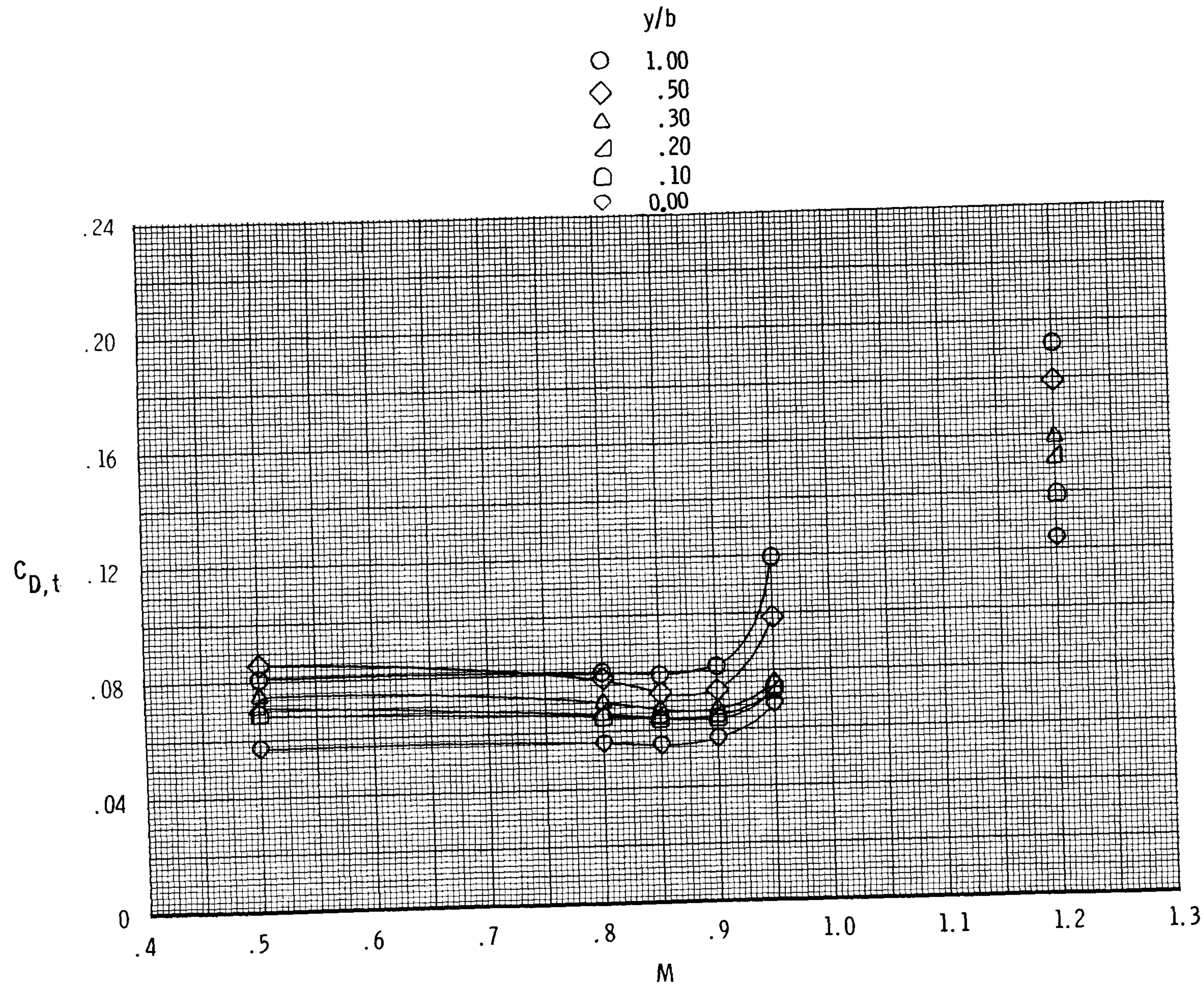

(a) Aft vertical tail, horizontal tails off.

Figure 16. Effect of tail span on variation of total aft-end drag coefficient with Mach number.

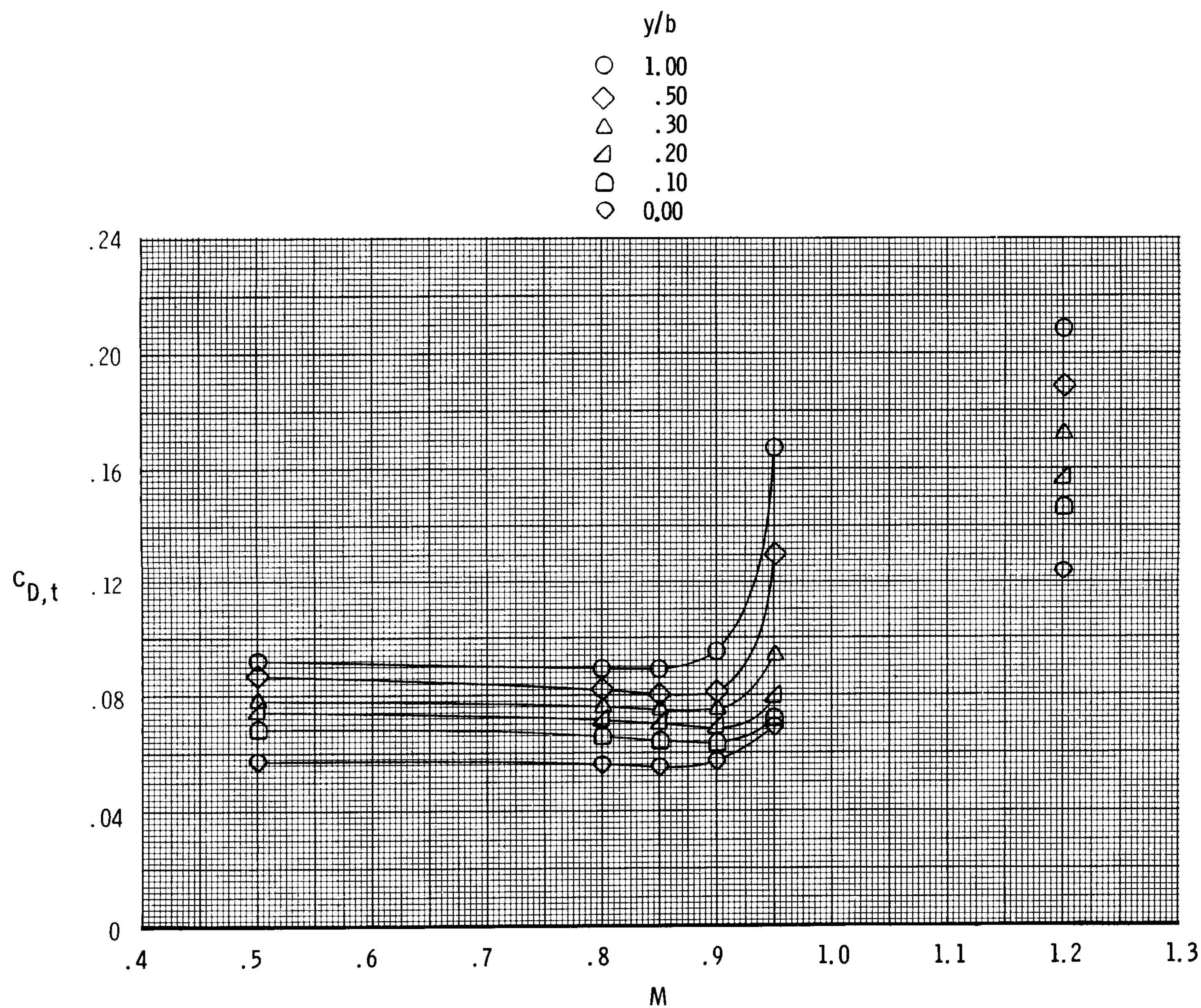

(b) Aft horizontal tails, vertical tail off.

Figure 16. Continued.

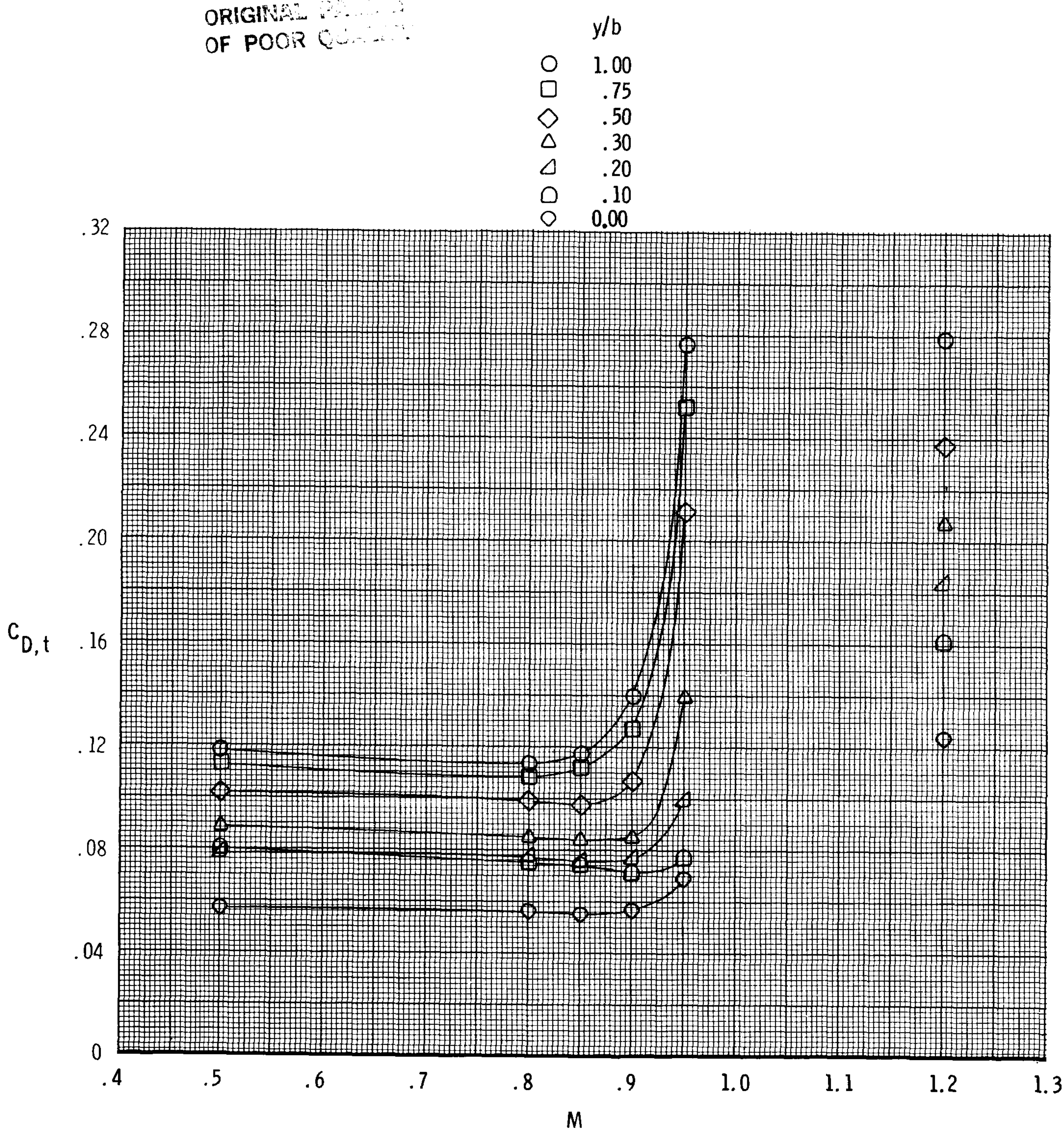

(c) Aft tails.

Figure 16. Continued.

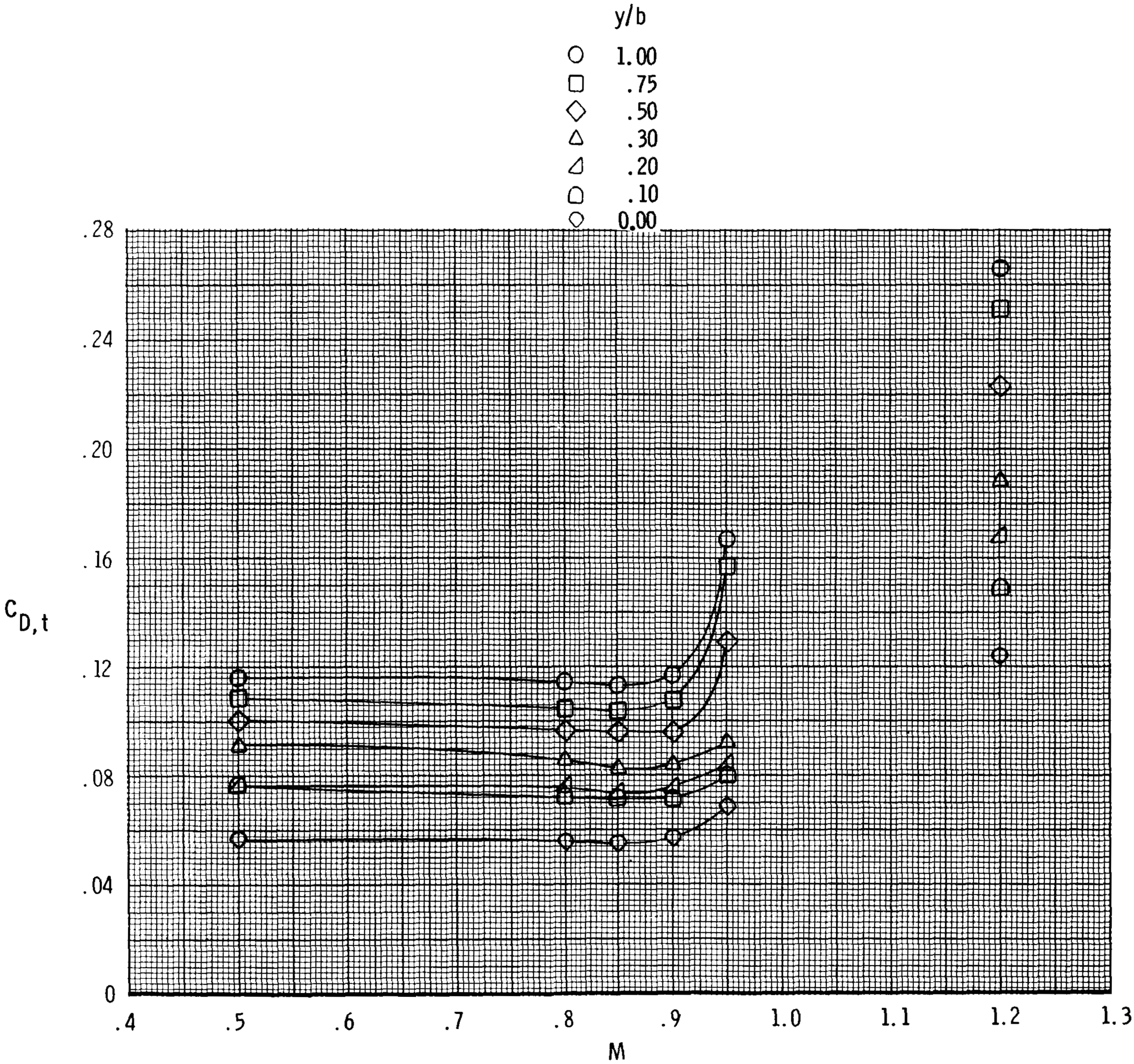

(d) Staggered tails.

Figure 16. Continued.

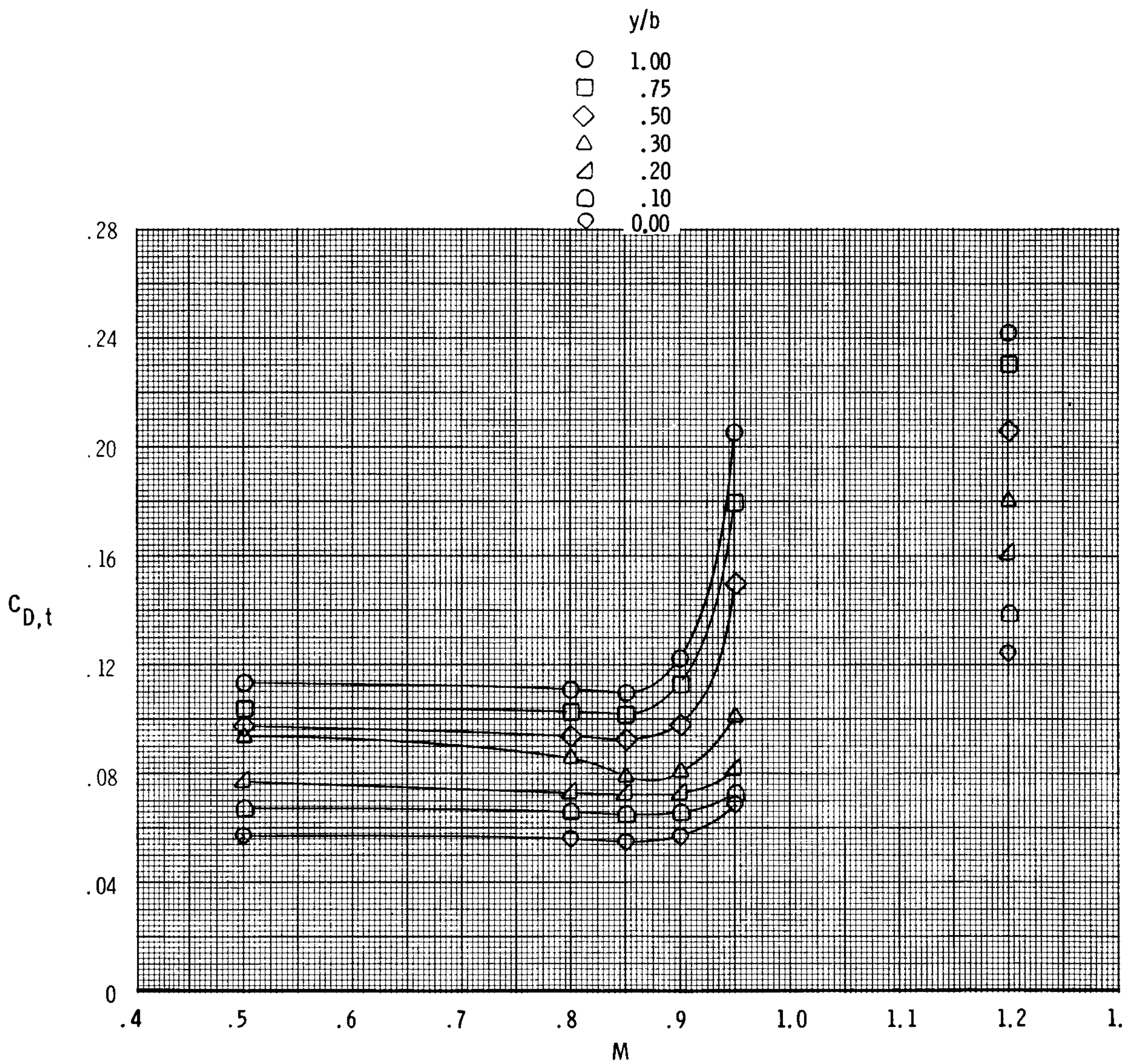

(e) Forward tails.

Figure 16. Concluded.

ORIGINAL PAGE IS
OF POOR QUALITY

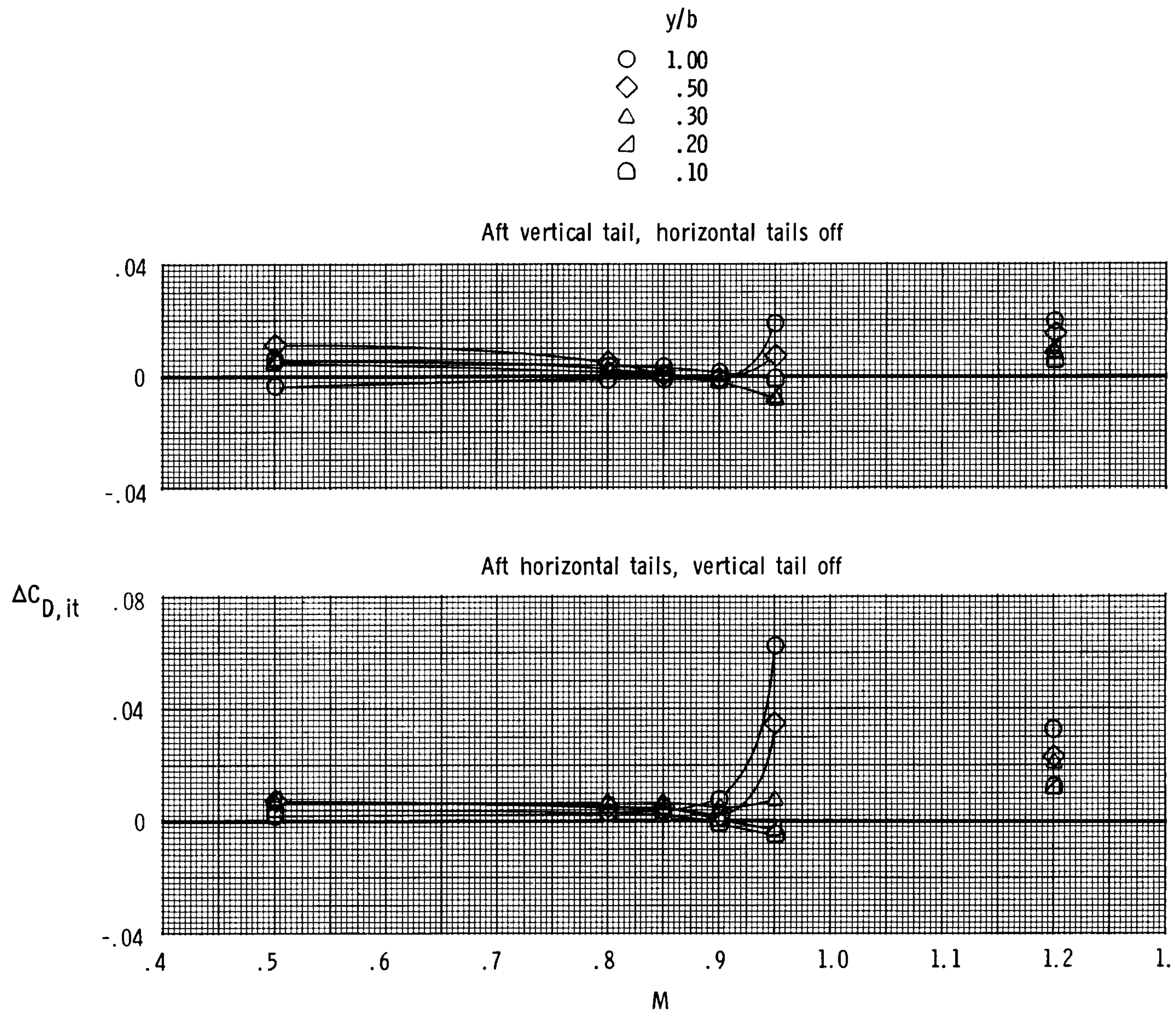

(a) Individual tail surfaces.

Figure 17. Effect of tail span on variation of total aft-end tail interference drag coefficient increment with Mach number.

ORIGINAL PAGE IS
OF POOR QUALITY

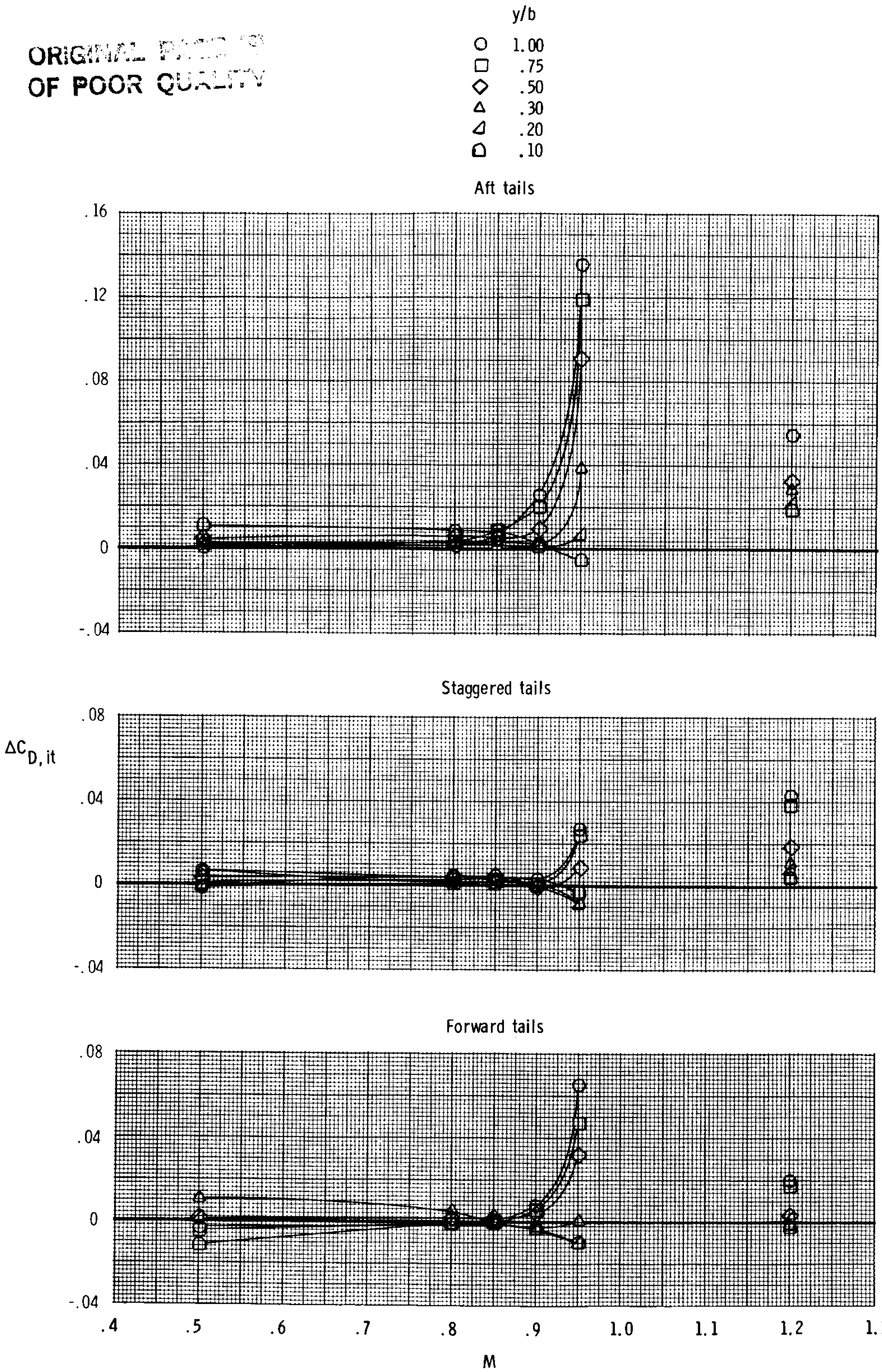

(b) Complete empennage arrangements.

Figure 17. Concluded.

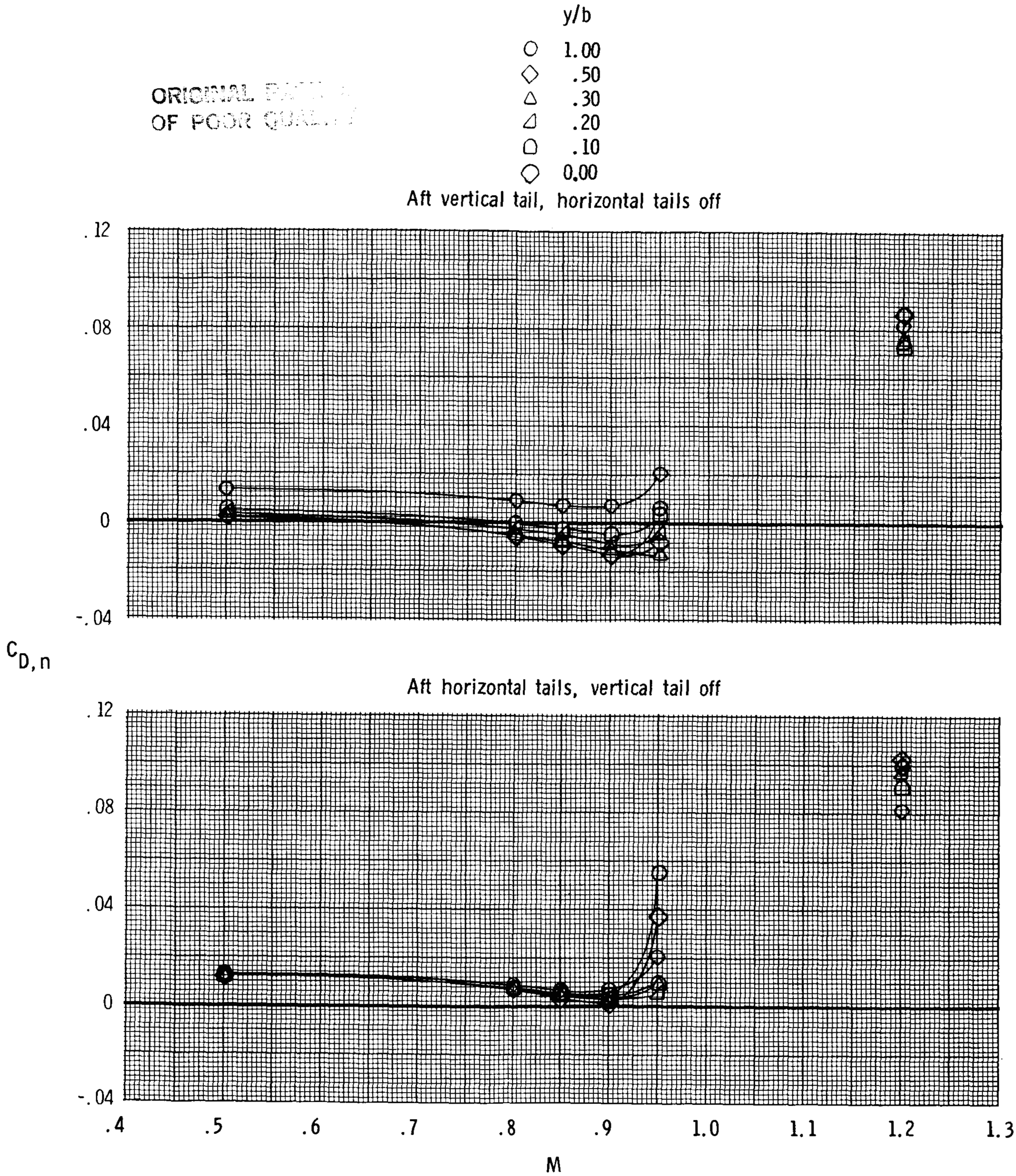

(a) Individual tail surfaces.

Figure 18. Effect of tail span on variation of nozzle drag coefficient with Mach number.

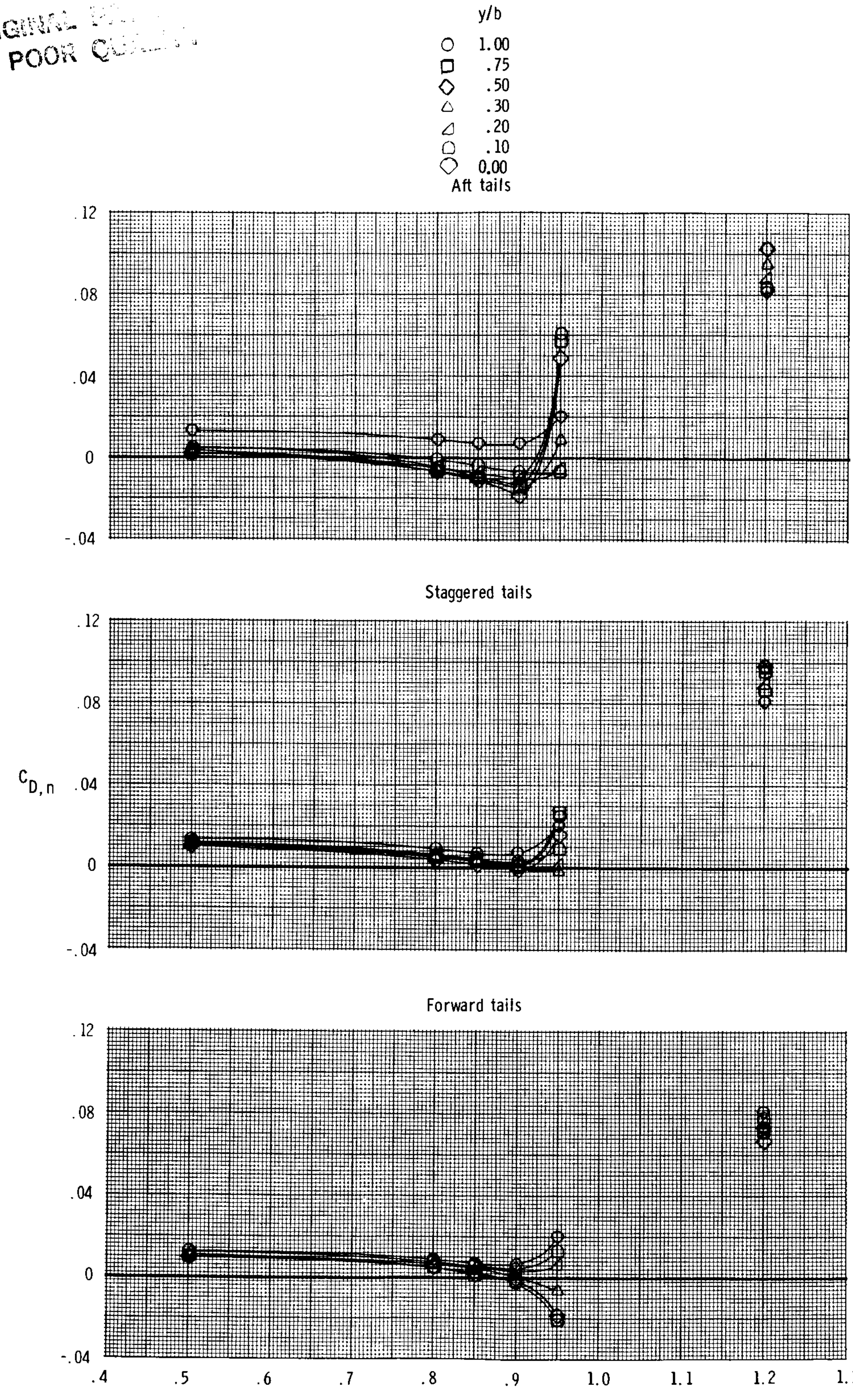

(b) Complete empennage arrangements.

Figure 18. Concluded.

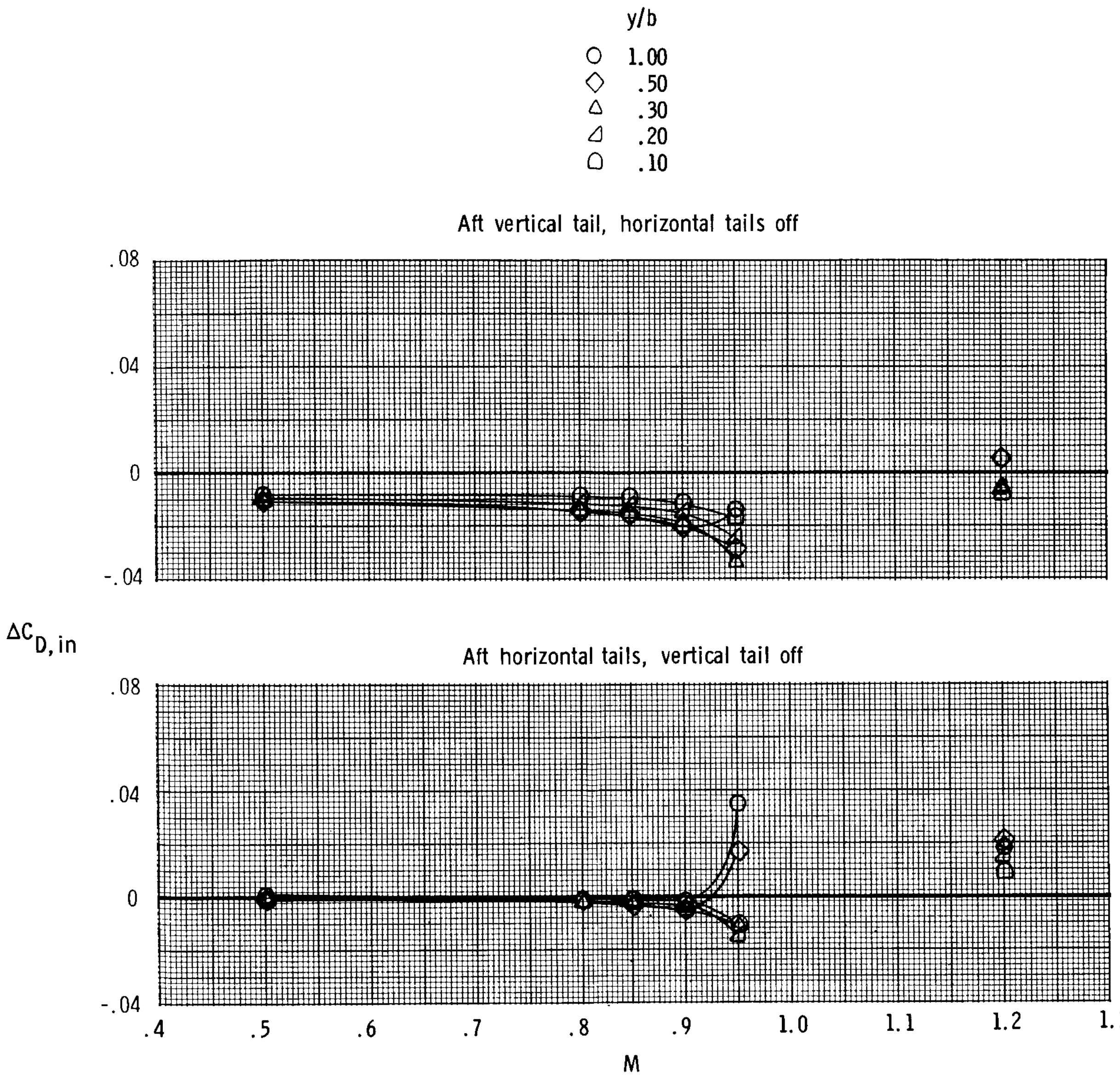

(a) Individual tail surfaces.

Figure 19. Effect of tail span on variation of nozzle tail interference drag coefficient increment with Mach number.

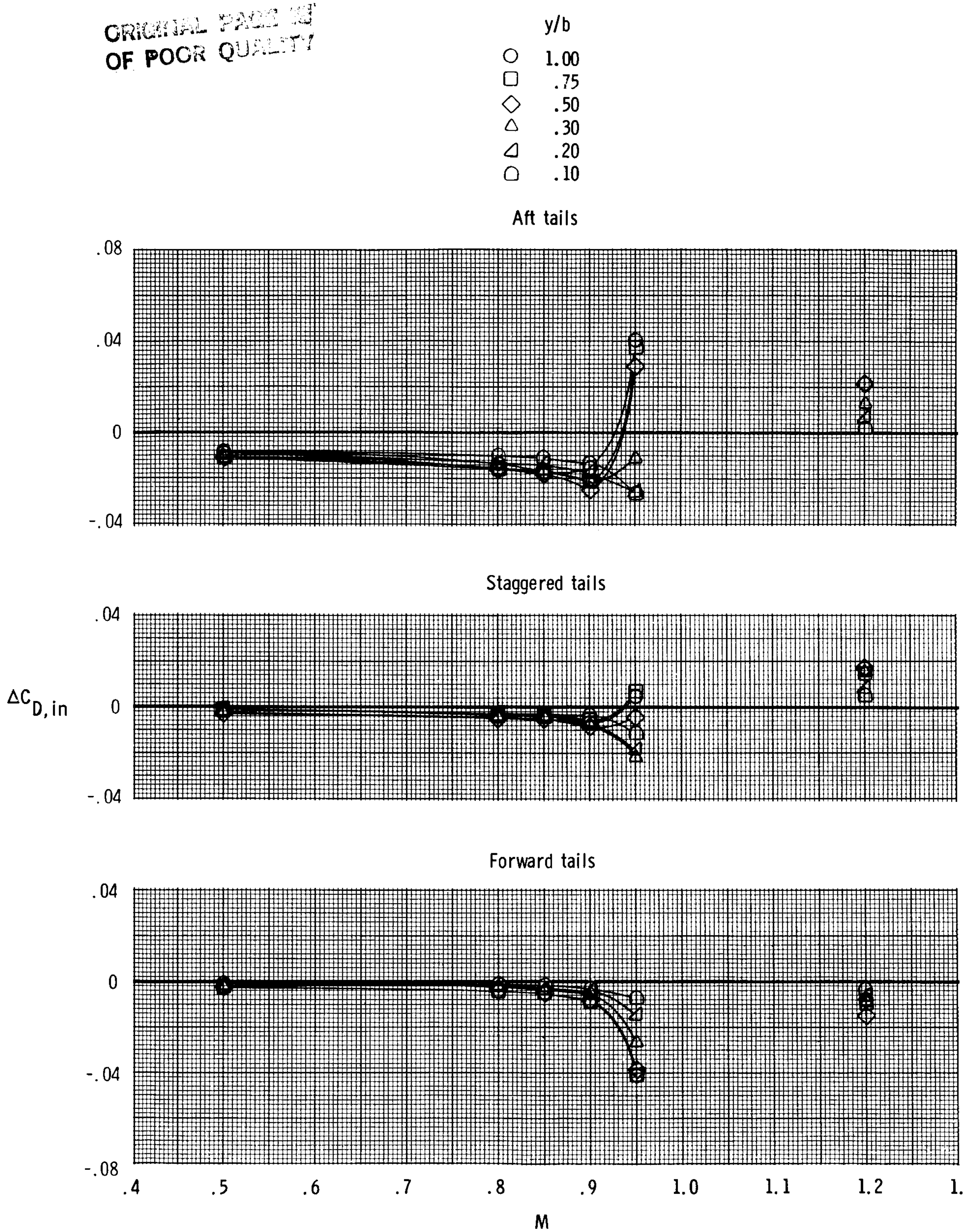

(b) Complete empennage arrangements.

Figure 19. Concluded.

ORIGINAL PAGE IS
OF POOR QUALITY

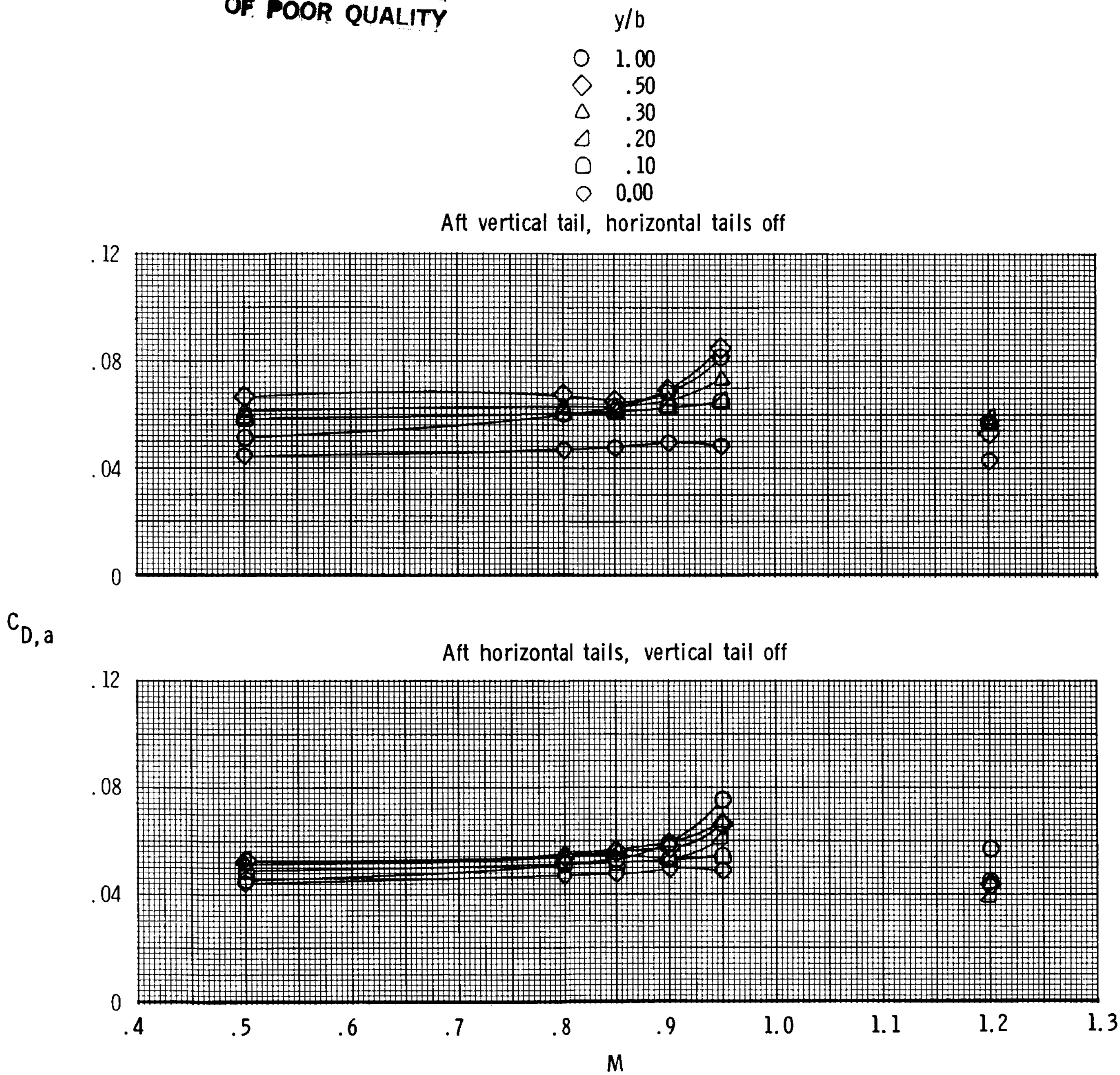

(a) Individual tail surfaces.

Figure 20. Effect of tail span on variation of afterbody drag coefficient with Mach number.

ORIGINAL PAGE IS
OF POOR QUALITY

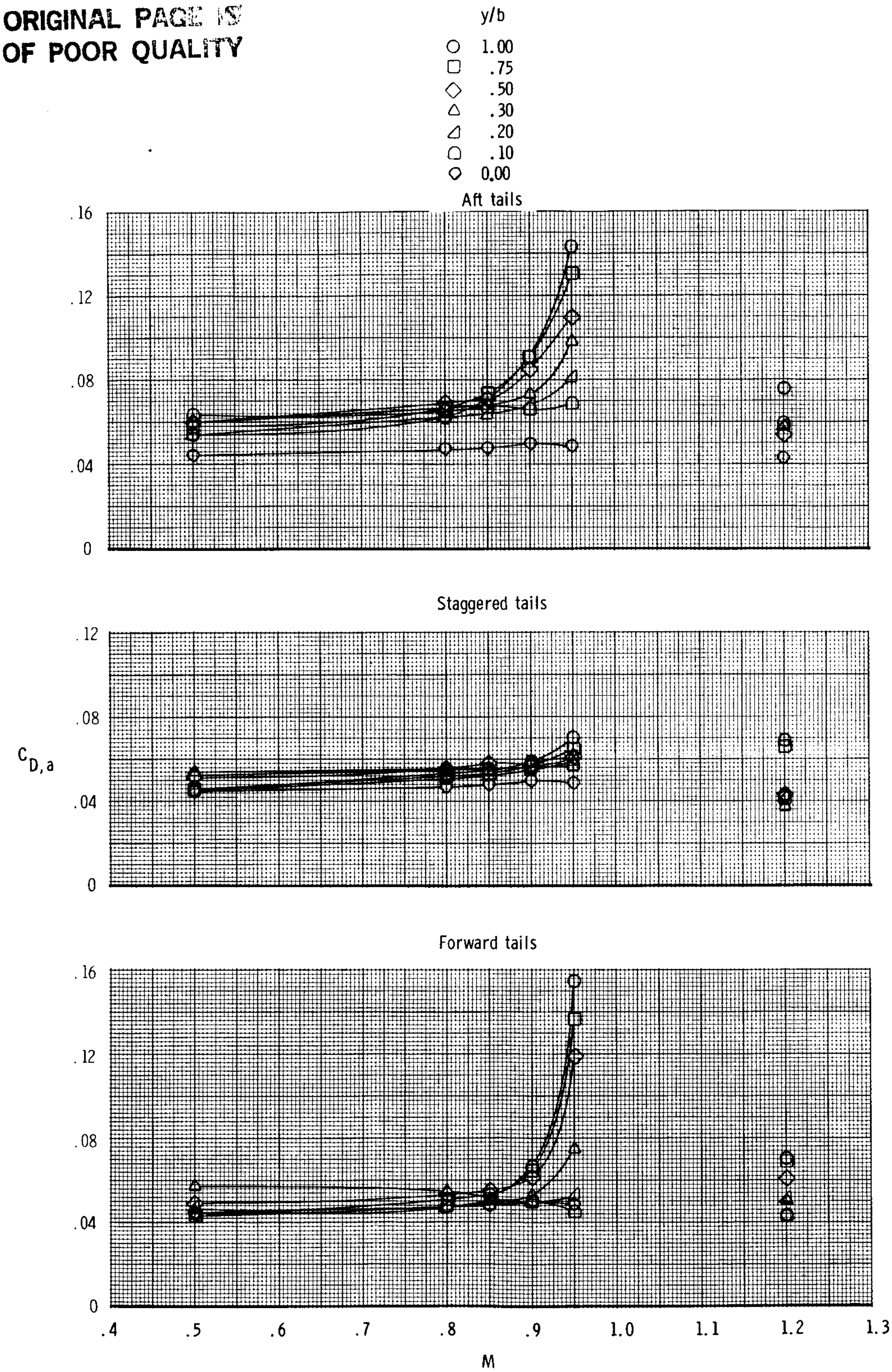

(b) Complete empennage arrangements.

Figure 20. Concluded.

ORIGINAL PAGE IS
OF POOR QUALITY

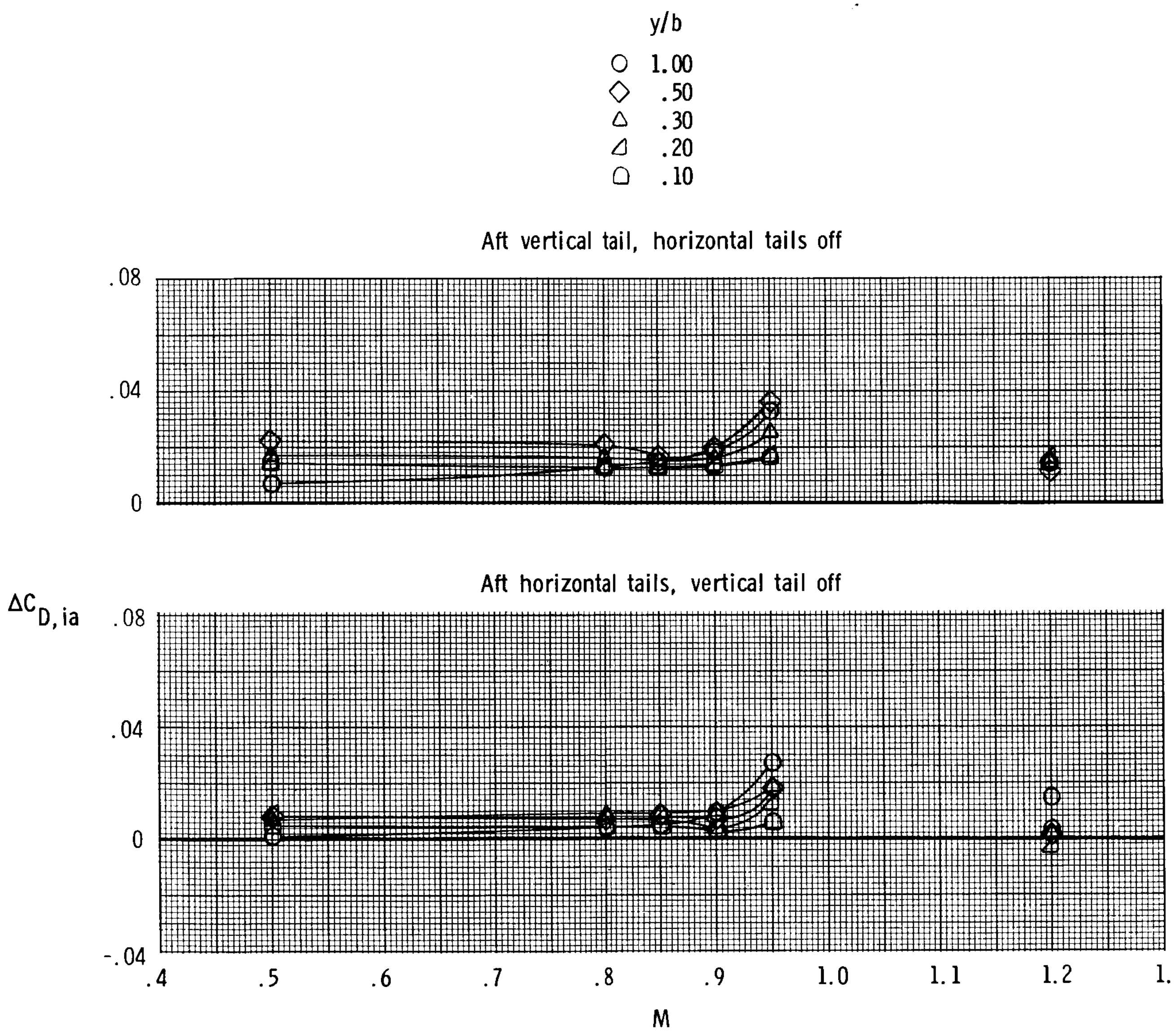

(a) Individual tail surfaces.

Figure 21. Effect of tail span on variation of afterbody tail interference drag coefficient increment with Mach number.

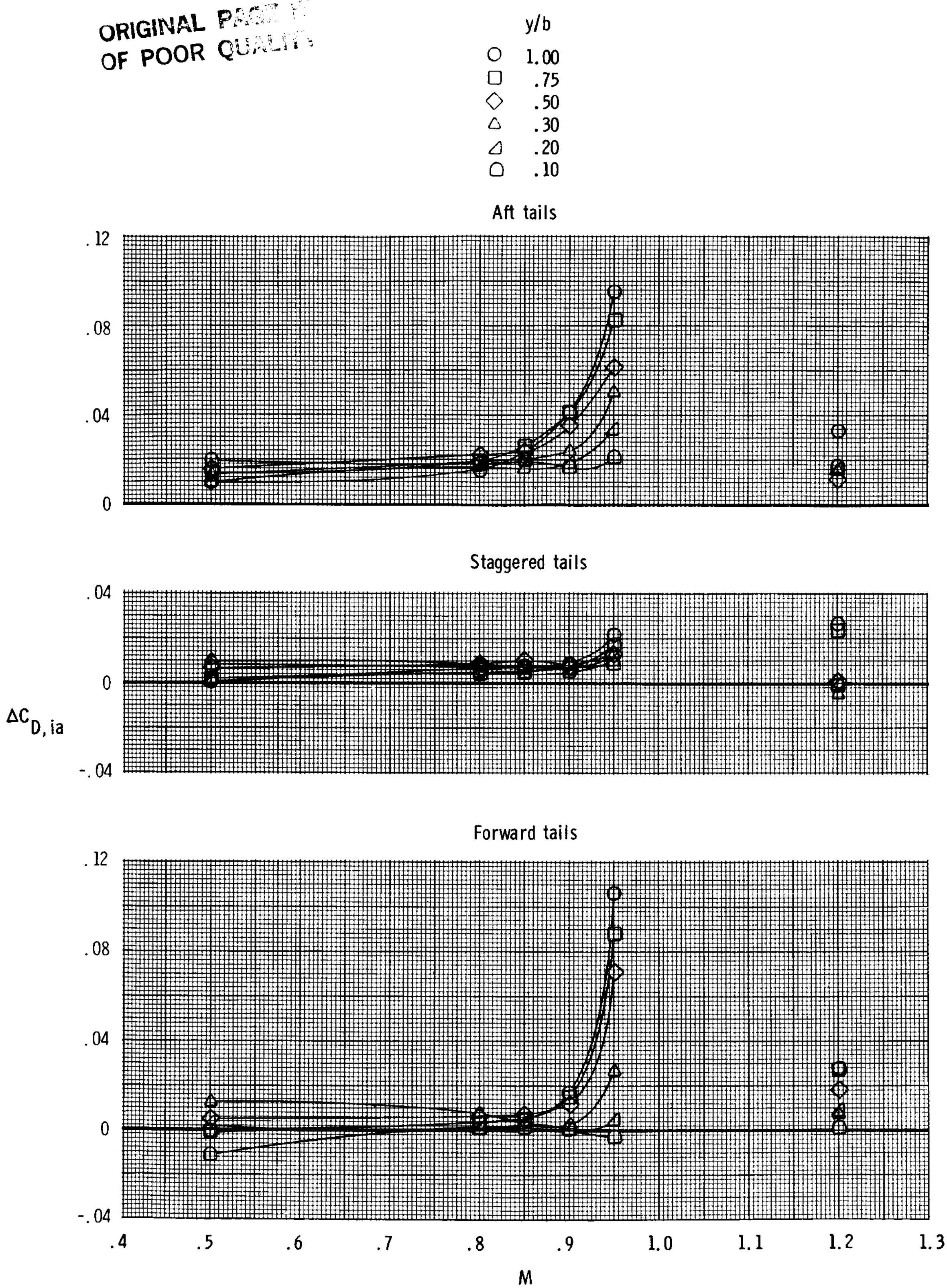

(b) Complete empennage arrangements.

Figure 21. Concluded.

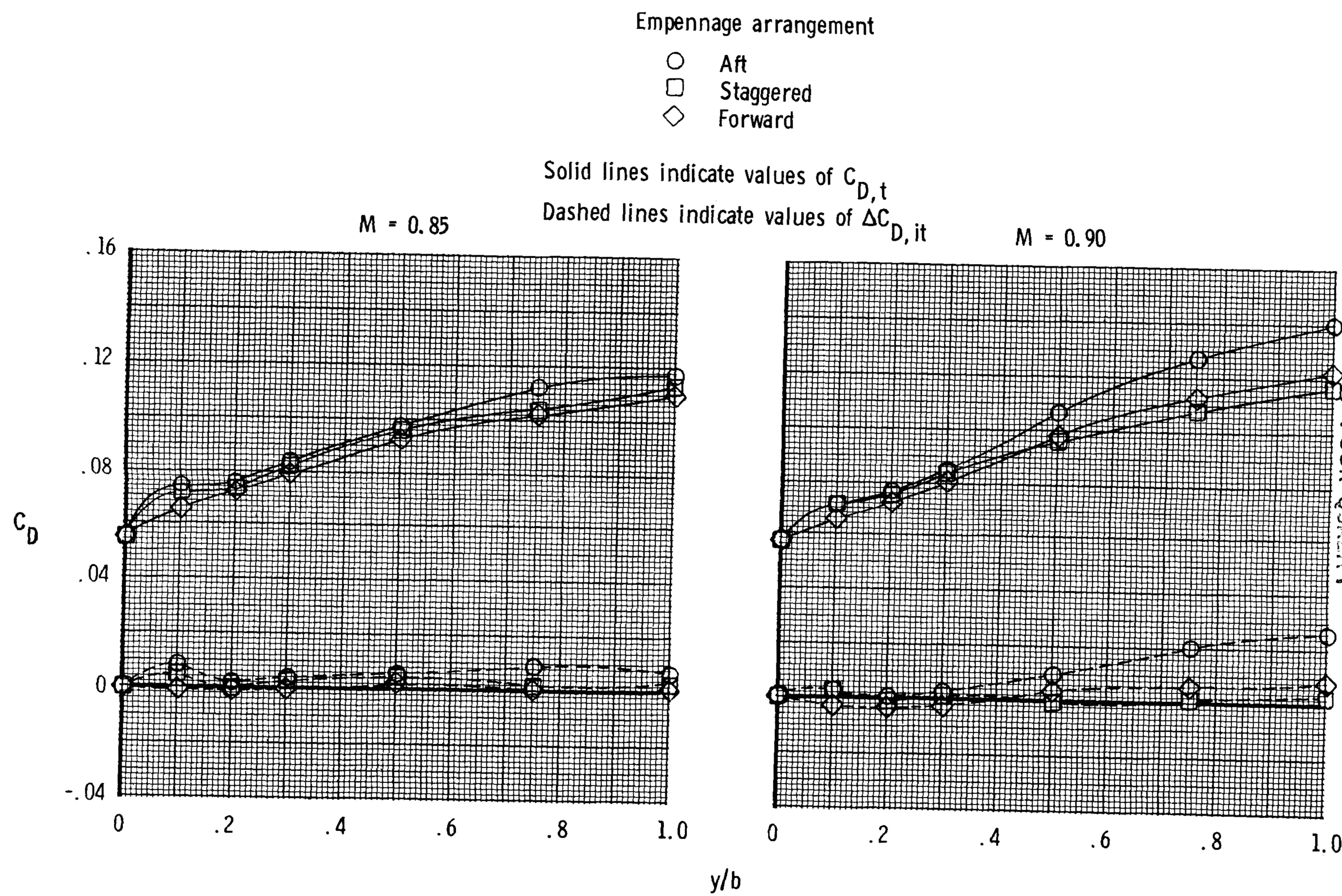

Figure 22. Effect of empennage arrangement on total aft-end and tail interference drag coefficients.

ORIGINAL PAGE IS OF POOR QUALITY

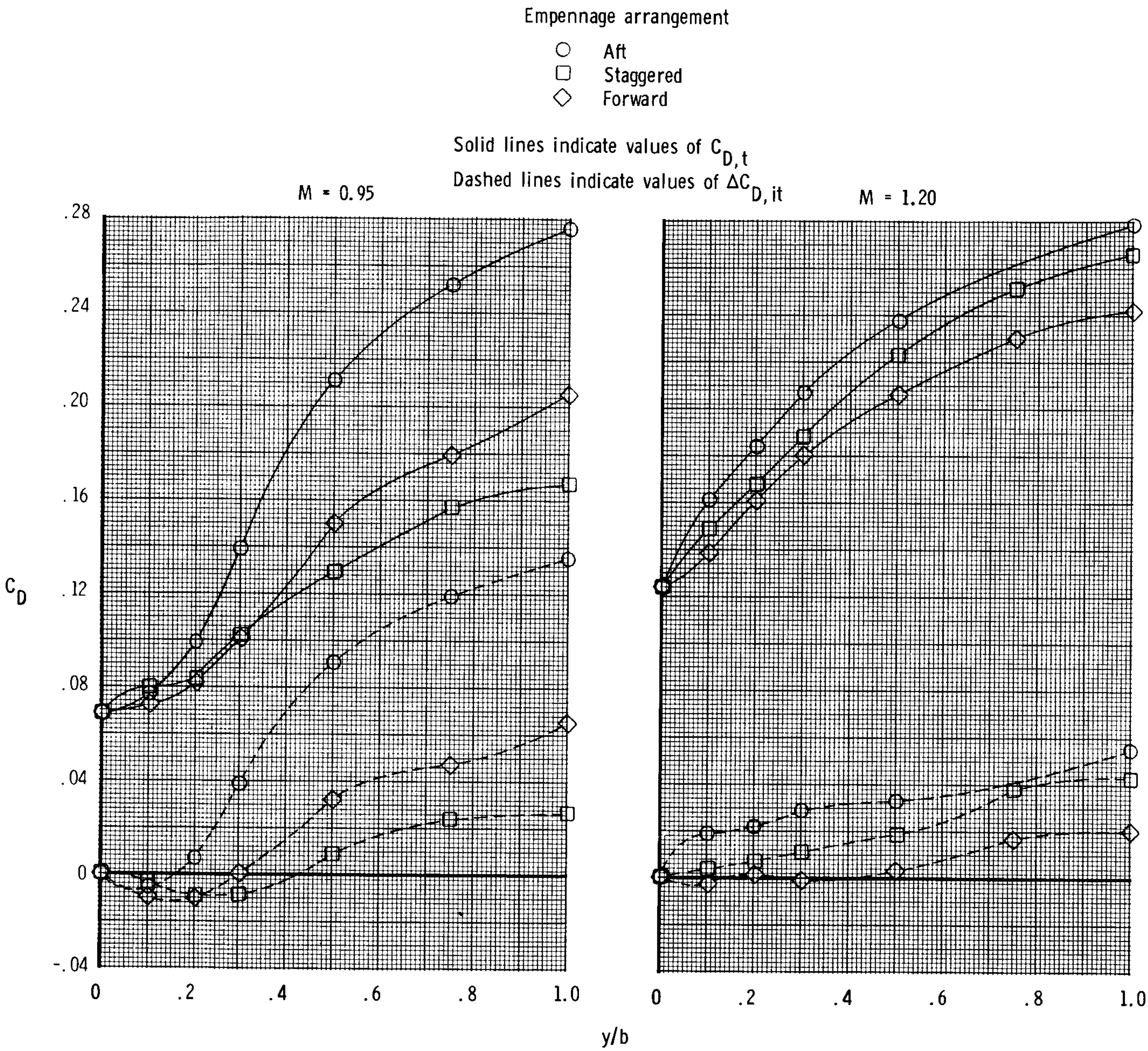

Figure 22. Concluded.

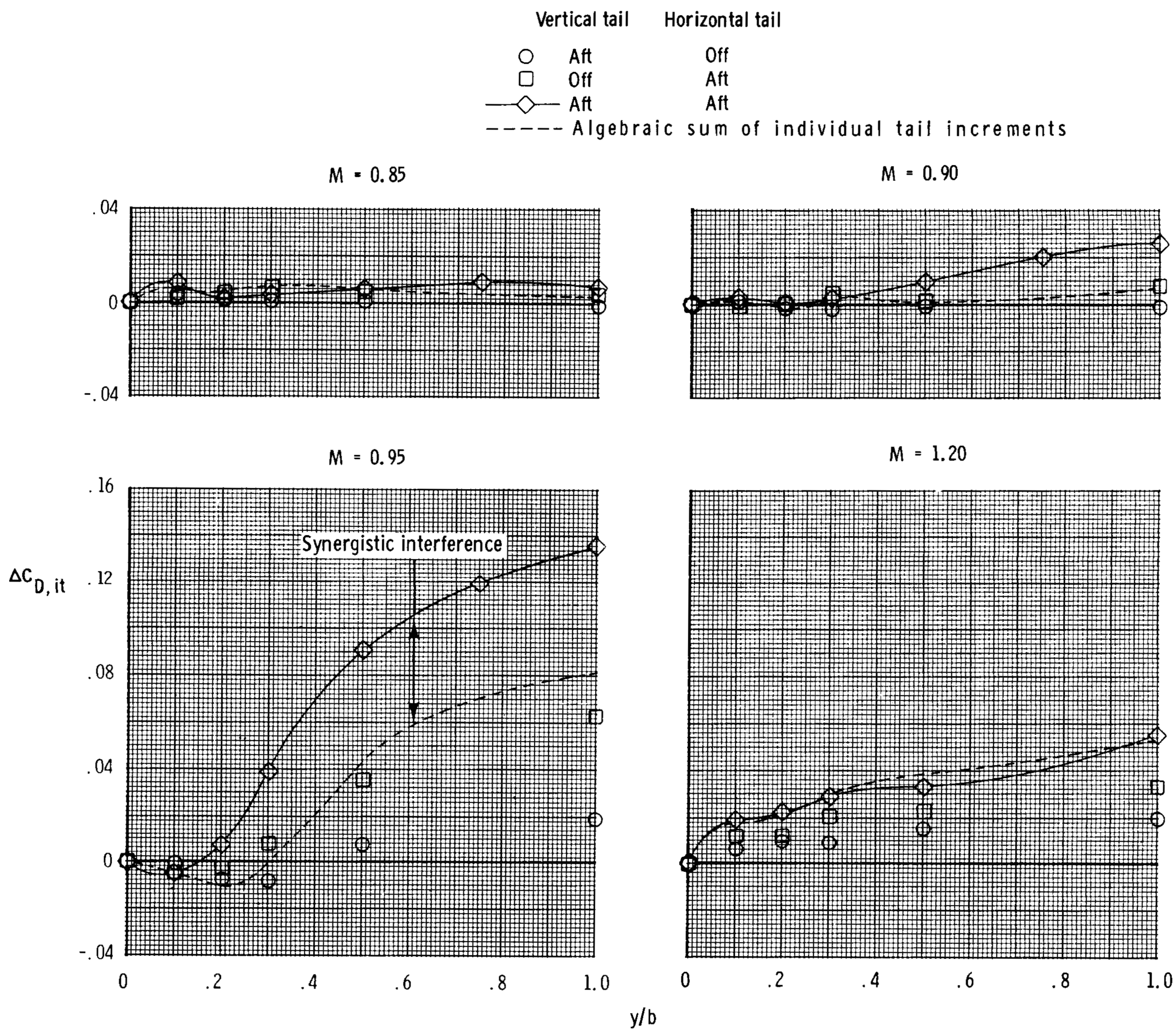

(a) Total aft-end tail interference.

Figure 23. Effect of tail location on synergistic tail interference.

ORIGINAL PAGE IS
OF POOR QUALITY

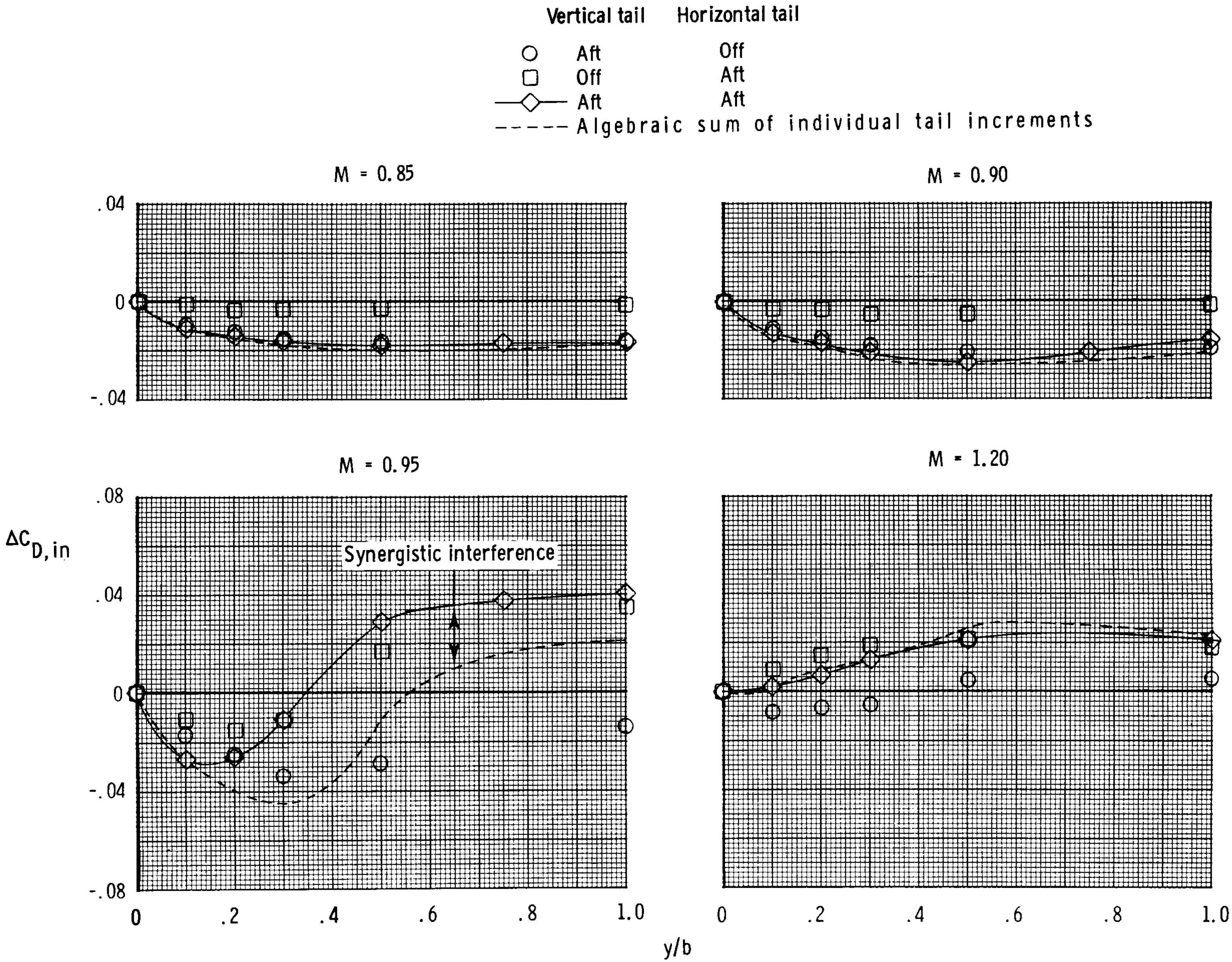

(b) Nozzle tail interference.

Figure 23. Continued.

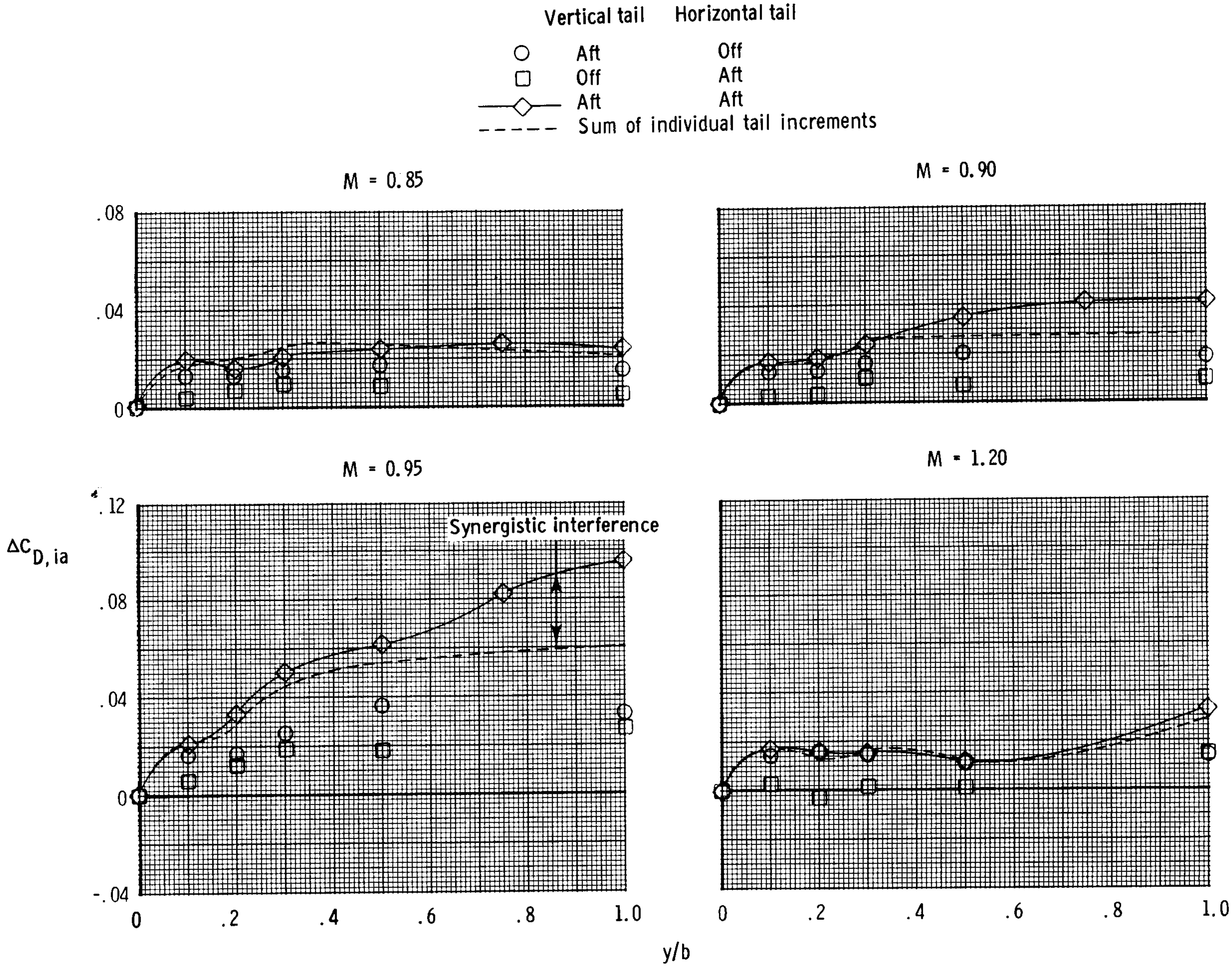

(c) Afterbody tail interference.

Figure 23. Concluded.

1. Report No.	2. Government Accession No.	3. Recipient's Catalog No.
NASA TP-2352		

4. Title and Subtitle
EFFECTS OF TAIL SPAN AND EMPENNAGE ARRANGEMENT ON DRAG OF A TYPICAL SINGLE-ENGINE FIGHTER AFT END

5. Report Date
September 1984

6. Performing Organization Code
505-40-90-01

7. Author(s)
James R. Burley II and Bobby L. Berrier

8. Performing Organization Report No.
L-15742

9. Performing Organization Name and Address
NASA Langley Research Center
Hampton, VA 23665

10. Work Unit No.

11. Contract or Grant No.

12. Sponsoring Agency Name and Address
National Aeronautics and Space Administration
Washington, DC 20546

13. Type of Report and Period Covered
Technical Paper

14. Sponsoring Agency Code

15. Supplementary Notes

16. Abstract

An investigation has been conducted in the Langley 16-Foot Transonic Tunnel to determine the effects of tail span and empennage arrangement on drag of a single-engine nozzle/afterbody model. Tests were conducted at Mach numbers from 0.50 to 1.20, nozzle pressures from 1.0 (jet off) to 8.0, and angles of attack from -3° to 9°, depending upon Mach number. Three empennage arrangements (aft, staggered, and forward) were investigated with several different tail spans. The results of the investigation indicate that tail span and position have a significant effect on the drag at transonic speeds. Unfavorable tail interference was largely due to the outer portion of the tail surfaces. The inner portion near the nozzle and afterbody did little to increase drag other than surface skin friction. Tail positions forward of the nozzle generally had lower tail interference.

17. Key Words (Suggested by Author(s))
Single-engine fighter
Nozzle drag
Afterbody drag
Empennage interference
Span effects

18. Distribution Statement
[redacted]

[redacted]

19. Security Classif. (of this report)	20. Security Classif. (of this page)	21. No. of Pages	22. Price
Unclassified	Unclassified	134	